Molecular modeling of hydrogen gas adsorption in hydrated clay environments in the context of geological disposal of radioactive waste

Pinar Citli

COLLEGE DOCTORAL PAYS DE LA LOIRE
ED MATIERE, MOLECULES MATERIAUX ET GEOSCIENCES

IMT Atlantique
Bretagne-Pays de la Loire
École Mines-Télécom

THÈSE DE DOCTORAT

L'ÉCOLE NATIONALE SUPÉRIEURE MINES-TÉLÉCOM ATLANTIQUE
BRETAGNE PAYS DE LA LOIRE - IMT ATLANTIQUE

ÉCOLE DOCTORALE N° 596
Matière, Molécules, Matériaux et Géosciences
Spécialité : *Chimie Physique et Chimie Theorique*

Par

Pinar CITLI

Molecular modeling of hydrogen gas adsorption in hydrated clay environments in the context of geological disposal of radioactive waste

Thèse présentée et soutenue à IMT Atlantique, Nantes, le 26 Février 2024
Unité de recherche : SUBATECH UMR 6457
Thèse N° : 2024IMTA0392

Rapporteurs avant soutenance :

Ali ZAOUI — Professeur, Université de Lille, France
Virginie MARRY — Professeure, Sorbonne Université, France

Composition du Jury :

Président :	Abdesselam ABDELOUAS	Professeur, IMT Atlantique, France
Examinateurs :	Ali ZAOUI	Professeur, Université de Lille, France
	Virginie MARRY	Professeure, Sorbonne Université, France
	Pascaline PRÉ	Professeure, IMT Atlantique, France
	Ozgur YAZAYDIN	Professeur, University College London, Angleterre
Dir. de thèse :	Andrey KALINICHEV	Directeur de Recherche, IMT Atlantique, Nantes, France

ACKNOWLEDGMENT

Foremost, I would like to express my sincere acknowledgment to the Ministry of National Education of the Republic of Türkiye for the financial support, which gave me the opportunity to pursue my doctoral study in the Subatech Laboratory at IMT Atlantique. I also would like to extend my sincere acknowledgment to the industrial chair "Storage and Disposal of Radioactive Waste" at Institut Mines-Télécom (IMT) Atlantique, funded by ANDRA, Orano, and EDF, for the financial support during my doctoral study.

Firstly, I would like to sincerely thank my thesis supervisor, Andrey G. Kalinichev, for his guidance throughout my PhD studies. I am grateful for his continuous support with molecular modeling and for encouraging me to attend winter and summer schools, where I gained fundamental knowledge in this field. Additionally, I thank him for encouraging me to present my research findings at numerous international conferences.

I would also like to thank Özgür Yazaydın and Laurent Truche, the members of my thesis individual monitoring committee (CSI). Their valuable comments and insightful ideas have greatly enriched my thesis. I am particularly thankful for their constructive feedback, which has helped to improve the quality of my work and also provided new directions for exploration.

Additionally, I would like to express my gratitude to Sylvia M. Mutisya from our modeling group. Sharing an office with her has provided a conducive environment for our insightful discussions about the project. I deeply appreciate her valuable encouragement, support and help with molecular modeling methods. I extend my gratitude to Denys Grekov for his invaluable support and help throughout my PhD studies on gas adsorption, and appreciate the valuable ideas he shared with me. I also would like to thank Narasimhan Loganathan for his help with the hybrid Monte Carlo/molecular dynamics (GCMD) simulation method, and Sébastien Le Crom for his helpful comments at the final stages of my PhD. I would like to thank all my colleagues from Radiochemistry group at Subatech Laboratory.

The majority of the calculations in this thesis were made using servers of the modeling group and Subatech's local serversfor which I am sincerely grateful. I would also like to ac-

knowledge the computational resources provided by GENCI (Grand Équipement National de Calcul Intensif) – [CINES, TGCC] (DARI A0120906921, A0140906921) Additionally, I extend my gratitude to Subatech's IT department, especially for their prompt assistance whenever needed.

Finally, I would like to extend my heartfelt gratitude to my family and friends, whose unwavering support has been invaluable to me. I am deeply grateful to my brother Utku, and my parents Türkan and Bedri Çitli, for their constant encouragement and endless support, despite the thousands of kilometers between us. I also thank Ali Ak for his continuous support and invaluable help. Additionally, I appreciate all the friends I have both here and back in Türkiye, for their support throughout my journey.

Abstract

Clay-rich formations are considered as optimal host rock for deep geological repository facilities for high-level radioactive waste due to their certain features such as low permeability of the host rocks, reducing environment, high thermal conductivity, and self-sealing properties. Gas, particularly H_2 which is expected to be the most abundant gas in the repository, may form during long-term storage through mechanisms such as anoxic corrosion and water radiolysis. Generation and accumulation of gases in the repository may potentially lead the gas pressure build-up, resulting in a risk of overpressure and fracture of the surrounding clay rock unless it diffuses, reacts, or gets absorbed by constituent clay rocks. Therefore, molecular-scale understanding of H_2 behavior in clay is essential for safe geological disposal and storage, and for developing effective strategies. In this thesis, montmorillonite, a common smectite widely found in host rock compositions and used as an engineered barrier, is chosen as the clay model. Atomistic simulations of H_2 adsorption within the interlayers of hydrated Na-, Ca-, and Cs-montmorillonites are conducted at 25, 50, and 90°C, up to 120 bar using Monte Carlo and hybrid Monte Carlo/molecular dynamics methods. To this end, the impact of several other factors, including the presence of water and pore size are investigated, aiming to improve the fundamental understanding of the physical and chemical processes governing interactions among H_2, aqueous solutions, and clay. Furthermore, hydrogen adsorption under extreme conditions is explored to determine the point of saturation in clays. The mole fraction of adsorbed hydrogen within the interlayers of hydrated clays demonstrates over-solubility compared to its solubility in water, attributed to the strong interaction between H_2 and the clay surface.

Keywords: Molecular simulations, adsorption, clays, montmorillonite, hydrogen

Résumé

Les déchets radioactifs sont générés en raison de l'utilisation répandue de matériaux radioactifs dans divers secteurs, notamment les centrales nucléaires, les industries non nucléaires, la défense, le secteur médical et la recherche. Les déchets de niveau intermédiaire à longue durée de vie (ILW-LL) se composent principalement de déchets issus des structures métalliques entourant le combustible, tels que les coques et les couvercles, qui proviennent du retraitement du combustible usé. De plus, il comprend une plus petite proportion de déchets technologiques résultant de l'utilisation et de la maintenance des installations nucléaires, des déchets générés lors du traitement des effluents liquides (boues bitumineuses) et des déchets activés provenant des réacteurs nucléaires. En revanche, les déchets de haute activité (HLW) proviennent principalement du retraitement du combustible usé. Ces déchets sont composés de résidus hautement radioactifs résultant de la dissolution chimique du combustible usé.

Étant donné les risques que les matériaux radioactifs posent pour la santé et l'environnement, il est crucial de garantir des procédures de gestion appropriées pour les déchets radioactifs. Il convient de noter que la gestion des déchets radioactifs varie d'un pays à l'autre, car il existe des différences dans les critères de classification et de caractérisation en fonction de leurs caractéristiques physiques, chimiques et radiologiques. En France, le stockage géologique profond est considéré comme essentiel pour la gestion sûre à la fois des ILW-LL et des HLW. Les déchets sont encapsulés dans du verre puis conditionnés dans des conteneurs en acier inoxydable avant d'être placés sur le site d'élimination désigné.

Tous les pays dotés de stratégies de gestion à long terme des déchets radioactifs ont adopté le concept de dépôts de stockage des déchets radioactifs avec un système à plusieurs barrières. Le système à plusieurs barrières, conçu pour isoler les déchets de la biosphère et former un concept de sécurité global, se compose à la fois de systèmes de barrières naturelles et artificielles.

La barrière naturelle fait référence à la formation géologique choisie comme roche hôte pour le dépôt de déchets radioactifs, ainsi qu'à son environnement environnant, y compris le cadre environnemental sélectionné pour l'installation de stockage. Afin de garantir

la sécurité et la durabilité du stockage géologique permanent des déchets nucléaires, les dépôts de déchets doivent satisfaire à un certain nombre de conditions physiques, chimiques et géo-thermo-mécaniques. Les roches riches en argile sont considérées comme des candidates optimales comme roches hôtes pour les installations de stockage géologique des déchets radioactifs. Ces roches possèdent des caractéristiques favorables qui fournissent un environnement stable et géologiquement isolé pour la confinement à long terme des déchets, comprenant une faible conductivité hydraulique, une bonne conductivité thermique, une auto-cicatrisation en raison de leurs propriétés de gonflement, une rétention élevée, une très faible perméabilité et des taux de diffusion lents. La roche argileuse Callovo-Oxfordien a été soigneusement sélectionnée comme roche hôte pour les dépôts de déchets radioactifs en France. Elle se compose de phases minérales argileuses (illite/smectite interstratifiée, micas, illite, kaolinite et chlorites) constituant jusqu'à 60 % de sa masse totale, ainsi que de quartz fin, de carbonates (principalement de la calcite avec un faible pourcentage de dolomite), et une quantité infime d'autres phases telles que la pyrite et les matériaux organiques.

Les barrières artificielles, qui font référence aux matériaux spécifiquement conçus, jouent un rôle important en tant que couches de sécurité initiales pour prévenir la dispersion des radionucléides dans les barrières naturelles. Elles peuvent être simplement divisées en trois catégories : la forme des déchets, les emballages de déchets, et les systèmes de remblayage et d'étanchéité. La forme des déchets, qui contient initialement toute la radioactivité, doit être robuste avec une libération minimale de radioactivité. La forme des déchets est généralement placée dans un conteneur métallique. Les réglementations dans de nombreux pays exigent de placer les déchets dans des emballages normalisés conçus pour simplifier la manipulation, le positionnement et la récupération des déchets, tout en assurant un confinement pendant des périodes prolongées en fonction du type de déchets. Afin de contrôler et de stabiliser les conditions thermo-hydro-mécaniques-chimiques, et d'assurer des perméabilités et/ou diffusivités faibles, ainsi qu'un retardement à long terme après la fermeture, le vide entourant les emballages de déchets doit être rempli d'un matériau de remblai et/ou de tampon compatible avec la barrière artificielle et géologique et correctement scellé. Des recherches approfondies ont été menées sur le remblai de bentonite, notamment pour la gestion des conteneurs de déchets produisant de la chaleur. La bentonite joue un rôle vital car elle agit comme un tampon autour des emballages individuels de déchets et fonctionne comme un joint de tunnel efficace, séparant efficacement les galeries d'élimination des puits accessibles depuis la surface. La bentonite,

contenant une quantité significative de minéral argileux appelé montmorillonite, et son mélange avec du sable sont choisis pour leur faible perméabilité hydraulique due à leur capacité d'auto-obturation et de gonflement pour aider à restaurer la caractéristique de faible conductivité hydraulique de la roche hôte perturbée suite à la construction du dépôt en scellant les vides dans la barrière installée.

En résumé, les argiles jouent un rôle crucial à la fois en tant que barrières naturelles et artificielles dans le stockage géologique profond des déchets radioactifs. Une compréhension de leur structure et de leurs caractéristiques est essentielle pour garantir la gestion à long terme, sûre et efficace des déchets radioactifs.

Sous les conditions finales qui surviennent pendant la phase de post-fermeture dans le dépôt de déchets radioactifs, la génération de gaz se produit en raison de la nature de certains composants clés dans les déchets. La génération de gaz dans un dépôt se produit dans des conditions anaérobies peu de temps après l'état initial, avec une température de la roche entre 10 et 50°C, en fonction de la profondeur. De plus, la roche hôte influence significativement la génération de gaz en raison de ses diverses caractéristiques telles que l'humidité, la minéralisation, la composition de l'eau souterraine et le pH.

Divers mécanismes peuvent conduire à la génération de gaz dans le dépôt. Les métaux se trouvent principalement dans les cellules de stockage, sous forme de composants structurels, de contenants ou de formes de déchets. La corrosion anaérobie des métaux en acier inoxydable tels que le fer conduit à la formation d'hydrogène, H_2. De plus, la radiolyse de l'eau due à la désintégration radioactive produit principalement H_2, mais aussi O_2, CO_2, et CH_4. La dégradation microbienne de la matière organique conduit à la production de CH_4 et de CO_2 comme principaux produits. La production d'hélium due à la désintégration alpha génère de la vapeur d'eau près de la cartouche de combustible usé, et les gaz radioactifs, tels que le Rn, sont libérés. De plus, de l'air sera également piégé dans le dépôt, principalement dans le remblai des galeries, après la fermeture. L'hydrogène est le gaz le plus abondant dans ces conditions de dépôt et d'environnement, car la corrosion métallique anaérobie est le processus prédominant, contribuant à plus de 90% des gaz produits (ANDRA, 2005a).

L'accumulation de gaz dans le dépôt peut entraîner une augmentation de la pression des gaz, ce qui augmente le risque de surpression et de fracture de la roche argileuse environnante, à moins qu'il ne se diffuse, réagisse ou soit absorbé par les roches argileuses qui ont une capacité de sorption élevée en raison de leurs grandes surfaces spécifiques.

Comme l'accumulation de pression de gaz pourrait affecter la stabilité du dépôt de déchets radioactifs, il est crucial d'étudier la capacité d'adsorption de gaz des minéraux argileux.

Pour développer des stratégies fiables et à long terme visant à prévenir la déstabilisation chimique et mécanique des dépôts de déchets radioactifs, il est crucial d'améliorer la compréhension quantitative à l'échelle moléculaire des processus sous-jacents. Les simulations atomistiques précédentes de l'adsorption de gaz dans les argiles étaient principalement axées sur l'adsorption de CO_2 et de CH_4, tandis qu'une attention limitée était accordée à l'adsorption de H_2 dans les argiles. Bien qu'il existe des études expérimentales sur l'adsorption d'hydrogène, les simulations se concentrent principalement sur la diffusion de l'hydrogène dans l'argile plutôt que sur son absorption. Par conséquent, il y a un manque de recherche sur l'adsorption de l'hydrogène et son absorption dans les argiles dans des conditions de température et de pression qui sont censées se développer dans les dépôts de déchets radioactifs de haute activité.

L'objectif de ce projet est de fournir une analyse structurée de l'adsorption de H_2 dans l'environnement argileux communément trouvé dans les dépôts de déchets radioactifs. À cette fin, cette thèse étudie l'impact de plusieurs facteurs cruciaux, notamment la température, la pression, la présence d'eau, la taille des pores/le niveau d'hydratation, et le type de cation intercalaire. Plus précisément, nous explorons l'adsorption de H_2 dans les inter-couches de montmorillonite à base de Na, de Ca et de Cs, à la fois sèche et hydratée (à différents niveaux), à des températures de 25, 50 et 90°C, et des pressions allant jusqu'à 120 bar, au moyen de méthodes Monte Carlo et hybrides Monte Carlo/dynamique moléculaire de simulation par ordinateur afin d'améliorer la compréhension fondamentale des processus physiques et chimiques contrôlant les interactions entre H_2, les solutions aqueuses et le type d'argile montmorillonite. De plus, l'étude vise à examiner l'adsorption de l'hydrogène à haute pression pour comprendre où le H_2 atteint la saturation dans la montmorillonite.

La modélisation computationnelle est une méthode qui utilise des modèles et des algorithmes basés sur l'ordinateur pour étudier des systèmes réels ou théoriques en les reproduisant. Cette approche permet l'analyse, la prédiction et l'interprétation du comportement des systèmes sans nécessiter d'expériences physiques pratiques. La modélisation computationnelle peut être appliquée à différentes échelles, en fonction de l'échelle de temps des processus et de la taille des systèmes.

Les méthodes de mécanique moléculaire basées sur des expressions analytiques paramétrisées qui prennent en compte les charges atomiques et les interactions entre les atomes sont utilisées dans ce projet. Ces méthodes permettent le calcul des propriétés structurales, thermodynamiques, de transport et dynamiques en générant un nombre significatif de configurations atomiques. Elles permettent également l'interprétation des résultats expérimentaux ou fournissent des orientations pour des expériences futures, ainsi que l'étude et la prédiction de conditions extrêmes qui ne peuvent pas être atteintes pratiquement par des expériences. Il existe deux méthodes classiques de modélisation moléculaire, à savoir Monte Carlo et Dynamique Moléculaire. Monte Carlo implique une moyenne d'ensemble des configurations moléculaires sur une chaîne de Markov aléatoire générée par calcul. La Dynamique Moléculaire, en revanche, traite d'une moyenne temporelle sur une trajectoire dynamique dans l'espace des phases du système simulé.

La méthode de Monte Carlo (MC) est basée sur un échantillonnage aléatoire. Les méthodes MC permettent la détermination des propriétés structurales et thermodynamiques en générant de nouvelles configurations à partir des configurations existantes, et des résultats statistiquement valides sont obtenus en faisant appel à la distribution de Boltzmann. Bien que les simulations MC aient un avantage significatif en termes de nécessité de moins de temps informatique par rapport aux simulations MD, il n'est pas possible de calculer des propriétés dynamiques telles que le coefficient de diffusion, le déplacement quadratique moyen ou la viscosité, car cette méthode n'est pas dépendante du temps.

Dans les simulations de Monte Carlo, les moyennes d'ensemble sont utilisées pour obtenir une moyenne statistique et certaines variables d'état sont constantes car ces simulations sont effectuées sous des ensembles de mécanique statistique à l'équilibre. Dans l'ensemble canonique grand (μVT), introduit pour la première fois par Norman and Filinov, 1969, le potentiel chimique, le volume et la température sont constants et c'est le seul ensemble dans lequel le nombre de particules est autorisé à fluctuer. De plus, c'est l'ensemble le plus pratique pour les études d'adsorption car le potentiel chimique et la température sont fixés.

La dynamique moléculaire (MD) est une méthode à l'échelle atomique basée sur la deuxième loi de Newton et utilisée pour simuler le mouvement d'un système classique de particules. Les applications de la MD présentent de nombreux avantages par rapport aux méthodes expérimentales. Les résultats de la simulation peuvent fournir une description atomistique des processus physiques et/ou chimiques et aider à l'interprétation des

résultats expérimentaux. De plus, elle permet de calculer non seulement les propriétés structurales et thermodynamiques, mais aussi les propriétés de transport et dynamiques telles que le coefficient de diffusion des gaz dissous, et également d'étudier et de prédire des conditions extrêmes telles que dans le stockage géologique des déchets radioactifs. Contrairement à la méthode de Monte Carlo (MC), qui déplace les particules de manière stochastique, la MD déplace les particules de manière déterministe. Elle génère les états (configurations et vitesses) en intégrant la deuxième loi de Newton, les équations du mouvement.

L'approche hybride Monte Carlo/dynamique moléculaire (MC/MD) intègre les méthodologies du Monte Carlo canonique grand (GCMC) et de la dynamique moléculaire (MD), permettant la détermination des détails d'adsorption, structurels et dynamiques au cours de la même simulation exécutée simultanément. Diverses approches existent pour effectuer ce type de simulations. La méthode de dynamique moléculaire canonique grand (GCMD) est une technique hybride Monte Carlo/dynamique moléculaire qui utilise un échantillonnage Monte Carlo pour l'insertion et la suppression de molécules de fluide avec une probabilité égale à chaque pas de temps de la dynamique moléculaire. Par conséquent, dans les simulations GCMD, le nombre de molécules fluctue de manière similaire aux simulations GCMC tout en maintenant des valeurs fixes pour la température, le volume de la cellule de simulation et le potentiel chimique des composants du fluide du réservoir. En plus de produire des isothermes d'adsorption et de gonflement thermodynamiques, un autre avantage du GCMD est sa capacité à permettre la flexibilité dans le cadre. Plus important encore, il permet le déplacement de couches lors de l'intercalation dans l'intercouche.

La montmorillonite, choisie comme modèle d'argile pour les simulations, a été construite selon la procédure suivante avec le logiciel Materials Studio. Initialement, la maille élémentaire de la pyrophyllite, caractérisée par la formule chimique $(Si_4)(Al2)O10(OH)_2$, a été construite à partir de données de structure cristalline (J. H. Lee and Guggenheim, 1981) obtenues par raffinement aux rayons X sur monocristal, avec les paramètres de maille suivants : a = 5.160, b = 8.966, c = 9.347 Å, et $\alpha = \beta = \gamma = 90°$. Ensuite, elle a été répliquée 4 fois dans chaque direction cristallographique a, b et c, respectivement. Ensuite, une couche TOT a été empilée sur une autre, ce qui a donné l'assemblage de deux couches TOT, chacune comprenant 32 mailles élémentaires et contenant un total de 1280 atomes. Après la création du super-réseau, des substitutions ont été réparties de manière aléatoire dans le modèle final pour éviter un arrangement trop structuré des sites

substitués lors de l'implémentation des conditions aux limites périodiques (Ngouana W. and Kalinichev, 2014). Un atome de Si est remplacé de manière aléatoire par une substitution en Al pour chaque 32 sites tétraédriques, et un atome d'Al est remplacé par une substitution en Mg pour chaque 8 sites octaédriques. Les modèles de montmorillonite qui ont été construits ont une charge de couche de -0.75 | e |. Par conséquent, 24 ions Na^+, 12 ions Ca^{2+} et 24 ions Cs^+ ont été ajoutés dans les intercouches pour compenser la charge nette négative du système.

Enfin, une minimisation d'énergie a été réalisée pour optimiser la géométrie de chaque structure en utilisant le module forcite dans le logiciel Materials Studio. Un algorithme d'optimisation intelligent est utilisé avec les paramètres de simulation par défaut. En plus des modèles de montmorillonite sèche, trois structures différentes de Na-montmorillonite hydratée ont été créées, chacune présentant différents niveaux d'hydratation, à savoir mono-, bi- et tri-couches hydratées Na-montmorillonite. Cela a été réalisé en ajoutant 5, 10 et 15 molécules de H2O dans l'intercouche de Na-montmorillonite correspondant à chaque maille unitaire ($O20(OH)_4$). De même, trois structures distinctes de Ca-montmorillonite, représentant chacune différents états d'hydratation (mono-, bi- et tri-couches), et deux structures distinctes de Cs-montmorillonite hydratée ont été formées, l'une au niveau d'hydratation monocouche et l'autre au niveau d'hydratation bicouche. Une minimisation d'énergie a été effectuée pour tous les systèmes en utilisant Materials Studio. Ensuite, des simulations de dynamique moléculaire ont été effectuées dans l'ensemble NPT, permettant l'expansion de l'espacement, en utilisant le module Forcite à 298 K et 1 bar pour les montmorillonites sèches et saturées en Na, Ca et Cs pendant 2 ns, avec les paramètres de simulation par défaut. Après que les simulations de MD ont été terminées, les molécules d'eau ont été retirées des intercouches des montmorillonites pour être ensuite incorporées ensemble avec les molécules d'hydrogène lors des simulations de Monte Carlo et de Monte Carlo/mécanique moléculaire hybride.

Pour réaliser des simulations avec un haut degré de précision, il est important de choisir délibérément et de mettre en œuvre un champ de forces approprié, qui est un ensemble de fonctions et de paramètres qui déterminent collectivement l'énergie potentielle associée aux interactions intermoléculaires dans le système. Dans cette thèse, le modèle ClayFF (Cygan et al., 2004) est utilisé pour les modèles de montmorillonite. Le modèle d'eau SPC/E (H. J. Berendsen et al., 1987), également appelé modèle de point de charge simple étendu, qui est un modèle rigide à trois sites, est utilisé dans cette étude. Le modèle H_2 à trois sites est employé et les paramètres ont été pris de Alavi et al. (2005). De plus, les

paramètres non liés pour Na^+ et Cs^+ ont été pris de P. Li et al., 2015. Les paramètres non liés pour Ca^{2+} ont été pris de P. Li et al., 2013.

Dans ce projet, deux techniques différentes ont été utilisées pour effectuer les simulations moléculaires, à savoir les méthodes de Monte Carlo et de Monte Carlo/mécanique moléculaire hybride.

Les simulations de Monte Carlo ont été effectuées dans l'ensemble canonique grand pour calculer les isothermes d'adsorption. Les simulations GCMC ont été réalisées en utilisant RASPA (Dubbeldam et al., 2013, 2016). Les simulations de Monte Carlo se composent de deux parties : l'équilibration et la production. La première équilibre les positions des atomes dans le système. La seconde consiste, en moyenne pendant chaque cycle sur chaque molécule, à tenter un mouvement de Monte Carlo. Un cycle se compose de N étapes, où N est le nombre de molécules avec un minimum de 20 étapes. La coupure générale de 10 Å a été utilisée pour calculer les interactions de Lennard-Jones. Seulement pour les systèmes secs, une coupure de 9 Å a été utilisée en raison de l'espacement basal plus petit. Le potentiel de Lennard-Jones est décalé sans correction de queue. La structure argileuse, la montmorillonite de Na, est considérée comme une structure rigide. Les adsorbats, l'hydrogène et l'eau, sont considérés comme des molécules rigides. De plus, les mouvements d'essai suivants ont été définis : translation à 20 %, rotation à 20 %, réinsertion à 20%, échange à 40%, et changement d'identité à 100%. 200 000 cycles d'équilibration ont été effectués pour garantir que le chargement des molécules atteint l'équilibre. Ensuite, trois cycles de production indépendants de 100 000 cycles ont été effectués pour obtenir de meilleures statistiques. Les positions atomiques sont enregistrées toutes les 1 000 cycles. Quinze moyennes par bloc obtenues, cinq de chaque cycle de production individuel, sont utilisées pour calculer les valeurs moyennes globales. L'écart-type avec un intervalle de confiance de 95% a été calculé à partir de ces 15 moyennes par bloc.
Dans l'ensemble GC, le volume de la boîte de simulation est fixe, où il est en équilibre avec le réservoir des adsorbats à température constante et potentiel chimique constant. Les potentiels chimiques ont été calculés à partir de la fugacité des adsorbats. L'équation d'état de Peng-Robinson (Peng and Robinson, 1976) a été utilisée pour calculer les coefficients de fugacité en utilisant les fractions molaires des adsorbats (hydrogène et eau). Les fractions molaires du mélange eau-hydrogène ont été déterminées par interpolation et extrapolation des données expérimentales de solubilité de H_2 dans le mélange H_2-H_2O (Gillespie and Wilson, 1980; Rahbari et al., 2019; Wiebe and Gaddy, 1934).

Les simulations ont été réalisées avec de légères variations en utilisant différentes approches, avec des cations "rigides" et des cations "mobiles". Dans le premier cas, les structures optimisées sont directement obtenues après avoir mené des simulations de dynamique moléculaire avec les cations (voir la sous-section 2.2), les cations étant ainsi inclus comme partie intégrante du réseau. Les simulations avec des cations "mobiles" nécessitent initialement de retirer les cations de la structure optimisée, suivie de l'adsorption des cations pour 25 000 cycles pour chaque étape d'équilibration et de production. Après avoir assuré un nombre égal de contre-ions dans chaque intercouche, l'adsorption binaire d'hydrogène et d'eau est effectuée en utilisant la même procédure.

Les simulations hybrides MC/MD ont été réalisées dans l'ensemble canonique grand afin de prendre en compte la flexibilité de la structure. Les simulations GCMD ont été effectuées en utilisant RASPA (Dubbeldam et al., 2016). Pour assurer la cohérence avec les simulations GCMC, des paramètres similaires pour les mouvements d'essai et la valeur de la coupure sont utilisés. Le MC/MD hybride, ou GCMD, est réalisé dans l'ensemble canonique grand. L'équation du mouvement est intégrée avec un pas de temps de 0,5 fs. Le système à chaque pression a d'abord été équilibré pendant 25 ns, suivi d'une exécution de production de 6 ns. Les positions atomiques sont enregistrées toutes les 5 ps. Les moyennes globales sont calculées à partir des 3 dernières ns de l'exécution de production. Ainsi, au total, quinze moyennes par bloc ont été obtenues, avec cinq de chaque cycle de production individuel, utilisées pour calculer les valeurs moyennes globales. L'écart type avec un intervalle de confiance de 95% a été calculé à partir de ces 15 moyennes.

Une investigation exhaustive est menée en utilisant les trajectoires et les positions atomiques obtenues à partir des simulations, afin d'explorer les sites d'adsorption potentiels pour les cations Na, Ca et Cs, l'hydrogène et les molécules d'eau dans les intercouches de montmorillonite, en utilisant des analyses telles que les profils de densité atomique, les cartes de densité de surface, les fonctions de distribution radiale et les nombres de coordination, ainsi que l'orientation des molécules de H_2. Des simulations supplémentaires pour l'analyse sont réalisées lorsqu'il y a au moins des molécules de H_2, en supposant une dans chaque intercouche sauf pour la montmorillonite sèche. Pour l'analyse, une exécution de production supplémentaire a été effectuée, en utilisant des simulations individuelles qui fournissent des valeurs médianes pour 100 000 cycles supplémentaires. Les positions des atomes ont été collectées à des intervalles de 10 cycles. Les simulations de Monte Carlo ont produit les positions des atomes dans 10 000 configurations, couvrant différentes probabilités.

Les résultats ont montré que l'adsorption de gaz H_2 augmente de manière proportionnelle avec l'augmentation de la pression, tandis qu'une diminution est observée avec l'augmentation de la température, conformément au comportement de solubilité du gaz d'hydrogène dans l'eau. La quantité d'hydrogène adsorbé augmente proportionnellement avec l'augmentation de la taille des pores et du niveau d'hydratation. L'adsorption de l'hydrogène ne se produit pas dans les modèles de montmorillonite Na- et Ca-sèche en raison de leur petite taille de pore, tandis qu'elle se produit dans la montmorillonite Cs-sèche. Dans le modèle de montmorillonite Ca-hydratée en monocouche, une quantité plus élevée d'H_2 est adsorbée par rapport aux modèles de montmorillonite Na-hydratée en monocouche et Cs-hydratée en monocouche en raison de la différence de volume de vide dans les pores interlamellaires. Cependant, il n'y a pas d'effet du type de cation interlamellaire dans les modèles hydratés en bicouche. La fraction molaire d'hydrogène adsorbé dans les intercouches des argiles hydratées montre une sur-solubilité par rapport à sa solubilité dans l'eau, attribuée à l'interaction forte entre H_2 et la surface de l'argile. Dans les modèles hydratés en bicouche à 298 K et 120 bar, la fraction molaire d'hydrogène est d'environ 7 à 8 fois plus élevée que celle de leur solubilité respective dans l'eau en vrac. Cependant, le type de cation interlamellaire n'a pas d'impact significatif sur le rapport H_2/H_2O. Les molécules d'hydrogène et d'eau ont tendance à s'adsorber près de la surface. Les cartes de densité de surface montrent que les molécules d'hydrogène sont principalement situées dans les cavités hexagonales de la surface de l'argile. Les fonctions de distribution radiale montrent qu'il n'y a pas de cation interlamellaire présent dans la première sphère de coordination de la molécule H_2. Dans n'importe quel modèle avec différents cations, les molécules d'hydrogène n'ont pas d'orientation spécifique par rapport à la surface, quelle que soit la température, la pression, le niveau d'hydratation et le type de cation interlamellaire.

De plus, les résultats de l'adsorption de H_2 à haute pression dans la montmorillonite hydratée et sèche contribuent à améliorer les stratégies pour les applications de stockage d'hydrogène. Dans le dépôt de déchets radioactifs géologiques profonds, sous la plage anticipée de pression et de température, la saturation de H_2 n'est pas réalisable. Cela indique que H_2 ne pose pas de risque d'accumulation de pression dans les conditions prévues et étudiées.

Mots-clés : Simulations moléculaires, adsorption, argiles, montmorillonite, hydrogène

Table of Contents

List of Figures

List of Tables

NOMENCLATURE

The following lists comprise the various symbols and abbreviations used in the main body of this thesis.

List of Abbreviations

ADP Atomic density profile

$ANDRA$ Agence nationale pour la gestion des déchets radioactifs

$Cigeo$ Centre industriel de stockage géologique

CN Coordination number

GC Grand Canonical

HLW High-level waste

$ILW - LL$ Intermediate-level long-lived waste

$LILW - SL$ Low- and intermediate-level short-lived waste

LJ Lennard-Jones

$LLW - LL$ Low-level long-lived waste

MC Monte Carlo

MD Molecular dynamics

mmt Montmorillonite

RDF Radial distribution function

$VLLW$ Very low-level waste

$VSLW$ Very short-lived waste

List of Symbols

1W Monolayer

2W Bilayer

3W Trilayer

Chapter 1

Introduction and Background

1.1 Radioactive waste disposal and storage

Radioactive waste refers to radioactive material that either does not have a planned or envisioned future use or has been reclassified (« Article L542-1-1 - Code de l'environnement - Légifrance », 2016). Radioactive wastes are being generated, due to the extensive usage of radioactive materials in various sectors such as nuclear power plants, non-nuclear industries, defense, medical, and research. Considering the risks that radioactive materials pose to health and the environment, it is crucial to ensure appropriate management procedures for the radioactive waste. It should be noted that the management of radioactive wastes varies between countries, as there are differences in classification and characterization criteria depending on their physical, chemical and radiological characteristics (IAEA, 2020; Misaelides, 2019). In France, these wastes and their respective management solutions can be classified based on their half-life and level of radioactivity, as shown in Table1.1.

The primary source of very short-lived waste (VSLW) is the medical and research sectors, where it is generated through the use of radionuclides. Short-lived waste is managed by storing it for a limited period, allowing its radioactivity content to diminish through the process of radioactive decay. Very low-level waste (VLLW), consists of inert materials such as concrete, metal, and plastic waste, predominantly originates from the operation, maintenance, and dismantling activities of nuclear plants, fuel cycle facilities, and research centers. Moreover, in contrast to VLLW, which predominantly consists of inert materials such as concrete, metal, and plastic waste, low- and intermediate-level short-lived waste (LILW-SL) primarily originates from the operation, maintenance, including clothing and tools, and dismantling of nuclear plants, fuel cycle facilities, and research centers. Both VLLW and LILW-SL require surface disposal. Low-level long-lived waste (LLW-LL) encompasses various waste categories, including graphite waste from the operation and dismantling of the first nuclear plants; radium-bearing waste, generated by some indus-

Table 1.1 – Classification of radioactive wastes and their management solutions (adapted from ANDRA, 2021a).

<table>
<tr><td></td><td></td><td colspan="3">Half-life of the radioactive elements contained in the waste</td></tr>
<tr><td></td><td></td><td>Very short-lived
(VSL)
(Half-life<100 days)</td><td>Mainly short-lived
(SL)
(Half-life≤31 years)</td><td>Mainly long-lived
(LL)
(Half-life>31 years)</td></tr>
<tr><td rowspan="4">Activity level of the radioactive waste</td><td>Very low-level waste
(VLLW)
<100 Bq/g}</td><td rowspan="3">Management through radioactive decay
(VSLW)</td><td colspan="2">Surface disposal (Industrial facility for grouping, storage and disposal)
(VLLW)</td></tr>
<tr><td>Low-level waste
(LLW-LL)
several hundred Bq/g
to one million Bq/g</td><td rowspan="2">Surface disposal
(Aube and Manche disposal facilities)
(LILW-SL)</td><td>Near-surface disposal under development
(LLW-LL)</td></tr>
<tr><td>Intermediate-level waste
(ILW)
around 1 million
to 1 billion Bq/g</td><td rowspan="2">Deep geological disposal under development
(Cigeo project)
(ILW-LL, HLW)</td></tr>
<tr><td>High-level waste
(HLW)
around several billion Bq/g</td><td>Not applicable</td></tr>
</table>

trial activities, such as the extraction of rare-earth metals; other types of waste, such as certain packages of legacy waste conditioned in bitumen, uranium conversion treatment residue, etc. For this particular type of waste, near-surface disposal is employed (ANDRA, 2021a).

Intermediate-level long-lived waste (ILW-LL) primarily consists of waste derived from the metal structures surrounding the fuel, such as hulls and caps, which originate from the reprocessing of spent fuel. Additionally, it includes a smaller proportion of technological waste resulting from the use and maintenance of nuclear facilities, waste generated during the treatment of liquid effluent (bituminised sludge), and activated waste from nuclear reactors. In contrast, high-level waste (HLW) primarily arises from the reprocessing of spent fuel. This waste is composed of highly radioactive residue resulting from the

chemical dissolution of the spent fuel. To ensure the safe management of both ILW-LL and HLW, deep geological disposal is considered essential. The waste is encapsulated in glass and subsequently conditioned in stainless steel containers before being placed in the designated disposal site (ANDRA, 2021a).

All countries with long-term radioactive waste management strategies have adopted the concept of radioactive waste disposal repositories with a multi-barrier system (Metlay, 2016). The multi-barrier system (Figure 1.1), designed to isolate the waste from the biosphere and form a comprehensive safety concept, consist of both natural and engineered barrier systems (Ewing et al., 2016; IAEA, 2020; Metlay, 2016; Misaelides, 2019; NEA, 2003). The natural barrier refers to the geological formation chosen as a host rock for radioactive waste repository and its surrounding including environmental setting selected for the disposal facility. On the other hand, engineered barrier system refers the specifically designed engineered materials, including waste form, waste canisters, buffer and back-fill materials, and sealing systems, placed in the repository (Ewing et al., 2016; IAEA, 2020; NEA, 2003). The concept of a multi-barrier system is to provide an additional layer of safety in case one barrier falls short of expected performance (Ewing et al., 2016).

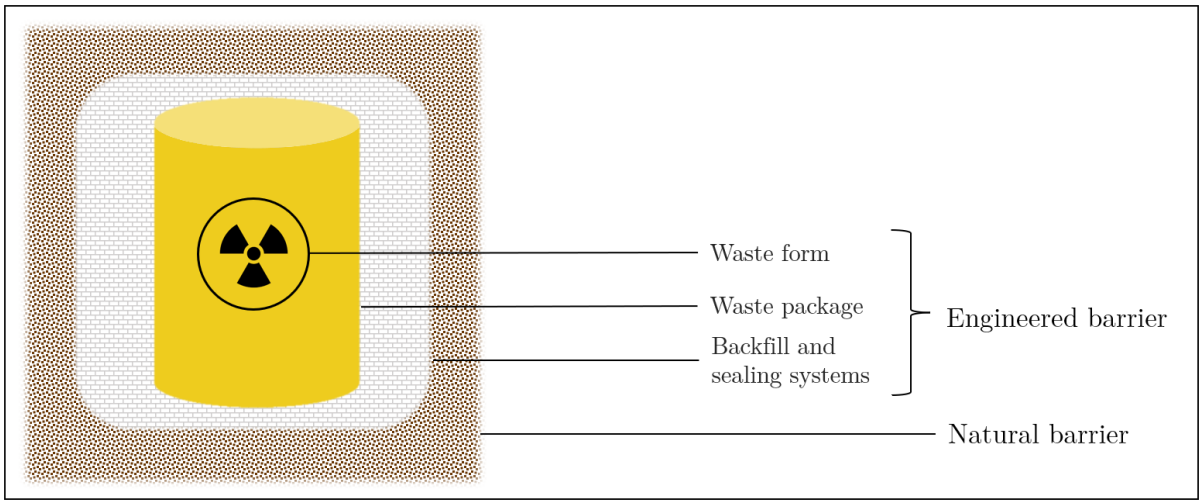

Figure 1.1 – Schematic representation of multi-barrier system for radioactive waste disposal

Natural barriers, geological formations, make use of the characteristics of the host rock and hydrological system surrounding the repository to cause a delay in the release of radionuclides into the biosphere (Ewing et al., 2016). Typically, deep geological formations are generally selected for the disposal and storage of high-level waste (HLW)

and intermediate-level long-lived waste (ILW-LL) from nuclear power plants and other sources (ANDRA, 2005a, 2005b, 2021a; IAEA, 2020; Nagra, 2002; ONDRAF/NIRAS, 2011). In order to ensure the safety and durability of permanent geological storage of nuclear waste, the waste repositories should satisfy a number of physical, chemical, and geo-thermo-mechanical conditions, such as low permeability of the host rocks, reducing environment, high thermal conductivity, and self-sealing properties. These features reduce the possibility of radionuclide mobility of the liquid or gas forms.

Countries have varying strategies and approaches for selecting a suitable host rock for potential radioactive waste disposal and storage sites, considering parameters such as depth, thickness, uniformity, tectonic stability, hydrogeology, and geochemistry. Four different rock types have been evaluated as potential host rock formations: crystalline rock, salt, clay, and volcanic tuff (Ewing et al., 2016; IAEA, 2020).

Crystalline rocks are chosen as host rocks in Sweden (Forsmark site) and Finland (Olkiluoto site) (Hedin and Olsson, 2016; IAEA, 2020). It is worth noting that the Onkalo geological disposal facility for spent fuel in Finland is the only one that has been built so far (IAEA, 2022). Moreover, several other countries, such as the Czech Republic, Japan, South Korea, Russia, and the United Kingdom, have widely explored and conducted research on granite and gneiss as possible host rocks (IAEA, 2020; Laverov et al., 2016). Crystalline rocks are known for their strong mechanical characteristics, adequate thermal conductivity, and low permeability and porosity. However, they also have fracture networks that introduce heterogeneity and can potentially raise hydraulic conductivity (Ewing et al., 2016; IAEA, 2020). One of the key safety features of the Forsmark site is the limited presence of water-conducting fractures at repository depth. Water flows faster through these fractures in the upper layers of bedrock but slows down at repository depths (Hedin and Olsson, 2016; IAEA, 2020). Another important aspect is the favorable chemical environment, which involves conditions that minimize risks at the repository depth and the appropriate level of salinity to maintain the stability of the bentonite barrier, an engineered barrier. Furthermore, very low potential for hosting metallic or industrial mineral deposits significantly diminishes the risk of future human interference (Hedin and Olsson, 2016). Nevertheless, it is important to note radionuclides may not be well retained if they release from the engineered barriers into the fracture network due to their limited retention (IAEA, 2020). Therefore, it is crucial to implement an engineered barrier system that ensures a high level of safety.

Rock salt formations has been explored as potential site for disposal repositories of HLW in Germany and the Netherlands, as well as for low-level (LL) radioactive waste in the United States of America (IAEA, 2020). Rock salt, known for its impermeability and ease of mining, has a medium level of mechanical strength and high thermal conductivity. However, the most significant feature of salt is self-sealing due to plastic deformation. The plasticity of rock salt allows it to rapidly heal fractures and naturally seal openings. As a result, a salt repository will be fully encapsulated and sealed shortly after waste is placed and the repository is closed (Ewing et al., 2016; IAEA, 2020). Nonetheless, the major drawback is the high solubility of salt. Minimizing any fracturing of the rock salt is crucial to preserve its exceptionally low permeability and prevent water influx causing dissolution and erosion (Berlepsch and Haverkamp, 2016).

Volcanic tuff formation at the Yucca Mountain, Nevada (USA) has been investigated as a potential host rock for HLW disposal repository by US Department of Energy (IAEA, 2020; Swift and Bonano, 2016). This site is located above water table, meaning that the repository remains unsaturated, giving it a unique characteristic (Ewing et al., 2016; IAEA, 2020; Swift and Bonano, 2016). Another key factor of this welded tuff site is its arid climate (IAEA, 2020). Moreover, the other advantages are the slow rate of water infiltration into the mountain, the capillary diversion of water around openings in unsaturated rock, and the extended path water follows through saturated rocks before approaching the surface (Swift and Bonano, 2016). However, a substantial amount of water is held within the pores and its swift movement along fractures in the unsaturated zone has introduced uncertainties, resulting in an oxidizing environment, which has raised concerns for the technical suitability assessment of the site (Ewing et al., 2016).

Clay-rich rocks are considered to be optimal candidates as the host rocks for geological radioactive waste repository facilities (Bardelli et al., 2014; Charlet et al., 2017; Ewing et al., 2016; Grambow, 2016; IAEA, 2020). These rocks possess favorable characteristics that provide a stable and geologically isolated environment for long-term waste containment, including low hydraulic conductivity, good thermal conductivity, self-healing due to their swelling properties, high retention properties, very low permeability and slow rates of diffusion (Bardelli et al., 2014; Charlet et al., 2017; Grambow, 2016). In France, the Callovo-Oxfordian clay rock, in Belgium, the Boom and Ypresian clays, and in Switzerland, the Opalinus clay rock have been carefully selected as host rocks for radioactive waste repositories (ANDRA, 2005a; IAEA, 2020; Nagra, 2002; ONDRAF/NIRAS, 2011).

In France, the safe disposal of HLW and ILW-LL in deep geological formations has been extensively studied and Cigéo (The Industrial Center for Geological Disposal) project is being carried out to design the deep geological waste disposal facility as illustrated in Figure 1.2 by Andra (National Agency for Radioactive Waste Management). The selected site is located in northeastern France, on the border between the Meuse and Haute-Marne departments. It has been decided to dispose the wastes at a depth of approximately 500 meters within the impermeable Callovo–Oxfordian argillaceous rock formation, surrounded by two geological formations (Dogger and carbonated Oxfordian) containing aquiferous sedimentary horizons with low permeabilities and slow runoffs, with a thickness of approximately 130 meters (ANDRA, 2005a, 2005b; Grambow, 2016; IAEA, 2020).

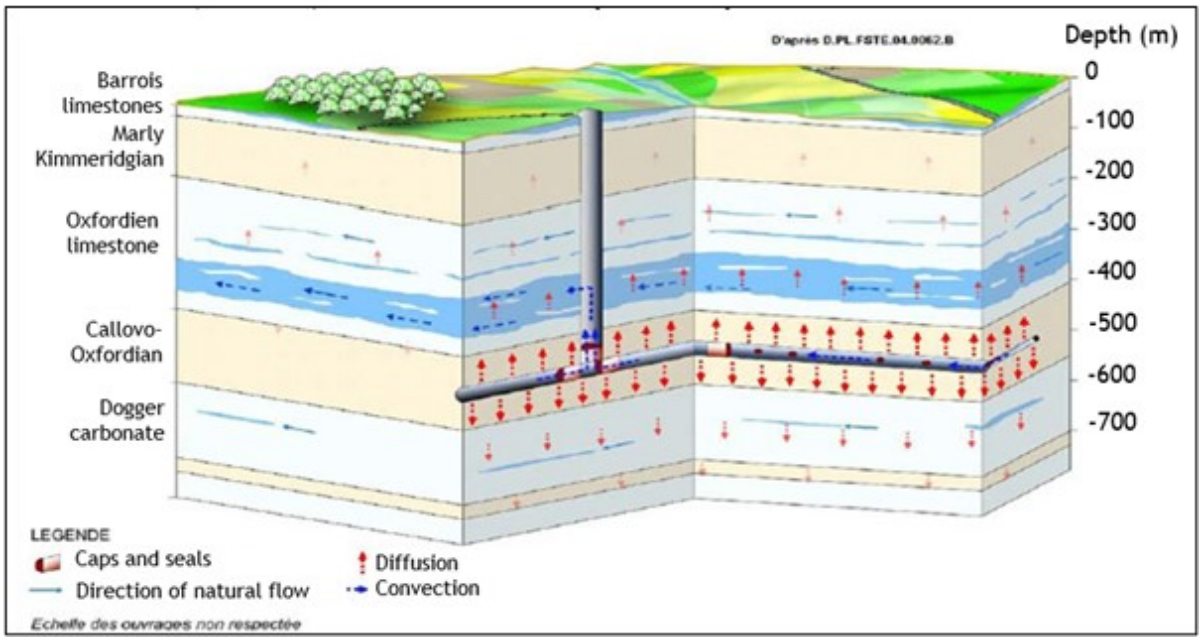

Figure 1.2 – Schematic representation of radioactive waste repository, featuring Callovo-Oxfordian and its surrounding rocks on the Meuse/Haute-Marne site (adapted from ANDRA, 2005a with permission)

The Callovo-Oxfordian clay rock exhibits lateral homogeneity and is characterized by low porosity (15-18 %), low permeability and high retention capability due to its mineralogical composition. It consists of argillaceous mineral phases making up to 60 % of its total mass, along with fine quartz, carbonates (mainly calcite with a small percentage of dolomite), and a trace amount of other phases such as pyrite and organic materials (ANDRA, 2005a;

Table 1.2 – Mineralogical composition of Callovo-Oxfordian clay rock

Mineralogical composition	Values (in mass)*
Clays	25-60%
Carbonates	15-50%
Quartz	25-35%
Organic materials	0.5-2%
Pyrite	2-3%

*ANDRA, 2005a

Bardelli et al., 2014). The mineral composition of Callovo-Oxfordian (COx) is given in Table 1.2 and the composition of clay minerals is discussed more detailed in section 1.2

Engineered barriers play an important role as initial safety layers to prevent the dispersion of radionuclides into natural barriers. They can be simply divided into three categories: waste form, waste packages, and backfill and sealing systems (Figure 1.1). As an illustration, schematic representation of Cigéo Geological Disposal Facility and its engineer barrier systems including HLW and ILW-LL cells and packages, and backfill and sealing systems is given in Figure 1.3.

The waste form, which initially contains all the radioactivity, must be robust with minimal radioactivity release.Therefore, it is crucial to adjust the properties of the waste form according to either the composition of the waste or the geological conditions in the repository. Common waste forms include UO_2 and MOX matrices for spent fuel, a borosilicate glass matrix for HLW, and a diverse range of waste matrices such as concrete-conditioned wastes for ILW, reflecting the variety of waste streams (Ewing et al., 2016; NEA, 2003).

The waste form is typically placed in a metal canister, often made of steel, copper, or advanced corrosion-resistant alloys. Regulations in many countries require placing the waste into standardized waste packages designed to simplify waste handling, positioning, and retrievability, while providing containment for extended periods depending on the type of waste. In order to control and stabilise the thermo-hydro-mechanical-chemical conditions, and to ensure low permeabilities and/or diffusivities, as well as long-term retardation after closure, the surrounding void of the waste packages must be filled with a backfill and/or buffer material compatible with the engineered and geological barriers

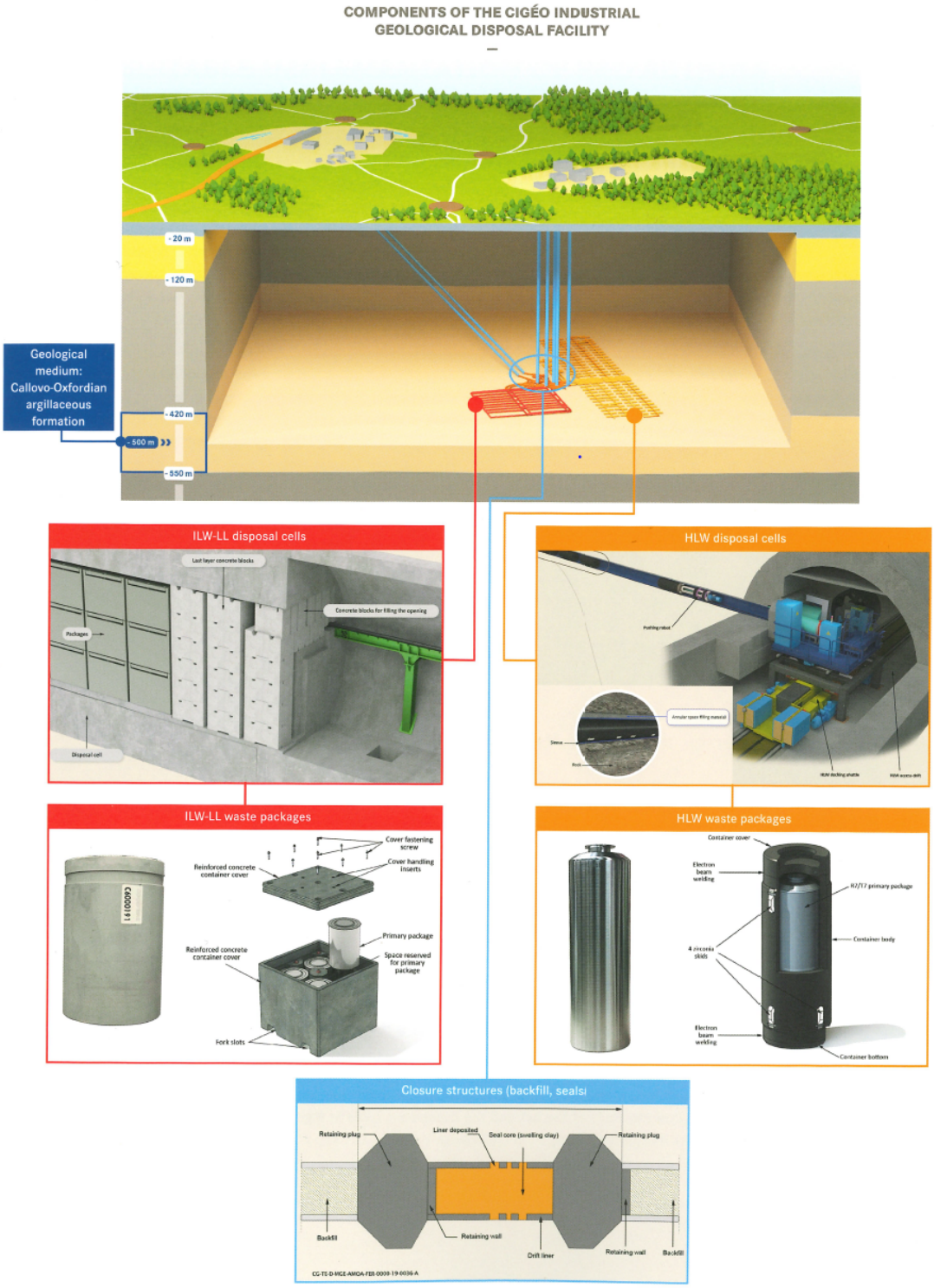

Figure 1.3 – Schematic representation of Cigéo Geological Disposal Facility and its engineered barrier systems including HLW and IWL-LL disposal cells and waste packages, and backfill and sealing systems (reproduced with permission from ANDRA, 2021b)

and properly sealed (Ewing et al., 2016; NEA, 2003).

Larger waste volumes may require using host rock materials and cement as a backfill material. Nevertheless, extensive research has been conducted on bentonite backfill, particularly for managing heat-producing waste canisters. Bentonite plays a vital role as it acts as a buffer around individual waste packages and functions as an efficient tunnel seal, effectively separating the disposal galleries from the shafts accessible from the surface. Bentonite, containing a significant amount of clay mineral called montmorillonite (is discussed more in detail in section 1.2), and its mixture with sand are chosen for their low hydraulic permeability due to their self-sealing and swelling capability to help restoring the low hydraulic conductivity feature of the disturbed host rock following repository construction by sealing the voids within the installed barrier (Ewing et al., 2016; Grambow, 2016; Sellin and Leupin, 2014).

In conclusion, clays play a crucial role as both natural and engineered barriers in deep geological radioactive waste disposal. A comprehension of their structure and characteristics is essential for ensuring the long-term, safe, and effective management of radioactive waste.

1.2 Clay minerals

Clays, as defined by Grim, 1968 are basically composed of a group of very small crystalline particles derived from one or several members of a mineral group commonly referred to as clay minerals, which are essentially hydrous aluminum silicates (Bergaya et al., 2006; Murray, 2007). As distinct from clay mineral, clay generally refers to a rock, a sedimentary deposit, or the alteration products of primary silicate minerals. The main difference lies in the fact that clay can only be natural, while clay minerals can be both natural and synthetic. Clay is typically fine-grained (<2 μm or <4 μm); however, there is no specific size criterion for clay minerals. Although phyllosilicates are the main components of clays, clay minerals may not include phyllosilicates. Despite both being plastic, certain types of clay may have exceptions. Lastly, both harden upon drying or firing (Bergaya et al., 2006).

Clay minerals typically consist of tetrahedral and octahedral sheets. A tetrahedral and an octahedral layer form a 1:1 layer (Figure 1.4a) structure, while an octahedral layer positioned between two tetrahedral layers constitute a 2:1 layer (Figure 1.4b). The thicknesses

of the 1:1 and 2:1 layers are approximately 0.7 and 1 nm, respectively.

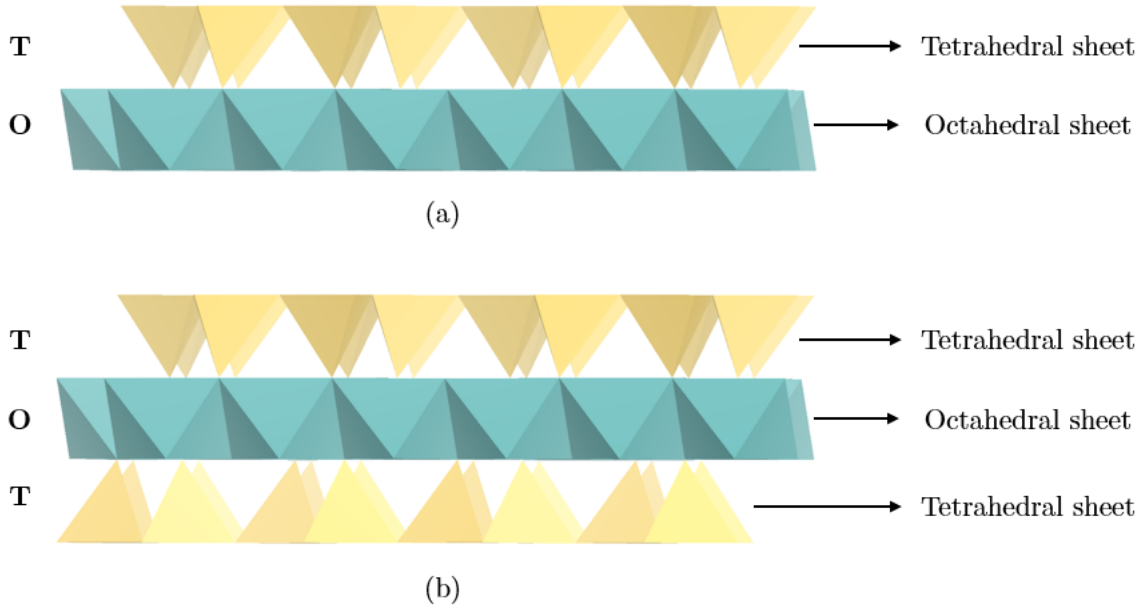

Figure 1.4 – Schematic representation of a) 1:1 (TO) and b) 2:1 (TOT) layer

The tetrahedral sheet (Figure 1.5b) is composed of tetrahedrons (SiO_4^{4-} in Figure 1.5a) linked to their neighbors by sharing three basal oxygen atoms, forming a hexagonal structure. There may be also Al^{3+} and Fe^{3+} cations as a substitutions for Si^{4+}. The octahedral sheet comprises of octahedrons (usually includes Al^{3+}, Fe^{3+}, Mg^{2+} and Fe^{2+} cations) which are linked by sharing edges (hydroxyl oxygen atoms). Unshared edges (apical oxygens) of octahedral layer are connected to tetrahedral apical oxygens. There are basically two different types of octahedral sheets. One is dioctahedral (Figure 1.5d) when aluminum (Figure 1.5c), with a positive valence of three, is the cation filling two-thirds of the positions to balance the charges. The other is trioctahedral (Figure 1.5g) when magnesium and/or iron (Figure 1.5e and f), with a positive charge of two, is present and all three positions are filled to maintain structural balance (Bailey, 1988; Bergaya et al., 2006; Murray, 2007).

Upon combining the tetrahedral and octahedral sheets in a layer, the structure can either be electrically neutral or exhibits a negative charge.The negative layer charge is resulting from :

— substitution of Al^{3+} for Si^{4+} in tetrahedral sheet,

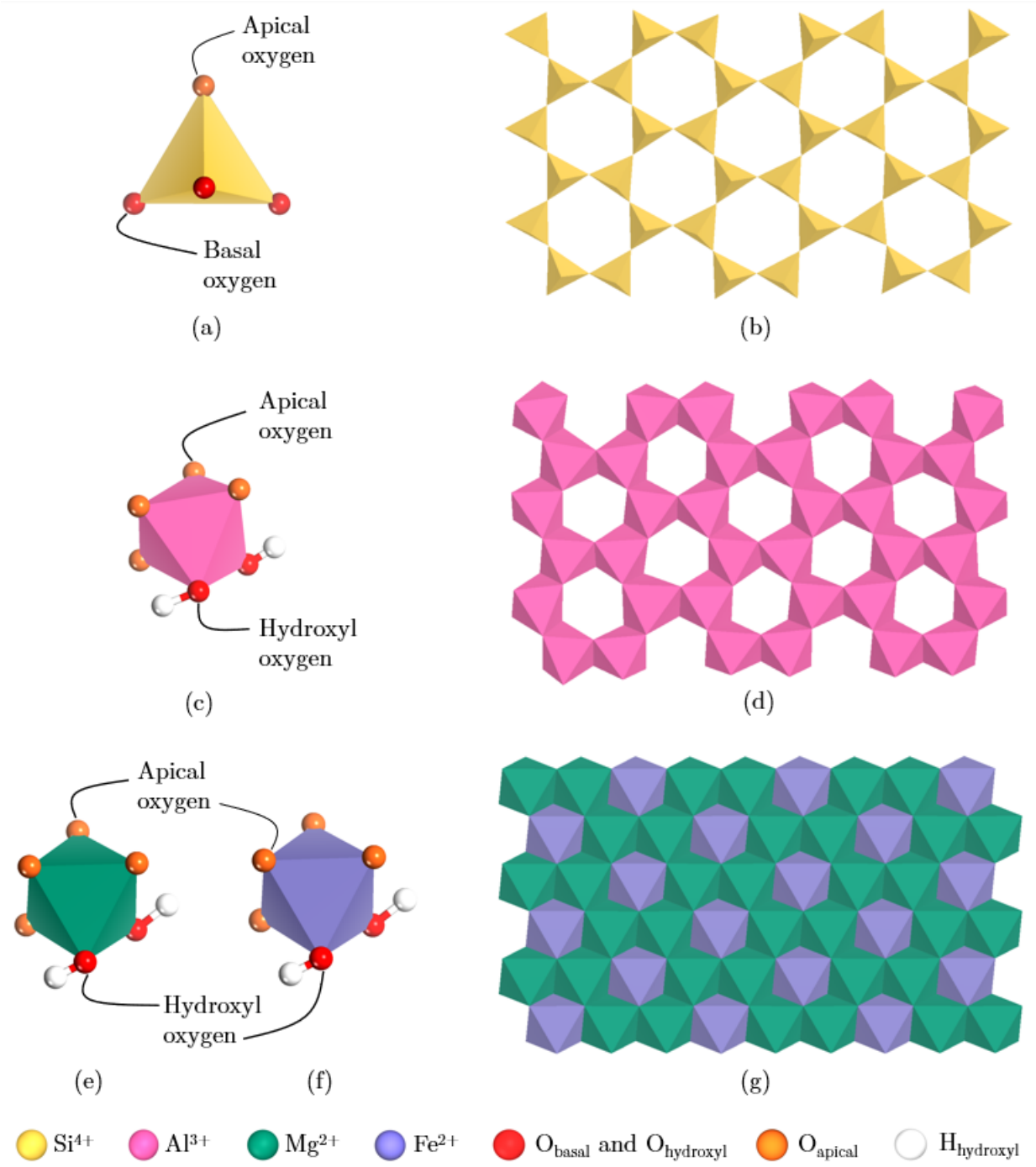

Figure 1.5 – Schematic representation of a) tetrahedra (with Si^{4+}) b) tetrahedral sheet, c) dioctahedra (with Al^{3+}), d) dioctahedral sheet, e) trioctahedra (with Mg^{2+}), f) trioctahedra (with Fe^{2+}) and g) trioctahedral sheet. Color legend: Si (yellow), Al (pink), Mg (green), Fe (Purple), basal and hydroxyl oxygen (red), apical oxygen (orange), and H (white).

— substitution of Al^{3+} or Mg^{2+} for lower charge cations in octahedral sheet, and

— the presence of vacancies (Bergaya et al., 2006).

The deficit in layer charge is compensated by the presence of interlayer cations.

Clay particles form by stacking layers, and these particles join together to create aggregates (Figure 1.6b). The arrangement of these particles or aggregates results in various morphology (Bergaya et al., 2006). Clay minerals have distinct surfaces, namely basal and edge surfaces, and an interlayer that may contain water and cations. A schematic representation of a clay particle is provided in Figure 1.6a, illustrating essential terms such as tetrahedral and octahedral sheets, basal spacing, interlayer distance, and basal and edge surfaces, used frequently in section 2.2 and in 3.

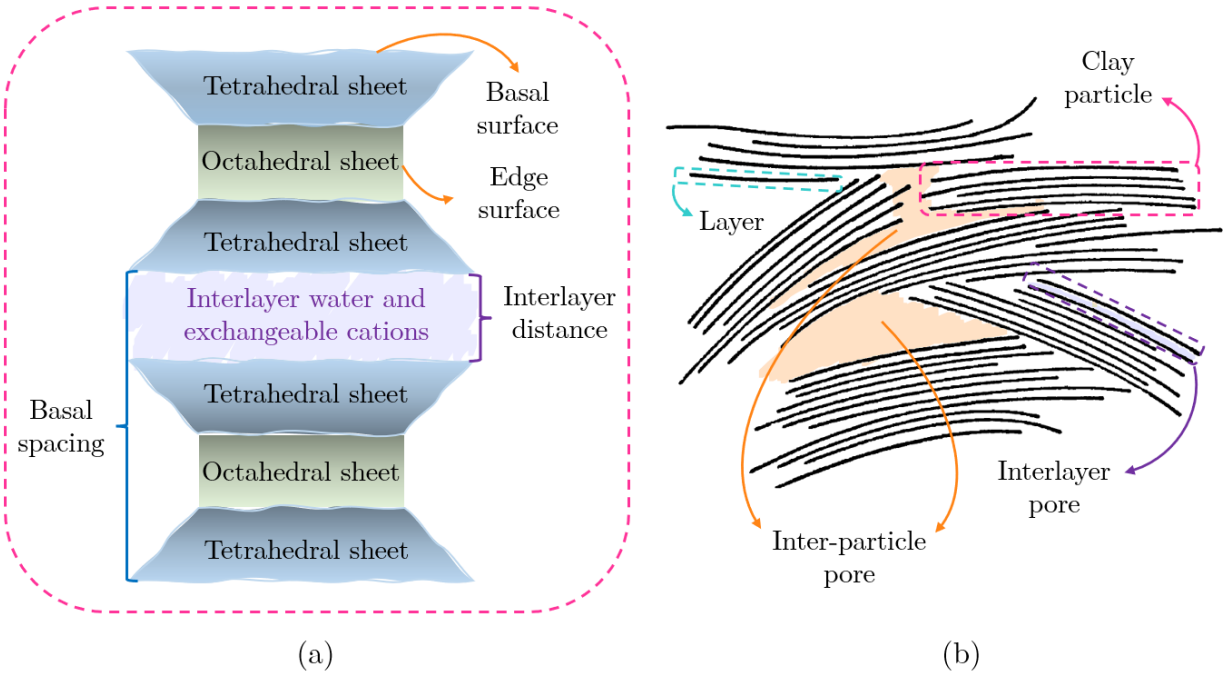

Figure 1.6 – Schematic representation of a) clay particle and b) aggregate of clay particles (adapted from Bergaya et al., 2006 with permission)

Clays exhibit different properties depending on the specific clay minerals, which is a result of their distinct structure and composition. In other words, the physical and chemical characteristics of a particular clay mineral rely on its unique structure and composition (Murray, 2007).

Clay minerals can be classified into seven major groups according to layer type, layer charge (x) per formula unit, and type of interlayer: serpentine-kaolin group, talc-pyrophyllite group, smectite group, vermiculite group, true mica group, brittle mica group, and chlorite group (Bailey, 1988). The classification of clay minerals is given in (Table 1.3).

Table 1.3 – Classification of clays minerals (adapted from Bailey, 1988)

Layer charge	Interlayer	Group	Subgroup	Species
1:1	None or H_2O only	Serpentine-kaolin x∼0	Serpentines	Chrysotile, lizardite, amesite, berthierine, cronstedtite, etc.
			Kaolins	Kaolinite, dickite, nacrite, halloysite
2:1	None	Talc-pyrophyllite x∼0	Talcs	Talc, willemseite
			Pyrophyllites	Pyrophyllite, ferripyrophyllite
	Hydrated exchangeable cations	Smectite x∼0.2-0.6	Saponites	Saponite, hectorite, sauconite, stevensite, etc.
			Montmorillonites	Montmorillonite, beidellite, nontronite, volkonskoite, etc.
	Hydrated exchangeable cations	Vermiculite x∼0.6-0.9	Trioctahedral vermiculites	Trioctahedral vermiculite
			Dioctahedral vermiculites	Dioctahedral vermiculite
	Non-hydrated cations	True mica x∼0.5-1.0	Trioctahedral true micas	Phlogopite, biotite, lepidolite, zinnwaldite, annite, etc.
			Dioctahedral true micas	Muscovite, illite, glauconite, tobelite, paragonite, etc.
	Non-hydrated cations	Brittle mica x∼2.0	Trioctahedral brittle micas	Clintonite, bityite, anandite, kinosg-hitalite
			Dioctahedral brittle micas	Margarite
	Hydroxide sheet	Chlorite x variable	Trioctahedral chlorites	Clinochlore, chamosite, nimite, pennantite, baileychlore
			Dioctahedral chlorites	Donbassite
			Di, trioctahedral chlorites	Cookeite, sudoite

Kaolinite, a type of kaolin mineral, has a structure of 1:1 (TO) layer having a neutral charge. Only two-thirds of the octahedral positions are filled by aluminum atoms, each surrounded by four oxygens and eight hydroxyls (Murray, 2007).

Smectite minerals exhibit a 2:1 layer structure, composed of two tetrahedral sheets (silica) sandwiching an octahedral sheet in between. The interlayer space between these 2:1 (TOT) layers is filled by water molecules and cations. The most common smectite minerals include sodium montmorillonite, calcium montmorillonite, saponite (magnesium montmorillonite), nontronite (iron montmorillonite), hectorite (lithium montmorillonite), and beidellite (aluminum montmorillonite) (Murray, 2007). It is reported that the ion exchange of Ca in the pore water with Na initially present in the montmorillonite may take place (Nagra, 2002).

Illite, a common type of mica, has a 2:1 (TOT) layer structure. Its interlayer cation potassium creates a robust structure with tightly bound layers, preventing water molecules from filling the interlayer space, unlike in smectites (Murray, 2007).

Chlorite is a common clay mineral type in shales. It has 2:1 layer structure having brucite sheet in the interlayer (Murray, 2007).

Table 1.4 – Clay mineral composition of Callovo-Oxfordian clay rock

Clay mineral composition	Values (in mass)*
Interlayer minerals illite/smectite	15-30 %
Micas/Illite	5-20 %
Kaolinite	up to 10 %
Chlorites	trace amount

*ANDRA, 2005a

The Callovo-Oxfordian (COx) clay formation comprises various clay minerals (Table 1.4). Interstratified illite/smectite, accounting for up to 30 %, along with micas and illite making up to 20 % of the total rock mass, are distributed throughout the entire thickness of COx. In the lower part of COx layer, kaolinite is present, constituting up to 10 % of the total rock mass. Additionally, a small percentage of chlorites is distributed throughout the entire thickness of COx formation (ANDRA, 2005a; Bardelli et al., 2014; Charlet et al., 2017).

1.3 Gas generation in the deep geological radioactive waste repository

Under the final conditions that arise during the post-closure phase in the radioactive waste repository, gas generation occurs as a result of the nature of certain key components in the waste. Gas generation in a repository occurs in anaerobic conditions shortly after the initial state, with rock temperature between 10 and 50°C, dependent on depth. Moreover, the host rock significantly influences gas generation due to its various features such as humidity, mineralization, groundwater composition, and pH (NEA, 2001).

Various mechanisms may lead to gas generation in the repository. Metals are mostly found in disposal cells, existing as structural components, containers, or waste forms (ANDRA, 2005a). Anaerobic corrosion of stainless steel metals such as iron anoxic corrosion:

$$3Fe + 4H_2O \rightleftharpoons Fe_3O_4 + 4H_{2(g)})$$

leads to the formation of hydrogen, H_2 (Bardelli et al., 2014; Charlet et al., 2017; NEA, 2001; Truche et al., 2013, 2018). Moreover, radiolysis of water due to radioactive decay produces mainly H_2, but also O_2, CO_2, and CH_4 (Charlet et al., 2017; NEA, 2001).

Microbial degradation of organic matter leads to the production of CH_4 and CO_2 as the main products (Charlet et al., 2017; NEA, 2001). Helium production due to alpha decay, water vapor is generated near the spent fuel cartridge, and the radioactive gases, such as Rn, are released (Charlet et al., 2017). Additionally, air will be also trapped in the repository, mainly in the back-fill of the drifts, after closure (ANDRA, 2005a).

Hydrogen is the most abundant gas in this repository conditions and the environment as anaerobic metal corrosion is the predominant process, contributing to over 90% of the produced gases (ANDRA, 2005a).

Gas accumulation in the repository may cause gas pressure build-up, resulting in a risk of overpressure and fracture of the surrounding clay rock unless it diffuses, reacts, or gets absorbed by clay rocks which have high sorption capacities due to their high surface areas (Bardelli et al., 2014; Charlet et al., 2017).

1.4 Gas adsorption in nanoporous materials

As gas pressure build-up could affect the stability of the radioactive waste repository, it is crucial to investigate the gas adsorption capacity of clay minerals. Many laboratory experiments were carried out on the gas adsorption and transportation in clays in the context of radioactive waste disposal (Bardelli et al., 2014; Didier et al., 2012; Mondelli et al., 2015). However, since those methods are time-consuming and costly, and sometimes they might be impossible and risky, it is crucial to perform an alternative method such as computational modeling. On the other hand, it is also important to interpret experimental results. In addition to experimental studies (Bardelli et al., 2014; Didier et al., 2012; Edge, 2014; Grekov et al., 2020; Mondelli et al., 2015; Ziemiański and Derkowski, 2022), some research groups investigated gas adsorption using Monte Carlo simulations (Jin and Firoozabadi, 2013, 2014; Kadoura et al., 2016; Yang et al., 2015; J. Zhang et al., 2016), molecular dynamics (Cygan et al., 2012; M.-S. Lee et al., 2018; Loganathan et al., 2020; Martos-Villa et al., 2014; Maruthi Sena and Krishnan, 2019), hybrid MC/MD methods (Botan et al., 2010; Loganathan, Bowers, Yazaydin, Kalinichev, and Kirkpatrick, 2018; Loganathan, Bowers, Yazaydin, Schaef, et al., 2018; Loganathan et al., 2017), which are widely used to perform CO_2 and/or water adsorption, and density function theory (Hwang and Pini, 2019; Hwang et al., 2019).

1.4.1 Hydrogen adsorption in clays

Some hydrogen sorption experiments were performed to investigate its uptake ability by different research groups. Bardelli et al. (2014) investigated hydrogen uptake capacity onto both raw and purified (does not include CaO) dry Callovo-Oxfordian (COx) clay rock samples at different temperatures (28 and 90°C) and pressures (0-90 bar). The average adsorption values were 0.12 and 0.24 wt % (600 and 1200 μmol/g) at 28°C in the 40-60 bar pressure range, where sorption was saturated, for raw and purified clay samples, respectively. In the same pressure range, average adsorption values were 0.1 and 0.2 wt.% (480 and 1020 μmol/g) at 90°C for raw and purified clay samples, respectively. These results indicate that clay rocks have significant potential to accumulate hydrogen. Since the effect of hydrogen adsorption on water saturated clay samples will decrease, the adsorption values obtained with dry clay samples were considered as maximum values (Bardelli et al., 2014). It is reported that hydrogen shown no sorption effect for Boom Clay and COx under fully water saturated conditions (Charlet et al., 2017).

Didier et al. (2012) investigated the hydrogen adsorption on synthetic Na-montmorillonite (includes different Fe (III) ratios by wt.) and Callovo-Oxfordian clay rock. Adsorption experiments were carried out at 90°C and 120°C with 0.45 bar partial pressure of H_2 for 30 to 45 days. The results have shown that the amount of adsorbed H_2 was not related to the ratio of the Fe (III) in clay structure. On the other hand, the difference in adsorption in these samples was explained with the presence of a little amount of Fe species in the interlayer, which may prevent the possible adsorption. The results have shown the H_2 uptake of 0.05 and 0.06 wt% for raw and purified COx samples, respectively. Although a higher adsorption value obtained at the lower temperature, it is observed that the temperature does not have a strong effect on adsorption (Didier et al., 2012). A similar study was carried out on synthesized Na-montmorillonite. Almost no structural and textural differences were observed between Fe-containing and non-Fe-containing samples. Adsorption value reached about 0.2 wt% at 90°C between 40 and 60 bar (Mondelli et al., 2015).

A recent study has revealed that the amount of hydrogen adsorbed under similar conditions is significantly lower than observed in previous experimental studies. Ziemiański and Derkowski, 2022 investigated hydrogen adsorption on smectites and illites at 25-70 °C up to 150 bar. The samples were dried at the temperature of between 40 and 315°C to reduce the water content. Thus, different basal spacings were obtained. H_2 intercalates into the smectitic interlayers, which have a basal spacing larger than 10.8 Å(Figure 1.7). The results of H_2 adsorption on Li-, Mg-, and Cs-montmorillonites shown that the density of H_2 adsorbed is not influenced by the type of cation (Figure 1.7). It is reported that majority of H_2 adsorption sites in smectites are likely located in the interlayers. Morever, the adsorption of H_2 consistently decreases with temperature increasing from 25 to 70°C.

1.4.2 Hydrogen adsorption in other nanoporous materials

Ryan et al. (2008) studied hydrogen adsorption in IRMOF-1, IRMOF-10 and IRMOF-16 using GCMC simulations at cryogenic temperature and 25°C and up to 12 MPa (Ryan et al., 2008). It is reported that their simulation results were consistent with the experimental results (Kaye et al., 2007).

In another study on molecular dynamics simulation of adsorption, molecular hydrogen adsorption on amorphous solid water surfaces was investigated (Molpeceres and Kästner,

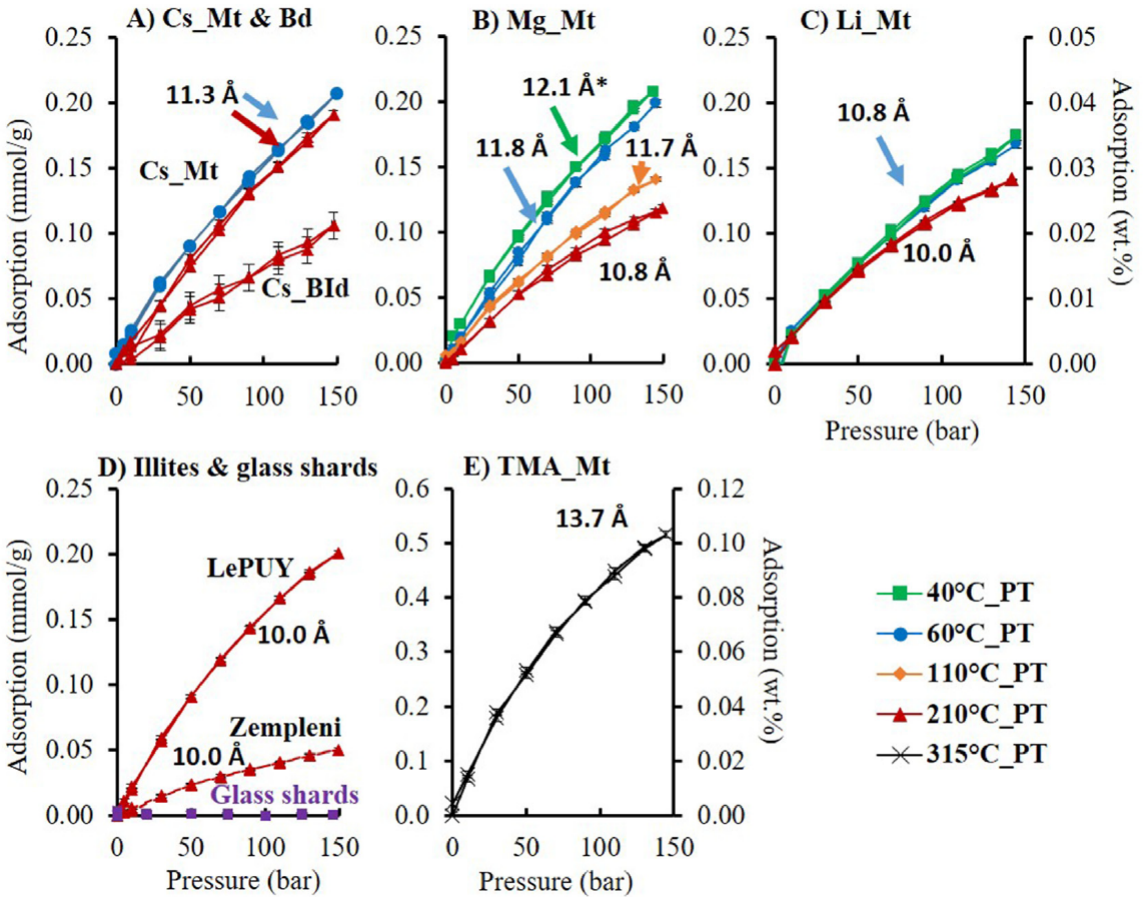

Figure 1.7 – Excess H_2 adsorption isotherms at 25°C on clay minerals and glass shards as a reference at 25°C up to 150 bar (Ziemiański and Derkowski, 2022).

2020). In this study, set of sticking coefficients for the hydrogen/amorphous solid water system were determined using quantum-chemistry-based molecular dynamics simulations, instead of force-field-based dynamics. This method is generally applicable to any kind of surface, amorphous or crystalline. In addition, it allows to study chemisorption, chemical reactions upon adsorption with surface atoms as well as pre-adsorbed species. The results have shown that the binding energy of molecular hydrogen was around 300 K and its distribution was broad. The sticking probability depends on adsorbate kinetic energy and surface temperature. Furthermore, it is observed that finite sticking probabilities above the thermal desorption temperature.

Summary of some atomistic simulations of H_2 adsorption performed by different research groups is given in Table 1.5).

Table 1.5 – Atomistic simulations of H_2 adsorptions performed by different groups

.

Researchers	Gas	Water presence	Adsorbent	Conditions	Force Field	Ensemble
Ding and Yazaydin, 2013	H_2 and CH_4	-	MOFs	77 and 298 K up to 500 bar	3-site H_2 model TraPPE force fiel	GCMC
Erdös et al., 2021	H_2	+	Zeolites	310 K up to 875 bar	TIP5P/Ew H_2 model (Deeg et al.)	GCMC
Deeg et al., 2013	H_2	-	Zeolites	77 K up to 1 bar	Deeg et al.	MC in NVT
Van Den Berg et al., 2006	H_2	-	Sodalite-type (SOD) structures	Up to 1000 K Up to 1 bar	van den Berg, 2005	GCMC
Ryan (2008)	H_2	-	IRMOF-1, IRMOF-10, IRMOF-16	77 and 298 K up to 12 MPa	DREIDING, Lorentz-Berthelot mixing rules (H_2-framework)	
Molperes and Kastner (2020)	H_2	-	amorphous solid water		quantum-chemistry-based MD	

1.4.3 Adsorption of other gases in clays

Clays, particularly smectite interlayer, also show a high affinity for CO_2. Carbon dioxide may cause interlayer expansion when it is adsorbed by smectite (Charlet et al., 2017). Grekov et al. (2020) investigated the adsorption of CH_4 and CO_2 in the interlayers of Na- and Mg- montmorillonite. Na-Mmt was dehydrated at a lower temperature than Mg-Mmt. This result was explained with localized water in the interlayer of Mg-Mmt due to strong bonding to the charge-balancing cations. While the surface areas of fully dehydrated clay samples were similar, the surface areas of partially dehydrated Mg-Mmt were 3 times larger than fully dehydrated samples. Adsorption experiments were carried out on fully and partially dehydrated smectite samples at 115 and 200°C for 24 h. Mg-Mmt adsorbed a higher amount of gas than Na-Mmt at 115°C due to interlayer expansion. However, the amount of adsorbed CH_4 and CO_2 on Mg-Mmt at 200°C were the same as Na-Mmt at 115°C due to interlayer space of Na-Mmt was already closed (Grekov et al., 2020).

Molecular simulations of carbon dioxide and methane adsorption in clay minerals using grand canonical Monte Carlo (GCMC) have been employed widely (Jin and Firoozabadi, 2013, 2014; Kadoura et al., 2016; Yang et al., 2015; J. Zhang et al., 2016). Jin and Firoozabadi (2013) investigated CH_4 and CO_2 adsorption in pyrophyllite and Na-montmorillonite clays with different pore sizes (1-4 nm) using GCMC simulations performed at 25°C and pressure up to 5 MPa. Two fixed clay sheets, each containing 32 unit clay cells, were used in simulations. The adsorption isotherms of gases in clay nanopores with 1 nm pore size illustrated that Na-montmorillonite has a higher sorption capacity for CO_2 than pyrophyllite in particular at lower pressures while pyrophyllite has a higher sorption capacity for CH_4. However, it was inferred that cation exchange has a strong effect on CO_2 sorption while it does not have a significant effect on CH_4 sorption. In addition, CO_2 sorption was higher than CH_4 in both clay nanopores. It is reported that the amount of CO_2 adsorption was higher in clay nanopores with small pore sizes due to strong electrostatic interactions. Although a similar adsorption behavior was observed in 4 nm clay nanopores, the reason for higher adsorption capacity for CO_2 with increasing pressure was attributed to large pores which lead to weakening of the correlations between the two layers on CH_4 adsorption. It is concluded tha while carbon dioxide are dominated by adsorption clay charges, methane adsorption is dominated by the surface area of the clay which is consistent with experimental results Jin and Firoozabadi, 2013).

Same researchers (Jin and Firoozabadi, 2014) also studied CH_4 and CO_2 adsorption in Na-montmorillonite nanopores with different pore sizes (1-4 nm) in the presence of water using GCMC. In order to investigate the effect of water on adsorption, two different approaches were used in simulations. Simulations were performed with a range of water density between 0 and 0.8 g/cm3 at 25°C and up to 6 MPa. The simulation results have shown that both CH_4 and CO_2 adsorption in both clay nanopores of pore size 1 and 4 nm decreases with increasing water content since water molecules have stronger affinity to clay surface. The density profiles also shown that H_2O molecules were adsorbed on Na-montmorillonite surface while CH_4 molecules are adsorbed inside the pores in different sizes. Although density distribution of CO_2 molecules exhibited similar behavior in clay pores with 1 nm pore size, CO_2 adsorption layer was stronger than CH_4. On the other hand, in larger pores, carbon dioxide molecules exist only in second (weaker) adsorption layer which was also observed in dry condition in their previous research (Jin and Firoozabadi, 2013, 2014).

Kadoura et al. (2016) investigated adsorption of CO_2, CH_4 and gas mixture by montmorillonite in presence of water (0.2-0.6 g/cm3) using GCMC method. Simulations were conducted at 25°C temperature and pressure up to 5 MPa on different montmorillonite samples (Na-, Cs-, and Ca-mmt) with different basal spacings (1.2–3 nm). Two clay layers each having 32 unit cells were used in simulations. Adsorption isotherms shown that adsorption capacity of montmorillonite decreased for H_2S, CO_2, CH_4 and N_2 gases, respectively. Isosteric heats decreased in the same order, consistently. The models used by the research group were consistent with single component (CH_4 and CO_2) experimental results. The simulations have shown that as water content increases in clays, adsorption of pure CH_4 and CO_2 decreases. On the other hand, CO_2 is preferentially adsorbed in the presence of high water content for 3 nm basal spacing in lower pressures. Among different montmorillonite clay samples, Ca contained montmorillonite shown the highest adsorption capacity where Cs contained one exhibited the lowest for the single component systems due to the cation hydration energies (Kadoura et al., 2016). The results are consistent with the results of another simulation (Jin and Firoozabadi, 2014) performed in water-fully saturated conditions; therefore, it can be concluded that water content decreases adsorption of CO_2 and CH_4.

Yang et al. (2015) investigated adsorption of carbon dioxide, methane and their mixtures in Na-montmorillonite (different basal spacing 1.4 and 2.1 nm) using GCMC simulations. The simulations were performed at 45°C temperature and pressure up to 20 MPa. The

results shown that montmorillonite has higher adsorption capacity for CO_2 than CH_4. In addition, it was concluded that CO_2 molecules are preferentially adsorbed as compared with the CH_4. When the adsorbed CO_2 amounts were compared in both small and large pores, it is seen that larger pores have higher adsorption capacity at higher pressures. The maximum amount of excess adsorption was obtained in the medium pressure range due to change in the bulk phase density of fluid (Yang et al., 2015).

Another research is conducted on CO_2 and CH_4 adsorption in illite clay (with 2 nm pore size) using GCMC method at different temperatures (25, 40 55, 85 and 150°C) and pressure up to 50 MPa (J. Zhang et al., 2016). In this study, effect of interlayer counter cations (K^+) was also investigated. In the simulations, 15 clay unit cells were used in a clay layer. Simulation result has shown that sorption capacity of illite increases as pressure increases and temperature decreases. Also, the results were compared with another research (Jin and Firoozabadi, 2013) on simulation of CH_4 and CO_2 adsorption in montmorillonite clay conducted in similar conditions and it is reported that the lower values for CH_4 uptake was determined. In addition, the experimental results of a research (Ji et al., 2012) contributed that montmorillonite has higher adsorption capacity for CH_4 than illite. Furthermore, radial distribution functions (RDF) of interlayer counter cation (K^+)-adsorbate (CO_2) at 25°C and 30 MPa illustrated that although CO_2 molecules do not have net charge, they have both partial charges and the linear quadrupole moment which lead to strong CO_2 and K^+ interactions, which dominates adsorbant-CO_2 interactions (J. Zhang et al., 2016). Since in the HLW repositories, particularly Callovo-Oxfordian formations, temperature is between 22 and 90°C and the pressure is up to 12 MPa (ANDRA, 2005a, 2005b), this research is conducted in conditions, which are similar in the HLW repositories.

1.4.4 Adsorption of other gases in nanoporous materials

It is reported that clays and metal-organic frameworks exhibits similar features in terms of adsorption behaviors (J. Zhang et al., 2016). Therefore, literature review was also made on MC simulations of gas adsorption in metal-organic frameworks (MOF) (Düren et al., 2004; Ryan et al., 2008; Walton et al., 2008). Düren et al. (2004) studied methane adsorption in a series of MOFs (IRMOF-1 and IRMOF-6) using GCMC at 25°C and pressure up to 4 MPa. In the simulations, DREIDING force field was used. The results were compared with the results obtained from experiments (Eddaoudi et al., 2000; H. Li et al., 1998) and MD simulation performed using UFF force field (Rappe et al., 1992).

It is reported that MC simulation results were in good agreement with MD simulation results and disagreement only observed within experimental results at lower pressures (Düren et al., 2004).

Walton et al. (2008) performed both experiments and GCMC simulations for carbon dioxide adsorption in IRMOF-1 at 195, 208, 218, 233, 273 K and 25°C and up to 120 kPa. Two different models were used in the simulations. While one of the models included only Lennard-Jones interactions, the other included both Lennard-Jones and Coulombic interactions. Comparison of simulations and experimental results shown that the amount of adsorbed CO_2 was highest in the simulation which included both interactions and lowest in the simulation which included only Lennard-Jones interactions. In addition, the adsorption isotherm obtained using the simulation which included both interactions was more consistent with the one obtained from the experiment (Walton et al., 2008). Ryan et al. (2008) studied hydrogen adsorption in IRMOF-1, IRMOF-10 and IRMOF-16 using GCMC simulations at cryogenic temperature and 25°C and up to 12 MPa. It is reported that their simulation results were consistent with the experimental results (Kaye et al., 2007).

There are some studies that molecular dynamics (MD) is applied to CO_2 and/or CH_4 gas adsorption in clays (Cygan et al., 2012; M.-S. Lee et al., 2018; Loganathan et al., 2020; Martos-Villa et al., 2014). Lee et al. (2018) investigated the intermolecular interactions between a mixture of CH_4, H_2O and CO_2, and hydrated Ca-montmorillonite using a dispersion corrected density functional based ab initio molecular dynamics simulation (AIMD) at 50°C and up to 12 MPa. Besides intermolecular interaction, polarization effects were examined. It is reported that while carbon dioxide displays a higher affinity for Lewis acidic sites in clays, a free energy analysis indicates that a full CO_2 monolayer is needed to displace CH_4. It is concluded that the adsorption mechanisms for CO_2 and CH_4 are radically different. Additionally, as a result of the interaction of CH_4 with water, it helps to move away from clay mineral (M.-S. Lee et al., 2018).

Loganathan et al. (2020) investigated carbon dioxide and methane partitioning and structures in two different illite clay minerals consisting different cations, K-illite and Na-illite, using constant reservoir composition molecular dynamics (CRC-MD) which is a new molecular modeling method. Simulations were performed at 50°C and 12.4 MPa (with equimolar CO_2-CH_4 mixture). They also stated that clay minerals are more attractive to CO_2 than CH_4. However, they indicate that protonated surfaces have greater

preference for methane than external surfaces, with the concentration near the surface close to that in the bulk fluid. In contrast, the CH_4 concentration in the first fluid layer on the external surfaces is less than the bulk (Loganathan et al., 2020).

Martos-Villa et al. (2014) studied both CO_2 and CO_2-CH_4 characterization in different Na rich smectites (montmorillonite and beidellite) in presence of water. The adsorption energies were calculated at 0 and 50 °C temperature and 40 bar pressure using molecular dynamics simulations. NPT ensemble was used in the simulations. In the simulations, different force field were used. Ab initio base DFT and CVFF force field were used in the simulations. It is reported that adsorption energy of montmorillonite-hydrate complexes was more negative than beidellite. This result illustrated that montmorillonite-hydrate complexes are more stable than beidellite- hydrate complexes (Martos-Villa et al., 2014).

Hwang et al. (2019) performed experiments and modeling for the adsorption of CO_2 and CH_4 on Na-montmorillonite clay at different temperatures (25-115 °C) and pressures (0.2-250 bar). The adsorption experiments were carried out at 25, 50, 80 and 115 °C. According to CO_2 and CH_4 isotherms, the amount of excess adsorption was increasing monotonically as pressure increases until the maximum value. After maximum points, the isotherms slightly decrease with increasing pressure. Lattice density functional theory (LDFT) was used to reproduce the experimentally observed adsorption isotherms assuming monolayer adsorption and Henry's law. Although LDFT model has some limitations such as the adoption of a specific structure and shape of the pore, the discretization of the pore into an integer number of layers and the use of the same lattice spacing for different adsorbates, it represents distribution of pore sizes and reveals adsorption behaviors. The LDFT model results were compatible with the experimental data. The adsorption enthalpy values were found to be at the lower end of the expected range. This was explained by weak sorbing ability of clays. In addition, CO_2 shown stronger affinity than CH_4 on Na-montmorillonite (Hwang et al., 2019). Same research group investigated adsoption of CO_2 and CH_4 on different clay samples (Na-montmorillonite, illite-smectite mixed layer and illite) at different temperatures (25, 50, 80 and 115°C) and pressures (0.2-300 bar). Na-montmorillonite and illite-smectite mixed layer illustrated similar CO_2 and CH_4 uptake capacities; however, illite showed smaller CO_2 and CH_4 uptakes due to its smaller total pore volume. The results showed that CO_2 and CH_4 uptakes were between 10 to 50 μmol/g at 1.5 bar in illite (Hwang and Pini, 2019).

Table 1.6 – Atomistic simulations of CO_2 and CH_4 adsorptions performed by different groups

.

Researchers	Gas	Water presence (g/cm3)	Adsorbent	Pore size (nm)	Conditions	Force Field	Ensemble
Jin and Firoozabadi (2013)	CH_4, CO_2	-	Pyrophyllite, Na-mnt	1-4	T: 25°C P: Up to 5MPa	TraPPE (CH_4), EPM2 (CO_2), Dreiding	Grand canonical (VT)
Jin and Firoozabadi (2014)	CH_4, CO_2	0-0.8	Na-mnt	1-4	T: 25°C P: Up to 6 MPa	Flexible three-site SPC-E (water) TraPPE (CH_4) Flexible EPM2 (CO_2) Dreiding (Clay atoms and Na ions)	Grand canonical (VT) MC
Kadoura et al. (2016)	CH_4-CO_2	0.2-0.6	Na-mnt, Cs-mnt, Ca-mnt	1.2-3	T: 25°C P: Up to 5 MPa	SPC/E model (water) CLAYFF (mnt) TraPPE (CH_4) Flexible EPM2 (CO_2) Dreiding	Grand canonical (VT) MC
Yang et al. (2015)	CH_4, CO_2, CH_4-CO_2	-	Na-Mnt	1.4 and 2.1	T: 45°C P: Up to 20 MPa	EPM2 (CO_2), TRAPPE (CH_4)	Grand canonical (VT)
Zhang et al. (2016)	CH_4, CO_2	-	Illite	2	T: 25,40, 55, 85 and 150°C P: Up to 50 MPa	EMP2 (CO_2), TraPPE (CH_4), CLAYFF	Grand canonical (VT)
Düren et al. (2004)	CH_4	-	IRMOF-1, IRMOF-6	-	T: 25°C P: 4 MPa	DREIDING	Grand canonical (VT)
Walton (2008)	CO_2	-	IRMOF-1	-	T: (-78, -65, -55, -40, 0 and 25°C P: up to 0.012 MPa	TraPPE (CO_2-CO_2), DREIDING	Grand canonical (VT)
Lee et al. (2018)	CH_4, CH_4-CO_2	N=4-16 moles	Ca-Mnt	1.4 and 2.1	T: 50°C P: Up to 12 MPa	AIMD	
Loganathan et al. (2020)	CO_2-CH_4	-	K-illite, Na-illite	0.3-7.6	T: 50°C P: 12.4 MPa	CRC-MD	
Martos-Villa et al. (2014)	CO_2, CH_4-CO_2		Na-Mnt Na-beidellite	-	T: 50°C P:4 MPa	DFT, CVFF	

Summary of atomistic simulations of CO_2 and CH_4 adsorption performed by different research groups is given in Table 1.6.

1.5 Diffusion of gases in nanoporous materials

Investigating the diffusion mechanism in clay rocks is crucial since the pore water oversaturates if the gas generation rate is larger than the diffusive flux (Bardelli et al., 2014). This may cause fissuring and fracturing due to increasing gas pressure. This section covers the diffusion of hydrogen and other gases in clays and other porous materials.

1.5.1 Hydrogen diffusion in clays

Due to the low permeability properties of non-fractured clay rocks, diffusive transport mechanisms are dominant in clay rocks. Hydrogen may migrate in and around the repository in several ways (Figure 1.8): dissolution in water and diffusion, two-phase water flow, transfer along fractures and microfractures occurred as a result from pressure build-up (ANDRA, 2005a).

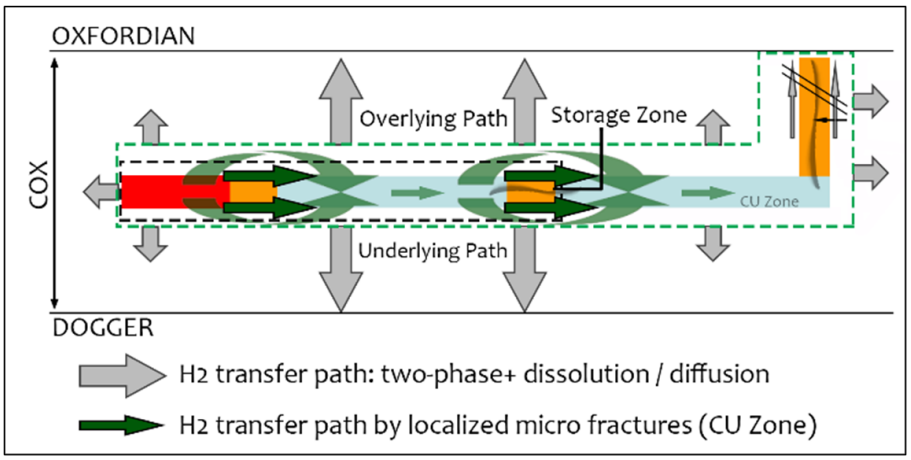

Figure 1.8 – Diagram of hydrogen transfer pathways in the repository and the surrounding Callovo-Oxfordian (adapted from ANDRA, 2005a with permission).

Bardelli et al. (2014) investigated mechanism of H_2 diffusion in both raw and purified (does not include CaO) dry Callovo-Oxfordian (COx) clay rock samples at different temperatures (5, 10, 25, 50, 100, 150 and 300 K) using quasi-elastic neutron scattering (QENS).

However, continuous diffusion was observed at 25 K and higher temperatures. In this study, H_2 diffusion was described via Fick's law model and determined the diffusion coefficients as $0.9 \pm 0.1 \times 10^{-7}$ and $0.8 \pm 0.1 \times 10^{-7}$ m^2s^{-1} at 50 K for purified and raw COx, respectively (Bardelli et al., 2014). It is reported that calculated diffusion coefficients in this study were of the same order of magnitude as those simulated in zeolites using molecular dynamics calculations by different research groups.

In another study, the neutron scattering technique was used to investigate the structure and dynamics of hydrogen molecules coordinated into the interlayer of hydrated Ca-laponite clay (Edge, 2014). Interlayer height of hydrated Ca-laponite was 2.82 Å, which is almost the same as the kinetic diameter of H_2 due to effect of the water molecules. The layer spacing of Ca-laponite was adjusted to fit the diameter of hydrogen by using water. It is confirmed by the analysis of Bragg intensities that H_2 was intercalated into two-dimensional interlayer pores. H_2 diffusion mechanisms were studied at 40, 60, 80 and 100 K temperatures. Hydrogen molecules transport through the interlayer region is via a jump diffusion mechanism with the diffusion coefficient of $2.3 \pm 0.5 \times 10^{-5}$ cm^2s^-1 at a temperature of 40 K, which is an order of magnitude slower than in bulk liquid water (Edge, 2014).

1.5.2 Diffusion of other gases in clays

Gadikota et al. (2017) studied diffusion of CO_2, CH_4, H_2 and noble gases (He, Ne, Ar, Kr, and Xe) in both bulk liquid water and water-saturated Na-montmorillonite clay mesopores and interlayer nanopores at 25°C using molecular dynamics (Gadikota et al., 2017). In the simulations, CLAYFF model force field and NVT ensemble are used. To determine self-diffusion coefficients, the mean-square displacement versus time graph was plotted using Einstein relation. They also compared the obtained diffusion coefficient values in both mesopores and nanopores with the experimental results that performed in NaCl aqueous solution at the same temperature. Those results have shown that both diffusion coefficients were almost the same for each gases. In addition, diffusion coefficient in mesopores calculated by simulation were obtained as similar with the results obtained in bulk water while the values of simulation predictions in nanopores were below. Therefore, investigating the diffusion in bulk water may shed light on understanding diffusion in mesopores since the similar results are obtained. Due to lack of experimental studies on gas diffusion in the literature, the results obtained in this study were compared by the

previous modeling predictions. It is reported that the results were consisted with former predictions. Also, the results are consistent with the results of MD simulation of noble gases diffusion which performed by Bourg and Sposito (2008).

H2-diffusion

Although gas diffusion in porous material, such as clay minerals, is slightly slower than diffusion in water, the order of magnitude of the diffusion coefficient are quite similar. Therefore, investigating gas diffusion in water may help to understand the diffusion mechanisms in bulk water (Edge, 2014; Gadikota et al., 2017). However, only the results obtained for mesopores were similar. Accordingly, it might be usual to investigate diffusion in bulk water for further aspects. Cygan et al. (2012) investigated the diffusion of CO_2 in water at 20, 30, 40, 50, 65, 75 and 85°C, and 20 MPa, besides adsorption and molecular interactions between CO_2 and Na-montmorillonite. CLAYFF force field, canonical (NVT) and NPT ensembles were used in molecular dynamics simulations. In this study, they built different model for both rigid and flexible CO_2 gases. They compared that obtained simulation results with the experimental result carried out by different research groups. As temperature increases, the difference in results between experimental and model were increased. On the other hand, results obtained from the models were almost the same as one obtained from experiments. In addition, models built for flexible CO_2 were more similar with experimental conditions (Cygan et al., 2012).

Maruthi Sena and Krishnan (2019) performed molecular dynamics to investigate the diffusion of CO_2 and H_2O in different montmorillonite samples (Cs^+, K^+, Na^+ and Ca^{2+}) 50°C temperature and 9 MPa pressure. Adaptive biasing force (ABF) method was used in the simulation. Among the different montmorillonite samples, Ca-montmorillonite has the highest diffusivity for CO_2 due to weaker CO_2 affinity for Ca^{2+}. On the other hand, it is reported that it has lowest diffusivity for H_2O due to its high activation barrier (Maruthi Sena and Krishnan, 2019).

Martos-Villa et al. (2014) also investigated both CO_2 and CO_2-CH_4 diffusions in different Na-rich smectites (montmorillonite and beidellite) in the presence of water at (273 and 323 K) 0 and 50 °C temperature (stable and unstable conditions) and 4 MPa pressure using molecular dynamics simulations. NPT ensemble was used in the simulations. Different force fields, ab initio base DFT and CVFF, were used in the simulations (Martos-Villa et al., 2014). The diffusion coefficients were calculated using mean square displacement. Obtained values of diffusion coefficients were in number of magnitude range of 10^{-21}-10^{-22}

m^2/s. Those values were quite lower when compared with other simulation results.

1.5.3 Diffusion of other gases in other nanoporous materials

Besides diffusion in clay-rich materials, diffusion in metal-organic frameworks (MOFs) has been studied widely (Ford et al., 2012; Skoulidas and Sholl, 2005). Ford et al. (2012) investigated self-diffusion of hydrocarbons in prototypical MOF (IRMOF-1) by both molecular dynamics simulations and pulsed field gradient NMR experiments. Diffusion coefficient determined by MD simulation for methane was lower than experimental results since they are not a measure of pure intracrystalline self-diffusion. Activation energies for hydrocarbons including methane, ethane, n-hexane, n-decane, n-dodecane, n-hexadecane, and benzene were determined by MD simulations. Methane shown the greatest discrepancy when simulation and experimental results are compared. This disagreement was explained by the fact that "the lightest hydrocarbons methane and ethane easily exchange between the intra- and intercrystalline space on the NMR time scale, and the methane and high-temperature ethane measurements strongly depend on the observation time, as previously ethane from PFG NMR. Due to the exchange with the gas phase, the reported NMR data represents upper limits for the activation energies of intracrystalline self-diffusion. Therefore, they are both higher than the MD results. This comparison shows that the temperature-dependent MD simulations yield activation energies, which, at least for methane and ethane, are consistent with those from PFG NMR. The MD data in IRMOF-1 fall remarkably near literature results for the bulk liquid. In addition, the effect of loading on diffusion was studied for methane, n-hexane and benzene by MD simulation. The results have shown that while loading has no significant effect on diffusion, it has concrete effects in the case of high loadings.

1.6 Objectives of the project

Clay-rich geological formations are widely considered to be optimal candidates as the host rocks for geological repository facilities of high-level radioactive waste due to their desirable features. Specifically, montmorillonite, a type of clay mineral, is commonly found in both the composition of the host rock and engineered barriers. In the repository, various mechanisms lead to the formation of H_2, CO_2, CH_4, H_2O vapor, and radioactive gases. In particular, the anoxic corrosion of stainless steel waste containers and water

radiolysis reactions caused by alpha decay generate H_2, reported as the most abundant gas in the repository. The accumulation of H_2 gas in the repository may cause gas pressure build-up, posing a risk of overpressure and fracture in the surrounding clay rock unless it diffuses, reacts, or is absorbed by the constituent clay rocks.

To develop reliable, long-term strategies aimed at preventing the chemical and mechanical destabilization of radioactive waste repositories, it is crucial to enhance the quantitative understanding at the molecular scale of the underlying processes. Previous atomistic simulations of gas adsorption in clays were predominantly focused on CO_2 and CH_4 adsorption, while limited attention given to H_2 adsorption in clays. Although there are experimental studies on hydrogen adsorption, simulations mostly concentrate on hydrogen diffusion in clay rather than its uptake. Therefore, there is a lack of research on hydrogen adsorption and its uptake in clays at temperature and pressure conditions that are expected to develop in the high-level radioactive waste repositories.

The objective of this project is to provide a structured analysis of H_2 adsorption in clay environment commonly found in radioactive waste disposal repositories. To this end, this thesis investigates the impact of several crucial factors, including temperature, pressure, the presence of water, pore size/hydration level, and the type of interlayer cation. More specifically, we explore H_2 adsorption in the interlayers of both dry and hydrated (at various levels) Na-, Ca-, and Cs-montmorillonite at temperatures of 25, 50, and 90°C, and pressures up to 120 bar, by means of Monte Carlo and hybrid methods Monte Carlo/molecular dynamics of computer simulation in order to improve fundamental understanding of the physical and chemical processes controlling the interactions between H_2, aqueous solutions, and montmorillonite type of clay. Additionally, the study aims to investigate hydrogen adsorption at high pressure to understand where H_2 reaches to saturation in montmorillonite.

Chapter 2

Models and Methods

2.1 Computational modeling and methods

Computational modeling is a method that uses computer-based models and algorithms to investigate real or theoretical systems by replicating them. This approach enables the analysis, prediction, and interpretation of system behavior without the need for physical, hands-on experiments. Computational modeling can be applied at varying scales, depending on the time scale of the processes and the size of the systems. In Figure 2.1, various scales of computational modeling are presented.

Modeling geological processes can be performed using continuum and finite element methods, often requires highly extended length and time scales, reaching kilometers and millions of years, respectively. Mesoscale modeling enables a more detailed simulation to investigate molecular fragments with relatively shorter length and time scales.

In contrast to macro- and meso-scale methods, quantum mechanics or molecular mechanics, used to perform molecular modeling are highly niche techniques that enable us to the study of electrons and atoms, respectively. The former includes much smaller system size (between Å and nanometers) with a time scale of femtoseconds to tens of picoseconds, enabling the study of chemical reactions. However, it has a drawback of requiring expensive computational time. The latter has a larger system size (between Å and micrometers) with a time scale of tens of femtoseconds to hundreds of nanoseconds.

Molecular mechanics methods based on parameterized analytical expressions that consider atomic charges and atom interactions (discussed in more details in subsection 2.3) are employed in this project. These methods enable the computation of structural, thermodynamic, transport, and dynamic properties by generating a significant number of atomic configurations. They also allow the interpretation of experimental findings or provide guidance for future experiments, as well as the study and prediction of extreme conditions that cannot be practically achieved by experiments. There are two classical

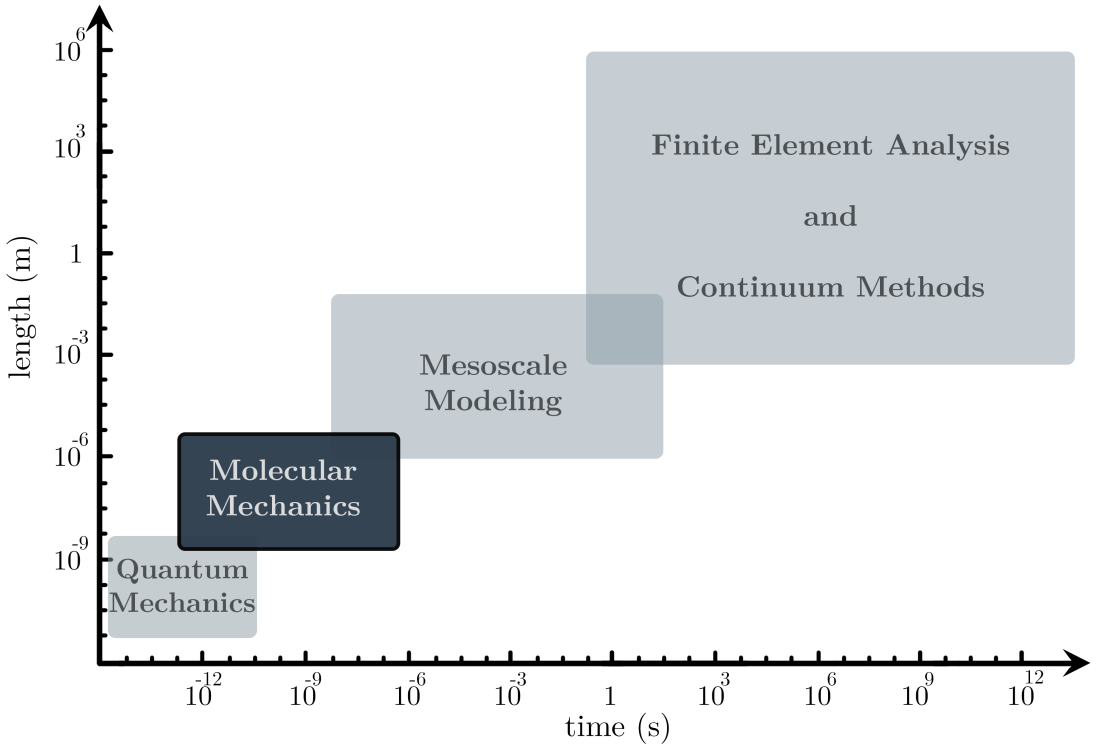

Figure 2.1 – Schematic representation of multi-scale modeling correspondence time and length scales.

methods for molecular modeling, namely Monte Carlo and Molecular Dynamics. Monte Carlo involves ensemble averaging of molecular configurations over a computationally generated random Markov chain. Molecular Dynamics, on the other hand, deals with time averaging over a dynamic trajectory in the phase space of the simulated system. These methods will be discussed in more detail in subsection 2.1.1 and 2.1.2, respectively.

Selecting the system size is a critical decision to avoid both expensive and prolonged computational time. However, it is equally important to consider the system at a macroscopic scale to understand its characteristics. One of the challenges in molecular modeling is the very small system size. To address this, periodic boundary conditions are applied to a system by surrounding a simulation box with copies of itself in all three dimensions, aiming to mimic its properties at a macroscopic scale. A two-dimensional representation of periodic boundary conditions is shown in Figure 2.2, where the simulation box containing the particles I, II, III and IV, located in the center, is surrounded by copies of itself.

In Figure 2.2, three aspects related to the application of periodic boundary conditions are

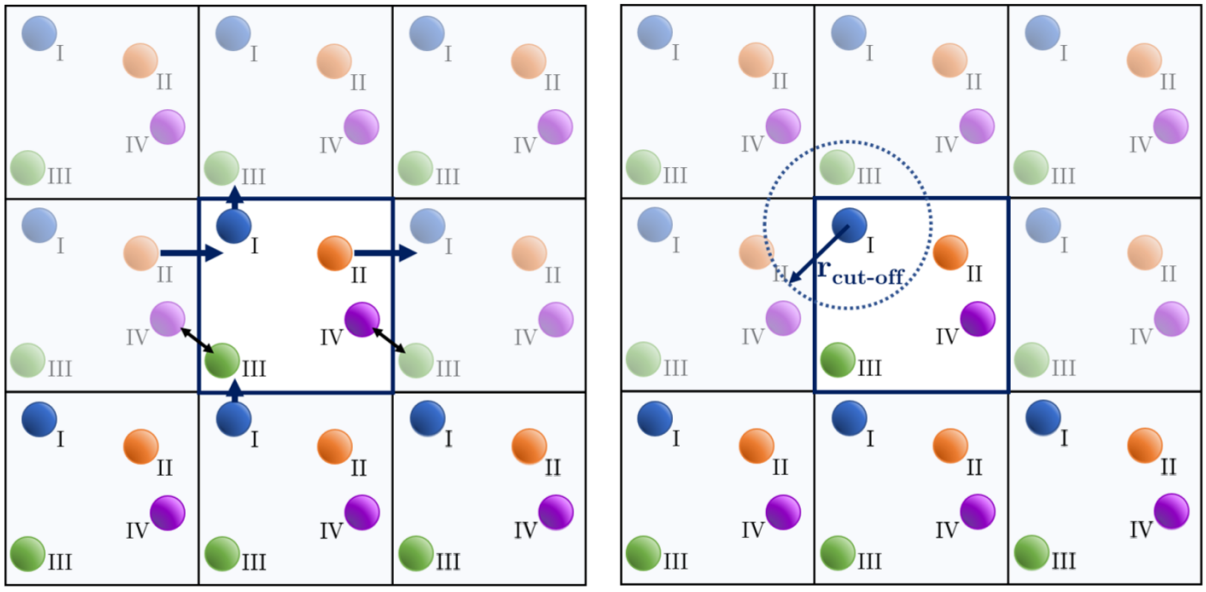

(a) (b)

Figure 2.2 – Two-dimensional representation of periodic boundary conditions. The simulation box, located in the center, is surrounded by copies of itself. a) Single-sided arrows indicate the displacement of particles, while double-sided arrows represent the shortest distance between particles. b) The dashed circle corresponds to the cut-off radius, $r_{cut-off}$, around particle I in the simulation box.

worth discussing. First, in a time-evolving system, it is assumed that if a particle (see particle I and II with single-sided arrows in Figure 2.2a) exits the simulation box (located at the center) on one side, it enters the same box on the other side. Secondly, the double-side arrows in Figure 2.2a indicate the shortest distance between particles III and IV. Although particle III in the simulation box can interact with other copies of particle IV in different replica boxes, only a single interaction between particles III and IV with the minimum interatomic distance is considered. This principle is referred to as the nearest or minimum image convention, aimed at minimizing the time-consuming part of either Monte Carlo or molecular dynamics simulation by reducing the number of non-bonded interactions (see subsection 2.3).

Another approach is to set a cut-off radius (see Figure 2.2b). To do that, a particle is assumed to be at the center of a sphere with a certain radius, called the cut-off radius. This approach is often used in a similar way to the previous one to focus computational resources on the most relevant interactions. In this context, the cut-off radius defines a

sphere around particle I, where only interactions with other particles in this sphere are considered. It is crucial to choose a cut-off value that prevents a particle from interacting with its own image or encountering the same molecule more than once. Therefore, in cubic simulation cells, the cut-off should not exceed half of the length simulation box. For rectangular cells, it should be no more than half the length of the shortest side.

2.1.1 Monte Carlo

Monte Carlo (MC) method is based on random sampling. MC methods enable the determination of structural and thermodynamic properties by generating new configurations from existing configurations and statistically valid results are obtained by appealing to Boltzmann distribution. Although MC simulations have a significant advantage of requiring less computer time compared to MD simulations, it is not possible to calculate dynamical properties such as self-diffusion coefficient, mean-square displacement or viscosity since this method is not time-dependent (Braun et al., 2019; Hinchliffe, 2003; Young, 2001).

In Monte Carlo simulations, ensemble averages are used to obtain a statistical average and some state variables are constant since these simulations are performed under equilibrium statistical mechanics ensembles (Cygan et al., 2009; Young, 2001). MC simulations can be performed in six different ensembles namely canonical, isobaric-isothermal, grand canonical, microcanonical, isotension-isothermal, and Gibbs.

Metropolis et al., 1953 introduced the first MC method in canonical (NVT) ensemble (Sadus, 2002). In canonical ensemble, the number of particles, volume, and temperature are the same and kept fixed in each cell that comprised the ensemble. Experiments are seldom carried out under these conditions (Frenkel and Smit, 1996; Hinchliffe, 2003). On the other hand, experiments are generally conducted at constant pressure and temperature. Therefore, isothermal-isobaric ensemble (NPT), which is first described by Wood (1968), is widely used in MC simulations (Frenkel and Smit, 1996).

In grand (μVT) canonical ensemble, which is introduced first by Norman and Filinov, 1969 the chemical potential, volume and temperature are constant and this is the only ensemble in which the number of particles is allowed to fluctuate. In addition, it is the most convenient ensemble for adsorption studies since chemical potential and temperature are fixed (Frenkel and Smit, 1996; Hinchliffe, 2003).

As given in Dubbeldam et al. (2013), in grand canonical ensemble, the partition function is given as:

$$Z(\mu, V, T) = \sum_{N=0}^{\infty} \frac{V^N e^{\beta\mu N}}{\Lambda^{3N} N!} \int e^{-\beta U(\mathbf{s}^N;\mathbf{h})} d^N\mathbf{s} \tag{2.1}$$

where the chemical potential μ, the volume V, and temperature T are fixed. The probability of a particular configuration is

$$P(\mathbf{s}^N, V) \propto \frac{V^N e^{\beta\mu N}}{\Lambda^{3N} N} e^{-\beta U(\mathbf{s}^N;\mathbf{h})} \tag{2.2}$$

The pressure p in the reservoir is related to chemical potential, which is described as:

$$\beta\mu = \beta\mu^0_{IG} + \ln(\beta f) \tag{2.3}$$

where $f = \phi p$ is the fugacity. The chemical potential of the ideal gas (μ^0_{IG}) is described as:

$$\mu^0_{IG} \equiv \frac{ln(\lambda^3)}{\beta} \tag{2.4}$$

Although it is not the same with pressure, fugacity has the same unit as pressure and is a measure of the activity of the gas where ϕ is the fugacity coefficient. Moreover, the acceptance rule for insertion is given as:

$$acc(N \to N+1) = min\Big(1, \frac{\beta V \phi p}{N+1} e^{-\beta[U_n(\mathbf{s}^{N+1};\mathbf{h}) - U_o(\mathbf{s}^N;\mathbf{h})]}\Big) \tag{2.5}$$

and acceptance rule for deletion is

$$acc(N \to N-1) = min\Big(1, \frac{N}{\beta V \phi p} e^{-\beta[U_n(\mathbf{s}^{N-1};\mathbf{h}) - U_o(\mathbf{s}^N;\mathbf{h})]}\Big) \tag{2.6}$$

In microcanonical (NVE) ensemble, first suggested by Creutz, 1983, the total number of particles, total energy and volume are constant in each cell. This method is more similar to MD method than MC since uses no random numbers (Frenkel and Smit, 1996; Hinchliffe, 2003). The isotension-isothermal ensemble Monte Carlo method is first described by Najafabadi and Yip, 1983. Although this constant-stress MC method is quite similar to the constant-pressure MC method, it cannot be used for homogeneous fluids since its simulation box does not have resistance for the deformation (Frenkel and Smit, 1996).

Gibbs ensembles (μPT) method which was first suggested by Panagiotopoulos, 1987 is usually used for investigating the phase coexistence of multicomponent fluids (Frenkel and Smit, 1996; Sadus, 2002). This method enables simulation phase equilibria where the pressure, temperature, and chemical potential are equal for each phase. The significant advantage of the method is that it does not require computing the relevant chemical potentials as a function of pressure at several compositions and as the system spontaneously finds the densities and compositions of the coexisting phases (Frenkel and Smit, 1996). In conclusion, among all ensembles, Gibbs and grand canonical are more convenient ensembles for the adsorption simulations. Numerous gas adsorption simulations were successfully performed in grand canonical ensemble (Botan et al., 2010; Jin and Firoozabadi, 2013, 2014; Kadoura et al., 2016; Ziemiański et al., 2020).

2.1.2 Molecular dynamics

Molecular dynamics (MD) is an atomic-scale method based on Newton's Second Law and used to simulate the motion of a classical system of particles. MD applications have many advantages over experimental methods. The simulation results can provide an atomistic description of physical and/or chemical processes and help the interpretation of experimental results. Moreover, it enables to compute not only structural and thermodynamic properties, but also the transport and dynamic properties such as the diffusion coefficient of dissolved gases, and also to study and predict extreme conditions such as in geological disposal of radioactive waste (Ma et al., 2019). Unlike Monte Carlo (MC), which moves particles stochastically, MD moves particles deterministically. It generates the states (configurations and velocities) by integrating Newton's second law, equations of motion (Equation 2.7).

$$F_i = m_i a_i \tag{2.7}$$

$$F_i = -\nabla_i U_i \tag{2.8}$$

F_i, m_i and a_i represents the interaction force, mass and acceleration of atom i, respectively. It should be noted that both F_i and a_i are the functions of positions and velocities of the atom i constantly. U_i denotes the interaction potential atom i with other atoms in the system (refer to Equation 2.8).

In molecular dynamics simulations, the total energy, E is a constant of motion in a system of N particles in volume V. Therefore, time averages obtained in MD simulations are equivalent to ensembles averages in microcanonical (NVE) ensemble if it is assumed that time and ensemble averages are equal. However, these simulations are usually performed in other ensembles (Frenkel and Smit, 1996).

2.1.3 Hybrid MC/MD

The hybrid Monte Carlo/molecular dynamics (MC/MD) approach integrates the methodologies of grand canonical Monte Carlo (GCMC) and molecular dynamics (MD), enabling the determination of adsorption, structural, and dynamical details through the same simulation run simultaneously. Various approaches exist for performing these types of simulations.

Grand Canonical Molecules Dynamics (GCMD) method (Boinepalli and Attard, 2003) is a hybrid Monte Carlo/molecular dynamics technique that utilizes Monte Carlo sampling for the insertion and deletion of fluid molecules with equal probability at each MD time step. Therefore, in GCMD simulations, the number of molecules fluctuates similarly to GCMC simulations while maintaining fixed values for the temperature, volume of the simulation cell, and chemical potential of the reservoir fluid components. In addition to producing thermodynamic adsorption and swelling isotherms, another advantage of GCMD is its ability to enable flexibility in the framework. Most importantly, it permits layer displacement during the intercalation within the interlayer. This method is widely used to perform CO_2 and/or water adsorption (Loganathan, Bowers, Yazaydin, Kalinichev, and Kirkpatrick, 2018; Loganathan, Bowers, Yazaydin, Schaef, et al., 2018; Loganathan et al., 2017).

2.2 Building montmorillonite models

Montmorillonite, chosen as the clay model for the simulations, was built using the following procedure with Materials Studio software. Initially, the unit cell of pyrophyllite, characterized by the chemical formula of $(Si_4)(Al_2)O_{10}(OH)_2$ was built using crystal structure data (J. H. Lee and Guggenheim, 1981) obtained by single crystal X-ray refinement, with the following unit cell parameters: a = 5.160, b = 8.966, c = 9.347 Å, and $\alpha = \beta = \gamma = 90°$. Subsequently, it was replicated as 4×4×1 along the crystallographic directions a, b, and c, respectively. Following this, one TOT layer was stacked upon another, resulting in the assembly of two TOT layers, each comprising 32 unit cells and containing a total of 1280 atoms. After creating the supercell, substitutions were randomly distributed throughout the final model to avoid an overly structured arrangement of the substituted sites upon implementing periodic boundary conditions (Ngouana W. and Kalinichev, 2014). One Si atom is randomly replaced with an Al substitution for every 32 tetrahedral sites, and one Al atom is replaced with a Mg substitution for every 8 octahedral sites. The montmorillonite models that have been built have a layer charge of -0.75 | e |. Therefore, 24 Na^+, 12 Ca^{2+} and 24 Cs^+ ions were added into the interlayers to compensate the net negative charge of the system and it transformed into:

$$Na_{24}(Si_{248}Al_8)(Al_{112}Mg_{16})O_{640}(OH)_{128}$$

$$Ca_{12}(Si_{248}Al_8)(Al_{112}Mg_{16})O_{640}(OH)_{128}$$

$$Cs_{24}(Si_{248}Al_8)(Al_{112}Mg_{16})O_{640}(OH)_{128}$$

Finally, energy minimization was performed to optimize the geometry of each structures using forcite module in Materials Studio software. Smart optimization algorithm is used with Polak-Ribiere conjugate-gradient algorithm, using default simulation parameters. Figure 2.3 illustrates the optimized Na-montmorillonite structure, whereas the optimized structures for Ca-montmorillonite (Figure A.1a) and Cs-montmorillonite (Figure A.1b) are presented in Appendix A.

Snapshots of the top and bottom TOT layers of an optimized model, as shown in Figure 2.3, are given with their respective yz plane views (Figure 2.4a,b) and xy plane views (Figure 2.4c,d). Both TOT layers are unique due to the random distribution of substitutions, resulting in distinct structural configurations.

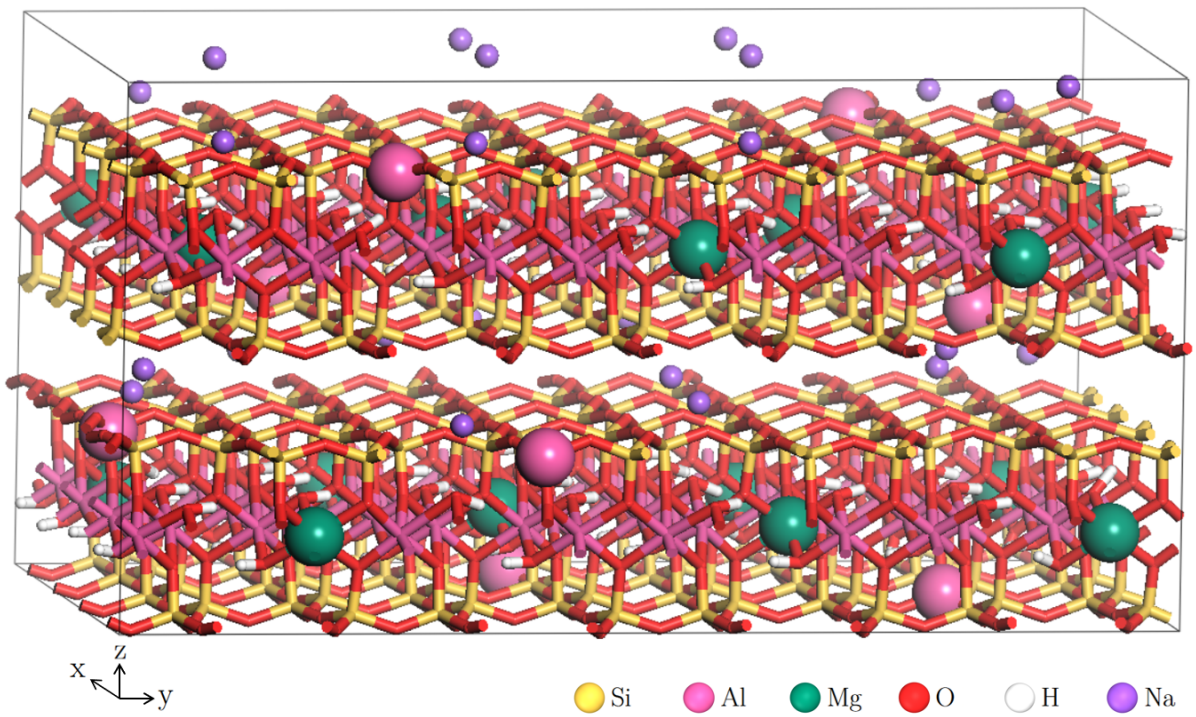

Figure 2.3 – Snapshot of dry Na-montmorillonite model after energy minimization. Color legend: Si (yellow), Al (pink), Mg (dark green); O (red); H (white), Na (purple).

In addition to the dry montmorillonite models, three different Na-montmorillonite structures were created, each exhibiting varying hydration levels namely, mono-, bi-, and tri-layer hydrated Na-montmorillonite. This was achieved by adding 5, 10, and 15 H_2O molecules into the interlayer of Na-montmorillonite corresponding to each unit cell ($O_{20}(OH)_4$). Similarly, three distinct Ca-montmorillonite structures, each representing different hydration states (mono-, bi-, and tri-layer) and two different hydrated Cs-montmorillonite structures were formed, one at the monolayer hydration level and the other at the bilayer hydration level. They transformed into:

$$Na_{24}(Si_{248}Al_8)(Al_{112}Mg_{16})O_{640}(OH)_{128}.nH_2O$$

$$Ca_{12}(Si_{248}Al_8)(Al_{112}Mg_{16})O_{640}(OH)_{128}.nH_2O$$

$$Cs_{24}(Si_{248}Al_8)(Al_{112}Mg_{16})O_{640}(OH)_{128}.nH_2O$$

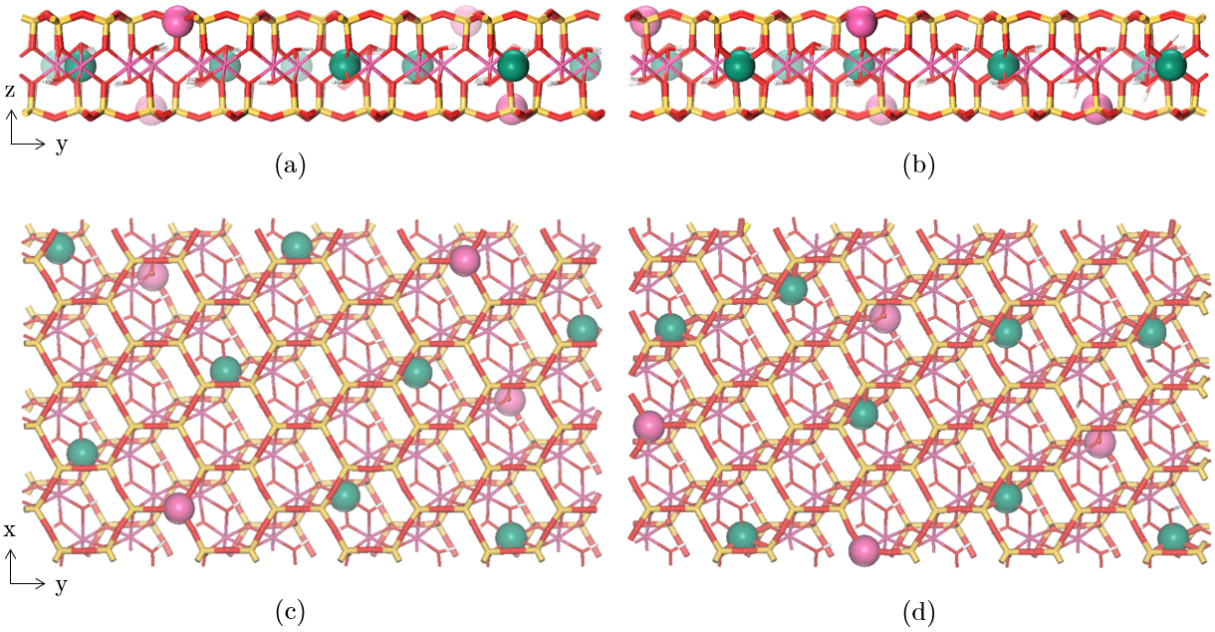

Figure 2.4 – Snapshots of a) yz plane view of top layer and b) bottom layer, and c) xy plane view of top layer and b) bottom layer. Color legend: Si (yellow), Al (pink), Mg (dark green); O (red); H (white).

where n, representing the number of water molecules, is equal to 0, 160, 320 and 480 for dry, mono-, bi- and tri-layer hydrated models, respectively.

Energy minimization was performed for all systems using Materials Studio. Subsequently, molecular dynamics simulations were performed in the NPT ensemble, allowing for the expansion of spacing, using the Forcite module at 298 K and 1 bar for both dry and saturated Na-, Ca- and Cs-montmorillonites for 2 ns, with default simulation parameters. The Na-montmorillonite models with different hydration levels used in the simulations are provided in Figure 2.5. Correspondingly, the Ca- and Cs-montmorillonite models can be found in the Appendix (Figure A.2 and A.3).

After conducting the MD simulations, models were obtained with basal spacings as listed in Table 2.1. The dry model is denoted by 0W, the monolayer hydrated model is symbolized by 1W, the bilayer hydrated model is marked as 2W, and the trilayer hydrated model is designated as 3W. Additionally, the dimensions of each model are given in Table 2.2.

Table 2.1 – The basal spacings of Na-, Ca-, and Cs-montmorillonite models at dry (0W), monolayer (1W), bilayer (2W), and trilayer (3W) hydration levels in Å

	Hydration level			
	0W	1W	2W	3W
Na-montmorillonite	9.32	13.03	16.04	20.06
Ca-montmorillonite	9.30	13.05	16.05	20.05
Cs-montmorillonite	10.38	13.05	16.06	-

Table 2.2 – Dimensions of each Na-, Ca-, and Cs-montmorillonite models in Å

	Dimension (Å)		
	x	y	z
Na-montmorillonite			
dry-Na-mmt	20.8039	36.0343	18.6440
1W-Na-mmt	20.6954	35.9603	26.0698
2W-Na-mmt	20.6932	35.9564	32.0824
3W-Na-mmt	20.7004	35.9690	40.1171
Ca-montmorillonite			
dry-Ca-mmt	20.8235	36.0890	18.6045
1W-Ca-mmt	20.7260	36.0134	26.1083
2W-Ca-mmt	20.7089	35.9837	32.1068
3W-Ca-mmt	20.6954	35.9602	40.1073
Cs-montmorillonite			
dry-Cs-mmt	20.7717	36.0040	20.7523
1W-Cs-mmt	20.7198	36.0027	26.1005
2W-Cs-mmt	20.7160	35.9961	32.1178

Figure 2.5 – Snapshots of a) dry and b) mono-, c) bi- and d) tri-layer hydrated Na-montmorillonite models. Color legend: Si (yellow), Al (pink), Mg (dark green); O (red); H (white), Na (purple).

After the MD simulations were completed (Figure 2.6a), water molecules were removed from the interlayers of the montmorillonites to be subsequently incorporated together along with hydrogen molecules during Monte Carlo and hybrid Monte Carlo/molecular dynamics simulations (Figure 2.6b).

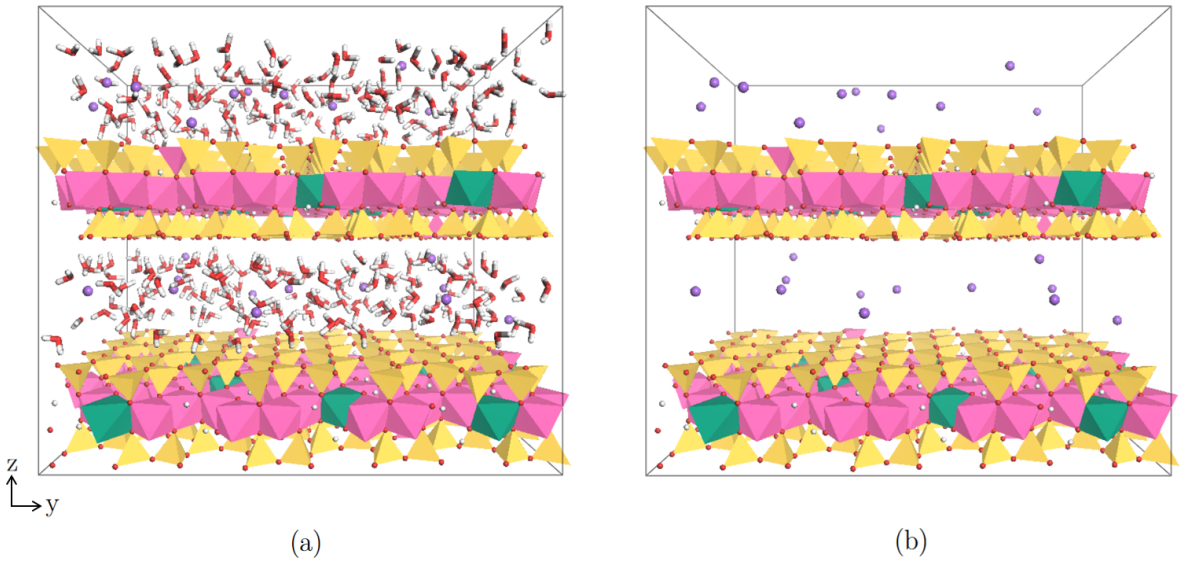

Figure 2.6 – Snapshot of bilayer hydrated Na-montmorillonite model a) with and b) without water molecules. Color legend: Si (yellow), Al (pink), Mg (dark green); O (red); H (white), Na (purple).

2.3 Interaction potentials

To perform simulations with a high degree of accuracy, it is important to deliberately choose and implement an appropriate force field which is a set of functions and parameters that collectively determines the potential energy associated with inter-molecular interactions in the system. These parameters are derived through the empirical fitting of certain material properties, such as structural and spectroscopic data, which are obtained from either hands-on experiments or quantum chemical computations.

The total potential energy (E) of the system (Eq 2.9) is represented as the summation of all bonded interactions, consisting of bond stretching and bending potentials, along with non-bonded interactions, which involve van der Waals and Coulombic forces. The bonded

interactions may also include torsion term; nevertheless, in this particular case, it is not present. Thus, it is not given in Equation 2.9. A schematic representation of the bonded and non-bonded potentials is illustrated in Figure 2.7.

$$E = E_{bond-stretch} + E_{angle-bend} + E_{vdw} + E_{coulomb} \tag{2.9}$$

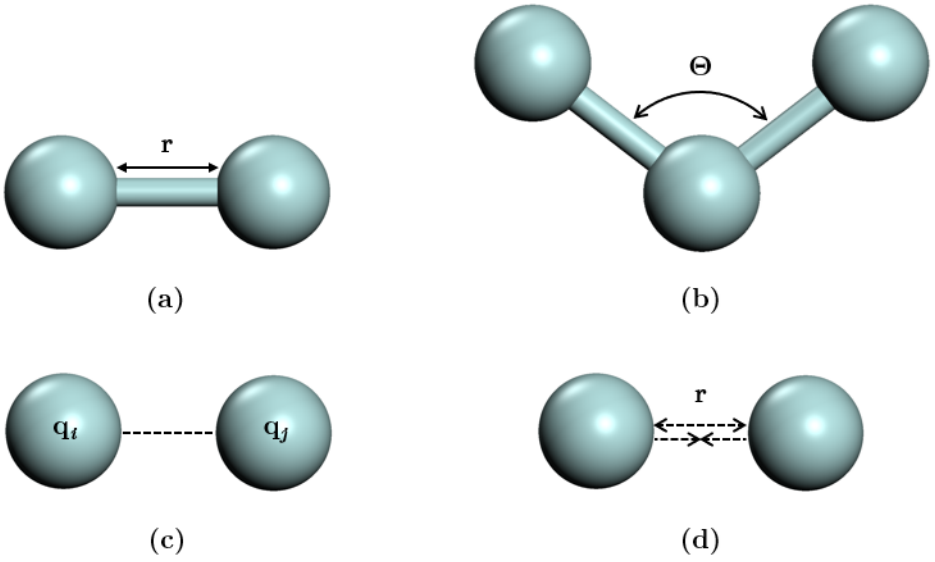

Figure 2.7 – Schematic representation of bonded potentials: a) bond scretch and b) angle bend, and non-bonded potentials c) Coloumbic d) Lennard-Jones

The electrostatic potential is determined using Coulombic energy, as shown in Eq 2.10, with q_i and q_j representing the charges of particles i and j, r denoting the distance, and ϵ_0 indicating the dielectric permittivity.

$$E_{coulomb} = \frac{1}{4\pi\epsilon_0}\frac{q_i q_j}{r} \tag{2.10}$$

The van der Waals energy is defined using Lennard-Jones potential represented in Eq 2.11 where ε and σ are empirical parameters of energy and distance, respectively. The interaction parameters (ε_{ij} and σ_{ij}) atoms are calculated by Lorentz-Berthelot general mixing rule (Eq 2.12 and 2.13).

$$E_{vdw} = 4\varepsilon \left[\left(\frac{\sigma}{r} \right)^{12} - \left(\frac{\sigma}{r} \right)^{6} \right] \tag{2.11}$$

$$\epsilon_{ij} = \sqrt{\varepsilon_i \epsilon_j} \tag{2.12}$$

$$\sigma_{ij} = \frac{\sigma_i + \sigma_j}{2} \tag{2.13}$$

One of the bonded parameters is the harmonic bond stretching energy, as defined in Eq 2.14 and the other is the harmonic angle bending energy, given in Eq 2.15. In these equations, k represents the force constant, r and θ denote bond length and bond angle, respectively.

$$E_{bond-stretch} = \frac{1}{2} k (r - r_0)^2 \tag{2.14}$$

$$E_{angle-bend} = \frac{1}{2} k (\theta - \theta_0)^2 \tag{2.15}$$

There are several force fields, such as Dreiding (Mayo et al., 1990), UFF (Universal Force Field) (Rappe et al., 1992 and CVFF (Consistent Valence Force Field) and its extended versions (CVFFH and CVFF-Interface) (Heinz et al., 2006, 2013) that have a wide range of or generic applications (Ding and Yazaydin, 2013; Düren et al., 2004; Garberoglio et al., 2005; Liu et al., 2007; Ryan et al., 2008; Walton et al., 2008). Some of these force fields have been applied in the study of clay and its systems (Jin and Firoozabadi, 2013, 2014; Martos-Villa et al., 2014; S. Zhang et al., 2018). However, there are other force fields specifically developed for clay phases to enhance accuracy and reproducibility (Boek et al., 1995; Cygan et al., 2004).

ClayFF is a force field developed for modeling multi-component mineral systems, specifically clay and clayey phases, including their interactions with aqueous solutions (Cygan et al., 2004). It relies on a description of metal-oxygen interactions that do not involve chemical bonding. In this approach, all atoms are treated as point charges. The interactions between metal and oxygen atoms are determined using Lennard-Jones (12-6) potential, given earlier in Eq 2.11, combined with electrostatic forces (Eq 2.10). ClayFF is widely used to perform the simulations of clay systems (Gadikota et al., 2017; Kadoura et

Table 2.3 – Nonbonded parameters for ClayFF (Cygan et al., 2004)

.

Species	Symbol	Charge (e)	ε (K)	σ (Å)
Hydroxyl hydrogen	ho	+0.4245	0.0000	0.0000
Hydroxyl oxygen	oh	-0.9500	78.20	3.1655
Bridging oxygen	ob	-1.0500	78.20	3.1655
Bridging oxygen with octahedral substitution	obos	-1.1808	78.20	3.1655
Bridging oxygen with tetrahedral substitution	obts	-1.1688	78.20	3.1655
Hydroxyl oxygen with substitution	ohs	-1.0808	78.20	3.1655
Hydroxyl hydrogen with substitution	hos	+0.4245	0.0000	0.0000
Tetrahedral silicon	st	+2.1000	0.0009	3.3020
Octahedral aluminum	ao	+1.5750	0.0007	4.2712
Tetrahedral aluminum	at	+1.5750	0.0009	3.3020
Octahedral magnesium	mgo	+1.3600	0.0005	5.2643

al., 2016; Loganathan, Bowers, Yazaydin, Kalinichev, and Kirkpatrick, 2018; Loganathan et al., 2020; Ngouana W. and Kalinichev, 2014; Sena et al., 2015; Teich-McGoldrick et al., 2015; J. Zhang et al., 2016; Ziemiański et al., 2020).

In this thesis, ClayFF is employed for montmorillonite models. ClayFF includes distinct charges not only for different types of atoms but also for the O atoms located at different coordination sites, thereby accommodating variations in their electrostatic behavior. Charge distribution on a unit cell of montmorillonite based on ClayFF is illustrated in Figure 2.8. The non-bonded parameters are provided in the Table 2.3.

ClayFF also incorporates bond stretch terms (2.14) for hydroxyl groups and angle bend terms (Eq 2.15) for metal-hydroxyl groups (Metal-OH). Moreover, it has been modified by re-evaluating and extending the parameterization of the metal-O-H bending terms

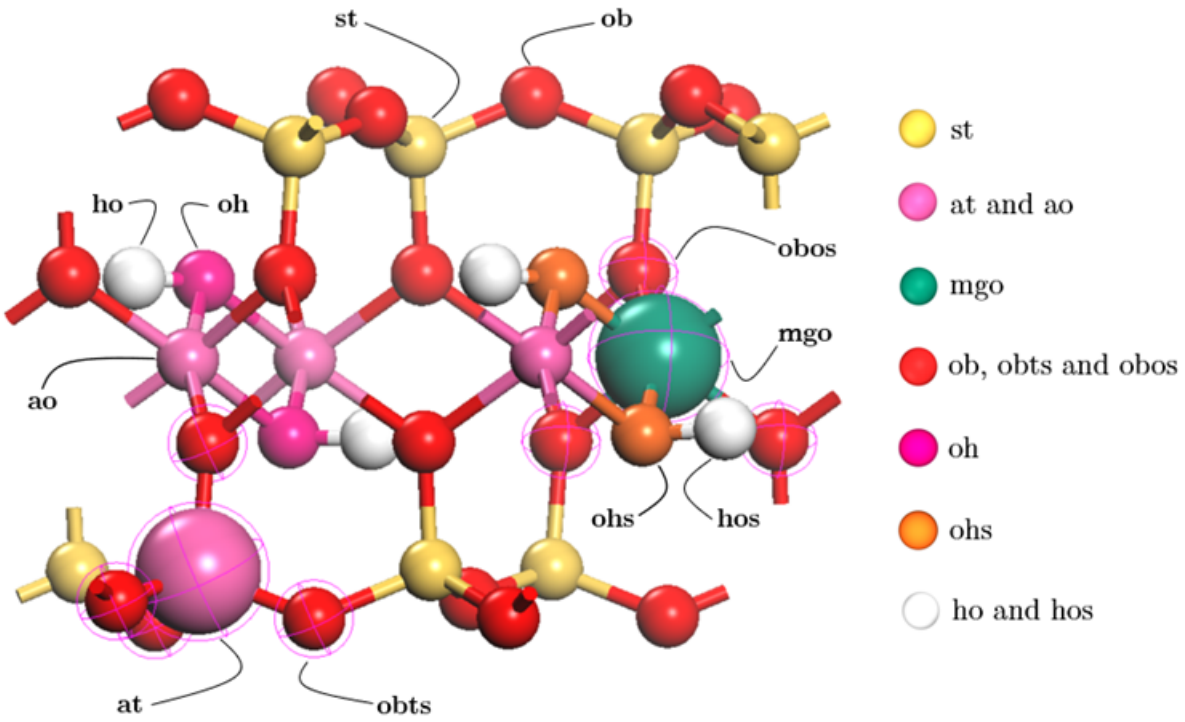

Figure 2.8 – Schematic representation of charge distribution on the unit cell of montmorillonite based on ClayFF. Acronyms: st (Si in the tetrahedral sheet), at (Al substitution in the tetrahedral sheet), ao (Al in the octahedral sheet), mgo (Mg substitution in the octahedral sheet), ob (bridging oxygen), obts (bridging oxygen in the tetrahedral sheet), obos (bridging oxygen in the octahedral sheet), oh (hydroxyl oxygen), ohs (hydroxyl oxygen with substitution), ho (hydroxyl hydrogen) and hos (hydroxyl hydrogen with substitution). Color legend: st (yellow); at and ao (pink); mgo (dark green); ob, obts and obos (red); ohs (pink); ohs (orange); ho and hos (white).

instead of metal-OH, which means that they consider not only the bending term for metal-hydroxyl, but also the bending between metal-O, and O-H atoms to improve the flexibility of the framework. (Pouvreau et al., 2017, 2019). In this work, the bonded parameters used for the framework are provided in Table 2.4.

Numerous water models have been developed, such as SPC (H. Berendsen et al., 1981), SPC/E (H. J. Berendsen et al., 1987) and TIP4P (Jorgensen et al., 1983). These models differ in the number of sites and/or flexibility. It is important to choose compatible force fields for different molecules or groups within a single system. In many studies, the SPC/E water model (H. J. Berendsen et al., 1987) has been employed together with

Table 2.4 – Bonded parameters for modified ClayFF (Pouvreau et al., 2019)

.

Metal-O-H angle bending	k (K/rad^2)	θ_0 (°)
ao-oh-ho (bulk)[1]	15096.62	116
mgo-ohs-hos (bulk)[1]	6038.65	120
Bond	**k (K/Å^2)**	**r_0 (Å)**
oh-ho[1,2]	557704.21	1
ohs-hos[1,2]	557704.21	1

[1]Pouvreau et al., 2019, [2]Cygan et al., 2004.

ClayFF (Gadikota et al., 2017; Ghasemi et al., 2022; Liu et al., 2022). Therefore, the SPC/E water model, namely the extended simple point charge model, which is a three-site and rigid model is used in this study. Furthermore, nonbonded parameters for Na^+ and Cs^+ were taken from P. Li et al., 2015. Nonbonded parameters for Ca^{2+} were taken from P. Li et al., 2013. These parameters were developed using SPC/E water model. Parameters of SPC/E water model and ions (Na^+, Ca^{2+} and Cs^+) that are used in thesis are given in Table 2.5. Schematic representation of ions and SPC/E water model are illustrated in Figure 2.11a,b.

There are several H_2 potentials in the literature that are generally used in the adsorption of hydrogen in water, MOF materials, and carbon nanotubes. One of them is the spherical H_2 model assumes a single sphere with no atomic charge developed by Mondal et al. (2013) and Sabo et al. (2006) based on the SPC/E water model. Spherical H_2 model is widely used in simulations (Gadikota et al., 2017; Smirnov and Stegailov, 2013). Moreover, the two-site H_2 model developed by Cracknell, 2001 is compared with the single H_2 model and they observed only a small difference. Tri-site H_2 model is a rigid model and diatomic molecule with atomic charges. The charges are located in hydrogen nuclei and also at the center of the mass of the H_2 molecule which was developed by different researchers (Marx and Nielaba, 1992; Silvera and Goldman, 1978). These models are widely improved by many researchers and commonly used in the simulations (Alavi et al., 2005, 2006; Buch, 1994; Darkrim and Levesque, 1998; Ding and Yazaydin, 2013; Garberoglio et al., 2005;

Table 2.5 – Nonbonded parameters for Na[1], Ca[2], Cs[1], SPC/E[3] water, tri-site H_2[4] model and He[5]

.

Species	Symbol	Charge (e)	$\varepsilon(K)$	σ(Å)
Aqueous sodium	Na	+1.0000	13.28	2.5907
Aqueous calcium	Ca	+2.0000	22.95	2.7083
Aqueous cesium	Cs	+1.0000	174.48	3.4799
Water oxygen	O_w	-0.8476	78.20	3.1655
Water hydrogen	H_w	+0.4238	0.00	0.0000
H in H_2	H_{H_2}	+0.4932	0.00	0.0000
Center of mass of H_2	H_{com}	-0.9864	34.30	3.0380
Helium	He	+0.0000	10.90	2.6400

[1]P. Li et al., 2015, [2]P. Li et al., 2013, [3]H. J. Berendsen et al., 1987, [4]Alavi et al., 2005, [5]Hirschfelder et al., 1954.

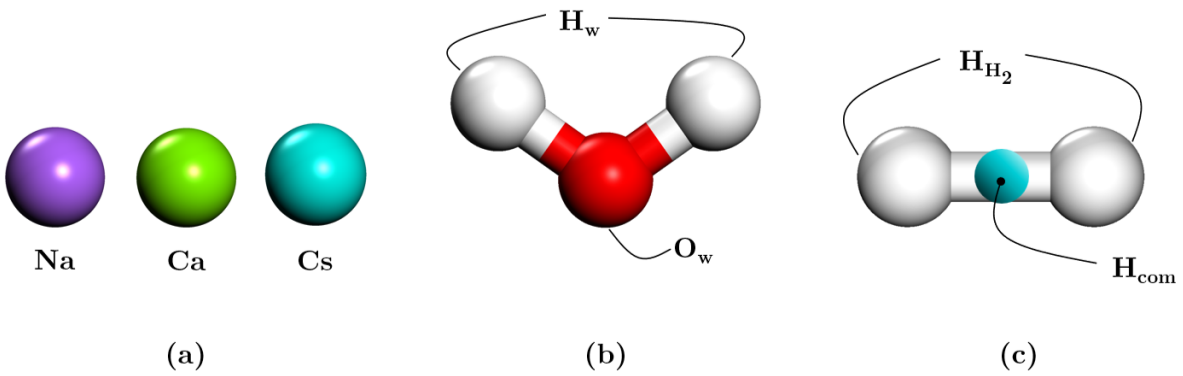

Figure 2.9 – Schematic representation of Na, Ca and Cs ions, SPC/E water, and tri-site hydrogen model

Gotzias et al., 2012; Karki and Chakraborty, 2021). Sabo et al. (2006) used different H_2 models in MD and MC simulations. In MD simulations, SPC water model and single

sphere H_2 model is used. During Monte Carlo (MC) simulations, they employed the SPC/E model in combination with a 3-site charge H_2 model developed by Alavi et al. (2005), a modified version of the model by Silvera and Goldman (1978). The SPC/E potential treats the H_2 molecule as a fixed structure with a bond length of 0.7414 Å and a quadrupole moment matching the experimental gas-phase value. They compared both single and 3-site models, but could not conclude that one is more accurate than the other. On the other hand, Tsimpanogiannis et al. (2021) compared different H_2 models, including single, 2-site, and 3-site models, and reported that the tri-site H_2 model improved by Alavi et al. (2005) shows the highest accuracy. Therefore, the tri-site H_2 model is employed in this thesis. Nonbonded parameters for the tri-site H_2 models are presented in Table 2.5, and a schematic representation of the tri-site H_2 model is illustrated in Figure **??**c. Additionally, nonbonded parameters for helium (He), used to calculate the void fraction (refer to subsection 2.4.1), were taken from Hirschfelder et al. (1954).

2.4 General simulation protocol

The typical simulation process consists of two defined stages: equilibration and production. To ensure the system had reached equilibrium, potential energy vs number of equilibration cycles and the number of water molecules vs number of equilibration cycles were monitored (Figure 2.10). In this project, two different techniques were used to perform molecular simulations namely Monte Carlo and hybrid MC/MD methods. Simulation protocol for grand canonical Monte Carlo and hybrid MC/MD were given in section 2.4.1 and 2.4.2, respectively.

2.4.1 Monte Carlo

Monte Carlo simulations were performed in grand canonical ensemble to calculate adsorption isotherms. GCMC simulations were performed using RASPA (Dubbeldam et al., 2013, 2016).

Monte Carlo simulations consist of two parts: equilibration and production. The former equilibrates the positions of the atoms in the system. The latter is on average during each cycle on each molecule a Monte Carlo move has been attempted. A cycle consists of N steps, where N is the amount of molecules with a minimum of 20 steps. The general cutoff of 10 Å was used to calculate Lennard-Jones interactions. Only for the dry systems, 9

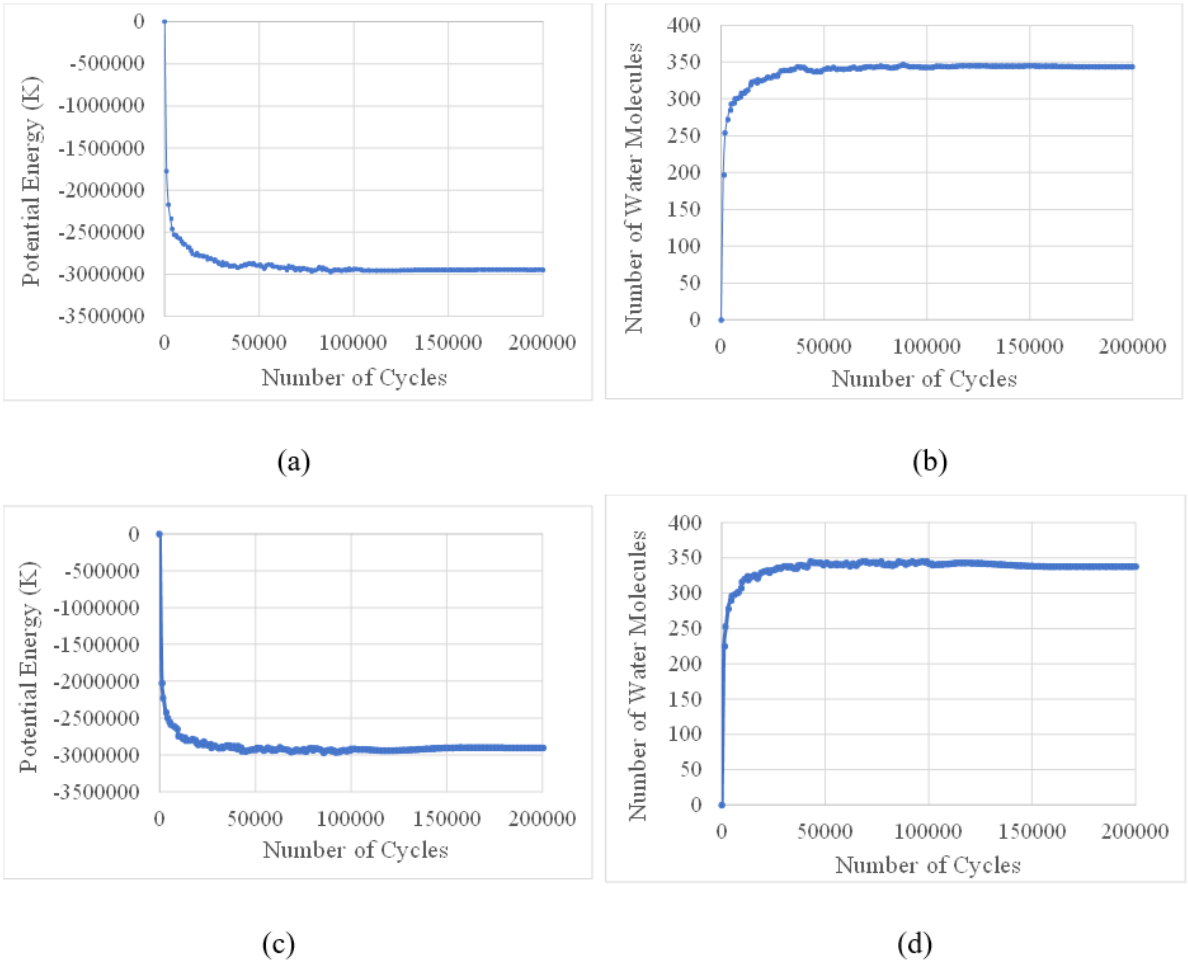

Figure 2.10 – Potential energy vs. number of equilibration cycles at 298 K and a) 1 bar c) 120 bar and number of adsorbed water molecules vs. number of equilibration cycles b) 1 bar d) 120 bar

Å cut-off used due to the smaller basal spacing. The Lennard-Jones potential is shifted without tail correction.

Clay structure, Na-montmorillonite is considered as a rigid structure. Adsorbates, hydrogen and water are considered as rigid molecules. In addition, the following trial moves were set: translation as 20%, rotation as 20%, reinsertion as 20%, swap as 40% and identity change as 100%. 200,000 equilibration cycles were performed to ensure the molecule loading is reached to equilibration. Then, three independent 100,000 production cycles were performed to obtain better statistics. The atomic positions are recorded every 1,000 cycles. Fifteen block averages obtained as five from each individual production cycle is used to calculate overall mean values. Standard deviation with 95% confidence interval were calculated from these 15 block averages.

The schematic representation of GCMC simulation is given in Figure 2.11. In GC ensemble, the volume of simulation box is fixed where it is in equilibrium with the reservoir of adsorbates at constant temperature and chemical potential. Chemical potentials were calculated from the fugacity of adsorbates. Peng-Robinson equation of state (Peng and Robinson, 1976) was used to calculate fugacity coefficients by using mol fractions of adsorbates (hydrogen and water). Mol fractions of hydrogen water mixture were determined by interpolation and extrapolation of experimental data of H_2 solubility in H_2-H_2O mixture (Gillespie and Wilson, 1980; Rahbari et al., 2019; Wiebe and Gaddy, 1934) and are given in Appendix B.

It is important to calculate excess adsorption to enable comparisons with experimental results, as they are typically provided as excess amounts. To do so, it is necessary to calculate the helium void fraction to determine the void volume of the clay structure. The helium void fraction is computed by probing the clay models with a helium molecule using the Widom particle insertion method (Dubbeldam et al., 2016). This method employs a probe particle inserted at random positions to assess the energy associated with its insertion into the system. These calculations were performed for each model using 2,000,000 production cycles. After determining the void volume, the excess amount of adsorption can be calculated as follows:

$$n_{excess} \equiv n_{absolute} - v\rho_{gas} \tag{2.16}$$

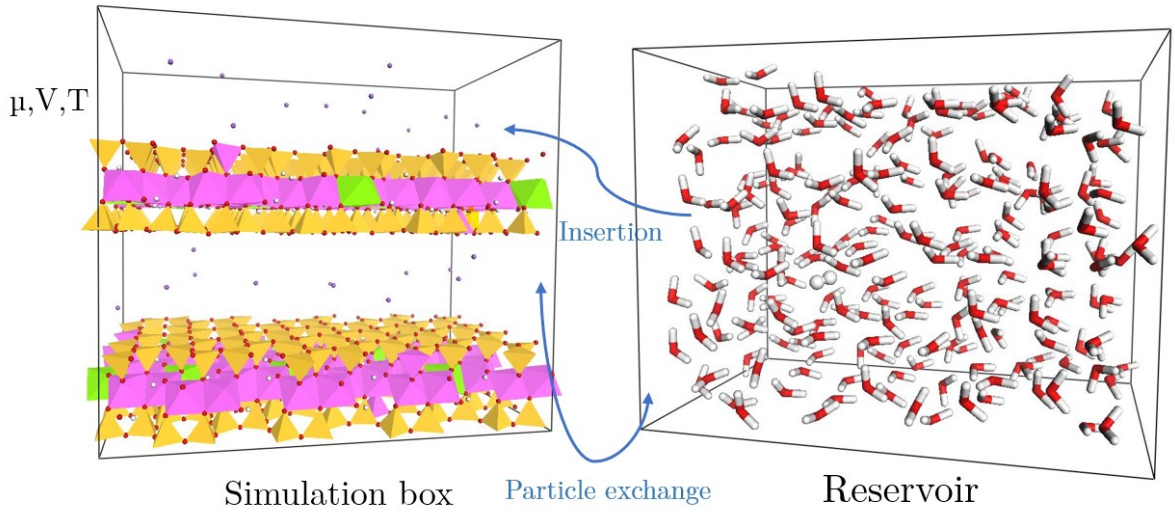

Figure 2.11 – Schematic representation of GCMC simulations

where n_{excess} and $n_{absolute}$ are the excess and absolute number of the molecules, respectively. V and ρ_{gas} refer to the volume of the framework and gas density that is calculated using Peng-Robinson equation of state (Peng and Robinson, 1976), respectively.

Simulations were performed with slight variations using different approaches as "rigid" cations and "mobile" cations. In the former, the optimized structures are directly obtained after conducting MD simulations with the cations (refer to subsection 2.2), thereby the cations are included as a part of the framework. Simulations with "mobile" cations initially requires to remove the cations from the optimized structure, followed by cation adsorption for 25,000 cycles for each equilibration and production run. Upon ensuring an equal number of counterions in each interlayer, binary adsorption of hydrogen and water is performed using the same procedure. It should be noted that in simulations with mobile cations, counterion adsorption is performed first, using only translation moves with insertion. Subsequently, during the following simulations, only translation is employed, and the cations are restricted from exiting the simulation box.

2.4.2 Hybrid MC/MD

Hybrid MC/MD simulations were performed in grand canonical ensemble to take the structure flexibility into account. GCMD simulations were performed using RASPA

(Dubbeldam et al., 2016). For consistency with GCMC simulations, similar settings for trial moves and cutoff value are used (refer to subsection 2.4.1). Unlike MC simulations, the bonded parameters for clay are used (refer to subsection 2.3).

Hybrid MC/MD, or GCMD, is carried out in grand canonical ensemble. The equation of motion is integrated with a time step of 0.5 fs. The system at each pressure condition was first equilibrated for 25 ns, followed by a 6 ns production run. The atomic positions are recorded every 5 ps. Overall means are calculated from the last 3 ns of the production run. Thus, in total, fifteen block averages obtained, with five from each individual production cycle, are used to calculate overall mean values. Standard deviation with a 95% confidence interval was calculated from these 15 block averages.

2.5 Simulation analysis

A comprehensive investigation is carried out, using trajectories and atomic positions obtained from the simulations, to explore potential adsorption sites for Na, Ca, and Cs cations, hydrogen, and water molecules in the montmorillonite interlayers. In this section, the analyses conducted for this purpose are described in details. The simulations are performed where there are at least H_2 molecules, assuming one at each interlayer except dry montmorillonite. For the analysis, an additional production run was carried out, using individual simulations that yields median values for another 100,000 cycles. The positions of atoms were collected at intervals of 10 cycles. Monte Carlo simulations produced the positions of atoms in 10,000 configurations, spanning various probabilities.

2.5.1 Atomic density profiles

Atomic density profiles defines the atomic distributions along the chosen axis in a model. In other words, it is a one-dimensional projection of the atomic densities on a chosen axis. In this thesis, positions of atoms in the "Z" axis are used for atomic density profiles. Along the "Z" axis, the number of atoms within a range of distance from z to $z + \triangle z$ is calculated and normalized by the number of atoms in the system and system volume.

$$\rho_A(z) = \frac{N_A(\triangle z)}{V} \tag{2.17}$$

Finally, the atomic distributions were determined by calculating the average over two statistically independent interlayers in each model using 1,000 configurations. With finite and small $\triangle z$ values, atomic density profiles can be represented as in Figure 2.12. The density distributions of H_2 molecules were computed using their centers of mass.

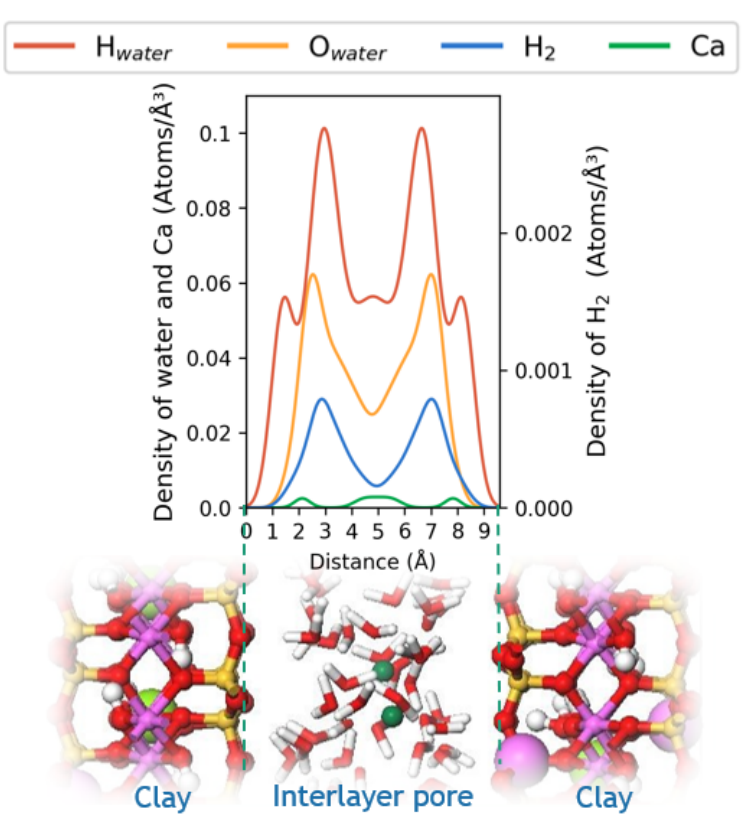

Figure 2.12 – Schematic representation of atomic density profiles in the interlayers

2.5.2 Surface density maps

Surface density maps are visual tools to analyze a layer of hydrogen-water mixture in a certain range from the surface. In other words, surface density maps shows the two-dimensional distributions of atoms in the xy plane. It defines the probability of finding each atom at a position (x, y) in a range of distance from z to $z + \delta z$, where z and $z + \delta z$ are distance in the "Z" axis.

Knowing the atoms are in the predefined range which is the first adsorption layer where they have close contact with the surface, surface density maps rely on the atomic positions in "X" and "Y" dimensions of the system, providing a complementary analysis to atomic density profiles which solely rely on atomic positions in the "Z" axis. Therefore, it helps to determine preferential adsorption sites of cations, hydrogen, and water molecules on the clay surface. In this thesis, surface atomic distribution maps, represented in Figure 2.13, illustrated over 10,000 configurations obtained by GCMC simulations. H_2 molecules were represented using their centers of mass.

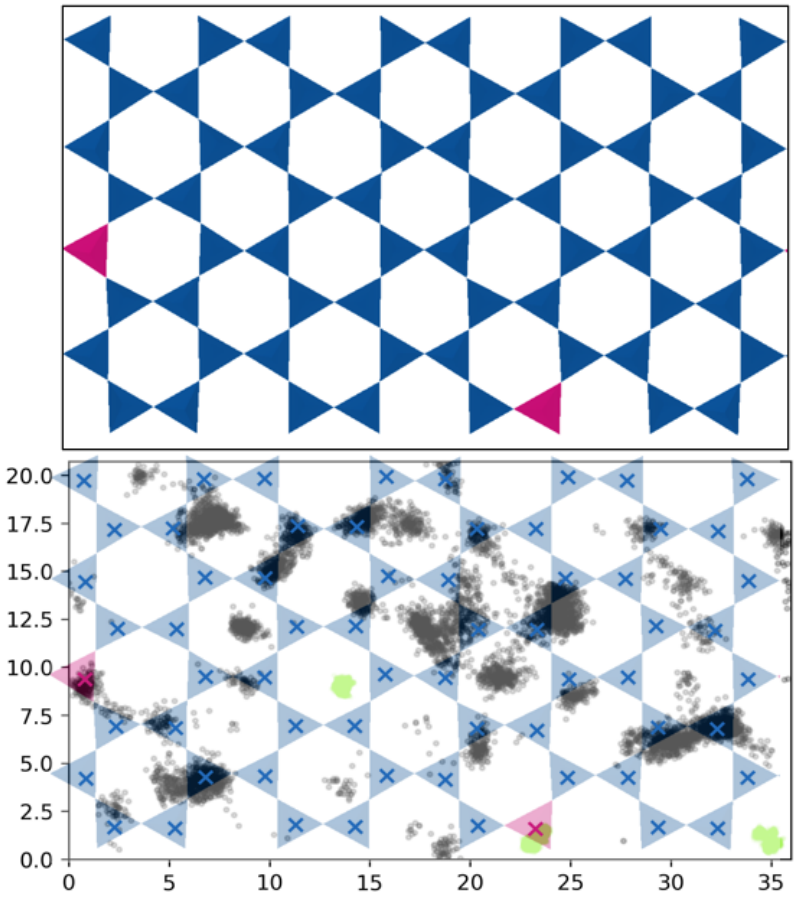

Figure 2.13 – Schematic representation of surface density maps. Color legend: Si (dark blue), Al (pink), Ca (green); H (black).

2.5.3 Radial distribution functions and coordination numbers

The pairwise radial distribution g_{AB} gives the probability density for a given atom B to be found anywhere in a spherical shell located between distance r and $r+\triangle r$ from another atom A.When $\triangle r$ approaches zero, the volume of the spherical shell and the number of atoms N in the shell approaches to zero. Therefore a finitely small value is often used for $\triangle r$.

The center of the radial coordinate system is positioned to the center of an atom A in the system. The total number of B atoms in each spherical shell thickness of $\triangle r$ is found. For a given A atom i, the density of each spherical shell, $p_i(r, \triangle r)$, is then calculated by dividing the number of B atoms in each shell ($N_B(r, \triangle r)$) by the shell volume, $V_{shell}(r, \triangle r)$:

$$p_i(r, \triangle r) = \frac{N_B(r, \triangle r)}{V_{shell}(r, \triangle r)} \tag{2.18}$$

where V_{shell} between radius r and $r + \triangle r$ can be calculated as:

$$V_{shell} = V_{sphere}(r + \frac{\triangle r}{2}) - V_{sphere}(r - \frac{\triangle r}{2}) \tag{2.19}$$

Then local radial coordinate system is moved on to the center of each A atom and average density of a shell is calculated by simply dividing the sum of p_{shell} values with the number of A atoms in the system (N_A).

$$p_{avg}((r, \triangle r)) = \frac{1}{N_A} \sum_{i=1}^{N_A} p_i(r, \triangle r) \tag{2.20}$$

Note that before calculating the average density of each shell, periodic boundary conditions need to be applied to eliminate boundary effects. Without loss of generality, periodic boundary conditions is applied by extending the simulation boundaries by replicating to neighboring coordinates.

Finally, the pairwise radial distribution function g_{AB} is calculated by normalizing the average local densities with the global density of the system, p_{avg}.

$$p_{avg} = \frac{N_{A+B}}{V_{system}} \tag{2.21}$$

where N_{A+B} is the total number of A and B atoms in the system and V_{system} is the system volume. Then, we can find the pairwise radial distribution function g_{AB} at distance r as:

$$g_{AB}(r) = \frac{p_i(r, \triangle r)}{p_{avg}} \tag{2.22}$$

In this thesis, g_{AB} is calculated up to 10 Å with 0.1 Å $\triangle r$ shell thicknesses. Schematic representation of radial distribution function for H_2-O_{water} pair is given in Figure 2.14.

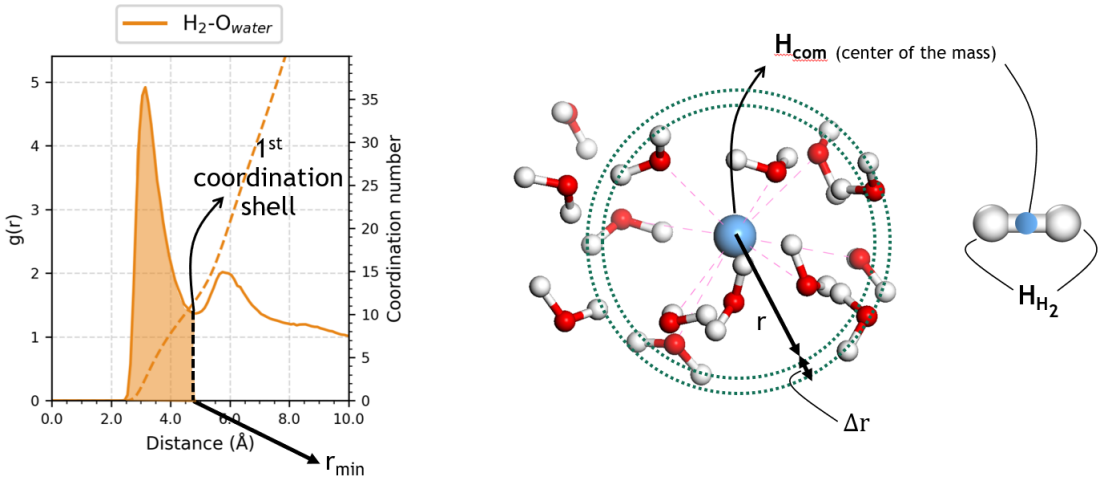

Figure 2.14 – Schematic representation of radial distribution functions and running coordination numbers

Coordination number $n_{AB}(r)$ indicates how many B atoms are found on average in the range of each coordination sphere centered at A atoms. It can be calculated by integrating the radial distribution function at the distance r, where r is chosen as the first minimum of a radial distribution function $g_{AB}(r)$.

$$n_{AB}(r) = 4\pi \int_0^r g_{AB}(r) r^2 dr \tag{2.23}$$

In addition, running coordination number is calculated by integrating the $g_{AB}(r)$ from 0 to r at each $\triangle r$ distance. In the analyses, running coordination numbers are plotted alongside the radial distribution functions. Note that the pairs of H_2 molecules with oxygen atoms of water (O_{water}), clay surface (Ob and Obts), and ions are plotted. The first sphere of the H_2 molecule is determined using the cutoff value where the H_2-Ob pair shows its first minimum. Schematic representation of running coordination numbers for H_2-O_{water} pair is illustrated in Figure 2.14.

2.5.4 Orientation of molecules

The analysis of molecular orientation was conducted to investigate the positioning of hydrogen molecules with respect to the clay surface (Figure 2.15). Therefore, the angles between the hydrogen molecules and the clay surface are calculated as depicted at the top in Figure 2.15 and the distribution of the angles are presented in the range of $[0, 180]$ degrees. Note that the angles 0 and 180 are identical and represents the parallel alignment of the hydrogen molecule to the surface.

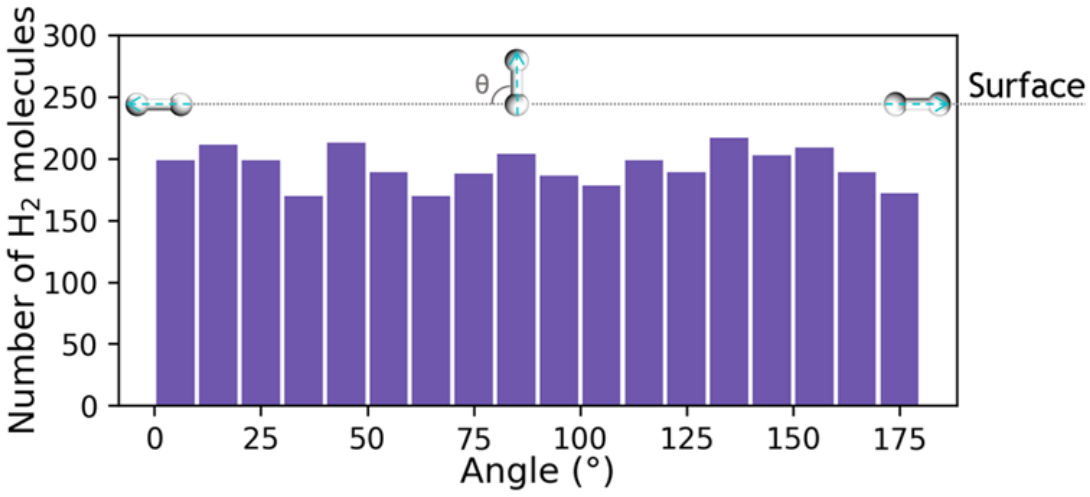

Figure 2.15 – Schematic representation of H_2 orientation with respect to the clay surface

Chapter 3

Results and Discussion

In this chapter, the results of the H_2 adsorption within the interlayers of Na-, Ca- and Cs-montmorillonite are discussed, with a particular focus on the influences of factors such as temperature, pressure, and/or pore size in the first three sections (Section 3.1, Section 3.2, and Section 3.3, respectively). Subsequently, the impact of different interlayer cations on H_2 adsorption was investigated in Section 3.4.

3.1 H_2 adsorption on Na-montmorillonite

This section delves into a detailed discussion of results, focusing on the effects of temperature, pore size, high pressure, interlayer cation mobility, and the flexibility of the clay structure on H_2 adsorption in Na-montmorillonite interlayers.

Table 3.1 – Summary of the simulations performed and discussed in Subsection 3.1.1 and Subsection 3.1.2

Hydration level	Temperature (K)	Pressure (bar)						
		1	20	40	60	80	100	120
0W	298	✓						✓
1W	298	✓	✓	✓	✓	✓	✓	✓
	323	✓	✓	✓	✓	✓	✓	✓
	363	✓	✓	✓	✓	✓	✓	✓
2W	298	✓	✓	✓	✓	✓	✓	✓
	323	✓	✓	✓	✓	✓	✓	✓
	363	✓	✓	✓	✓	✓	✓	✓
3W	298	✓	✓	✓	✓	✓	✓	✓
	323	✓	✓	✓	✓	✓	✓	✓
	363	✓	✓	✓	✓	✓	✓	✓

The summary of the simulations performed to investigate the influence of temperature and pore size/hydration level, where both the interlayer cation and the framework were kept fixed in their positions, is given in Table 3.1, and discussed in Subsection 3.1.1 and Subsection 3.1.2, respectively.

Table 3.2 – Summary of the simulations performed and discussed in Subsection 3.1.3

Hydration level	Temperature (K)	Pressure (bar)								
		200	300	400	500	600	700	800	900	1000
2W	298	✓	✓	✓	✓	✓	✓	✓	✓	✓

Table 3.3 – Summary of the simulations performed and discussed in Subsection 3.1.4 and Subsection 3.1.5

Hydration level	Temperature (K)	Interlayer cation mobility	Framework flexibility	Pressure (bar)						
				1	20	40	60	80	100	120
2W	298	mobile Na	rigid	✓	✓	✓	✓	✓	✓	✓
		mobile Na	flexible	✓	✓	✓				

To investigate the influence of high pressure while maintaining both interlayer cation and the framework rigid as in Table 3.1, the simulations performed are given in Table 3.2, and discussed in Subsection 3.1.3. Additionally, simulations are conducted to investigate the mobility of the interlayer cation (discussed in Subsection 3.1.4) and flexibility of clay structure (discussed in Subsection 3.1.5 and summarized in Table 3.3).

3.1.1 Effect of temperature on H_2 adsorption

Simulations of hydrogen adsorption on monolayer (1W), bilayer (2W) and trilayer (3W) hydrated Na-montmorillonite performed at 3 different temperatures: 298, 323 and 363 K, and up to 120 bar. Figures 3.1, 3.2, and 3.3 illustrate the adsorption isotherms of hydrogen and water versus total pressure obtained at temperatures of 298 K, 323 K, and 363 K for each Na-montmorillonite model. The amount of adsorbed H_2 and water content is presented as absolute number of H_2 and water molecules per supercell in the respective isotherms. Supercell in this context refers to simulation supercell (Figure 2.5).

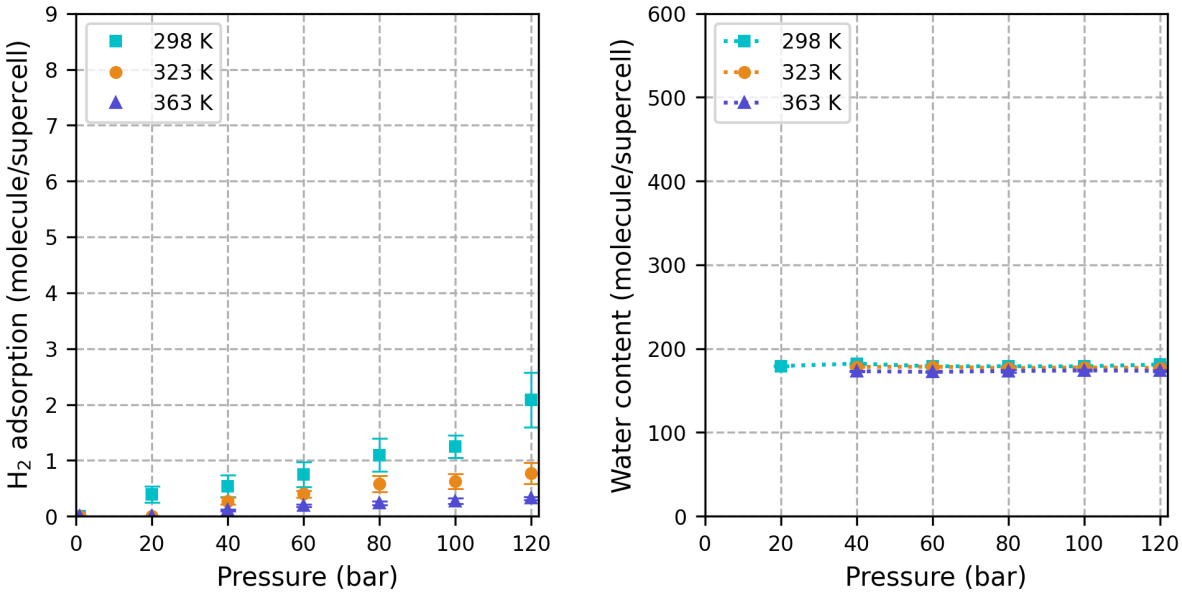

(a) (b)

Figure 3.1 – Adsorption isotherms of a) H_2 and b) water on 1W-Na-mmt at 298, 323 and 363 K

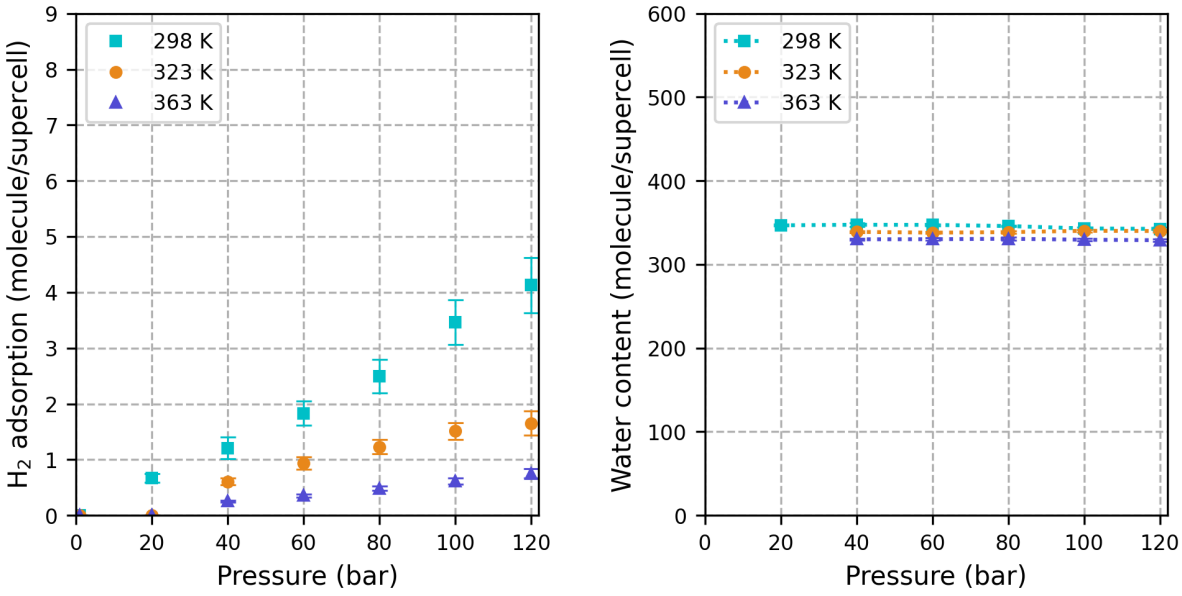

(a) (b)

Figure 3.2 – Adsorption isotherms of a) H_2 and b) water on 2W-Na-mmt at 298, 323 and 363 K

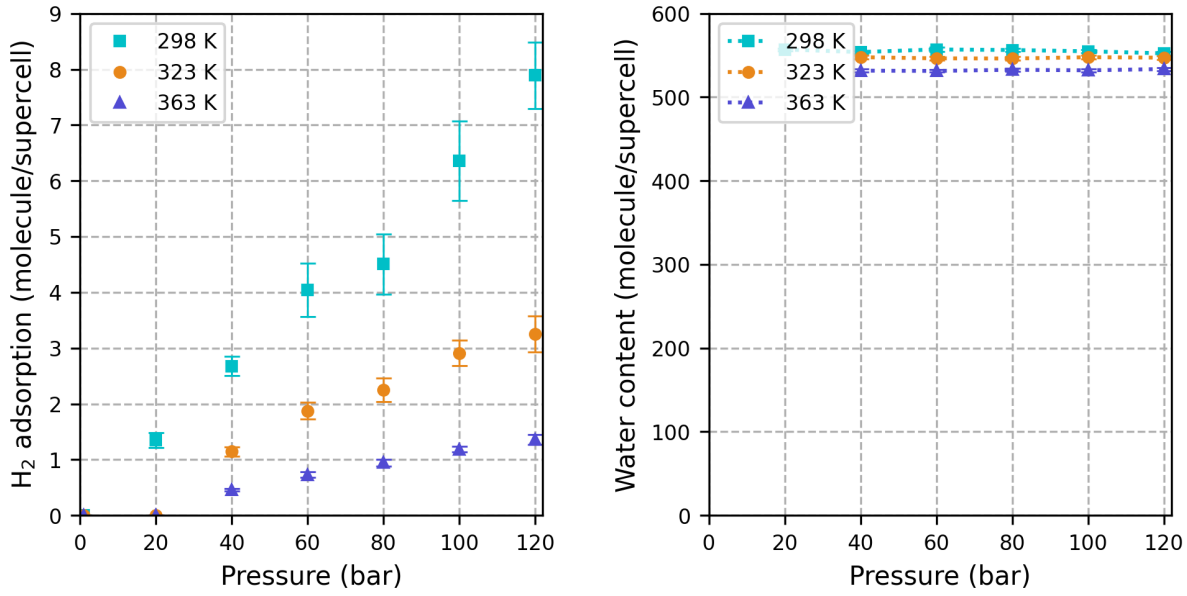

(a) (b)

Figure 3.3 – Adsorption isotherms of a) H_2 and b) water on 3W-Na-mmt at 298, 323 and 363 K

No adsorption was observed at 1 bar for all hydration levels and temperatures, as shown in Figures 3.1, 3.2, and 3.3. Additionally, there was no adsorption at 20 bar and 323 K, as well as at 363 K, for all hydration levels. As the temperature increases, the amount of adsorbed H_2 decreases, while the amount of water also slightly decreases. This trend aligns with the fact that the solubility of H_2 decreases as the temperature increases (refer to H_2 solubility data in Appendix B). Conversely, as the pressure increases, the amount of adsorbed H_2 shows a sharp increase, while water adsorption remains constant. This increase becomes more pronounced as the temperature decreases.

In simulations performed at 120 bar, the 1W-Na-mmt model showed very low adsorption at 323 K and 363 K, while at 298 K, 2 molecules were adsorbed (Figure 3.1), assuming that each molecule are present in an interlayer. This assumption is important for further analyses, as the choice of each condition to be analyzed is based on it. Similarly, simulations performed with the 2W-Na-mmt model at 120 bar revealed less than one molecule adsorbed at 363 K, less than 2 molecules at 323 K, and 4 molecules at 298 K (Figure 3.2). Lastly, the amounts of adsorbed H_2 in 3W-Na-mmt model at 323 and 363 K are slightly more than 3 and 1 molecules, respectively, whereas it is approximately 8

molecules at 298 K (Figure 3.3). The amount of water molecules in the interlayers of the 1W-Na-mmt model at 298, 323, and 363 K is 180±1, 178±1, and 173±1, respectively. For the 2W-Na-mmt model, the corresponding values are 345±2, 339±1, and 330±1 at the same temperatures. In the case of the 3W-Na-mmt model, the amount of water molecules at 298, 323, and 363 K are 555±2, 547±1, and 532±1 molecules, respectively. Detailed simulation results of absolute and excess adsorption amounts of H_2 and water in molecule/supercell, are tabulated in the Appendix C (Table C.1-C.9).

Tabulated simulation results of absolute and excess adsorption amounts of H_2 and water in mmol/g framework are given in Tables 3.4-3.12 to enable a comparison of the obtained results with experimental data from the literature.

Table 3.4 – Adsorbed amount of H_2 and water content in 1W-Na-mmt at 298 K in mmol/g

Pressure (bar)	Adsorbed H_2 (mmol/g)			Water content (mmol/g)		
	Absolute	Excess	Error	Absolute	Excess	Error
1	0.000	0.000	0.000	-	-	-
20	0.017	0.015	0.003	7.609	1.772	0.022
40	0.023	0.020	0.007	7.732	1.894	0.011
60	0.032	0.027	0.003	7.596	1.759	0.012
80	0.047	0.040	0.008	7.599	1.762	0.017
100	0.053	0.045	0.005	7.594	1.758	0.023
120	0.088	0.079	0.020	7.685	1.849	0.075

Table 3.5 – Adsorbed amount of H_2 and water content in 1W-Na-mmt at 323 K in mmol/g

Pressure (bar)	Adsorbed H_2 (mmol/g)			Water content (mmol/g)		
	Absolute	Excess	Error	Absolute	Excess	Error
1	0.000	0.000	0.000	-	-	-
20	0.000	0.000	0.000	-	-	-
40	0.012	0.009	0.000	7.563	1.824	0.010
60	0.017	0.013	0.001	7.577	1.838	0.026
80	0.025	0.019	0.003	7.506	1.767	0.014
100	0.027	0.019	0.002	7.538	1.799	0.017
120	0.033	0.024	0.005	7.516	1.777	0.026

Table 3.6 – Adsorbed amount of H_2 and water content in 1W-Na-mmt at 363 K in mmol/g

Pressure (bar)	Adsorbed H_2 (mmol/g)			Water content (mmol/g)		
	Absolute	Excess	Error	Absolute	Excess	Error
1	0.000	0.000	0.000	-	-	-
20	0.000	0.000	0.000	-	-	-
40	0.005	0.002	0.000	7.346	1.787	0.020
60	0.008	0.004	0.000	7.314	1.754	0.005
80	0.010	0.004	0.001	7.354	1.794	0.046
100	0.012	0.004	0.001	7.386	1.824	0.027
120	0.014	0.005	0.001	7.365	1.803	0.021

Table 3.7 – Adsorbed amount of H_2 and water content in 2W-Na-mmt at 298 K in mmol/g

Pressure (bar)	Adsorbed H_2 (mmol/g)			Water content (mmol/g)		
	Absolute	Excess	Error	Absolute	Excess	Error
1	0.000	0.000	0.000	-	-	-
20	0.028	0.025	0.002	14.718	3.513	0.035
40	0.051	0.045	0.004	14.747	3.543	0.057
60	0.078	0.069	0.007	14.740	3.536	0.030
80	0.106	0.093	0.011	14.681	3.478	0.020
100	0.147	0.131	0.014	14.562	3.359	0.011
120	0.175	0.157	0.015	14.536	3.335	0.077

Table 3.8 – Adsorbed amount of H_2 and water content in 2W-Na-mmt at 323 K in mmol/g

Pressure (bar)	Adsorbed H_2 (mmol/g)			Water content (mmol/g)		
	Absolute	Excess	Error	Absolute	Excess	Error
1	0.000	0.000	0.000	-	-	-
20	0.000	0.000	0.000	-	-	-
40	0.026	0.020	0.001	14.385	3.370	0.008
60	0.040	0.031	0.002	14.346	3.332	0.018
80	0.052	0.041	0.004	14.370	3.355	0.029
100	0.064	0.050	0.005	14.439	3.424	0.028
120	0.070	0.053	0.002	14.428	3.413	0.039

Table 3.9 – Adsorbed amount of H_2 and water content in 2W-Na-mmt at 363 K in mmol/g

Pressure (bar)	Adsorbed H_2 (mmol/g)			Water content (mmol/g)		
	Absolute	Excess	Error	Absolute	Excess	Error
1	0.000	0.000	0.000	-	-	-
20	0.000	0.000	0.000	-	-	-
40	0.011	0.005	0.001	14.009	3.339	0.027
60	0.015	0.006	0.000	14.012	3.341	0.008
80	0.021	0.009	0.001	14.036	3.363	0.036
100	0.026	0.012	0.001	13.987	3.313	0.036
120	0.032	0.015	0.001	13.961	3.285	0.038

Table 3.10 – Adsorbed amount of H_2 and water content in 3W-Na-mmt at 298 K in mmol/g

Pressure (bar)	Adsorbed H_2 (mmol/g)			Water content (mmol/g)		
	Absolute	Excess	Error	Absolute	Excess	Error
1	0.000	0.000	0.000	-	-	-
20	0.057	0.052	0.000	23.641	4.947	0.011
40	0.114	0.103	0.003	23.510	4.816	0.003
60	0.171	0.156	0.005	23.642	4.949	0.033
80	0.191	0.171	0.010	23.613	4.922	0.008
100	0.270	0.244	0.001	23.549	4.858	0.026
120	0.335	0.304	0.008	23.445	4.756	0.058

The results of H_2 adsorption on the 1W-Na-mmt model at 298 K (Table 3.4) were compared with experimental results H_2 adsorption on Li-montmorillonite performed by Ziemiański and Derkowski (2022). In this experimental work, it is noted that the sample with a basal spacing of 10.8 Å exhibited adsorption both in the interlayer and on the external surface. The adsorbed amount of H_2 in the interlayer was then estimated. Despite the challenges in direct comparison due to variations in cation type, basal spacing, and water content, the results were compared with the understanding that the 1W-Na-mmt model is the most similar to the Li-montmorillonite with a basal spacing of 10.8 Å among all models. This comparison reveals that in both studies, the excess amount of adsorbed H_2 at 298 K is on the order of magnitude of 10^{-2} in mmol/g. The results obtained in

Table 3.11 – Adsorbed amount of H_2 and water content in 3W-Na-mmt at 323 K in mmol/g

Pressure (bar)	Adsorbed H_2 (mmol/g)			Water content (mmol/g)		
	Absolute	Excess	Error	Absolute	Excess	Error
1	0.000	0.000	0.000	-	-	-
20	0.000	0.000	0.000	-	-	-
40	0.049	0.039	0.000	23.249	4.872	0.031
60	0.080	0.066	0.005	23.190	4.813	0.051
80	0.096	0.077	0.002	23.182	4.804	0.055
100	0.124	0.100	0.005	23.248	4.870	0.012
120	0.138	0.110	0.008	23.225	4.846	0.070

Table 3.12 – Adsorbed amount of H_2 and water content in 3W-Na-mmt at 363 K in mmol/g

Pressure (bar)	Adsorbed H_2 (mmol/g)			Water content (mmol/g)		
	Absolute	Excess	Error	Absolute	Excess	Error
1	0.000	0.000	0.000	-	-	-
20	0.000	0.000	0.000	-	-	-
40	0.019	0.010	0.001	22.567	4.765	0.042
60	0.031	0.016	0.001	22.552	4.748	0.058
80	0.040	0.021	0.001	22.610	4.803	0.036
100	0.050	0.026	0.001	22.582	4.773	0.032
120	0.058	0.029	0.001	22.648	4.836	0.031

this study are slightly higher, which can be explained by the larger basal spacing of the 1W-Na-mmt model, measuring 13.03 Å.

The atomic density profiles of hydrogen and oxygen atoms of water, and hydrogen molecules in 2W-Na-montmorillonite interlayer pore at 298 K under pressures of 80 and 120 bar, are given in Figure 3.4a and Figure 3.4b, respectively. The density profiles provide the atomic distribution within a single pore, derived by averaging the data from two statistically independent pores. Interlayer pore distances are defined by considering the positions of bridging oxygens on the tetrahedral sheets. The center of mass is used for the positions of hydrogen molecules. Both O atoms (O_{water}) of H_2O and H_2 molecules exhibit two peaks

at around 2.4 and 2.9 Å at 80 bar (Figure 3.4a) and 2.5 and 2.7 Å at 120 bar (Figure 3.4b), respectively. These peaks are positioned identically relative to the surface, indicating their preferred adsorption sites close to the surface due to the strong interaction between solid and fluid. The hydrogen atoms (H_{water}) of water molecules also form two major peaks around 3 Å, located at the same position relative to the surface at both 80 and 120 bar yet with shoulders which suggests that one of the hydrogen atoms of some water molecules is positioned closer to the surface. Similar orientations of water molecules are observed in other works performed using bilayer hydrated Na-montmorillonite or the one with a pore size of 10 Å and explained by the formation of hydrogen bonds with O atoms on the surfaces (Botan et al., 2010; Ngouana Wakou, 2014; Owusu et al., 2022). Furthermore, the density of hydrogen also increases as the pressure increases; however, there is no significant difference in the number of water molecules between 80 bar (Figure 3.4a) and 120 bar (Figure 3.4b).

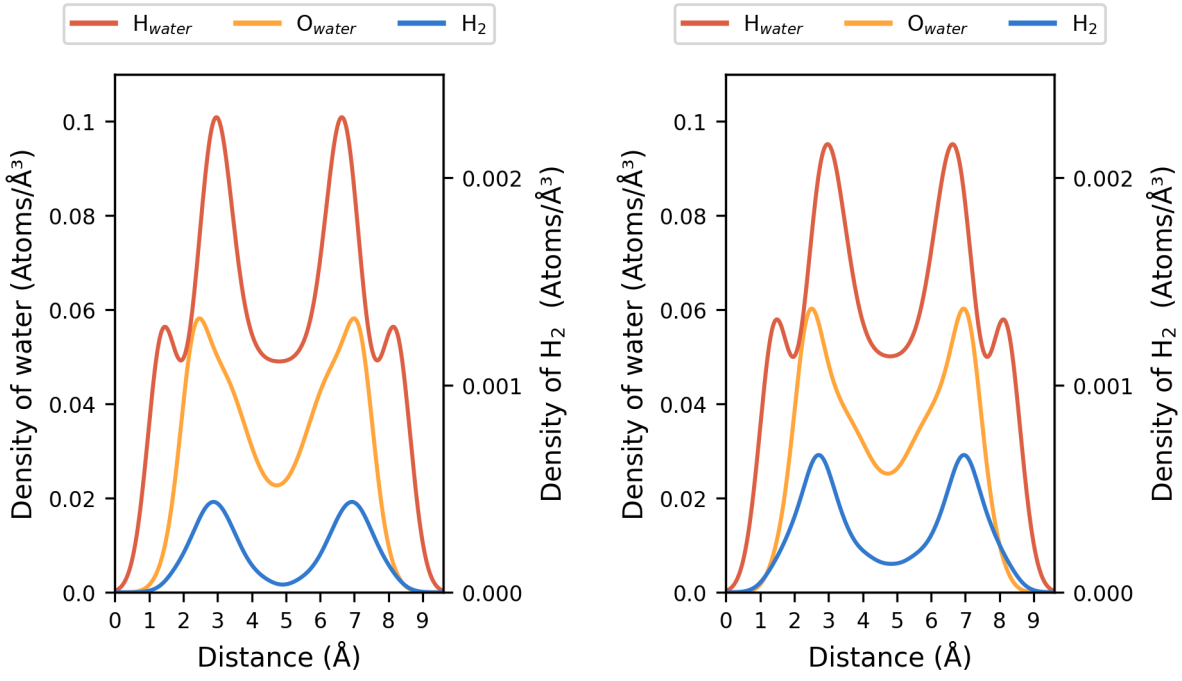

(a) (b)

Figure 3.4 – Atomic density profiles of water hydrogen and oxygen atoms, and hydrogen molecule on 2W-Na-mmt at 298 K and a) 80 bar and b) 120 bar

The density profiles of hydrogen and oxygen atoms of water, along with hydrogen molecules in 3W-Na-montmorillonite interlayer pore at 298 K and 40, 80 and 120 bar, and 323 K

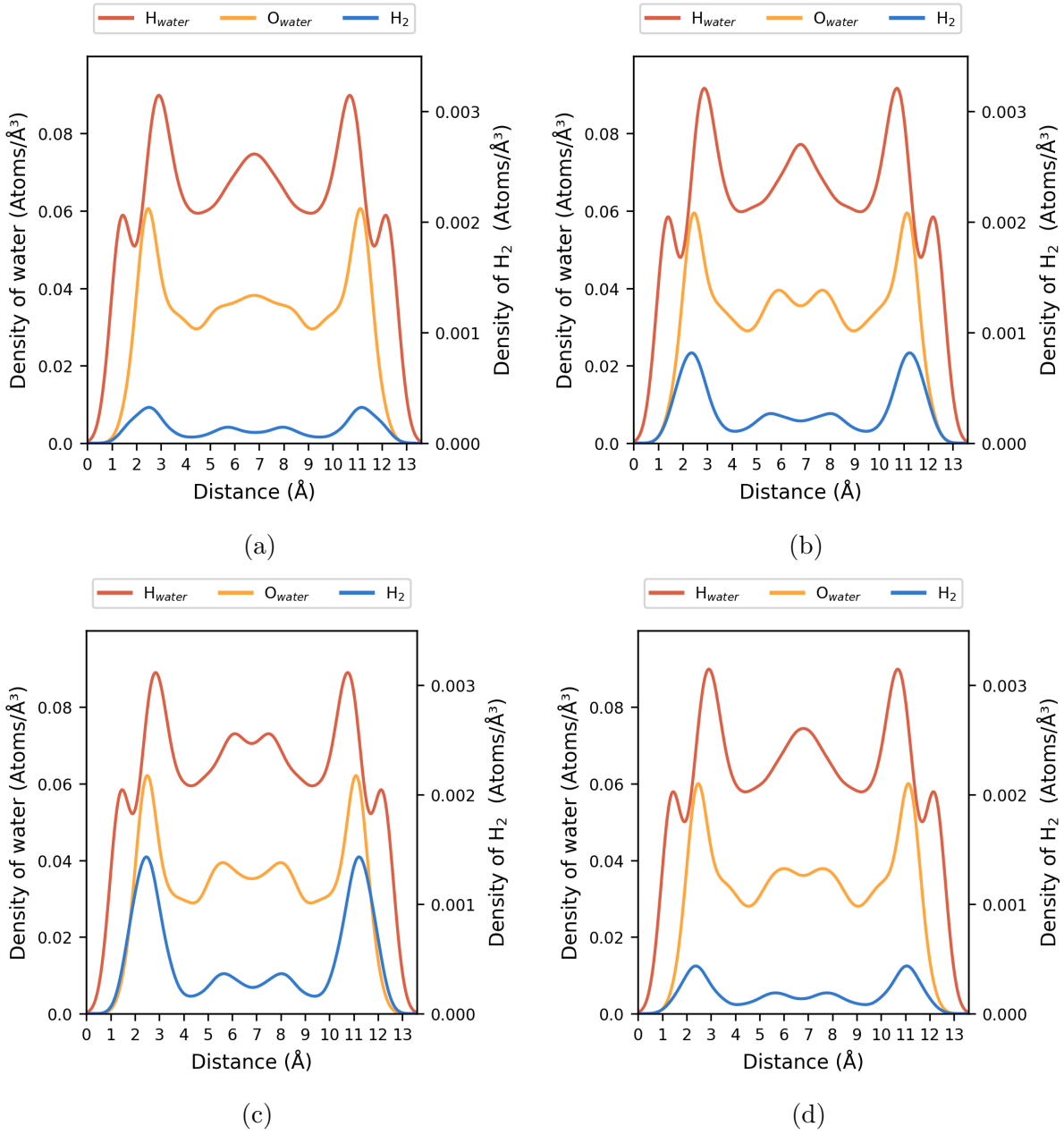

Figure 3.5 – Atomic density profiles of water hydrogen and oxygen atoms, and hydrogen molecule on 3W-Na-mmt at 298 K and a) 40 bar, b) 80 bar and c) 120 bar, and d) 323 K and 120 bar

and 120 bar are presented in Figure 3.5. At 298 K and 40 bar (Figure 3.5a), both O atoms of H_2O and H_2 molecules exhibit two major and sharper peaks at 2.5 Å, aligning with the same positions relative to the surface. Moreover, the former forms a broader

peak (at 6.8 Å), and the latter exhibits a weak double peak (at 5.7 Å) in the middle of the pore, respectively. H atoms of water molecules also form two major peaks, with a shoulder, at 2.9 Å, and a weaker peak in the middle of the pore at the same position as O_{water}. At 298 K and 80 bar (Figure 3.5b), both O_{water} atoms and H_2 molecules exhibit two sharper peaks at 2.4 Å, with double weaker peaks in the middle of pores around 5.9 and 5.5 Å, respectively. H_{water} atoms also form two major peaks with a shoulder and a weaker peak in the middle of the pore at the same position, with the same patterns observed at 40 bar. At 298 K and 120 bar (Figure 3.5c), both O atoms of H_2O and H_2 molecules form two sharper peaks at 2.5 Å, with two double weaker peaks in the middle of pores at 5.6 Å. H atoms of water exhibit two major peaks at 2.8 Å, with a shoulder and double weaker peaks at 6.1 Å. Similar to Figure 3.4, the density of hydrogen molecules increases as the pressure rises dramatically, while the density of water molecules remains nearly constant (see Figure 3.5a, 3.5b and 3.5c). At 323 K and 120 bar (Figure 3.5b), both H_2O and H2 molecules exhibit two sharper peaks at 2.5 Å and 2.4 Å, respectively, with double weaker peaks in the middle of pores around 5.9 and 5.6 Å. H_{water} atoms form two major peaks with a shoulder and a weaker peak in the center of the pore at 2.9 and 6.8 Å, respectively. Due to the interactions of H atoms of water with the surface that observed as shoulders show that the water molecules at first adsorption layers (near to the surfaces up to around 4.5 Å) are oriented. The atomic density profiles of water molecules show that 3W-Na-mmt model exhibits multilayer adsorption at various temperature and pressure conditions. Hydrogen molecule density decreases with increasing temperature, while the density of water molecules remains the same (see Figure 3.5c and 3.5d). Moreover, density profiles illustrated at 298 K and 40 and 80 bar, and 323 K and 120 bar are similar to the trilayer hydrated model employed by Ngouana Wakou (2014). However, the density profile at 298 K and 120 bar is more similar to the 4-layer hydrated model. This can be attributed to the increased number of H_2 molecules at this condition, causing some water molecules to shift towards the mid-plane.

Radial distribution functions and running coordination numbers of H_2-Na, H_2-Ob, H_2-Obts, and H_2-O_{water} pairs in 2W-Na-mmt at 298 K and 80, and 120 bar are illustrated in Figure 3.6. The first coordination shell is defined where the first minimum for the H_2-Ob pair occurs, and it is around 4.2 Å for both pressure conditions. Na ions are not present in the first coordination shell of H_2 which indicates that their predominant coordination is closer to mid-plane. In Table 3.13, coordination numbers of O atoms (CN_{Owater}) of water and clay (CN_{Ob} and CN_{Obts}), and Na ions (CN_{Na}) at the first shell of H_2 molecule in

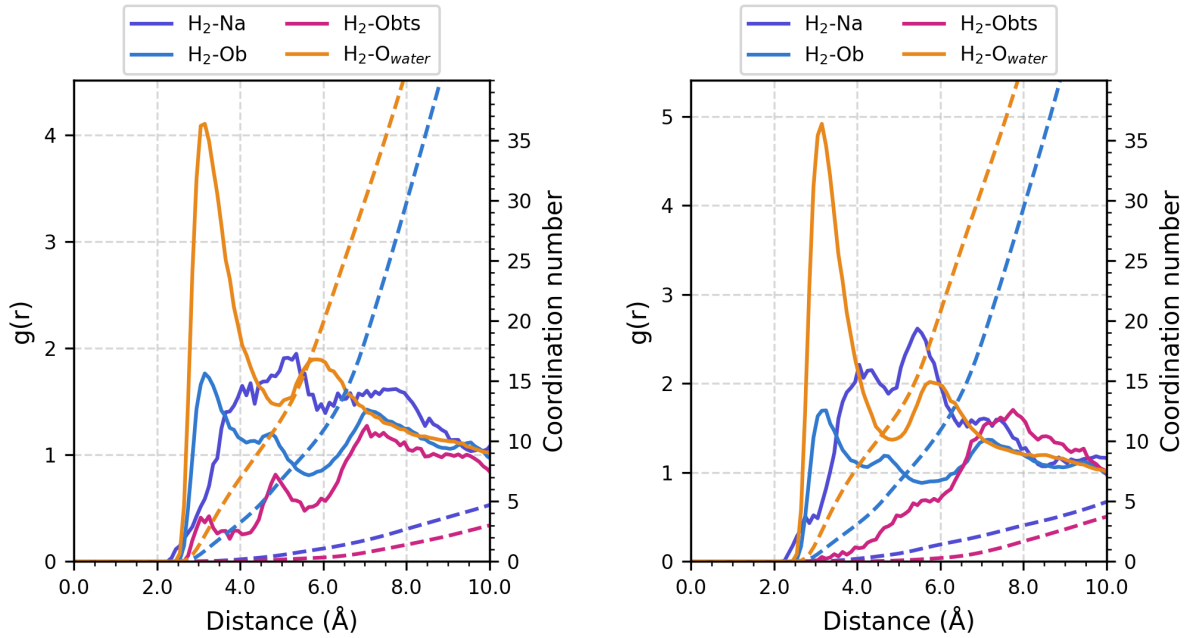

(a) (b)

Figure 3.6 – Radial distribution functions and running coordination numbers of H_2-Na, H_2-Ob, H_2-Obts and H_2-O_{water} pairs in 2W-Na-mmt at 298 K and a) 80 bar and b) 120 bar

Table 3.13 – Coordination numbers of O atoms (O_{water}) of water and clay (Ob and Obts), and Na ions at the first shell of H_2 molecule in 2W-Na-mmt at 298 K and, 80 and 120 bar, and 3W-Na-mmt at 298 and 323 K, and 120 bar

Model	Temperature (K)	Pressure (bar)	$CN_{Total-O}$	$CN_{O_{water}}$	CN_{Ob}	CN_{Obts}	CN_{Na}	r_{max}	r_{min}
2W-Na-mmt	298	80	11.37	7.66	3.66	0.05	0.21	3.15	4.15
	298	120	12.80	8.99	3.80	0.02	0.32	3.25	4.25
3W-Na-mmt	298	120	12.18	8.73	3.43	0.03	0.15	3.25	4.25
	323	120	11.95	9.19	2.74	0.01	0.17	3.25	4.25

2W-Na-mmt at 298 K, and 80 and 120 bar are listed. $N_{Total-O}$ indicates the total number of O atoms in the first shell of H_2. r_{max} and r_{min} that is chosen as cutoff, represent the first maximum and minimum of H_2-Ob pair, respectively. Although there is a slight difference due to the difference in the pore size and water content, coordination numbers

are obtained with this study are in agreement with the findings reported in other studies (Gadikota et al., 2017; Owusu et al., 2022). As pressure rises, the number of O_{water} increases gradually in the first shell of H_2 (Figure 3.6).

In Figure 3.14, radial distribution functions and running coordination numbers of H_2-Na, H_2-Ob, H_2-Obts and H_2-O_{water} pairs in 3W-Na-mmt at 298 and 323 K, and 120 bar are presented. Similar to Figure 3.6, both Na ions and Obts atoms are not present at the first coordination shell of H_2 due to their relatively low concentration. Temperature does not affect coordination numbers in the first shell of H_2.

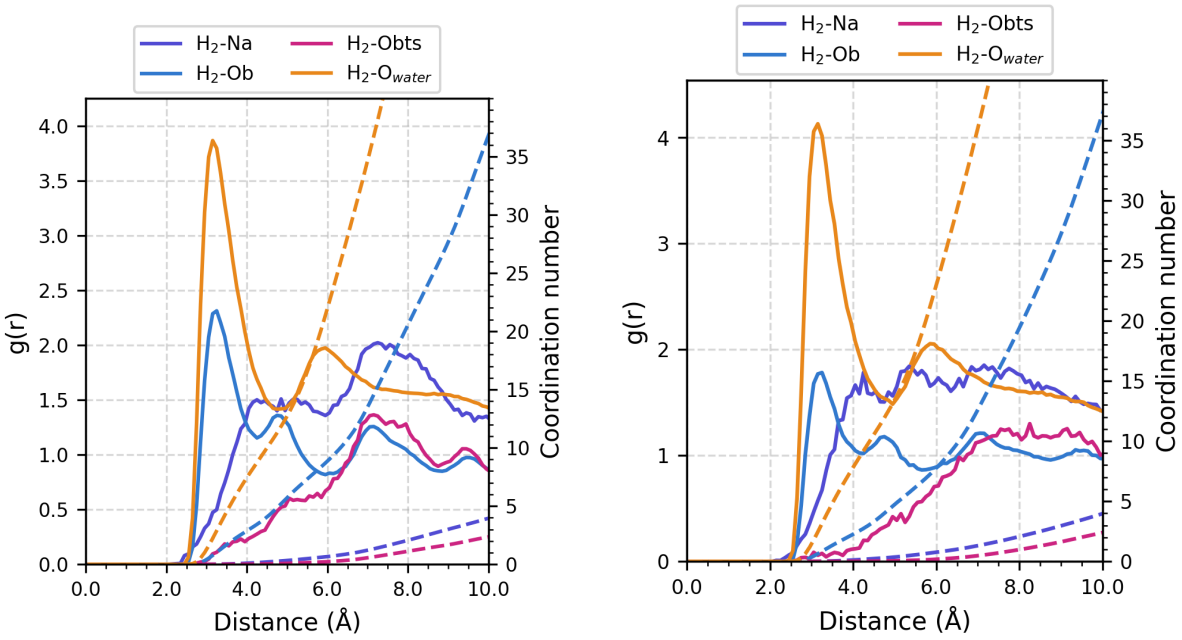

(a) (b)

Figure 3.7 – Radial distribution functions and running coordination numbers of H_2-Na, H_2-Ob, H_2-Obts and H_2-O_{water} pairs in 3W-Na-mmt at a) 298 K, and b) 323 K and 120 bar

As discussed in Section 2.3, a tri-site H_2 model was employed. Therefore, the orientation of hydrogen molecules relative to the Na-montmorillonite surface within a distance the first adsorption layer was investigated to explore whether charge impacts hydrogen adsorption due to the favorable adsorption site of hydrogen molecules. Figure 3.8a illustrates the orientation of H_2 molecules within the interlayers of 2W-Na-mmt at 298 K and, 80 bar and 120 bar. Similarly, Figure 3.8b presents the orientation of H_2 molecules within the

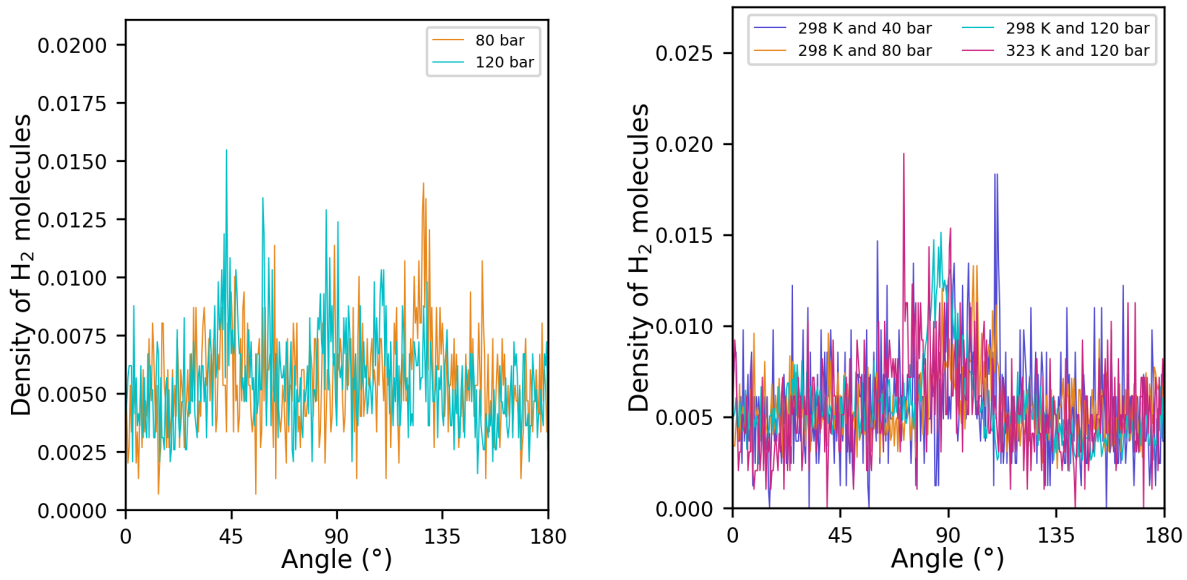

(a) (b)

Figure 3.8 – The orientation of H_2 molecules within the interlayers of a) 2W-Na-mmt at 298 K and 80 and, 12 bar b) 3W-Na-mmt at 298 K and 40, 80, and 120 bar, and 323 K and 120 bar with respect to the surface

interlayers of 3W-Na-mmt at 298 K and 40, 80, and 120 bar, as well as at 323 K and 120 bar. The results show that, regardless of temperature or pressure conditions in different models have different basal spacing, there is no preference or favored orientation for H_2 molecules in relation to the surface.

3.1.2 Effect of hydration level/pore size on H_2 adsorption

Hydrogen and water adsorption on monolayer (1W), bilayer (2W) and trilayer (3W) hydrated Na-montmorillonite are presented in Figure 3.9, 323 K in Figure 3.10 and 363 K in Figure 3.11. Helium void fractions were calculated for dry, 1W, 2W and 3W Na-montmorillonites as 0.003 , 25, 39 and 52 %. In the dry model, adsorption was not observed as a result of small basal spacing constrained molecules to enter into the pores. As the hydration level increases, the amount of H_2 adsorbed increases due to both larger pore size and increasing amount of water content. The difference in the amount of adsorbed hydrogen increases as the temperature decreases in different models with varying hydration levels. Detailed simulation results of absolute and excess adsorption amounts of H_2 and water in molecule/supercell and mmol/g, are tabulated in the Appendix C (Table

C.1-C.9) and Tables C.1-C.9, respectively.

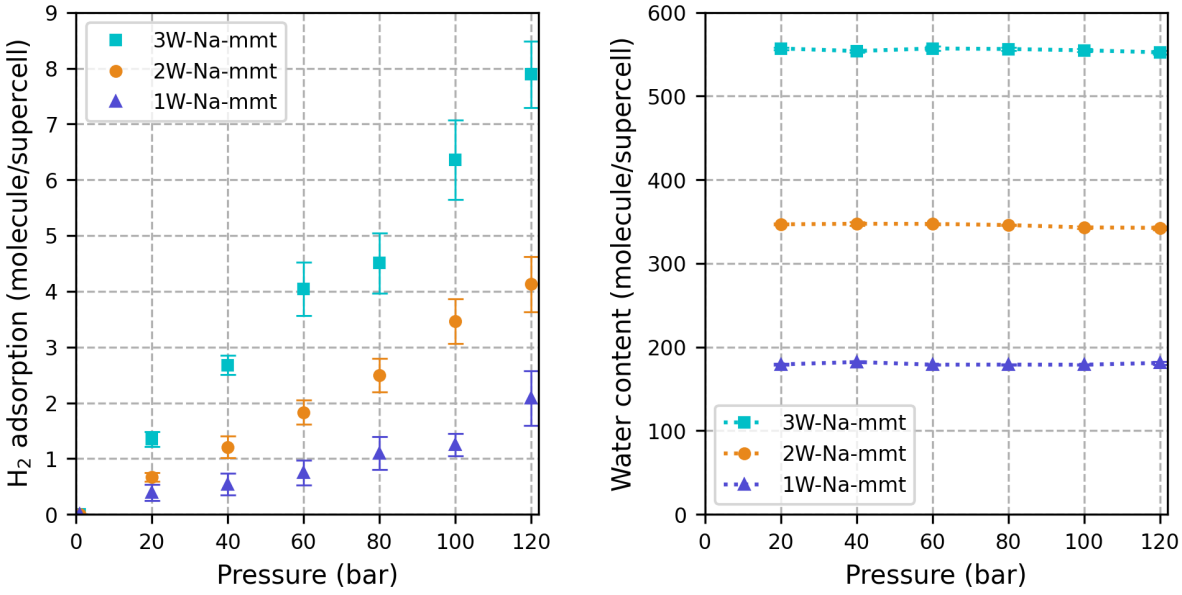

(a) (b)

Figure 3.9 – Adsorption isotherms of a) hydrogen and b) water on 1W-Na-mmt, 2W-Na-mmt and 3W-Na-mmt at 298 K

The solubility of H_2 is also investigated in the interlayers of 1W-Na-mmt, 2W-Na-mmt and 3W-Na-mmt at 298, 323 and 363 K up to 120 bar (Figure 3.12). At 298 K, the mole fraction of adsorbed hydrogen within the interlayers of all three different layer hydrated Na-montmorillonites exhibits a pronounced oversolubility in comparison to its solubility in bulk water (Figure 3.12a). At 20 bar, the mole fraction of adsorbed hydrogen is approximately 0.002 in the interlayers of all models. At 120 bar, it reaches 0.011 in mono- and bi-layer hydrated models, 0.14 in the trilayer hydrated model, meaning that the mole fraction of hydrogen is approximately 7 times greater than its solubility in bulk in 1W- and 2W-Na-mmt, and 8 times greater in 3W-Na-mmt. The solubility of H_2 decreases as temperature increases. However, it is still 2 to 4 times greater in hydrated Na-montmorillonites at 323 K (Figure 3.12b). To conclude, the solubility of H_2 increases as the hydration level increases in Na-montmorillonite models.

The density profiles of hydrogen and oxygen of water, and hydrogen molecules in the interlayer pores of 1W-Na-mmt, 2W-Na-mmt and 3W-Na-mmt at 298 K and 120 bar are given in Figure 3.13. In the monolayer hydrated Na-montmorillonite model, H_2 molecules

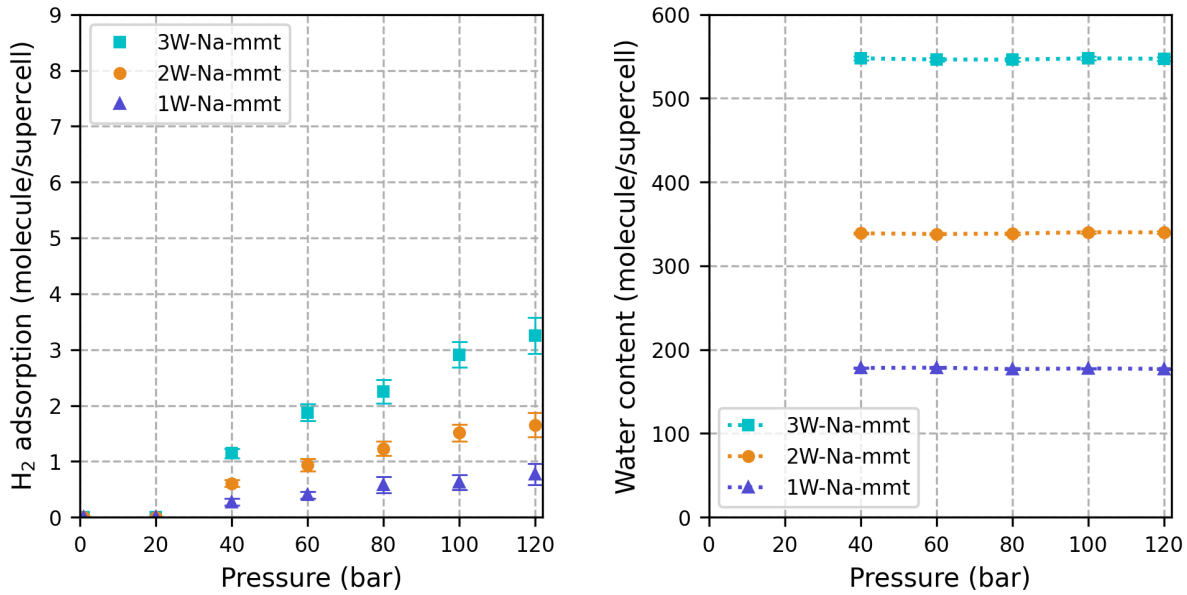

(a) (b)

Figure 3.10 – Adsorption isotherms of a) hydrogen and b) water on 1W-Na-mmt, 2W-Na-mmt and 3W-Na-mmt at 323 K

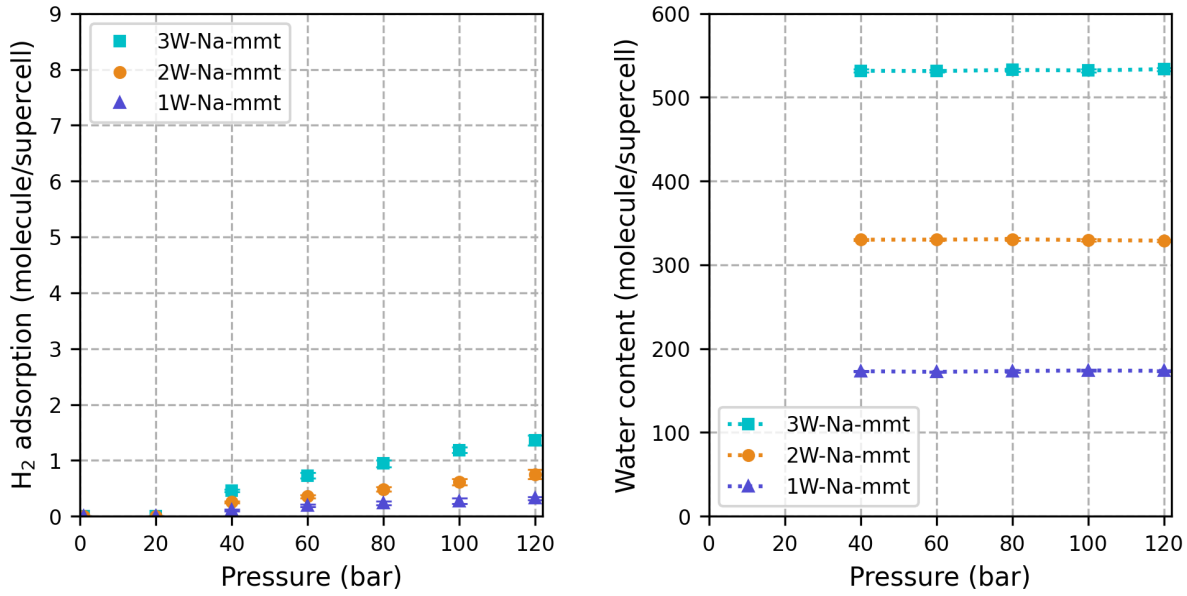

(a) (b)

Figure 3.11 – Adsorption isotherms of a) hydrogen and b) water on 1W-Na-mmt, 2W-Na-mmt and 3W-Na-mmt at 363 K

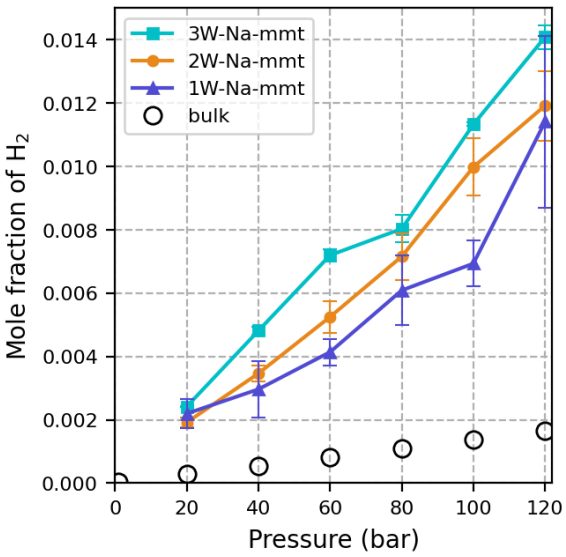

(a)

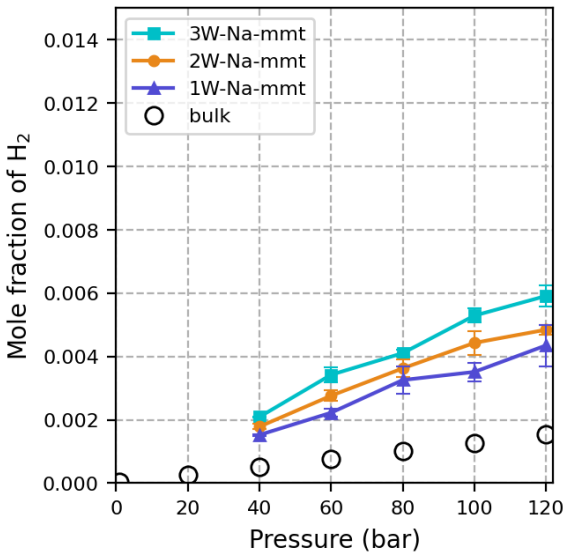

(b)

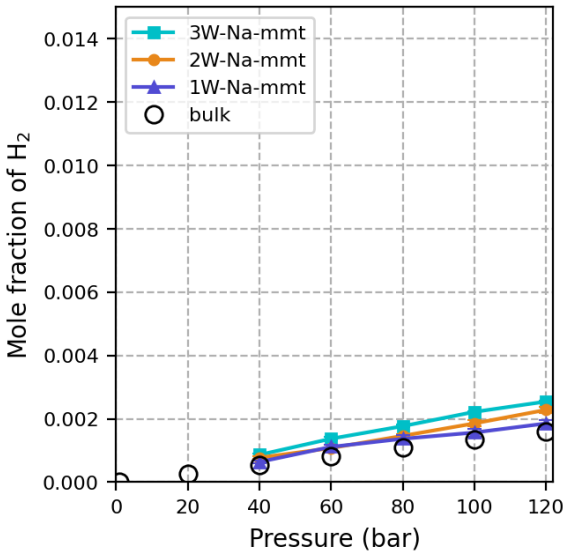

(c)

Figure 3.12 – Solubility of H_2 in the interlayers of 1W-Na-mmt, 2W-Na-mmt, 3W-Na-mmt and in bulk at a) 298 K, b) 323 K and c) 363 K. Bulk values (Table B.1 in Appendix B) at 298 and 323 K are taken from Rahbari et al., 2019; Wiebe and Gaddy, 1934, and at 363 K are taken from Gillespie and Wilson, 1980; Rahbari et al., 2019.

form a sharp peak in the center of the pore at 3.3 Å, O atoms (O_{water}) of water form a double peak in the center of the pore, the first one at 2.7 Å, and H atoms (H_{water}) of water form a sharp peak in the center at 3.3 Å with a shouldering around 1.6 Å which indicates

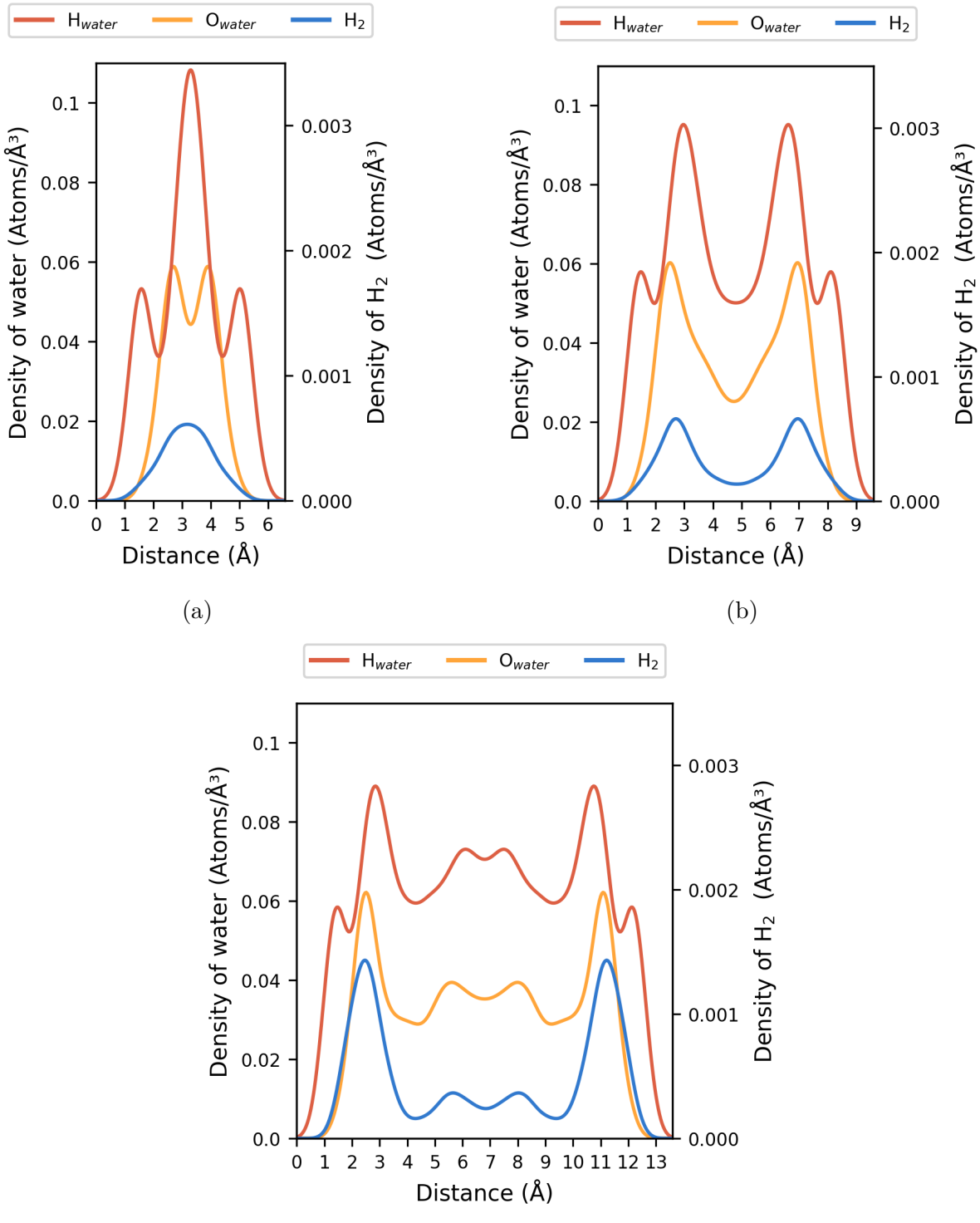

Figure 3.13 – Atomic density profiles of water hydrogen and oxygen atoms, and hydrogen molecules at 298 K and 120 bar on a) 1W-Na-mmt, b) 2W-Na-mmt and c) 3W-Na-mmt

that one of the H atoms of water molecules are oriented towards to Na-montmorillonite surface (Figure 3.13a) that is similar to density profile of water produced by Ngouana Wakou (2014) in monolayer hydrated Na-montmorillonite model. As pore size increases, two layers of O_{water} get close to the surface, and H_2 molecules and H_{water} forms also two peaks closer to the surface at the same position as relative to the surface (Figure 3.13b) in bilayer hydrated Na-montmorillonite. In the trilayer hydrated Na-montmorillonite, H_2 molecules and O_{water} exhibit two major peaks located at the same position relative to the surface while H_{water} form also two major peaks located at the same position relative to the surface with shouldering and also both H_2 and water molecules form weaker double-peaks in the center of the pores due to increasing number of molecules (Figure 3.13c). The density profiles demonstrate that both H_2 and water molecules are adsorbed in the center of the interlayer pore of monolayer hydrated model. However, as the hydration level increases in bilayer and trilayer models, both H_2 and water molecules tend to be adsorbed closer to the surfaces of the interlayer.

Table 3.14 – Coordination numbers of O atoms (O_{water}) of water and clay (Ob and Obts), and Na ions at the first shell of H_2 molecule in 1W-Na-mmt, 2W-Na-mmt and 3W-Na-mmt at 298 K and 120 bar

Model	$CN_{Total-O}$	$CN_{O_{water}}$	CN_{Ob}	CN_{Obts}	CN_{Na}	r_{max}	r_{min}
1W-Na-mmt	6.92	3.84	3.06	0.03	0.13	3.35	3.65
2W-Na-mmt	12.80	8.99	3.80	0.02	0.32	3.25	4.25
3W-Na-mmt	12.18	8.73	3.43	0.03	0.15	3.25	4.25

Radial distribution functions and running coordination numbers of H_2-Na, H_2-Ob, H_2-Obts, and H_2-O_{water} pairs in 1W-Na-mmt, 2W-Na-mmt and 3W-Na-mmt at 298 K and 120 bar are illustrated in Figure 3.14. Coordination numbers of O atoms (CN_{Owater}) of water and clay (CN_{Ob} and CN_{Obts}), and Na ions (CN_{Na}) at the first shell of H_2 molecule in 2W-Na-mmt at 298 K, and 80 and 120 bar are presented in Table 3.14. $N_{Total-O}$ indicates the total number of O atoms in the first shell of H_2. The first maximum and minimum of H_2-Ob pair are defined as r_{max} and r_{min}, respectively. At all 3 hydration levels, H_2-Ob pair shows its first maximum around the distance of 3.30 Å. r_{min} is used to calculate the coordination numbers of atoms in the first shell of H_2. A H_2 molecule is surrounded by around 4 water molecules in the interlayers of 1W-Na-mmt while it is coordinated with

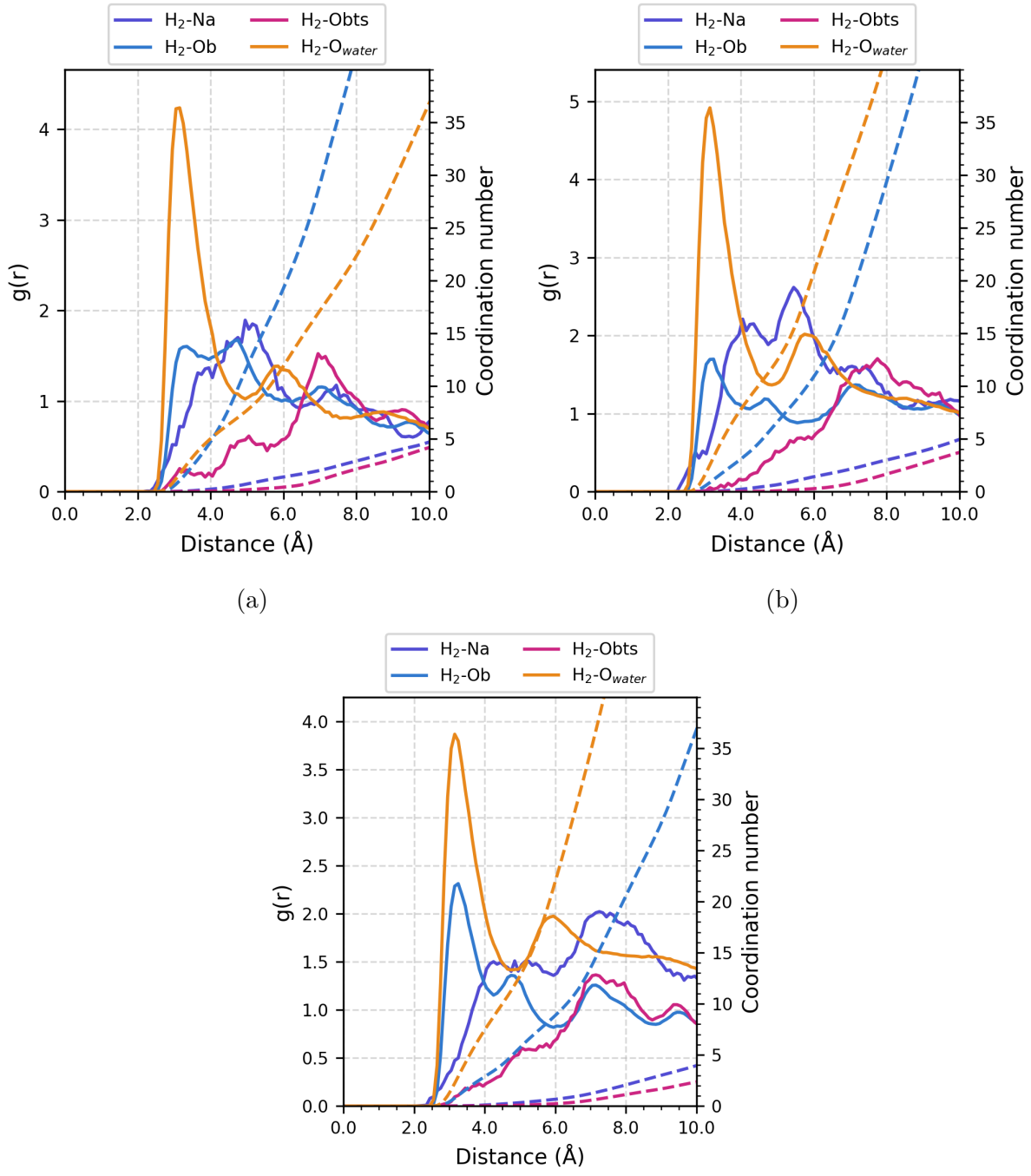

Figure 3.14 – Radial distribution functions and running coordination numbers of H_2-Na, H_2-Ob, H_2-Obts and H_2-O_{water} pairs in a) 1W-Na-mmt, b) 2W-Na-mmt and c) 3W-Na-mmt at 298 K and 120 bar

approximately 9 water molecules in the interlayers of bi- and tri-layer hydrated Na-mmt. The increase in pore size and, consequently, the amount of water causes an increase in the number of O_{water} atoms in the first shell of H_2.

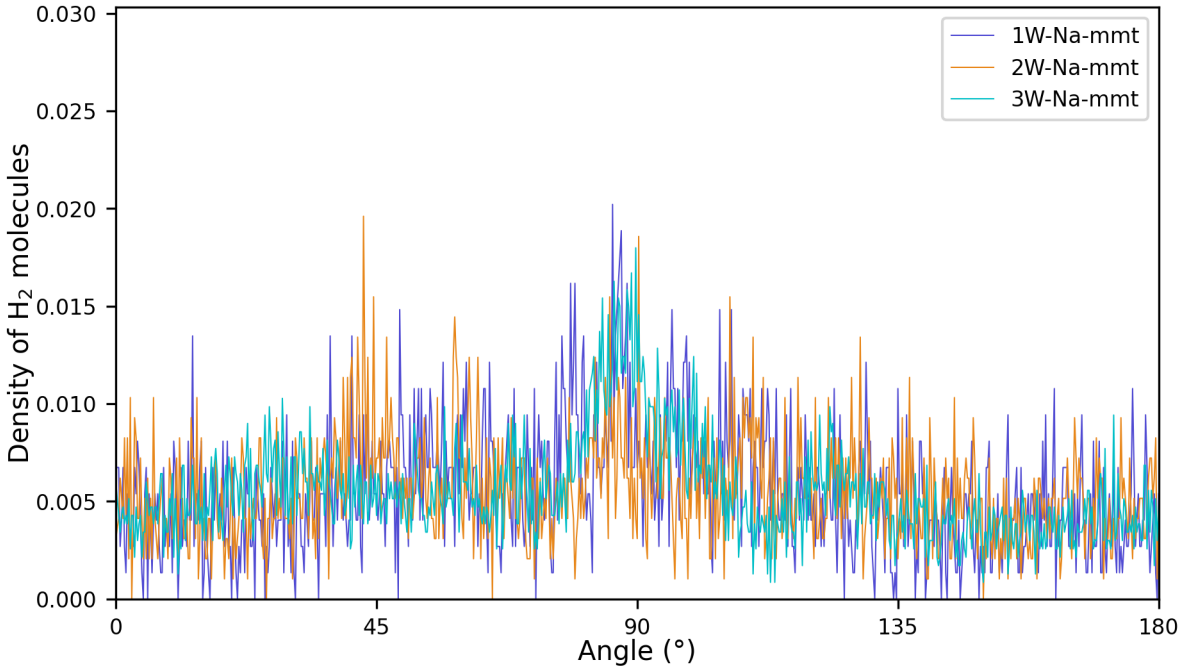

Figure 3.15 – The orientation of H_2 molecules within the interlayers of a) 1W-Na-mmt, b) 2W-Na-mmt and c) 3W-Na-mmt at 298 K and 120 bar

Figure 3.15 illustrates the orientation of H_2 molecules within the interlayers of 1W-Na-mmt, 2W-Na-mmt and 3W-Na-mmt at 298 K and 120 bar. The results show that, regardless of hydration level or pore size, there is no distinct preference or favored orientation for H_2 molecules in relation to the surface.

3.1.3 H_2 adsorption at high pressure

Hydrogen adsorption simulations using bilayer Na-montmorillonite were conducted at 298 K, up to 1000 bar, to explore the H_2 saturation capacity. The high-pressure H_2 and water adsorption isotherms are illustrated in Figure 3.16. The amounts of adsorbed hydrogen and water on 2W-Na-mmt at 298 K, up to 1000 bar, in molecules per supercell are detailed in Appendix C (Table C.10).

Figure 3.16 clearly demonstrates that the quantity of adsorbed H_2 exhibits a notable increase as the pressure rises, reaching 13.9±1.2 and 26.1±1.4 H_2 molecules per simulation supercell. The amount of water remains constant up to around 100 bar, at 346.8±0.7 molecules, between 100 and 500 bar, at 340.6±2.1, and between 600 and 1000 bar, at 334.7±1.7 molecules. Although there is a relatively slight decrease in water adsorption within the higher pressure range, when compared to hydrogen adsorption, this trend is negligible. It is important to note that even at 1000 bars, H_2 saturation has not been achieved. Tabulated simulation results of absolute and excess adsorption amounts of H_2 and water in mmol/g framework are also given in Table 3.15.

Table 3.15 – Adsorbed amount of H_2 and water content in 2W-Na-mmt at 298K up to 1000 bar in mmol/g

Pressure (bar)	Adsorbed H_2 (mmol/g)			Water content (mmol/g)		
	Absolute	Excess	Error	Absolute	Excess	Error
1	0.000	0.000	0.000	-	-	-
20	0.028	0.025	0.002	14.718	3.513	0.035
40	0.051	0.045	0.004	14.747	3.543	0.057
60	0.078	0.069	0.007	14.740	3.536	0.030
80	0.106	0.093	0.011	14.681	3.478	0.020
100	0.147	0.131	0.014	14.562	3.359	0.011
120	0.175	0.157	0.015	14.536	3.335	0.077
200	0.286	0.256	0.011	14.506	3.306	0.025
300	0.418	0.373	0.021	14.382	3.184	0.056
400	0.503	0.445	0.036	14.354	3.158	0.097
500	0.588	0.516	0.013	14.390	3.196	0.071
600	0.705	0.620	0.017	14.292	3.100	0.030
700	0.843	0.745	0.022	14.152	2.961	0.047
800	0.868	0.757	0.007	14.269	3.079	0.064
900	0.945	0.823	0.019	14.197	3.009	0.041
1000	1.106	0.971	0.035	14.131	2.943	0.014

The atomic density profiles of hydrogen (H_{water}) and oxygen (O_{water}) atoms of water, and hydrogen molecules in the 2W-Na-montmorillonite interlayer pore at 298 K and 200, 400, and 600 bar are given in Figure 3.17. At 200 bar, O_{water} atoms and H_2 molecules exhibit two peaks at the same position relative to the surface, around 2.6 Å (Figure 3.17a), and

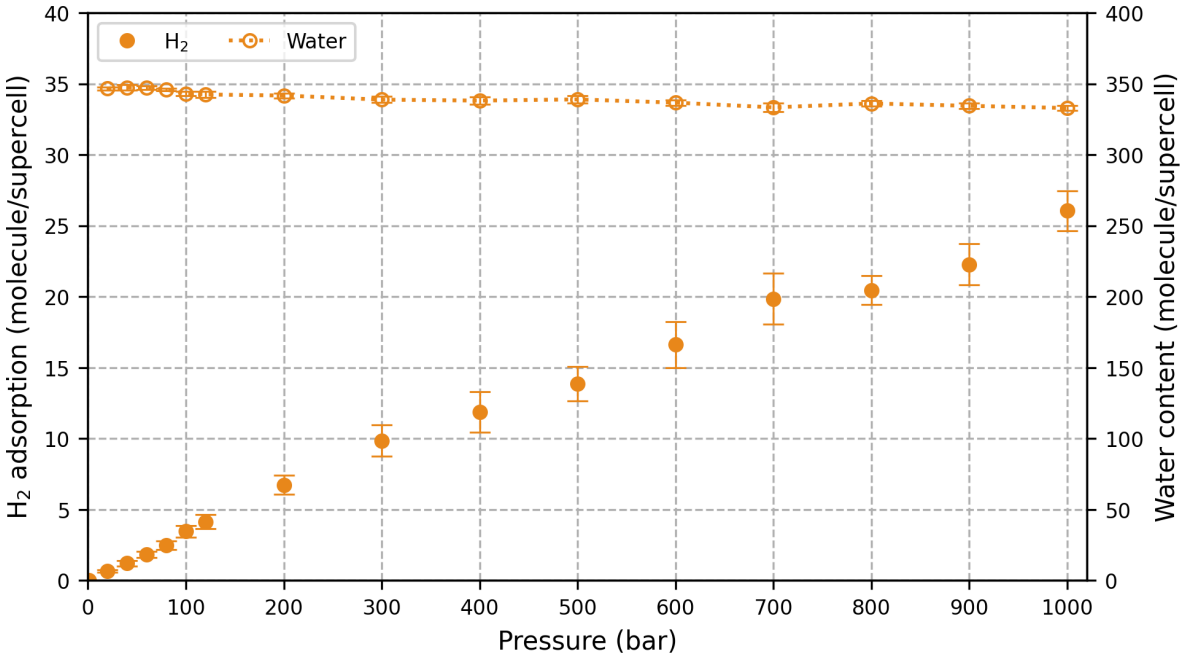

Figure 3.16 – H_2 adsorption isotherm at high pressure at 298K

H_{water} atoms also form two peaks, one located at 2.9 Å with a shoulder at 1.4 Å. At 400 bar, O_{water} atoms, H_{water} atoms, and H_2 molecules exhibit two peaks at the same position relative to the surface, around 2.5, 3, and 2.7 Å, respectively (Figure 3.17b), with peaks of H_{water} atoms having a shoulder at 1.5 Å. At 600 bar (Figure 3.17c), H_2 molecules and H_{water} atoms form identical peaks as at 400 bar, and O_{water} atoms exhibit two peaks, one at 2.6 Å. The density of H_2 increases as the pressure increases; however, there is no noticeable difference in the number of water molecules. Additionally, density profiles are similar to the ones at relatively low pressure (refer to Figure 3.4).

The surface atomic density maps are provided in Figure 3.18 illustrated within an adsorption layer (refer to Figure 3.17) that is parallel to the surface. The color legend in the figure assigns black to H_2 molecules, orange to H_2O molecules, purple to Na ions, blue to Si atoms, and pink to Al atoms. Figure 3.18a, c and e shows the center of the mass of H_2 molecules while Figure 3.18b, d and f shows O atoms of H_2O molecule for better visibility. The surface maps clearly indicate that as the pressure increases, the density of hydrogen exhibits a noticeable increase. It should be noted Na ions were kept fixed in their position in these simulations. In these rigid Na-montmorillonite models, where one tetrahedral

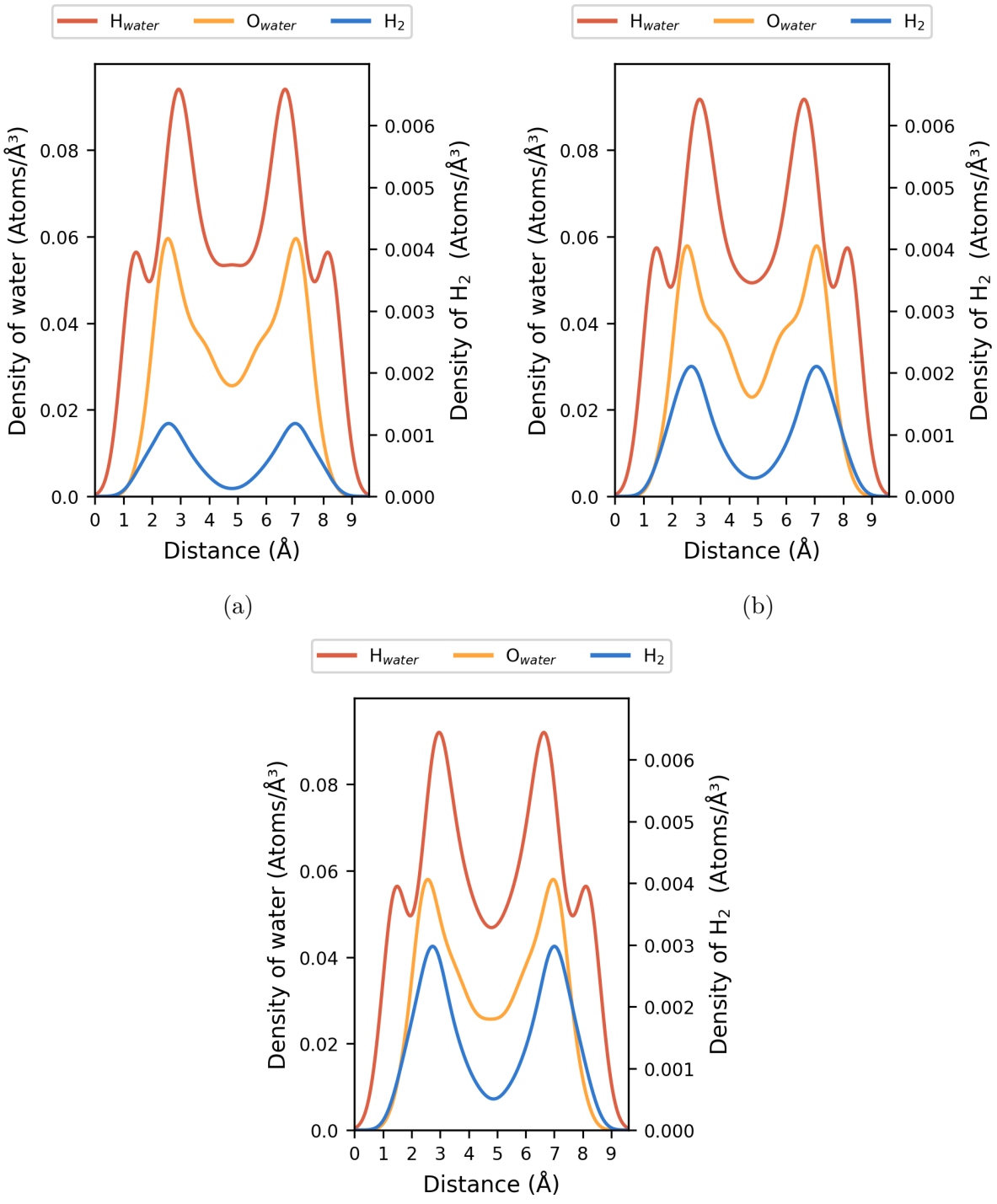

(a)

(b)

(c)

Figure 3.17 – Atomistic density profiles of water hydrogen and oxygen atoms, and hydrogen molecule at a) 200 bar b) 400 bar c) 600 bar

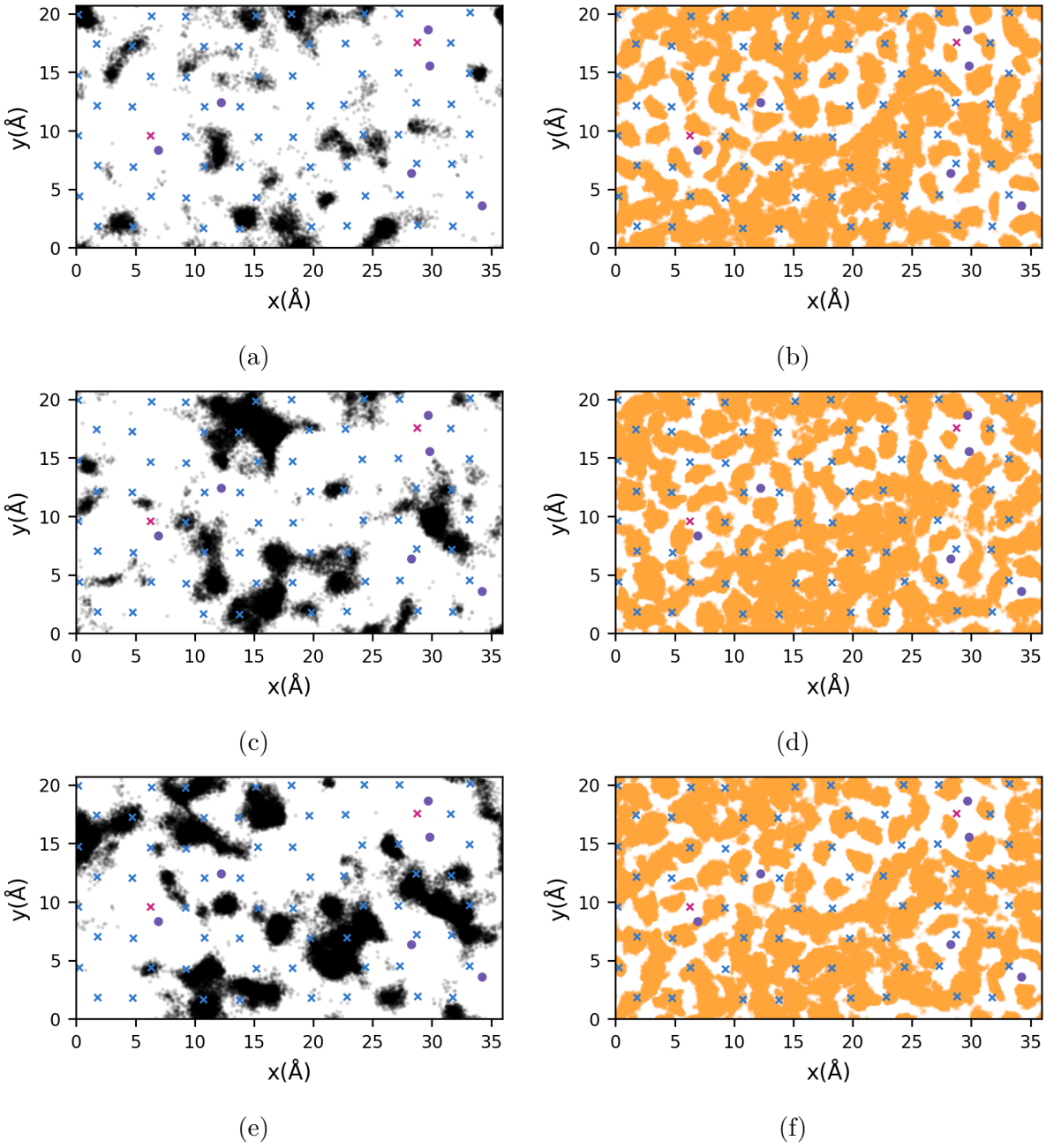

Figure 3.18 – Surface atomic distribution of hydrogen molecules a) 200, c) 400, e) 600 bar and oxygen atoms of water molecules at b) 200, d) 400, f) 600 bar. Color legend: H_2 molecules (black), H_2O molecules (orange), Na ions (purple), Si atoms (blue) and Al atoms (pink)

substitution is surrounded by two sodium ions, it is observed that hydrogen molecules do not prefer to adsorb in close proximity to the substitution site (Si replaced by Al). As

the pressure increases, particularly at 600 bar (Figure 3.18e), it can be clearly seen that hydrogen molecules are mostly adsorbed in the hexagonal cavities. This observation may be attributed to the increased amount of hydrogen, which also enhances statistics.

Table 3.16 – Coordination numbers of O atoms (O_{water}) of water and clay (Ob and Obts), and Na ions at the first shell of H_2 molecule in 2W-Na-mmt at 298 K and, 200, 400 and 600 bar

Pressure (bar)	$CN_{Total-O}$	$CN_{O_{water}}$	CN_{Ob}	CN_{Obts}	CN_{Na}	r_{max}	r_{min}
200	11.65	7.94	3.67	0.04	0.29	3.25	4.15
400	12.11	8.03	4.02	0.06	0.31	3.15	4.25
600	12.08	8.17	3.90	0.02	0.28	3.15	4.25

Figure 3.20 illustrates the radial distribution functions and running coordination numbers of H_2-Na, H_2-Ob, H_2-Obts, and H_2-O_{water} pairs in 2W-Na-mmt at 298 K and 200, 400 and 600 bar. Coordination numbers of O atoms (CN_{Owater}) of water and clay (CN_{Ob} and CN_{Obts}), and Na ions (CN_{Na}) at the first shell of H_2 molecule in 2W-Na-mmt at 298 K and 200, 400 and 600 bar are given in Table 3.16. The first maximum and minimum of H_2-Ob pair are around 3.2 and 4.2 Å, respectively. Unlike at lower pressures (refer to Figure 3.6 and Table 3.13), at higher pressures, no changes are observed with increasing pressure. H_2 molecule is coordinated with approximately 8 water molecules in the interlayers of 2W-Na-mmt at 298 K and between 200 and 600 bar.

Figure 3.19 illustrates the orientation of H_2 molecules within the interlayers of 2W-Na-mmt at 298 K and 200, 400 and 600 bar. The results show that, there is no preference or favored orientation for H_2 molecules in relation to the surface at high pressure.

3.1.4 Effect of interlayer cation mobility on H_2 adsorption

Hydrogen adsorption on 2W-Na-mmt at 298 K was investigated using two different approaches. In one system, the Na ions were maintained as rigid, while in the other system, the Na ions were allowed to be mobile. The isotherms are presented in Figure **??**. The isotherms indicate that the mobility of cations has no impact on the quantity of H_2 adsorbed. Additionally, the water content remains the same. Amount of adsorbed hydrogen on 2W-Na-mmt with "rigid" and "mobile" Na at 298 K up to 120 bar is given in Appendix

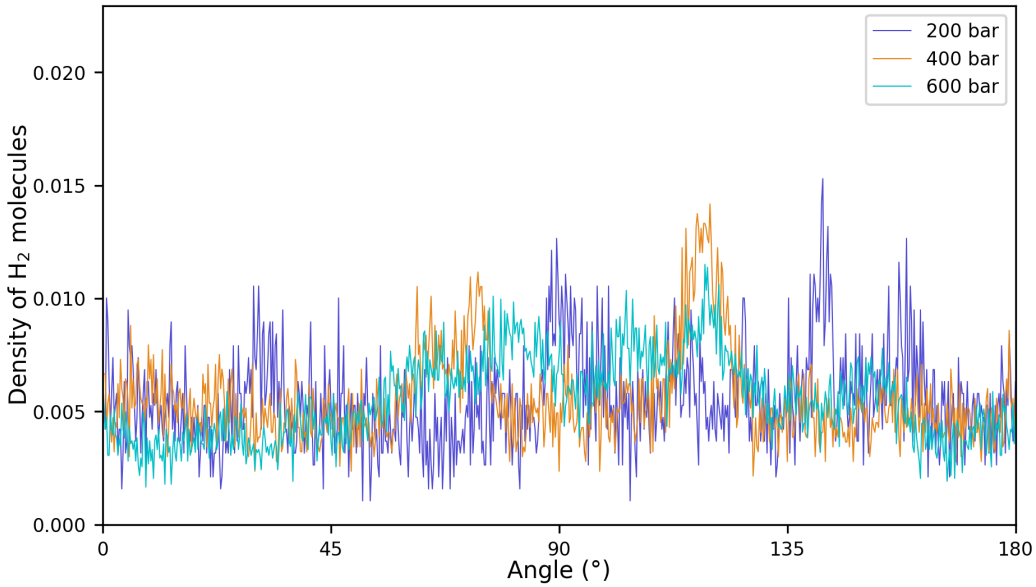

Figure 3.19 – The orientation of H_2 molecules within the interlayers of 2W-Na-mmt at 298 K and, a) 200 bar, b) 400 bar and c) 600 bar

C (Table C.4 and C.11). Tabulated simulation results of absolute and excess adsorption amounts of H_2 and water in mmol/g framework can be found in Tables 3.7 and 3.17.

Table 3.17 – Adsorbed amount of H_2 and water content in 2W-Na-mmt ("mobile Na") at 298 K up to 120 bar in mmol/g

Pressure (bar)	Adsorbed H_2 (mmol/g)			Water content (mmol/g)		
	Absolute	Excess	Error	Absolute	Excess	Error
1	0.000	0.000	0.000	-	-	-
20	0.033	0.029	0.002	14.762	2.695	0.052
40	0.043	0.036	0.001	14.971	2.905	0.015
60	0.087	0.077	0.002	14.777	2.711	0.046
80	0.117	0.104	0.009	14.707	2.642	0.029
100	0.159	0.143	0.004	14.574	2.510	0.050
120	0.175	0.155	0.015	14.690	2.626	0.064

The solubility of H_2 is investigated within the interlayers of both 2W-Na-mmt models: one with "rigid" Na and the other with "mobile" Na (see Figure 3.22). Nearly identical mole fractions were obtained with both methodologies. The solubility of H_2, determined

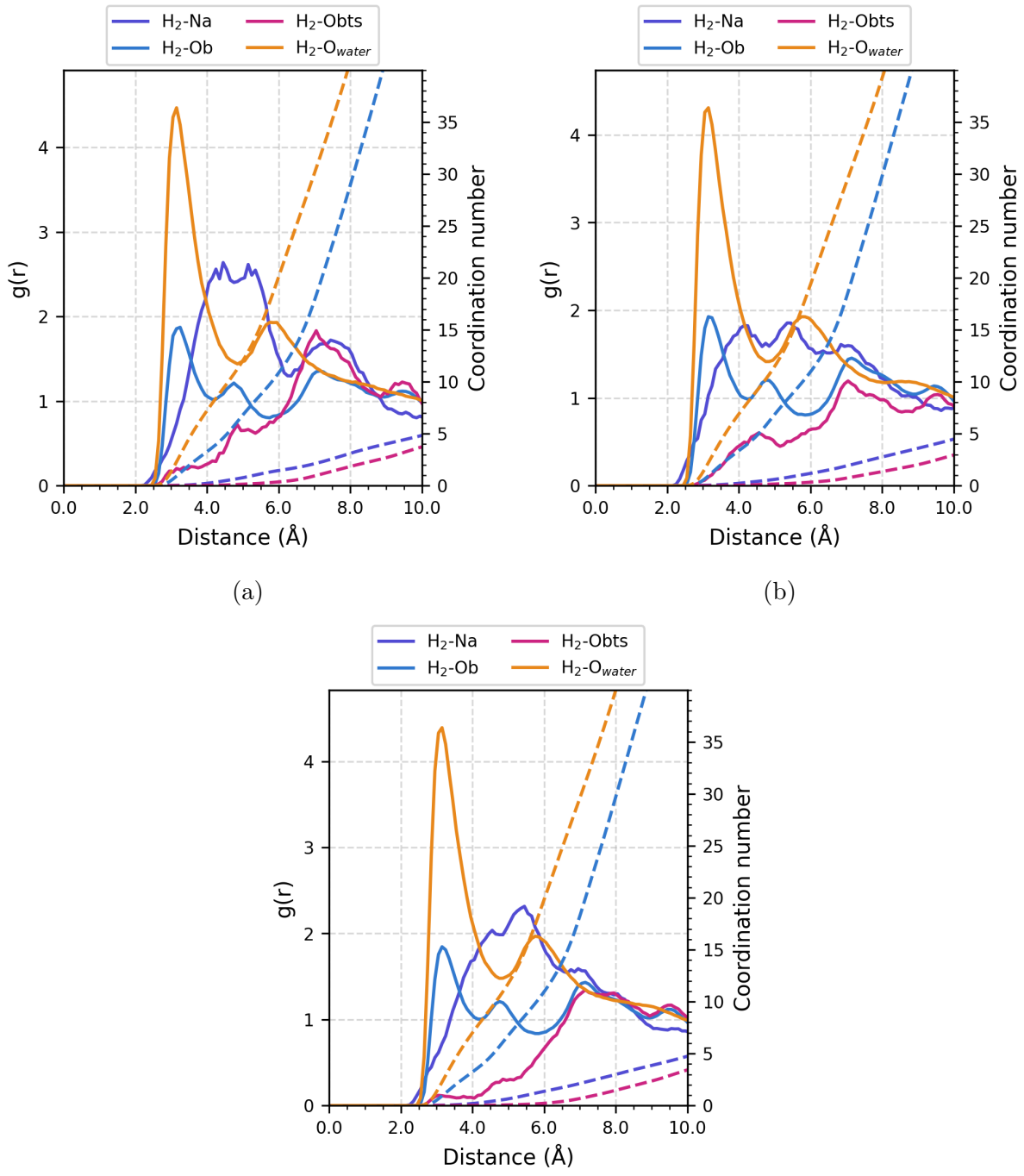

Figure 3.20 – Radial distribution functions and running coordination numbers of H_2-Na, H_2-Ob, H_2-Obts and H_2-O_{water} pairs in 2W-Na-mmt at 298 K and a) 200 bar, b) 400 bar and c) 600 bar

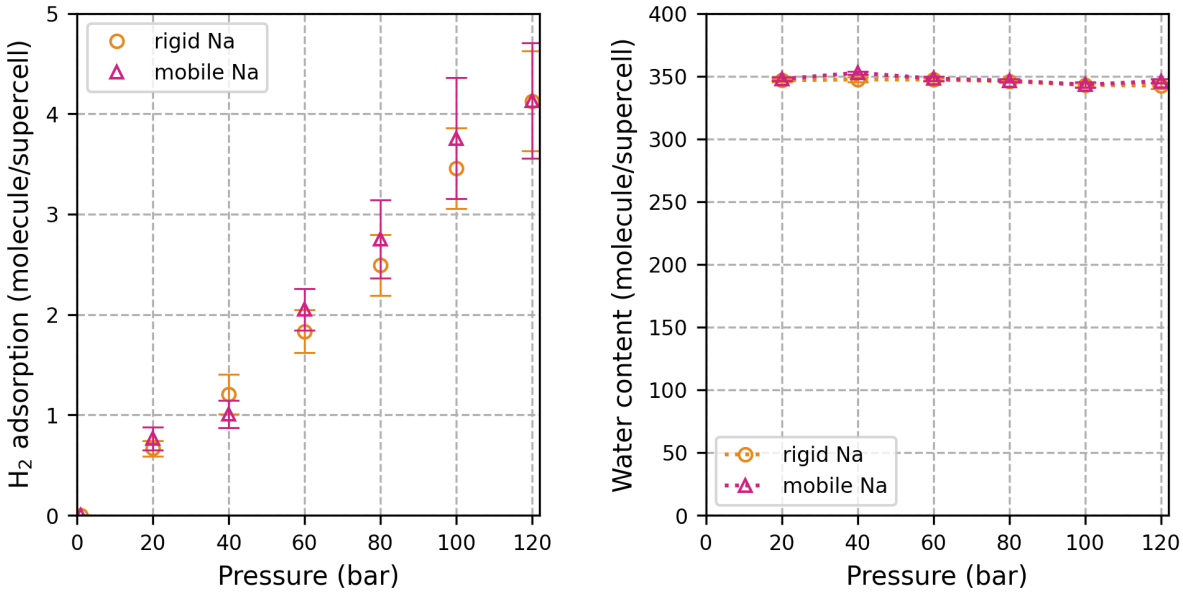

(a) (b)

Figure 3.21 – Adsorption isotherms of a) hydrogen and b) water on on bilayer hydrated "rigid" and "mobile" Na-montmorillonites at 298K

through various approaches, exhibited an approximately sevenfold increase compared to its solubility in bulk.

In both approaches, where the counter ion, Na, was kept either rigid or mobile, the quantity of adsorbed H_2 and water content remains the same. However, the comparison between these approaches is carried out also with a focus on structural properties to understand better the accuracy of the simulations.

The atomic density profiles of hydrogen (H_{water}) and oxygen (O_{water}) atoms of water, H_2 molecules, and Na ions in the interlayer pore of 2W-Na-montmorillonite with "mobile" Na ion at 298 K and 120 bar are given in Figure 3.23. Similar to 2W-Na-mmt with "rigid" Na (Figure 3.4b), O_{water} atoms and H_2 molecules exhibit two peaks at the same position relative to the surface, around 2.6 Å. H_{water} atoms also form two peaks, one located at 3 Å with a shoulder at 1.5 Å. The atomic distribution of Na was also investigated. The density profile of Na^+ shows that Na^+ forms two minor peaks close to the surface, one at 1.7 Å and a major peak in the middle of the pore at 4.8 Å. The similar density profiles of Na^+ ions indicate the formation of mostly the outer-sphere complexes in bilayer hydrated Na-mmt, are reported by Botan et al. (2010), Loganathan et al. (2017), Ngouana Wakou

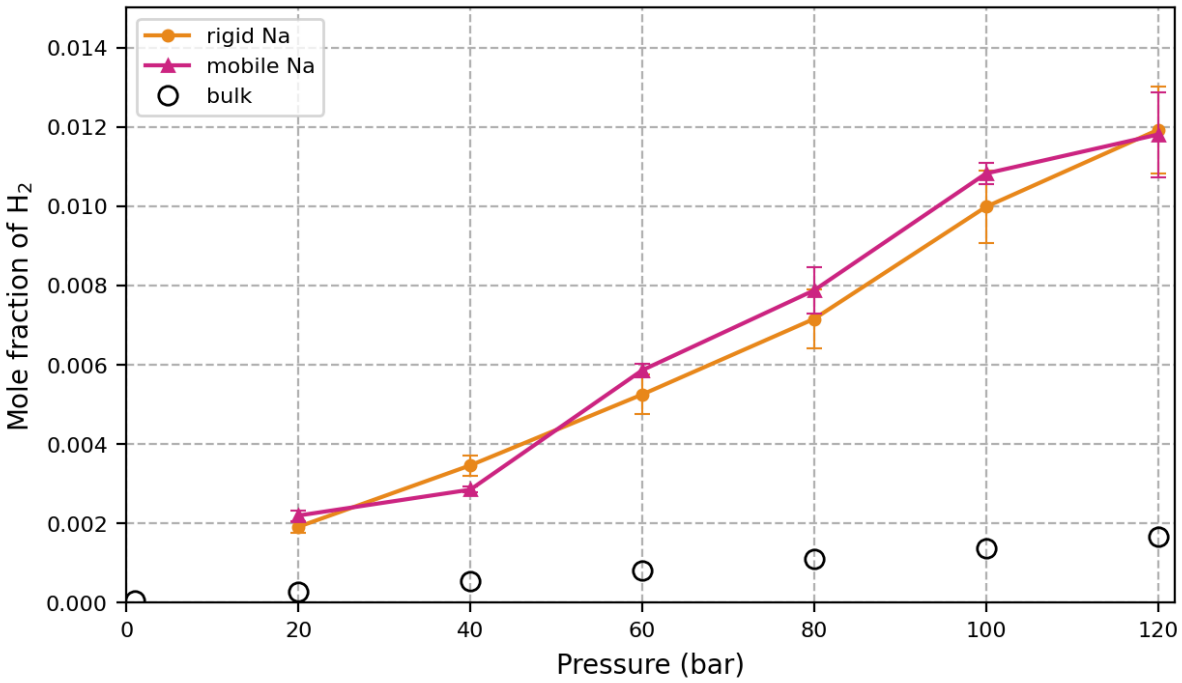

Figure 3.22 – Solubility of H_2 in the interlayers of 2W-Na-mmt with "rigid" and "mobile" Na, and in bulk at 298 K. Bulk values (Table B.1 in Appendix B) at 298 K are taken from Rahbari et al., 2019; Wiebe and Gaddy, 1934.

(2014), and Owusu et al. (2022).

The surface atomic density maps are given in Figure 3.24. The color legend in the figure assigns black to H_2 molecules, orange to H_2O molecules, purple to Na ions, blue to Si atoms, and pink to Al atoms. Figure 3.24a and c shows the center of the mass of H_2 molecules while Figure 3.24b and d shows O atoms of H_2O molecule. Surface maps for mobile Na reveal that the sites with a high probability of Na cation presence correspond to locations where tetrahedral substitution (Al) occurs (Figure 3.24c). This suggests that tetrahedral substitution hinders the adsorption of H_2 molecules. On the other hand, Figure 3.24a illustrates that hydrogen molecules are not preferentially adsorbed near to the substitutions even though one of them is free in the rigid model. Figure 3.24d shows that Na cations are hydrated with water molecules.

Radial distribution functions and running coordination numbers of H_2-Na, H_2-Ob, H_2-Obts and H_2-O_{water} pairs in 2W-Na-mmt with "mobile" Na at 298 K and 120 and 120 bar are illustrated in Figure 3.25. Coordination numbers of O atoms (CN_{Owater}) of water and clay (CN_{Ob} and CN_{Obts}), and Na ions (CN_{Na}) at the first shell of H_2 molecule in 2W-Na-

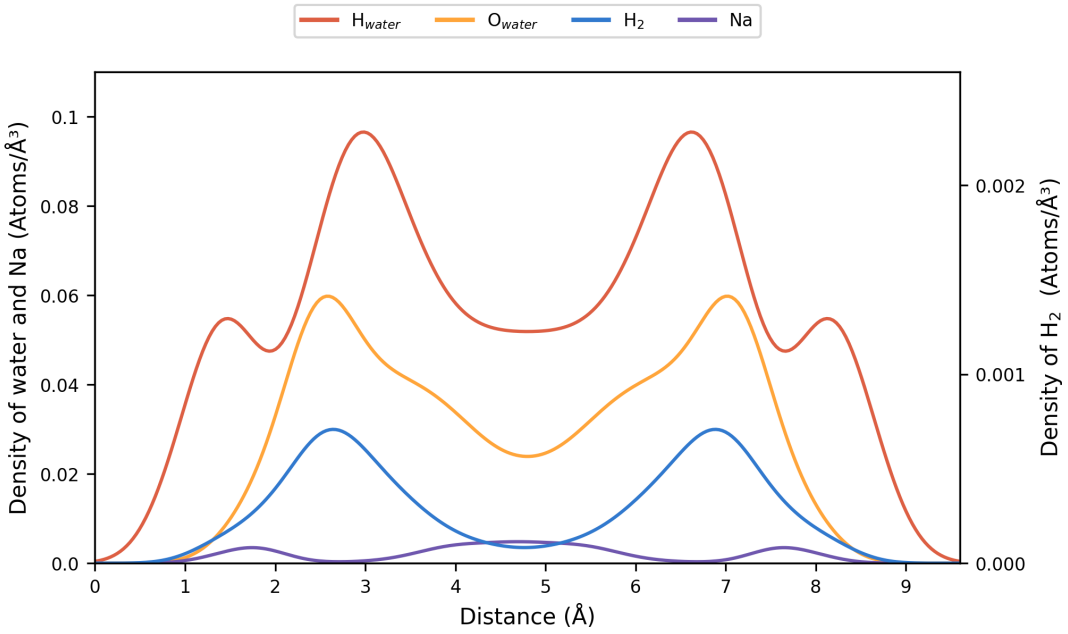

Figure 3.23 – Atomic density profiles of water hydrogen and oxygen atoms, and hydrogen molecule in 2W-Na-mmt with "mobile" Na at 298 K and 120 bar

Table 3.18 – Coordination numbers of O atoms (O_{water}) of water and clay (Ob and Obts), and Na ions at the first shell of H_2 molecule in 2W-Na-mmt with "mobile" Na at 298 K and 120 bar

Model	$CN_{Total-O}$	$CN_{O_{water}}$	CN_{Ob}	CN_{Obts}	CN_{Na}	r_{max}	r_{min}
"Mobile" Na	12.49	8.60	3.85	0.04	0.28	3.25	4.25
"Rigid" Na	12.80	8.99	3.80	0.02	0.32	3.25	4.25

mmt with "mobile Na" at 298 K and 120 bar are given in Table 3.18 in comparison to the same model at same conditions where Na ions were kept fixed in their position at the same conditions. No noticeable difference is observed in the coordination of atoms.

Figure 3.26 illustrates the orientation of H_2 molecules within the interlayers of 2W-Na-mmt at 298 K and 120 bar. The results show that, cation mobility does not affect the orientation of H_2 molecules in relation to the surface.

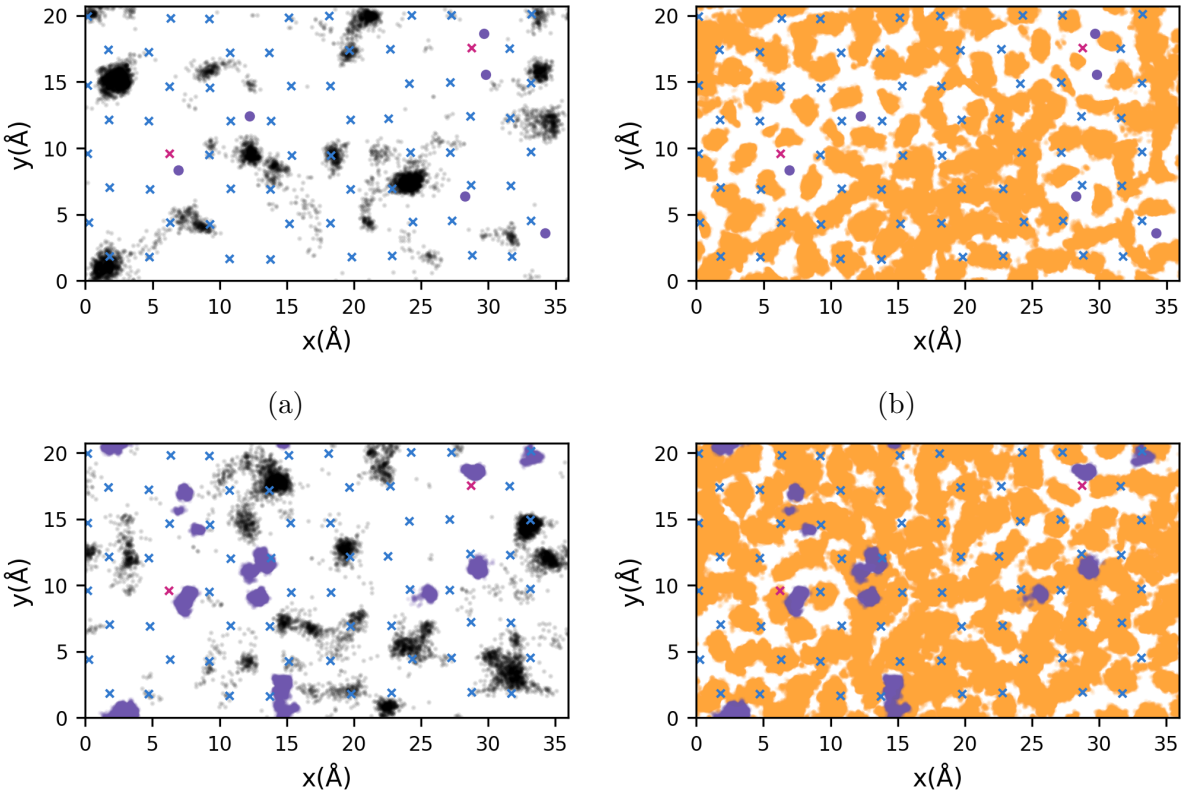

Figure 3.24 – Surface atomic distribution of hydrogen molecules on a) "rigid" and c) "mobile" Na-montmorillonite and water oxygen atoms on b) rigid and d) mobile Na-montmorillonite. Color legend: H_2 molecules (black), H_2O molecules (orange), Na ions (purple), Si atoms (blue) and Al atoms (pink)

3.1.5 Effect of clay framework flexibility on H_2 adsorption

H_2 adsorption simulations were carried out using a flexible 2W-Na-montmorillonite framework with hybrid Monte Carlo/Molecular Dynamics (MC/MD) method (Boinepalli and Attard, 2003; Dubbeldam et al., 2016). Due to the extended and resource-intensive computational requirements, exceeding even those of GCMC simulations, which themselves require a considerable prolonged time in proportion to the amount of water, results were obtained only for pressure conditions of 1, 20, and 40 bar. The isotherms are presented in Figure 3.27 in comparison with isotherms obtained using 2W-Na-montmorillonite with "rigid" and "mobile" Na, and rigid framework. Amount of adsorbed hydrogen on 2W-Na-mmt with "rigid" and "mobile" Na at 298 K up to 120 bar can be found in Appendix C (Table C.4, C.11 and C.12). Additionally, absolute and excess adsorption amounts of H_2

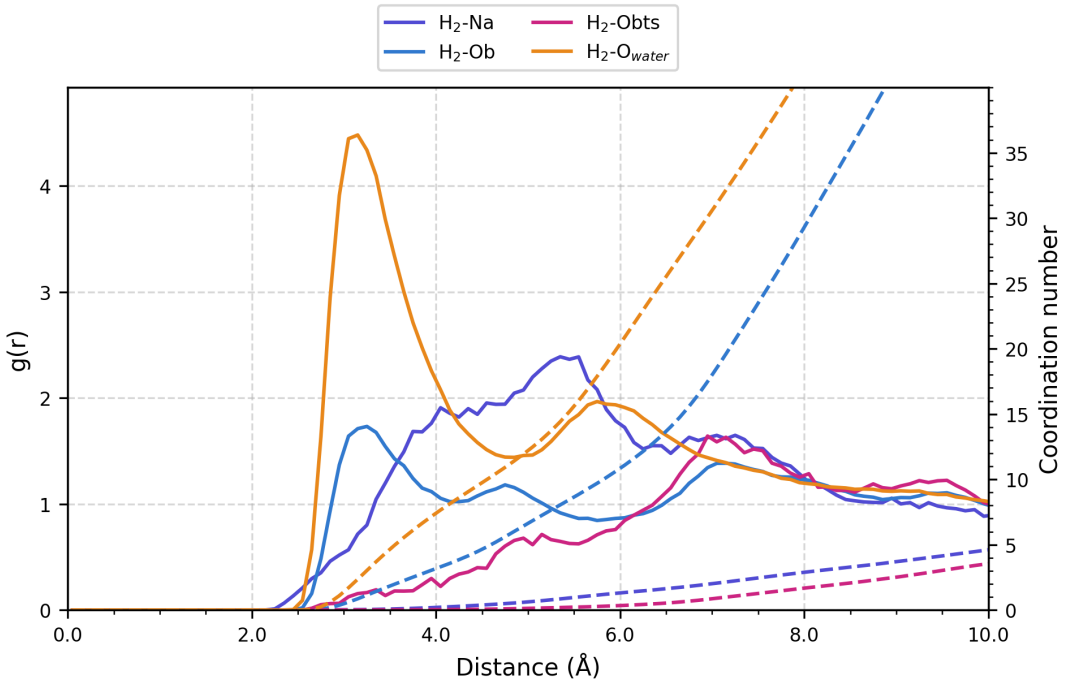

Figure 3.25 – Radial distribution functions and running coordination numbers of H_2-Na, H_2-Ob, H_2-Obts and H_2-O_{water} pairs in 2W-Na-mmt model with "mobile" Na at 298 K and 120 bar

and water in mmol/g framework are listed in Tables 3.19.

Table 3.19 – Adsorbed amount of H_2 and water content in 2W-Na-mmt (with flexible framework) at 298 K and, 20 and 40 bar in mmol/g

Pressure (bar)	Adsorbed H_2 (mmol/g)			Water content (mmol/g)		
	Absolute	Excess	Error	Absolute	Excess	Error
1	0.000	0.000	0.000	-	-	-
20	0.014	0.010	0.000	16.062	3.995	0.015
40	0.021	0.014	0.002	16.255	4.189	0.018

Similar to the results obtained using GCMD simulations with flexible frameworks, no H_2 adsorption obtain at 1 bar. These findings indicate that the flexibility of the framework results in a reduced H_2 adsorption while the amount of water increases. Consequently, in the interlayers of 2W-Na-mmt with a flexible framework, there is a decrease in the mole fraction of H_2; however, it remains twice to three times higher compared to its solubility

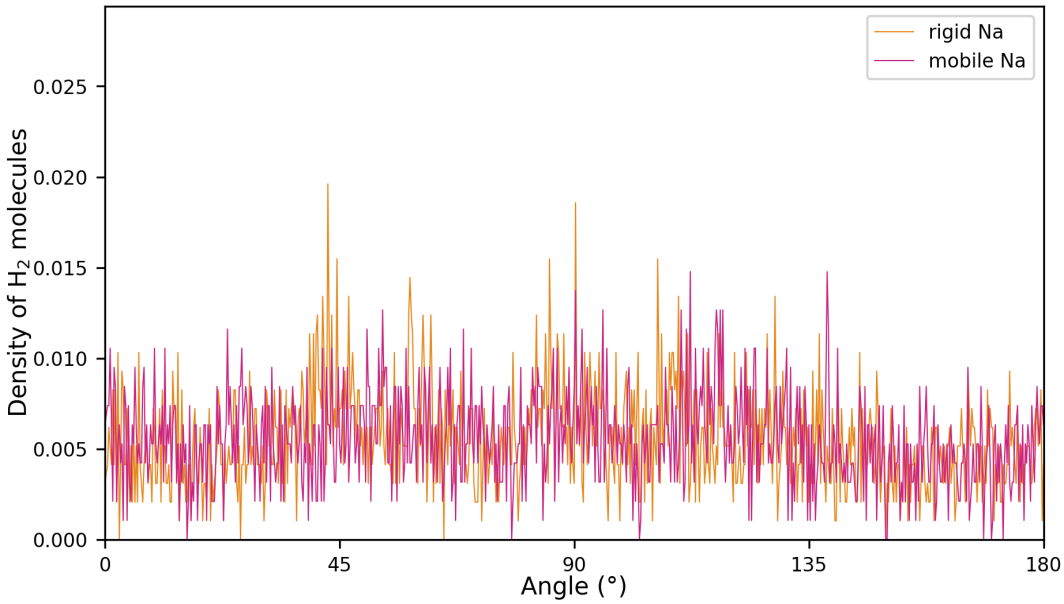

Figure 3.26 – The orientation of H_2 molecules within the interlayers of 2W-Na-mmt with "rigid" Na and "mobile" Na at 298 K and 120 bar

in water. Despite slight variations in the results, all simulations were conducted using the rigid framework due to unfeasible time constraints. Furthermore, it is noteworthy that the order of magnitude remains consistent across these approaches. Additionally, it should be emphasized that the outcomes obtained through fixed frameworks align with experimental results.

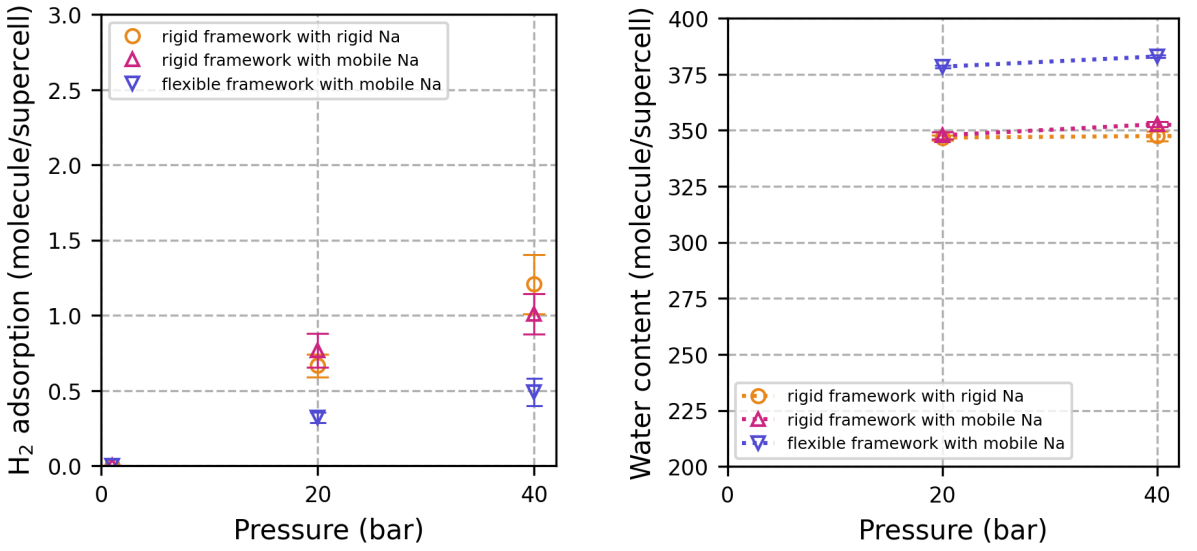

(a) (b)

Figure 3.27 – Adsorption isotherms of a) hydrogen and b) water on bilayer hydrated "rigid" and "mobile" Na-montmorillonites with rigid and flexible framework at 298K and, 20 and 40 bar

3.2 H_2 adsorption on Ca-montmorillonite

This section discusses results of H_2 adsorption in Ca-montmorillonite interlayers with a particular emphasis on the effects of temperature and pore size.

Table 3.20 – Summary of the simulations performed and discussed in Subsection 3.2.1 and Subsection 3.2.2

Hydration level	Temperature (K)	Pressure (bar)						
		1	20	40	60	80	100	120
0W	298	✓						✓
1W	298	✓	✓	✓	✓	✓	✓	✓
2W	298	✓	✓	✓	✓	✓	✓	✓
	323	✓	✓	✓	✓	✓	✓	✓
3W	298	✓	✓	✓	✓	✓	✓	✓

The summary of the simulations performed to investigate the influence of temperature and pore size/hydration level is given in Table 3.20, and discussed in Subsection 3.2.1

and Subsection 3.2.2, respectively. In all simulations conducted within this context, the interlayer cation was kept mobile, while the framework remained rigid.

3.2.1 Effect of temperature on H_2 adsorption

Hydrogen adsorption on bilayer (2W) hydrated Ca-mmt was performed at two different temperatures (298 and 323 K) up to 120 bar. Hydrogen adsorption isotherms are given in Figure 3.28. Amount of adsorbed hydrogen was given as absolute number of H_2 molecules per supercell. No adsorption was observed at 1 bar and temperatures of both 298 and 323 K, and at 20 bar and 323 K. As the temperature increases, the amount of H_2 adsorbed decreases similar to section 3.1.1 while the amount of water remains the same. Additionally, this difference becomes more pronounced as pressure increases. Amount of adsorbed hydrogen on 2W-Ca-mmt at 298 K and 323 K up to 120 bar is given in Appendix D (Table D.1 and D.2). Simulation results of absolute and excess adsorption amounts of H_2 and water in mmol/g framework are listed in Table 3.21 and 3.22.

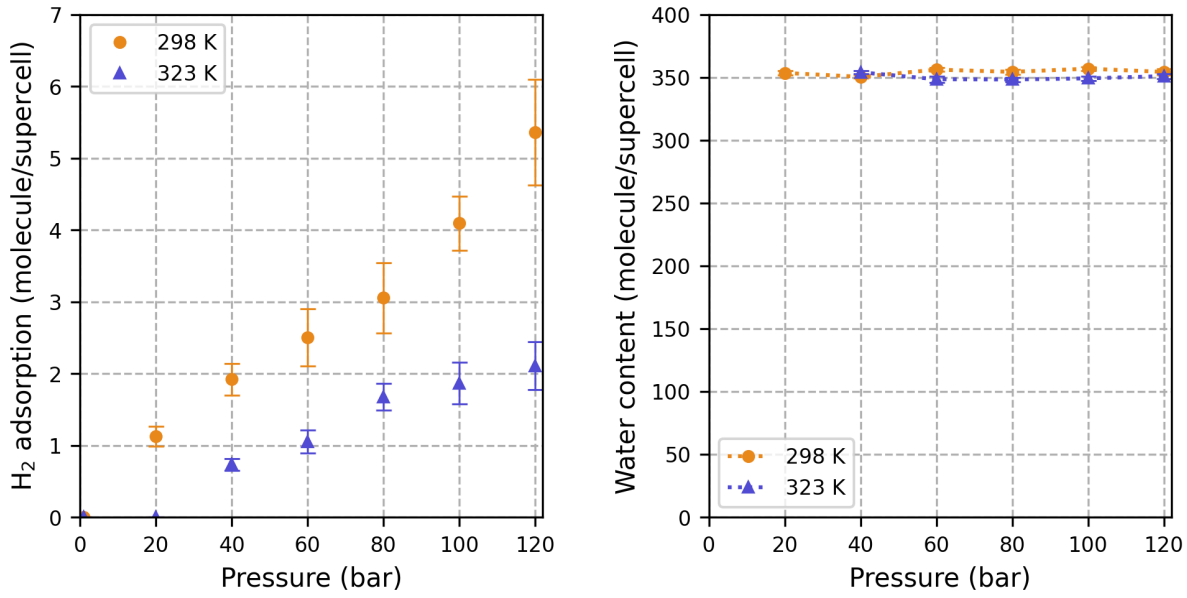

(a) (b)

Figure 3.28 – Adsorption isotherms of a) hydrogen and b) water on 2W-Ca-mmt at 298 and 323 K

Figure 3.29 shows that oversolubility is observed at both temperatures. Despite the slight variation in bulk H_2 solubility at different temperatures (with a slightly higher solubility

Table 3.21 – Adsorbed amount of H_2 and water content in 2W-Ca-mmt at 298 K up to 120 bar in mmol/g

Pressure (bar)	Adsorbed H_2 (mmol/g)			Water content (mmol/g)		
	Absolute	Excess	Error	Absolute	Excess	Error
1	0.000	0.000	0.000	-	-	-
20	0.048	0.044	0.002	15.051	2.632	0.041
40	0.082	0.075	0.006	14.919	2.500	0.010
60	0.107	0.096	0.008	15.162	2.743	0.039
80	0.093	0.116	0.010	15.087	2.669	0.069
100	0.174	0.157	0.008	15.194	2.777	0.044
120	0.228	0.208	0.019	15.085	2.669	0.070

Table 3.22 – Adsorbed amount of H_2 and water content in 2W-Ca-mmt at 323 K up to 120 bar in mmol/g

Pressure (bar)	Adsorbed H_2 (mmol/g)			Water content (mmol/g)		
	Absolute	Excess	Error	Absolute	Excess	Error
1	0.000	0.000	0.000	-	-	-
20	0.000	0.000	0.000	-	-	-
40	0.031	0.025	0.001	15.071	3.147	0.019
60	0.045	0.036	0.004	14.837	2.912	0.072
80	0.071	0.059	0.005	14.828	2.903	0.025
100	0.079	0.064	0.007	14.866	2.941	0.053
120	0.090	0.072	0.010	14.943	3.017	0.050

at 298 K), a significant disparity is observed in the H_2 solubility within the interlayers of 2W-Ca-mmt. At 298 K, the mole fraction of H_2 is approximately four times that of its bulk value. Meanwhile, the mole fraction of H_2 increases to around seven to eight times its bulk value at 323 K.

Figure 3.30 illustrates density profiles for H_2 molecules and hydrogen and oxygen atoms of water, along with hydrogen molecules and Ca ions within the interlayer of 2W-Ca-montmorillonite at 298 K and 80 bar, 298 K and 120 bar and, 323 K and 120 bar. At 298 K and 80 bar, both O atoms of H_2O (O_{water}) and H_2 molecules exhibit two peaks at around 2.6 Å (Figure 3.30a). However, peaks of H_2 molecules move slightly towards

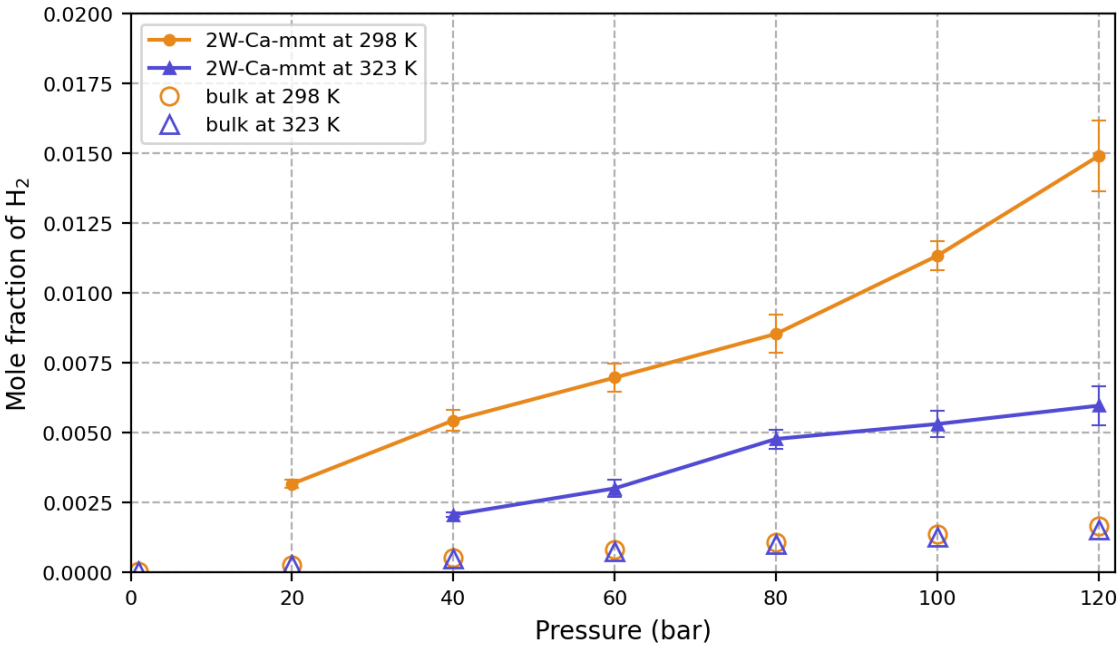

Figure 3.29 – Solubility of H_2 in the interlayers of 2W-Ca-mmt and in bulk at 298 K and 323 K. Bulk values (Table B.1 in Appendix B) at 298 and 323 K are taken from Rahbari et al., 2019; Wiebe and Gaddy, 1934.

the center located at 2.9 Å while peaks of O_{water} remain at the same position around 2.5 Å at 120 bar (Figure 3.30b). The hydrogen atoms (H_{water}) of water molecules also form two major peaks around 2.9 Å, located at the same position relative to the surface at both 80 and 120 bar with shoulders at 1.5 Å showing that one of the hydrogen atoms of some water molecules is positioned closer to the surface similar to Figure 3.4. Moreover, Ca ions form a major peak around 4.8 and 4.9 Å in the center of pores with smaller two peaks near to the surfaces around 2.2 and 2.1 Å, at 80 and 120 bar, respectively. At 298 K and 120 bar, both O_{water} atoms and H_2 molecules exhibit two peaks at around 2.6 and 2.7 Å, respectively (Figure 3.30c). H_{water} atoms exhibits two major peaks around 3 Å and with a shoulder at 1.5 Å. Similarly, Ca ions form a major peak around 4.9 Å in the center of the pore with smaller two peaks near the surfaces around 2.2 Å. On the other hand, Ngouana Wakou (2014) reported that Ca ion forms only a major peak in mid-plane of bilayer hydrated Ca-montmorillonite.

Radial distribution functions and running coordination numbers of H_2-Ca, H_2-Ob, H_2-Obts, and H_2-O_{water} pairs in 2W-Ca-mmt at 298 K and 80 bar, 298 K and 120 and 323 K and 120 bar are presented in Figure 3.31. The first coordination shell is determined

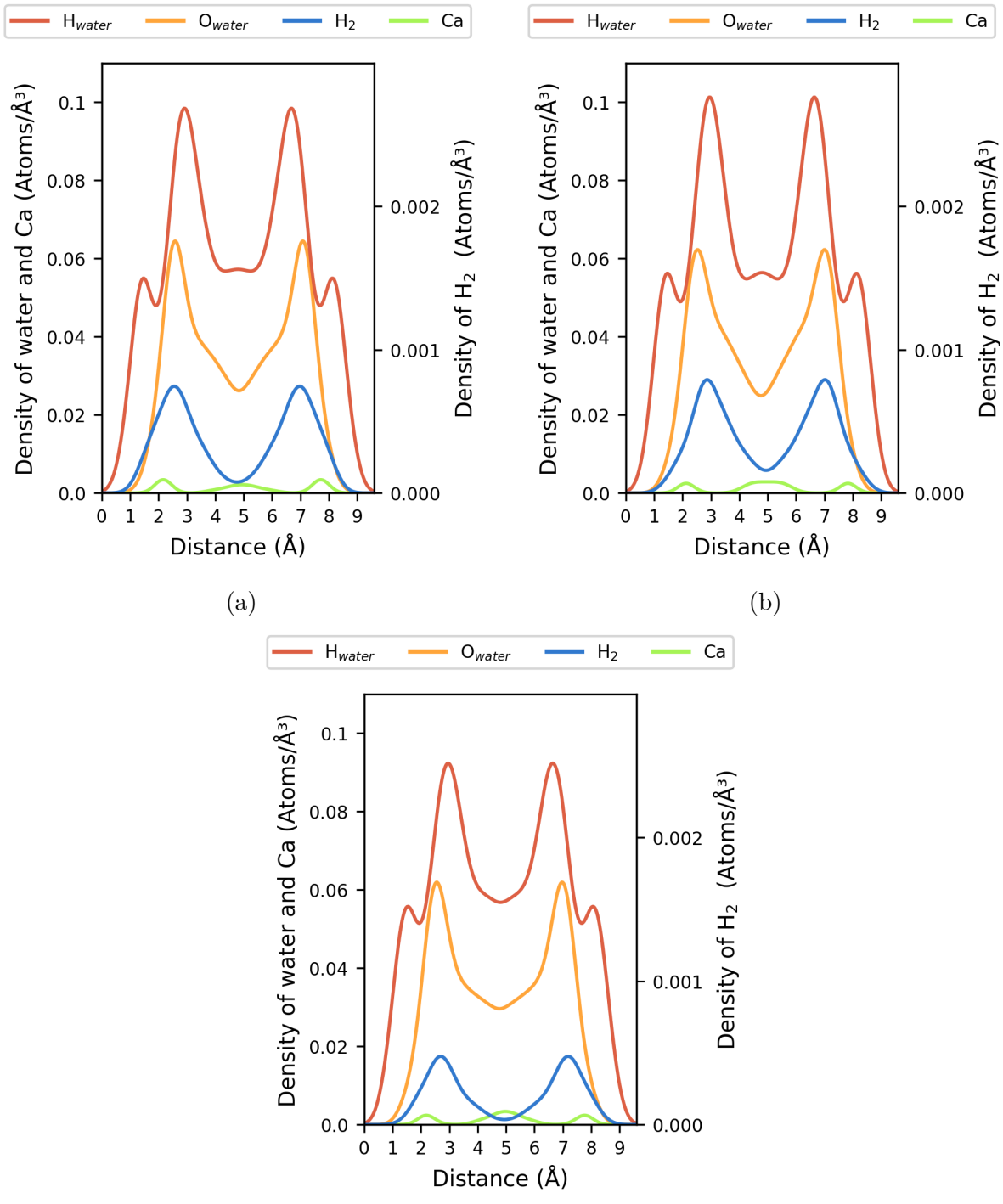

Figure 3.30 – Atomic density profiles of water hydrogen and oxygen atoms, and hydrogen molecule on 2W-Ca-mmt at a) 298 K and 80 bar, b) 298 K and 120 bar and c) 323 K and 120 bar

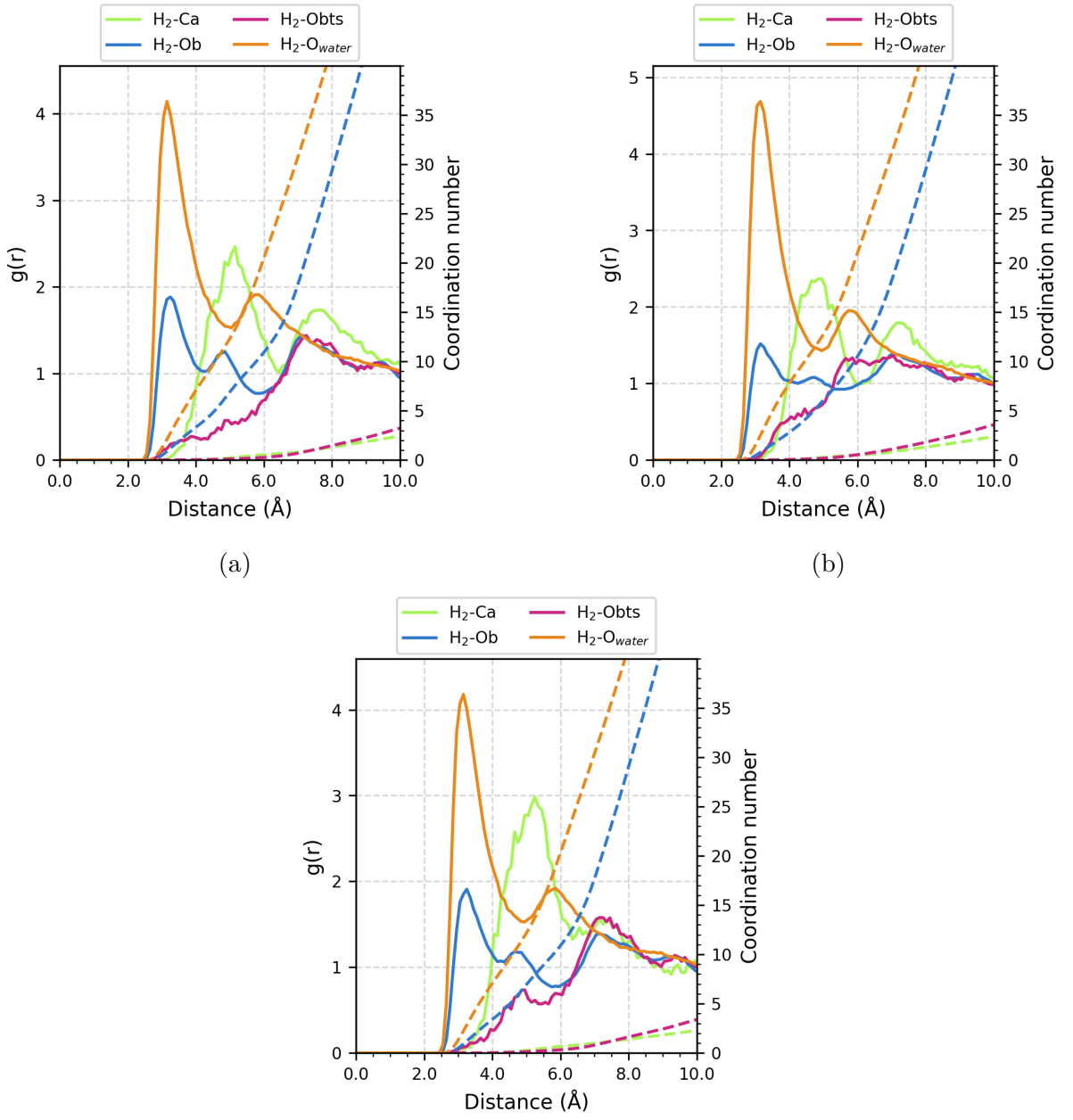

Figure 3.31 – Radial distribution functions and running coordination numbers of H_2-Na, H_2-Ob, H_2-Obts and H_2-O_{water} pairs in 2W-Ca-mmt at a) 298 K and 80 bar, b) 298 K and 120 bar and c) 323 K and 120 bar

at the first minimum (r_{min}) for the H_2-Ob pair occurs around 4.2 Å. Ca^{2+} ions are not present in the first coordination shell of H_2 and indicates that their predominant coordi-

Table 3.23 – Coordination numbers of O atoms (O_{water}) of water and clay (Ob and Obts), and Ca ions at the first shell of H_2 molecule in 2W-Ca-mmt at 298 K and 80 bar, 298 K and 120 and 323 K and 120 bar

Temperature (K)	Pressure (bar)	$CN_{Total-O}$	$CN_{O_{water}}$	CN_{Ob}	CN_{Obts}	CN_{Ca}	r_{max}	r_{min}
298	80	12.40	8.35	4.00	0.04	0.05	3.25	4.25
298	120	12.59	9.05	3.47	0.07	0.07	3.15	4.25
323	120	11.67	7.82	3.83	0.03	0.05	3.25	4.15

nation is closer to the center of the pores similar to Na^+ ions (refer to Section 3.1). In Table 3.23, coordination numbers of O atoms (CN_{Owater}) of water and clay (CN_{Ob} and CN_{Obts}), and Ca^{2+} ions (CN_{Ca}) at the first shell of H_2 molecule in 2W-Ca-mmt at the same pressure/temperature conditions are listed. $N_{Total-O}$ indicates the total number of all O atoms in the first shell of H_2. As pressure increases, the number of O_{water} remains the same, while the number of Ob rises. The total number of O decreases with an increase in temperature. One H_2 molecule is surrounded by around 9 water molecules at 298 K and 120 bar and it is surrounded by approximately 8 water molecules at 298 K and 80 bar, and at 323 K and 120 bar. To conclude, as pressure increases and temperature decreases there is a small difference in the number of water molecules in the first sphere of H_2.

Figure 3.32a illustrates the orientation of H_2 molecules within the interlayers of 1W-Na-mmt, 2W-Na-mmt and 3W-Na-mmt at 298 K and 120 bar. The results show that, regardless of temperature and pressure, there is no preference or favored orientation for H_2 molecules in relation to the surface.

3.2.2 Effect of hydration level/pore size on H_2 adsorption

Hydrogen adsorption on monolayer (1W), bilayer (2W) and trilayer (3W) hydrated Ca-mmt performed at 298 K up to 120 bar. Hydrogen adsorption isotherms are given in Figure 3.33. Helium void fractions were calculated for dry, 1W, 2W and 3W Ca-montmorillonites as 0.00004, 0.29, 0.43 and 0.54 %. In dry Ca-montmorillonite model, adsorption was not observed as similar to dry Na-montmorillonite (Subsection 3.1.2). As the hydration level increases, the amount of H_2 adsorbed increases due to both larger pore size and increasing

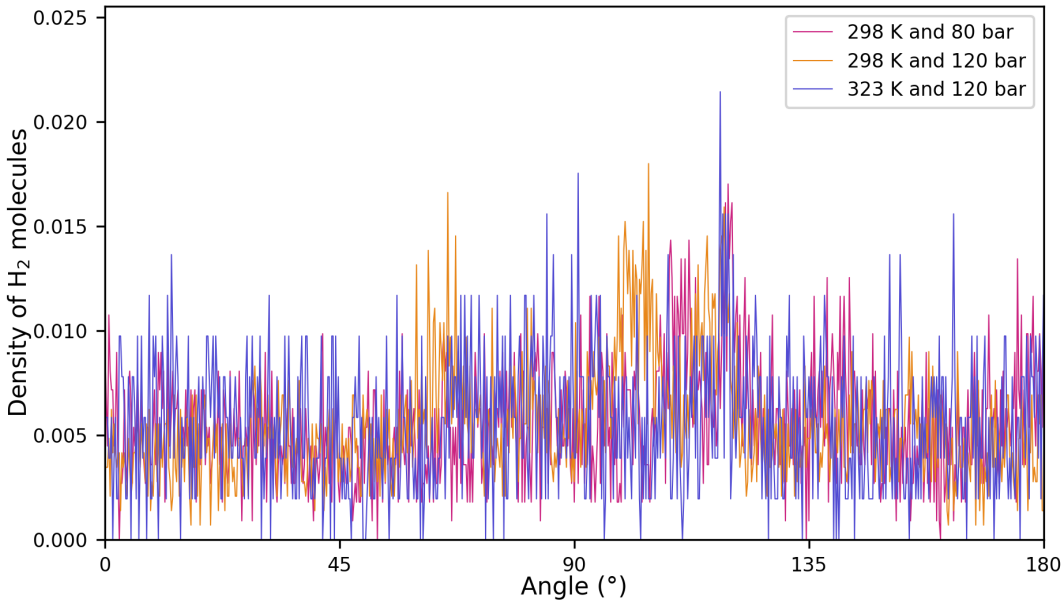

Figure 3.32 – The orientation of H_2 molecules within the interlayers of 2W-Ca-mmt at a) 298 K and 80 bar, b) 298 K and 120 bar and c) 323 K and 120 bar with respect to the surface

amount of water. Amount of adsorbed hydrogen on 1W-Ca-mmt and 3W-Ca-mmt at 298 K up to 120 bar is given in Appendix D (Tables D.1, D.3, and D.4).

Table 3.24 – Adsorbed amount of H_2 and water content in 1W-Ca-mmt at 298 K in mmol/g

Pressure (bar)	Adsorbed H_2 (mmol/g)			Water content (mmol/g)		
	Absolute	Excess	Error	Absolute	Excess	Error
1	0.000	0.000	0.000	-	-	-
20	0.031	0.029	0.003	8.243	1.420	0.023
40	0.040	0.037	0.002	8.375	1.553	0.024
60	0.076	0.070	0.001	8.339	1.517	0.040
80	0.125	0.117	0.008	8.175	1.353	0.010
100	0.135	0.125	0.003	8.218	1.397	0.006
120	0.145	0.133	0.009	8.293	1.473	0.011

Tabulated simulation results of absolute and excess adsorption amounts of H_2 and water in mmol/g framework are given in Tables 3.24, 3.21 and 3.25. The results of H_2

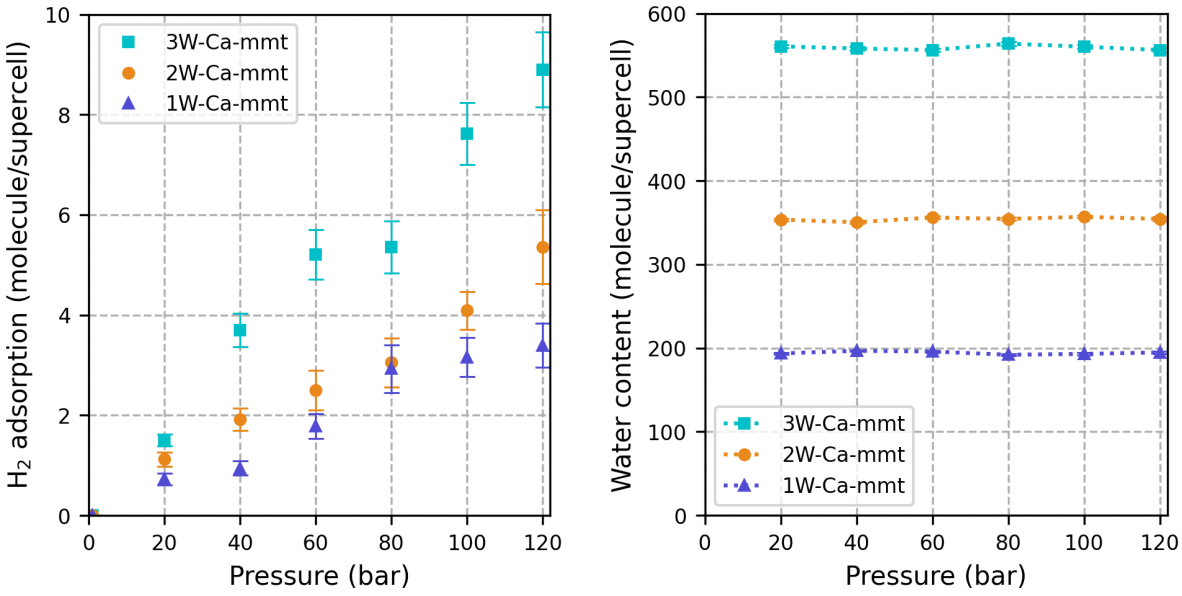

(a) (b)

Figure 3.33 – Adsorption isotherms of a) hydrogen and b) water on 1W-Ca-mmt, 2W-Ca-mmt and 3W-Ca-mmt at 298 K

Table 3.25 – Adsorbed amount of H_2 and water content in 3W-Ca-mmt at 298 K up to 120 bar in mmol/g

Pressure (bar)	Adsorbed H_2 (mmol/g)			Water content (mmol/g)		
	Absolute	Excess	Error	Absolute	Excess	Error
1	0.000	0.000	0.000	-	-	-
20	0.064	0.058	0.002	23.870	4.412	0.061
40	0.158	0.147	0.012	23.762	4.305	0.089
60	0.222	0.206	0.011	23.683	4.227	0.031
80	0.228	0.206	0.009	24.009	4.554	0.071
100	0.324	0.298	0.018	23.853	4.399	0.030
120	0.379	0.347	0.028	23.682	4.230	0.087

adsorption on the 1W-Ca-mmt model at 298 K were compared with experimental results of Mg-montmorillonite (Ziemiański and Derkowski, 2022). Partially hydrated Mg-montmorillonite sample with a basal spacings of 12.1 Å showed the excess amount of adsorbed H_2 in the interlayers of Mg-montmorillonite is estimated around 0.09 mmol/g at 100 bar. Moreover, the total excess amount of adsorbed H_2 on Mg-montmorillonite is

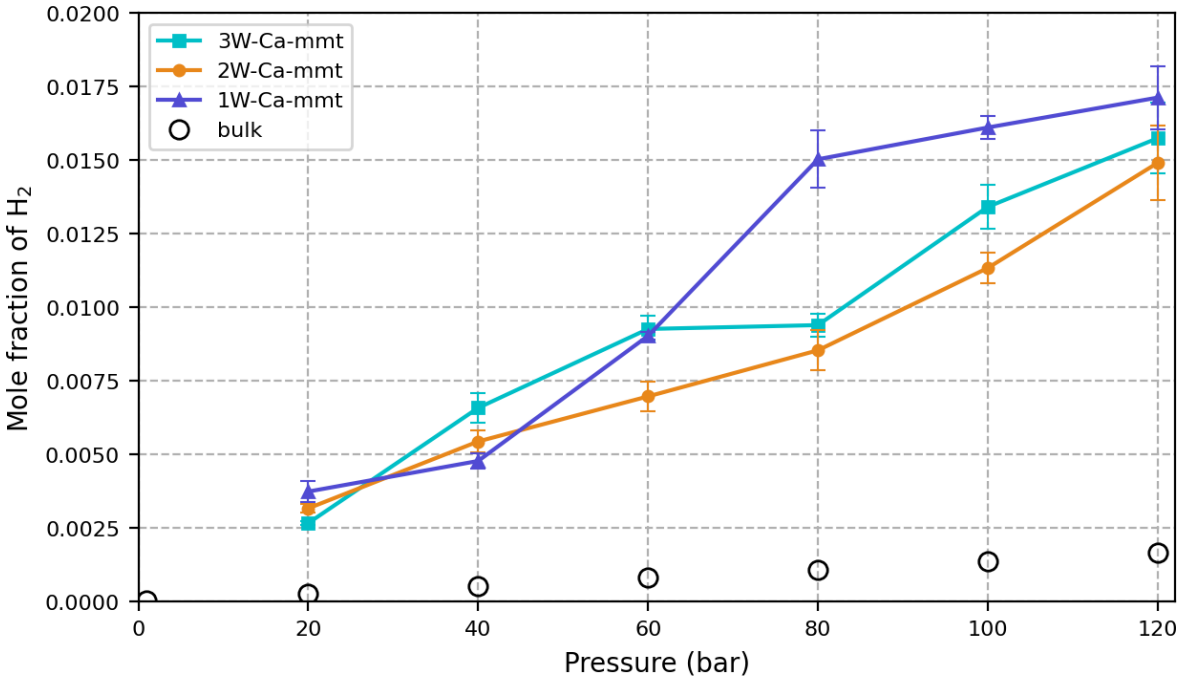

Figure 3.34 – Solubility of H_2 in the interlayers of 1W-Ca-mmt, 2W-Ca-mmt, 3W-Ca-mmt and in bulk at 298 K. Bulk values (Table B.1 in Appendix B) at 298 K are taken from Rahbari et al., 2019; Wiebe and Gaddy, 1934.

obtained around 0.16 mmol/g at 100 bar that proves that H_2 molecules are dominantly adsorbed in the interlayers of clays. In this work, the excess amount of adsorbed H_2 in the interlayers of Ca-montmorillonite with the basal spacing of 13.05 Å is around 0.13 mmol/g at 100 bar (Table 3.24) showing that the simulation results are consistent with the experimental data.

The investigation extends to the solubility of H_2 within the interlayers of 1W-Ca-mmt, 2W-Ca-mmt, and 3W-Ca-mmt at 298 K, up to 120 bar (refer to Figure 3.34). Fluctuations are noticeable among different hydration levels at various pressures; nevertheless, oversolubility is observed at all pressure points. At 120 bar, the solubility is very similar in all three models namely 1W-Ca-mmt, 2W-Na-mmt and 3W-Na-mmt. The mole fraction of H_2 reaches up to 9 times its solubility in bulk water.

The density profiles of hydrogen and oxygen of water, hydrogen molecules and Ca ions in monolayer (1W), bilayer (2W) and trilayer (3W) hydrated Ca-mmt interlayer pores at 298 K and 120 bar are given in Figure 3.35. In the monolayer hydrated Ca-montmorillonite model, the H_2 molecules form a sharp peak in the center of the pore at 3.3 Å, H atoms

of water form a sharp peak at the same position as H_2 molecules with shouldering at 1.7 Å. O atoms of water form double peaks in the center of pore, one at 2.7 Å. Ca ions form two peaks around 2.1 Å in the center of pore (Figure 3.35a). As pore size and hydration level increases, two layers of O_{water} gets close to the surface forming sharper peaks, and H_2 molecules and H_{water} forms also two peaks closer to the surface at the same position as (O_{water} relative to the surface (Figure 3.13b) in bilayer hydrated Na-montmorillonite. Additionally, Ca ions remains mostly in the center; however, it also form two weaker peaks close to the surfaces (Figure 3.35b). Similar to Figure 3.13c, H_{water} atoms in the 3W-Na-mmt form two major peaks with a shoulder (at 1.4 Å) and a weaker peak in the middle of the pore at 2.9 and 6.8 Å, respectively. Moreover, O_{water} atoms and H_2 molecules exhibit two sharp peaks near the surfaces at 2.5 and 2.6 Å, respectively, both with weaker double peaks in the center of the pore. Ca ions form two peaks, one at 1.9 and the other at 3.9 Å, close to both surface making four peaks in total (Figure 3.35c). This shows that Ca ions are adsorbed close to the surface as two layers, unlike in 2W-Ca-mmt.

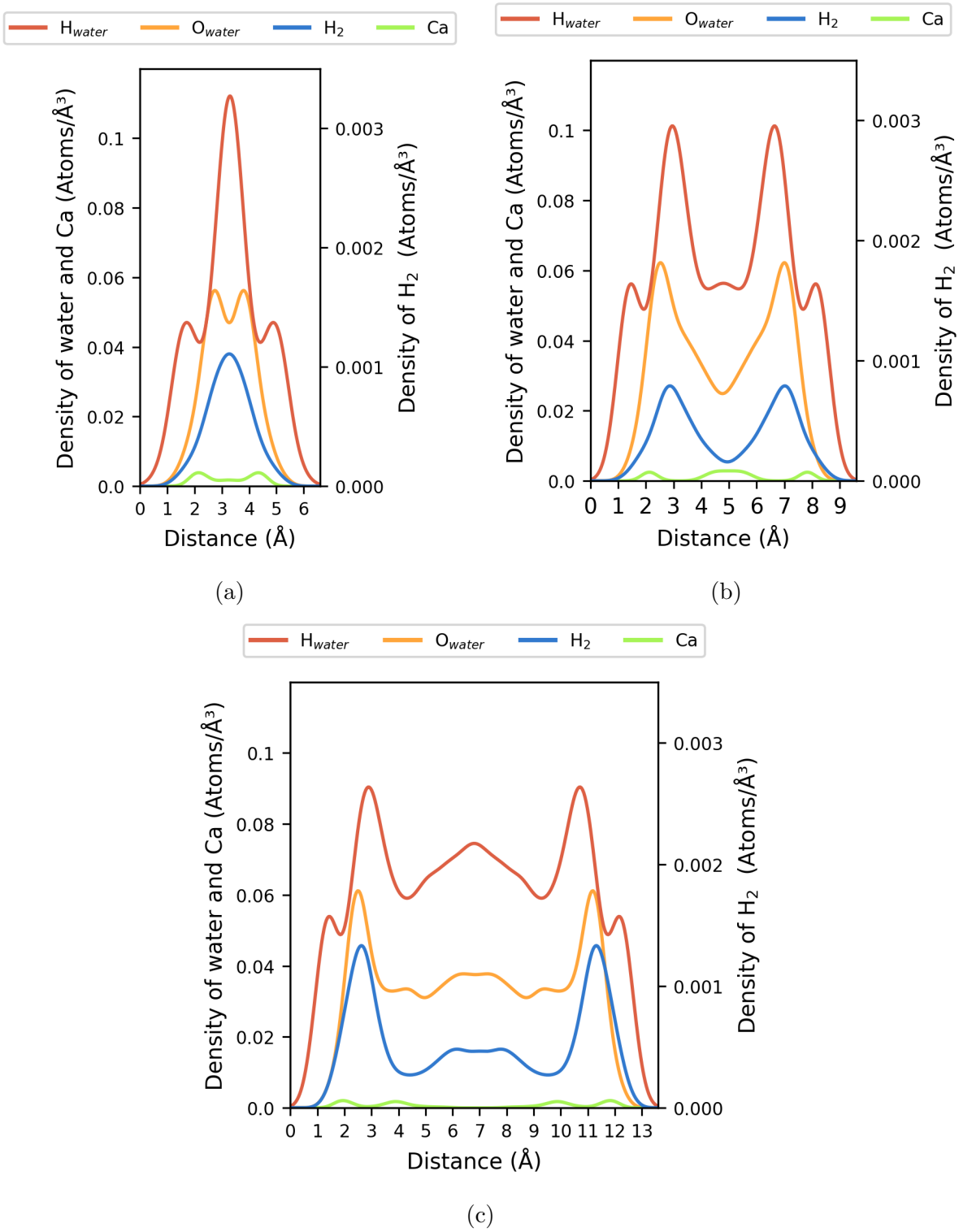

Figure 3.35 – Atomic density profiles of water hydrogen and oxygen atoms, and hydrogen molecules at 298 K and 120 bar on a) 1W-Ca-mmt, b) 2W-Ca-mmt and c) 3W-Ca-mmt

Radial distribution functions and running coordination numbers of H_2-Ca, H_2-Ob, H_2-Obts, and H_2-O_{water} pairs in 1W-Ca-mmt, 2W-Ca-mmt and 3W-Ca-mmt at 298 K and 120 bar are illustrated in Figure 3.36. At all 3 hydration levels, H_2-Ob pair shows its first maximum (r_{max}) around 3.2 Å. r_{min} of H_2-Ob pair is used to calculate the coordination numbers of atoms in the first shell of H_2. Coordination numbers of O atoms (CN_{Owater}) of water and clay (CN_{Ob} and CN_{Obts}), and Ca ions (CN_{Ca}) at the first shell of H_2 molecule are listed in Table 3.26. $N_{Total-O}$ indicates the total number of O atoms in the first shell of H_2. 1 H_2 molecule is surrounded by around 5, 9 and 8 water molecules in the interlayers of mono-, bi-, and tri-layer hydrated Ca-montmorillonites, respectively. The increase in pore size and, consequently, the amount of water causes an increase in the number of O_{water} atoms in the first shell of H_2. Nevertheless, there is no alteration for hydration level from bilayer to trilayer.

Table 3.26 – Coordination numbers of O atoms (O_{water}) of water and clay (Ob and Obts), and Ca ions at the first shell of H_2 molecule in 1W-Ca-mmt, 2W-Ca-mmt and 3W-Ca-mmt at 298 K and 120 bar

Model	$CN_{Total-O}$	$CN_{O_{water}}$	CN_{Ob}	CN_{Obts}	CN_{Ca}	r_{max}	r_{min}
1W-Ca-mmt	10.30	5.38	4.90	0.03	0.03	3.35	4.05
2W-Ca-mmt	12.59	9.05	3.47	0.07	0.07	3.15	4.25
3W-Ca-mmt	10.56	8.06	2.47	0.02	0.01	3.15	4.05

Figure 3.37 illustrates the orientation of H_2 molecules within the interlayers of 1W-Ca-mmt, 2W-Ca-mmt and 3W-Ca-mmt at 298 K and 120 bar. The results show that, regardless of hydration level or pore size, there is no preference or favored orientation for H_2 molecules in relation to the surface.

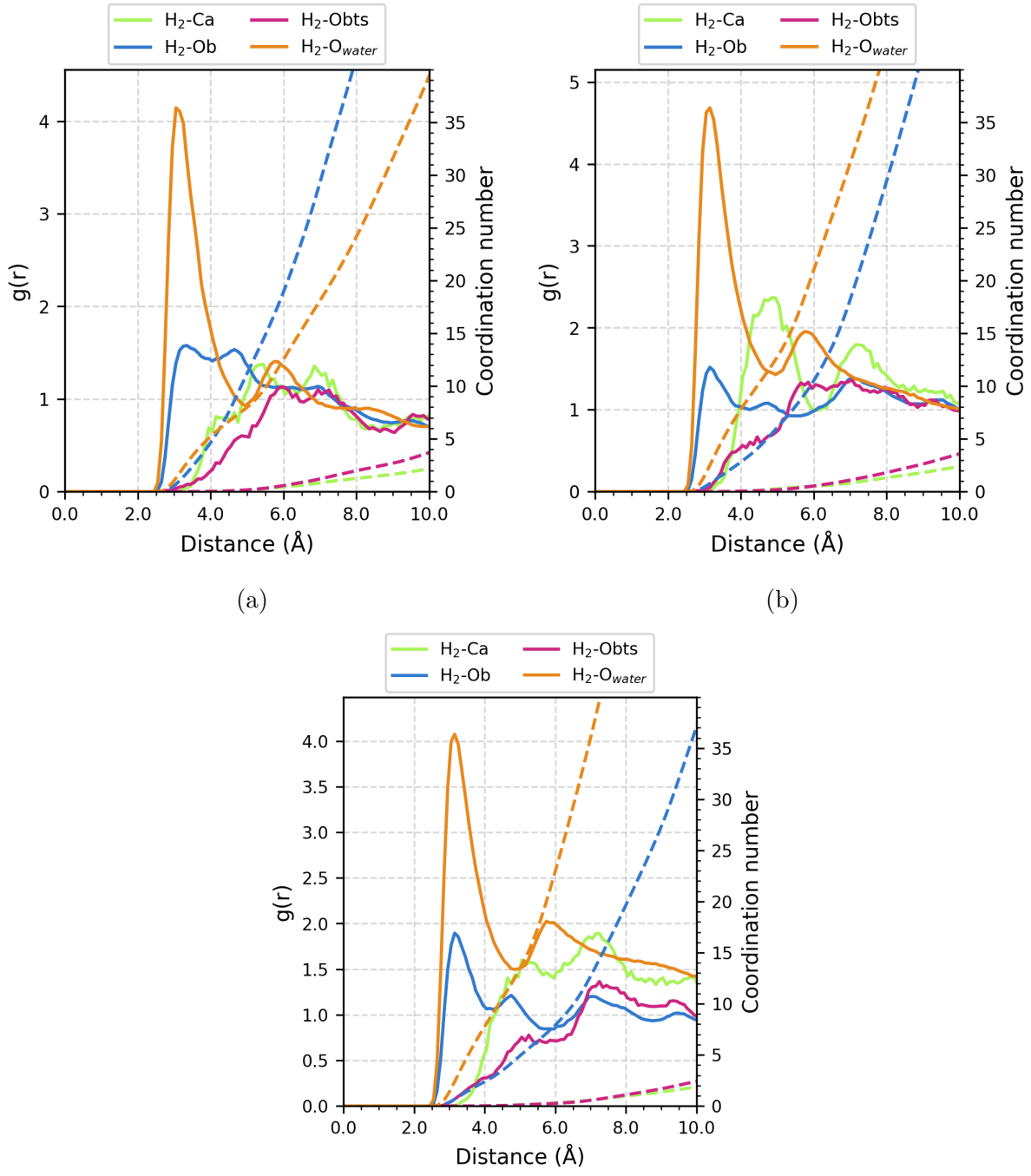

Figure 3.36 – Radial distribution functions and running coordination numbers of H_2-Na, H_2-Ob, H_2-Obts and H_2-O_{water} pairs in a) 1W-Ca-mmt, b) 2W-Ca-mmt and c) 3W-Ca-mmt at 298 K and 120 bar

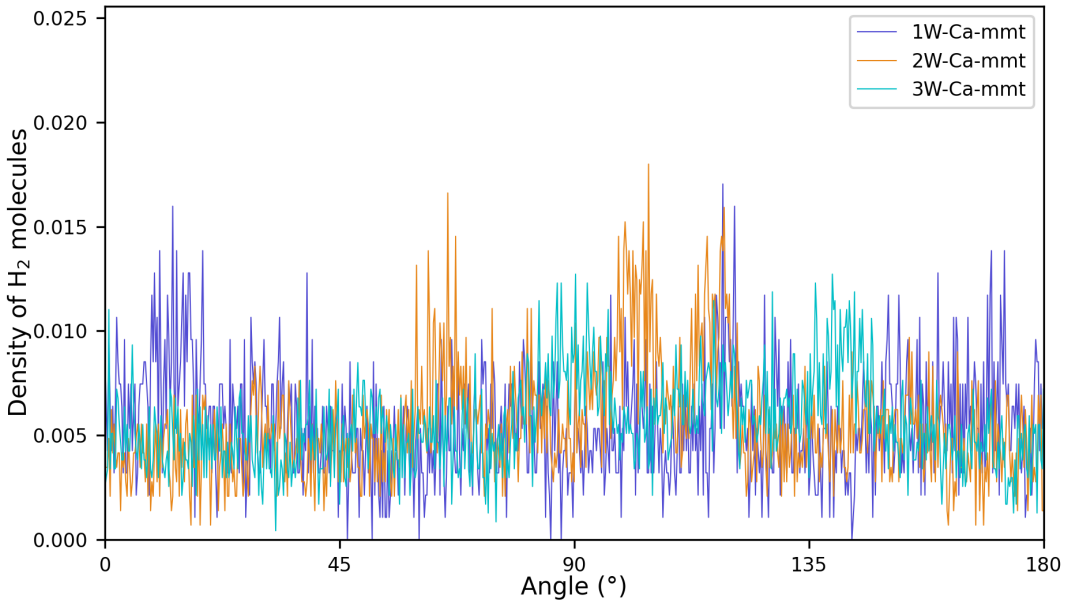

Figure 3.37 – The orientation of H_2 molecules within the interlayers of a) 1W-Ca-mmt, b) 2W-Ca-mmt and c) 3W-Ca-mmt at 298 K and 120 bar

3.3 H_2 adsorption on Cs-montmorillonite

In this section, effects of pore size/hydration level and water presence on H_2 adsorption in Cs-montmorillonite interlayers were investigated and discussed.

Table 3.27 – Summary of the simulations performed and discussed in Subsection 1-2

Hydration level	Temperature (K)	Pressure (bar)						
		1	20	40	60	80	100	120
0W	298	✓	✓	✓	✓	✓	✓	✓
1W	298	✓	✓	✓	✓	✓	✓	✓
2W	298	✓	✓	✓	✓	✓	✓	✓

The summary of the simulations performed are listed in Table 3.27, and discussed in Subsection 3.3.1. Moreover, H_2 adsorption and desorption in dry Cs-montmorillonite interlayers at high pressure (up to 10,000 bar) is investigated and discussed in Subsection 3.3.2. The interlayer cation was kept mobile, while the framework remained rigid in the simulations conducted in this section.

3.3.1 Effect of hydration level/pore size and water presence on H_2 adsorption

Hydrogen adsorption on dry, monolayer (1W) and bilayer (2W) hydrated Cs montmorillonite were performed at 298 K and up to 120 bar. Helium void fractions were calculated for dry, 1W and 2W-Cs-montmorillonites as 2, 23 and 41 %. Hydrogen adsorption isotherms are given in Figure 3.38. In dry Cs-montmorillonite model, hydrogen adsorption was unlike other dry Na- and Ca-montmorillonite models due to larger pore size. This shows that H_2 adsorption in clay interlayers is influenced by the presence of water, but it is not solely dependent on it. Moreover, the amount of H_2 adsorbed significantly increases with water presence and further rises with increasing water content. Amount of adsorbed hydrogen on dry, 1W- and 2W-Cs-mmt at 298 K up to 120 bar is given in Appendix E (Table E.2 - E.3).

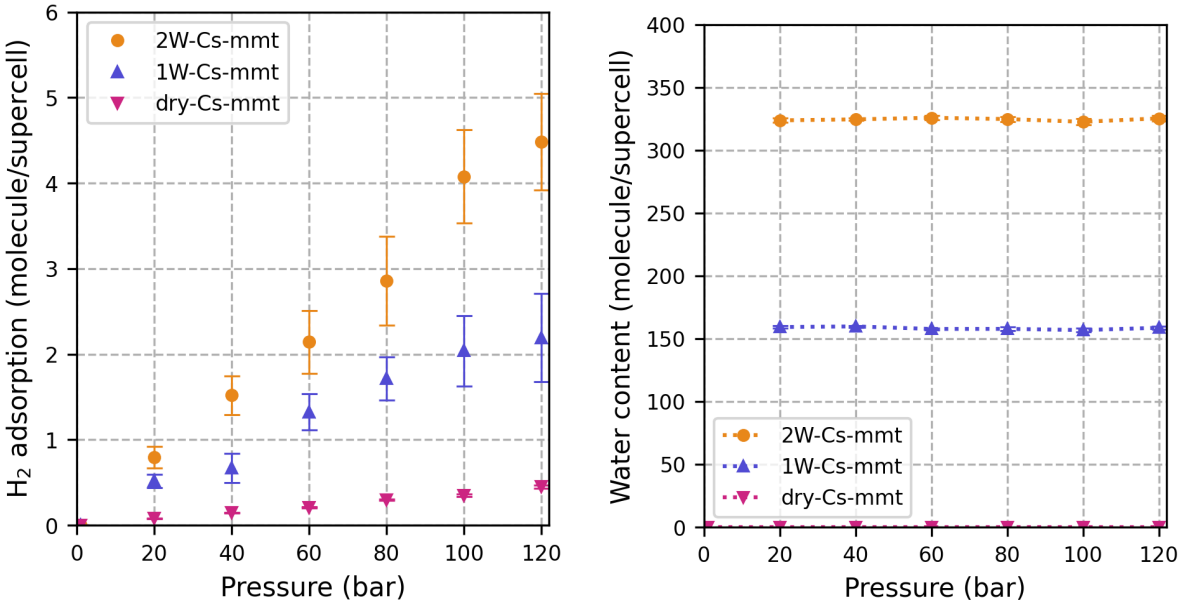

(a) (b)

Figure 3.38 – Adsorption isotherms of a) hydrogen and b) water on dry, 1W- and 2W-Cs-montmorillonites at 298 K

Tabulated simulation results of absolute and excess adsorption amounts of H_2 and water in mmol/g framework are given in Tables 3.28, 3.29 and 3.31. The results of H_2 adsorption on the 1W-Cs-mmt model at 298 K were compared with experimental results of Cs-

Table 3.28 – Adsorbed amount of H_2 and water content in 1W-Cs-mmt at 298 K up to 120 bar in mmol/g

Pressure (bar)	Adsorbed H_2 (mmol/g)			Water content (mmol/g)		
	Absolute	Excess	Error	Absolute	Excess	Error
1	0.000	0.000	0.000	-	-	-
20	0.020	0.018	0.002	6.080	1.233	0.021
40	0.025	0.023	0.005	6.099	1.252	0.018
60	0.051	0.047	0.002	6.022	1.175	0.019
80	0.065	0.060	0.001	6.024	1.178	0.040
100	0.078	0.071	0.003	5.988	1.142	0.028
120	0.084	0.076	0.011	6.057	1.211	0.030

Table 3.29 – Adsorbed amount of H_2 and water content in 2W-Cs-mmt at 298 K up to 120 bar in mmol/g

Pressure (bar)	Adsorbed H_2 (mmol/g)			Water content (mmol/g)		
	Absolute	Excess	Error	Absolute	Excess	Error
1	0.000	0.000	0.000	-	-	-
20	0.030	0.027	0.005	12.357	1.729	0.041
40	0.058	0.052	0.004	12.388	1.760	0.028
60	0.082	0.073	0.009	12.437	1.809	0.011
80	0.109	0.097	0.017	12.397	1.770	0.060
100	0.156	0.141	0.012	12.314	1.687	0.051
120	0.171	0.154	0.012	12.418	1.793	0.061

montmorillonite produced by Ziemiański and Derkowski (2022). Partially hydrated Cs-montmorillonite samples with a basal spacings of 11.3 Å showed that the total excess amount of adsorbed H_2 on Cs-montmorillonite is around 0.14 and 0.15 mmol/g at 100 bar for the samples with different water content. Although, it is challenging to make a one-to-one comparison directly with the adsorbed amounts in the interlayers, the excess amount of adsorbed H_2 in the interlayers of Cs-montmorillonite with the basal spacing of 13.05 is around 0.07 mmol/g at 100 bar (Table 3.28) in this work. This difference can be explained by higher water content. Moreover, the model used in the simulation does not have an external surface. Therefore, the adsorption value is the adsorbed amount only in the interlayers.

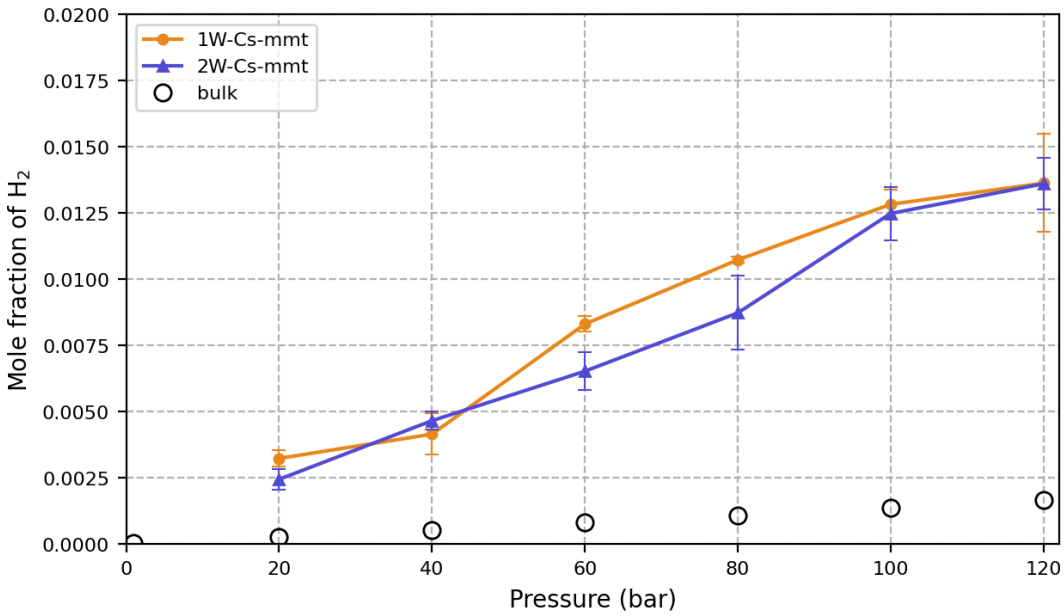

Figure 3.39 – Solubility of H_2 in the interlayers of 1W-Cs-mmt and 2W-Cs-mmt, and in bulk at 298 K. Bulk values (Table B.1 in Appendix B) at 298 K are taken from Rahbari et al., 2019; Wiebe and Gaddy, 1934.

The solubility of H_2 is investigated in the interlayers of mono- and bi-layer hydrated Cs-montmorillnoite at 298 K up to 120 bar (Figure 3.39). Both 1W-Cs-mmt and 2W-Cs-mmt leads the oversolubility in the interlayers. There is a small difference in mole fraction of H_2 between two models at 60 and 80 bar. However, the mole fractions remains similar between the models at other tested pressure levels. It folds approximately 8 times more in the interlayer of Cs-montmorillonite than in water, referred to as bulk.

The density profiles of hydrogen and oxygen of water, ydrogen molecules and Cs ions in dry, monolayer (1W) and bilayer (2W) hydrated Cs montmorillonite interlayer pores at 298 K and 120 bar are given in Figure 3.40. In dry model, both H_2 molecules and Cs are at the same position in the center of the pore around 2 Å (Figure 3.40a). It should be noted that there is not a single H_2 molecule at this condition. However, the analysis were done to be able to make a comparison with hydrated model. In the monolayer hydrated Cs-montmorillonite model, the H_2 molecules form a sharp peak in the center of the pore as similar to dry model, the O atoms of water form two peaks in the center of pore, and the H atoms of water form a sharp peak shouldering in the center (Figure 3.40b). Cs ions form two prominent peaks closer to the surfaces with a weaker peak in the center of the pore. The density of hydrogen molecules increases as the pressure increases. In

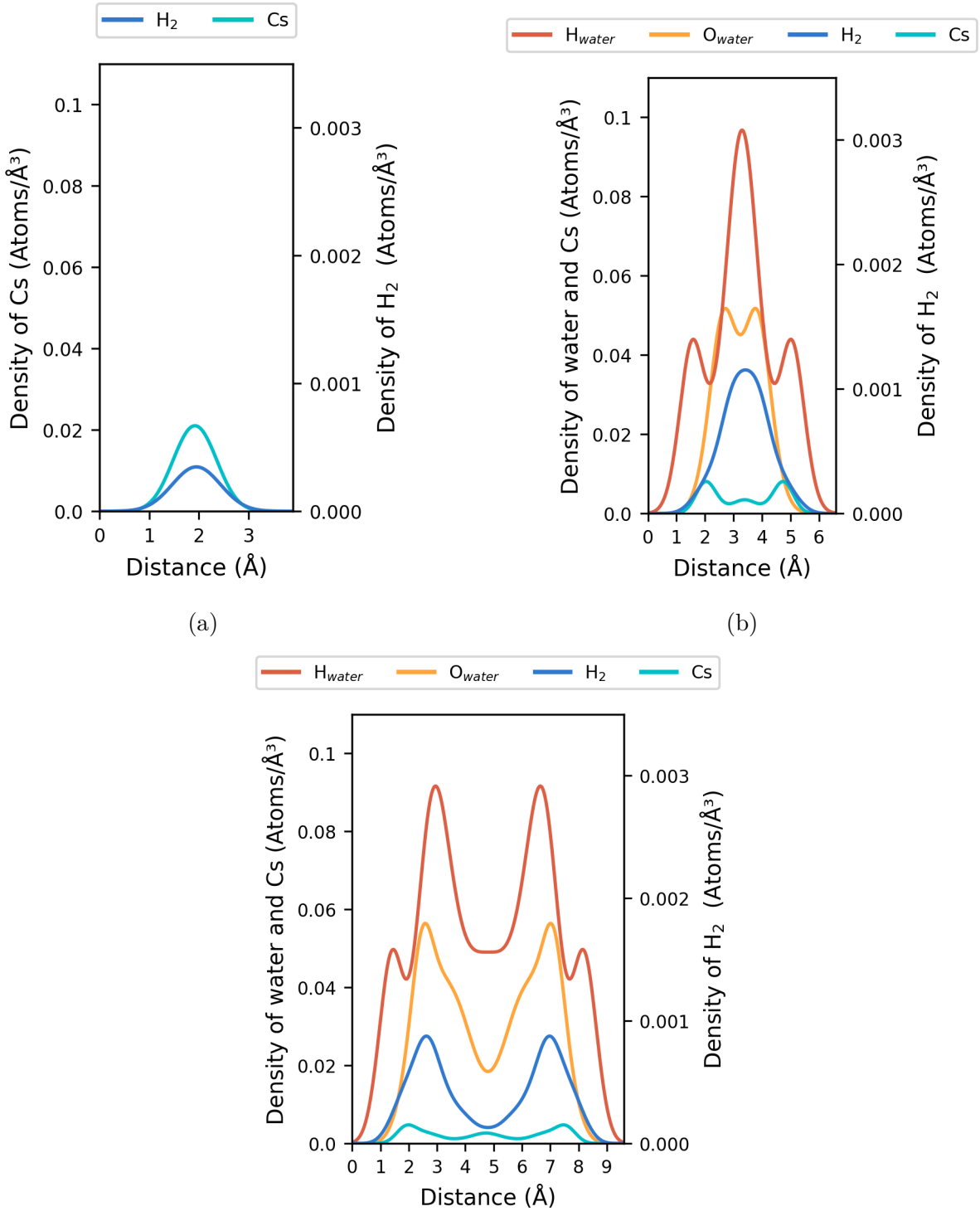

Figure 3.40 – Atomic density profiles of water hydrogen and oxygen atoms, and hydrogen molecules in a) dry-Cs-mmt, b) 1W-Cs-mmt and c) 2W-Cs-mmt at 298 K and 120 bar

the bilayer hydrated Cs-montmorillonite, H_2 molecules and O atoms of water molecules exhibit two peaks located at the same position relative to the surface while H atoms of water molecules form also two major peaks located at the same position relative to the surface with shouldering. Cs ions form two prominent peaks near to the surfaces with a weaker peak in the center of the pore (Figure 3.40c). To conclude, H_2 and water molecules are located at the same distance from the surface as Cs ions, regardless of water presence or pore size.

Table 3.30 – Coordination numbers of O atoms (O_{water}) of water and clay (Ob and Obts), and Cs ions at the first shell of H_2 molecule in 1W-Cs-mmt and 2W-Cs-mmt at 298 K and 120 bar

Model	$CN_{Total-O}$	$CN_{O_{water}}$	CN_{Ob}	CN_{Obts}	CN_{Cs}	r_{max}	r_{min}
1W-Cs-mmt	7.34	3.94	3.38	0.03	0.16	3.35	3.75
2W-Cs-mmt	11.27	7.58	3.64	0.06	0.21	3.25	4.15

Radial distribution functions and running coordination numbers of H_2-Cs, H_2-Ob, H_2-Obts, and H_2-O_{water} pairs in 1W-Cs-mmt and 2W-Cs-mmt at 298 K and 120 bar are showed in Figure 3.41. Coordination numbers of O atoms (CN_{Owater}) of water and clay (CN_{Ob} and CN_{Obts}), and Na ions (CN_{Cs}) at the first shell of H_2 molecule are presented in Table 3.30. $N_{Total-O}$ refers to the total number of O atoms in the first shell of H_2. The first maximum and minimum of H_2-Ob pair is defined as r_{max} and r_{min}, respectively. r_{min} of H_2-Ob pair is at 3.35 and 4.15 Å for monolayer (1W) and bilayer (2W) hydrated Cs-montmorillonite, respectively. They are used to calculate the coordination numbers of atoms in the first shell of H_2. A H_2 molecule is surrounded by around 4 and 8 water molecules in the interlayers of mono- and bi-, hydrated Cs-mmt, respectively. As pore size and hydration level increases the number of O_{water} in the first shell of H_2 due to increasing number of water molecules. In addition, the number of Ob in the first shell rises as hydration level and pore size decreases due to reducing pore distance. Although Cs^+ ions are at an equal distance from the surface (refer to Figure 3.40 for both H_2 and water, they are not found in the first sphere of hydrogen molecules.

Figure 3.42 presents the orientation of H_2 molecules within the interlayers of dry and, 1W and 2W hydrated Cs-mmt at 298 K and 120 bar. The results show that, regardless of either water presence or hydration level and pore size, there is no favored orientation for

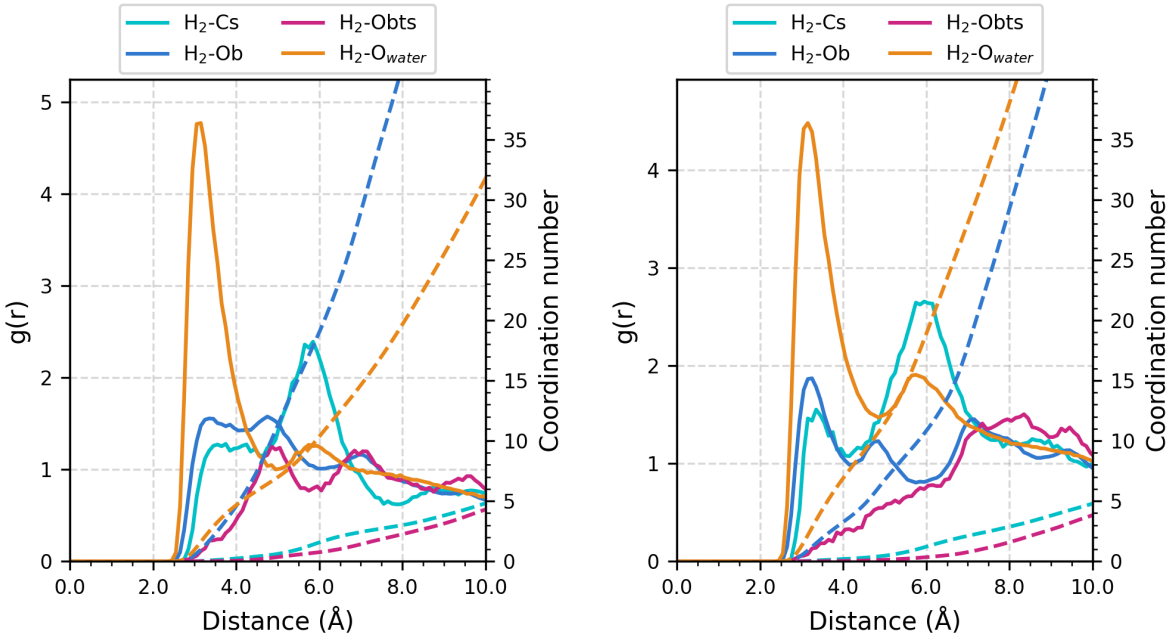

Figure 3.41 – Radial distribution functions and running coordination numbers of H_2-Cs, H_2-Ob, H_2-Obts and H_2-O_{water} pairs in a) 1W-Cs-mmt and b) 2W-Cs-mmt at 298 K and 120 bar

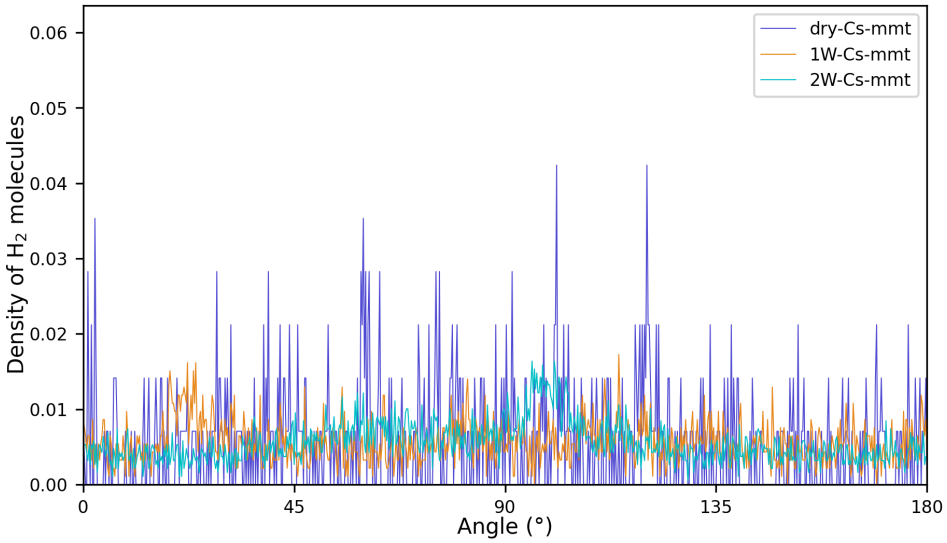

Figure 3.42 – The orientation of H_2 molecules within the interlayers of a) dry-Cs-mmt, b) 1W-Cs-mmt and c) 2W-Cs-mmt at 298 K and 120 bar

H_2 molecules within the interlayers of Cs-mmt related to its surface.

3.3.2 H_2 adsorption at high pressure on dry Cs-montmorillonite

Hydrogen adsorption and desorption on dry Cs-montmorillonite was performed at 298 K up to 10,000 bar to investigate the H_2 saturation capacity and H_2 adsorption isotherm is given in Figure 3.43. The isotherm illustrates a significant increase in the amount of adsorbed hydrogen as the pressure rises, eventually reaching saturation at approximately 7000 bar. Hysteresis is not observed similar to available hydrogen adsorption and desorption experiment in the literature (Ziemiański and Derkowski, 2022). Amount of adsorbed hydrogen both obtained by adsorption and desorption on dry-Cs-mmt at 298 K up to 1000 bar is given in Appendix E (Table E.4).

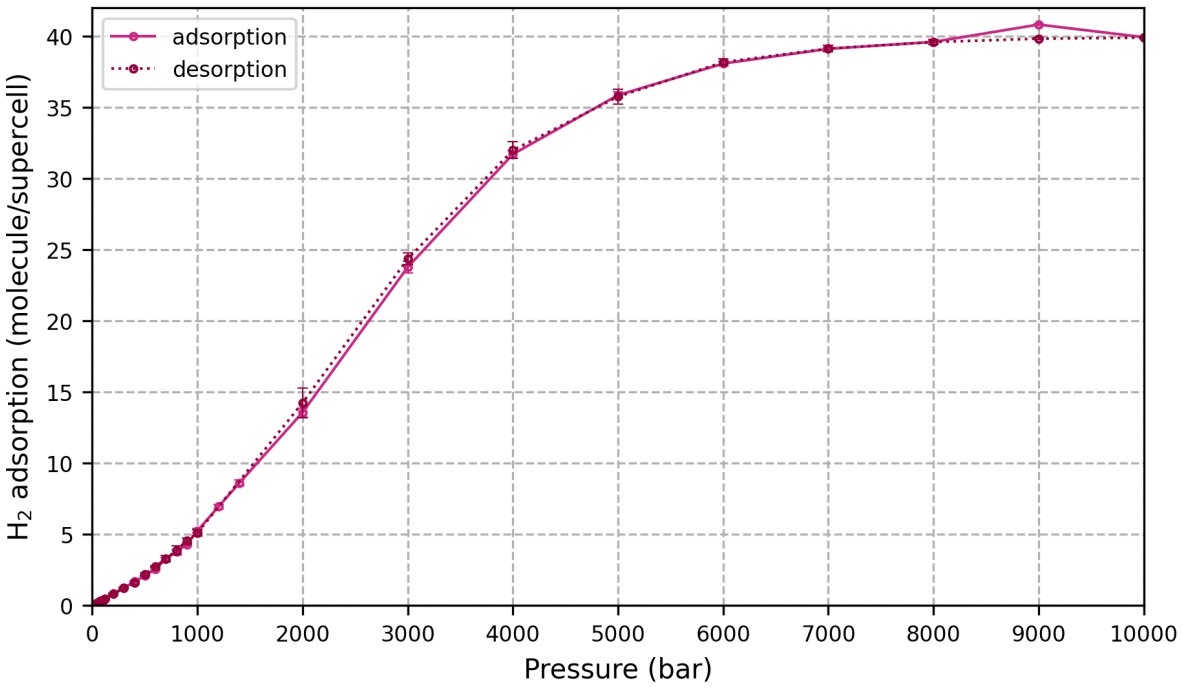

Figure 3.43 – H_2 adsorption isotherm on dry Cs-montmorillonites at 298K

The density profiles of hydrogen molecules and Cs ions in dry Cs-montmorillonite interlayer pores at 298 K and 120 bar are given in Figure 3.44. At both pressure levels, H_2 molecules and cesium ions are at the same position in the center of the pore around 2 Å. Density of H_2 increases rapidly as pressure increases to 500 bar.

Table 3.31 – Adsorbed and desorbed amount of H_2 in dry-Cs-mmt at 298 K in mmol/g

Pressure (bar)	Adsorbed H_2 (mmol/g)		Desorbed H_2 (mmol/g)	
	Absolute	Error	Absolute	Error
1	0.000	0.000	0.000	0.000
20	0.003	0.000	0.003	0.000
40	0.006	0.000	0.006	0.001
60	0.008	0.000	0.009	0.001
80	0.011	0.000	0.012	0.001
100	0.013	0.000	0.014	0.001
120	0.017	0.000	0.018	0.003
200	0.031	0.000	0.031	0.002
300	0.048	0.001	0.046	0.003
400	0.064	0.001	0.061	0.003
500	0.080	0.001	0.083	0.004
600	0.097	0.002	0.104	0.001
700	0.125	0.001	0.125	0.009
800	0.145	0.004	0.148	0.012
900	0.164	0.001	0.173	0.008
1000	0.200	0.002	0.195	0.009
1200	0.265	0.002	-	-
1400	0.329	0.002	-	-
2000	0.518	0.004	0.543	0.039
3000	0.908	0.007	0.930	0.016
4000	1.211	0.005	1.221	0.023
5000	1.369	0.003	1.365	0.020
6000	1.454	0.004	1.457	0.009
7000	1.493	0.001	1.494	0.008
8000	1.512	0.001	1.511	0.006
9000	1.558	0.000	1.521	0.002
10000	1.524	0.002	1.523	0.002

Radial distribution functions and running coordination numbers of H_2-Cs, H_2-Ob and H_2-Obts pairs in dry-Cs-mmt at 298 K and, 120 and 500 bar are illustrated in Figure 3.45. Coordination numbers of O atoms clay (CN_{Ob} and CN_{Obts}) and Na ions (CN_{Cs}) at the first shell of H_2 molecule in dry-Cs-mmt are also listed in Table 3.32. $N_{Total-O}$ indicates

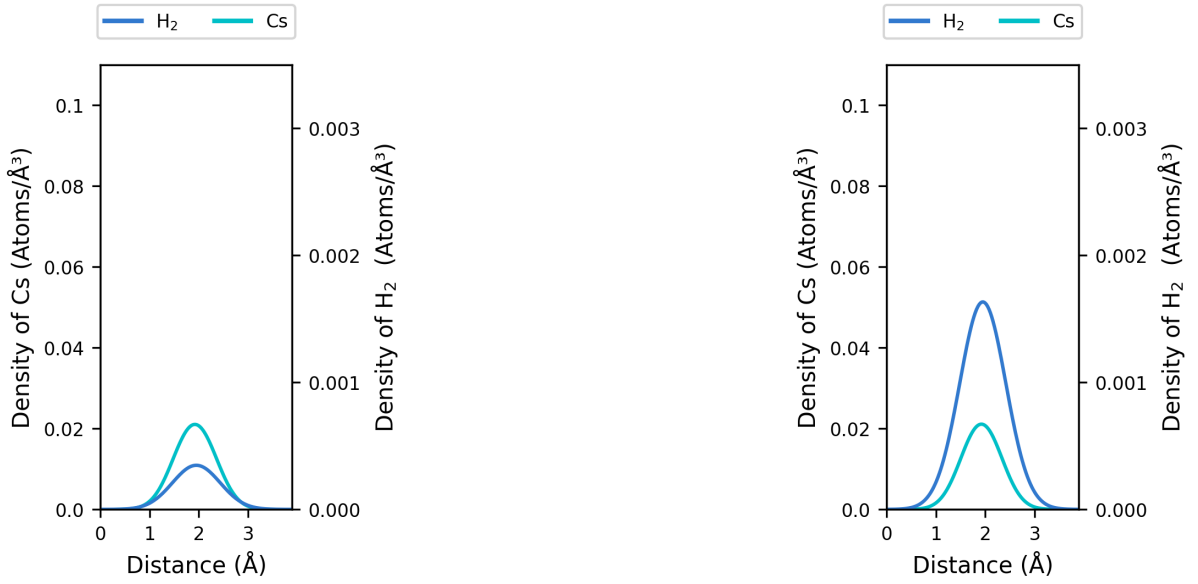

(a) (b)

Figure 3.44 – Atomic density profiles of H_2 molecules and Cs ions in dry-Cs-mmt, at 298 K and, a) 120 and 500 bar

Table 3.32 – Coordination numbers of O atoms of clay (Ob and Obts), and Cs ions at the first shell of H_2 molecule in dry-Cs-mmt at 298 K and, 120 and 500 bar

Temperature (K)	Pressure (bar)	$CN_{Total-O}$	CN_{Ob}	CN_{Obts}	CN_{Cs}	r_{max}	r_{min}
298	120	11.90	11.36	0.54	0.06	3.15	4.15
298	500	11.94	11.40	0.54	0.01	3.15	4.15

the total number of Ob and Obts atoms in the first shell of H_2. The first maximum and minimum of H_2-Ob pair is defined as r_{max} and r_{min}, respectively. At two different pressure levels, H_2-Ob pair shows its first maximum at a distance of 3.15 Å. r_{min} of H_2-Ob pair at 4.15 Å is used to calculate the coordination numbers of atoms in the first shell of H_2. One H_2 molecule is encompassed by around 11 O atoms of siloxanes which is reasonable given the very small pore size leading to coordination with the oxygens on the both surface. However, Cs ions are not present at the first coordination sphere of H_2.

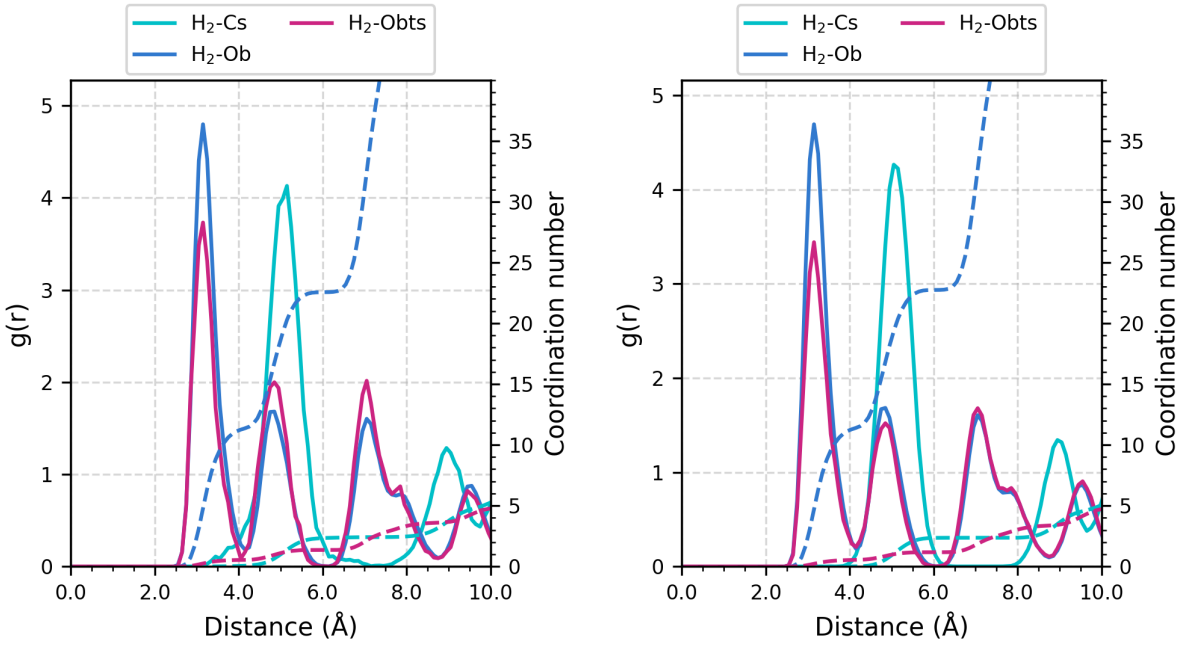

Figure 3.45 – Radial distribution functions and running coordination numbers of H_2-Cs, H_2-Ob, H_2-Obts and H_2-O_{water} pairs in dry-Cs-mmt, at 298 K and, a) 120 and 500 bar

3.4 Effect of interlayer cations on H_2 adsorption

In this section, the results of hydrogen adsorption on Na-,Ca-, and Cs-montmorillonite are investigated to understand the effect of interlayer cation type. Isotherms of hydrogen adsorption on monolayer hydrated Na-, Ca- and Cs-montmorillonites are given in Figure 3.46, and bilayer hydrated Na-, Ca- and Cs-montmorillonites are given in Figure 3.47.

Among the various cations investigated, calcium exhibited the higher level of hydrogen adsorption (Figure 3.46). This can be attributed to the smaller volume occupied by calcium within the pore than the other cations, thereby creating a more available space (29%) for hydrogen molecules to adsorb in the interlayers of 1W-Ca-mmt. This difference becomes more pronounced with increasing pressure. Following this trend, 1W-Cs-mmt exhibits a higher amount of hydrogen adsorption at pressure levels below 120 bar, indicating that the presence of Cs cations enhances hydrogen adsorption compared to Na cations in their respective models. However, at 120 bar, there is no noticeable difference between monolayer hydrated Na- and Cs-mmt, which have void spaces of 25% and 23%,

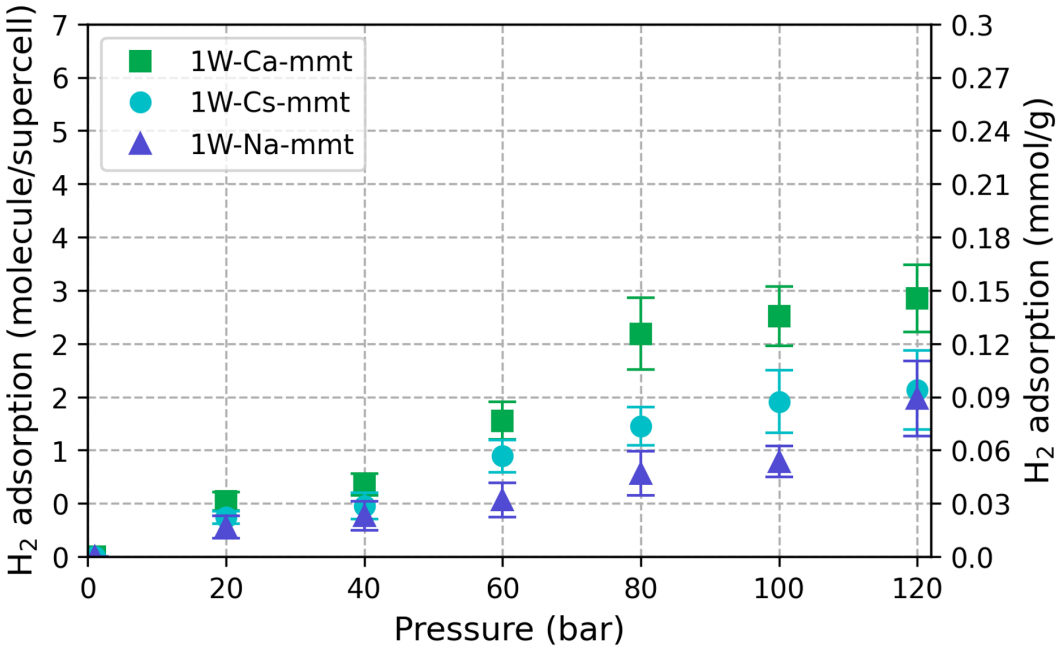

Figure 3.46 – Hydrogen adsorption on 1W-Na-mmt, 1W-Ca-mmt and 1W-Cs-mmt at 298 K

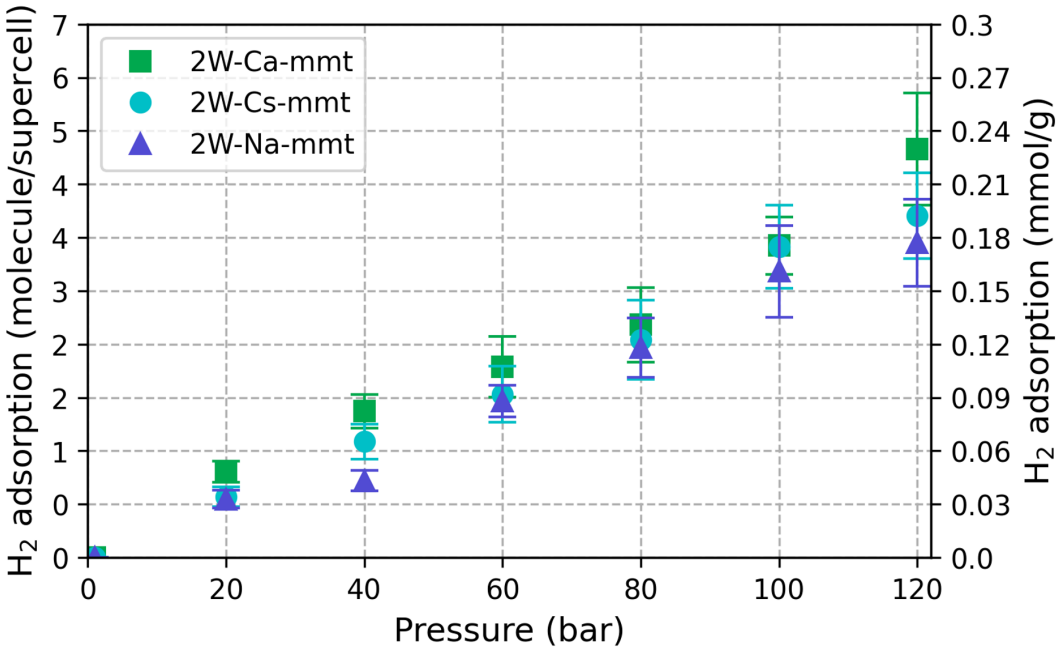

Figure 3.47 – Hydrogen adsorption isotherms of 2W-Na-mmt (rigid and mobile Na), 2W-Ca-mmt and 2W-Cs-mmt at 298 K

respectively. Figure 3.47 shows that there is no interlayer cation effect in more hydrated model. Furhermore, interlayer cation type has no significant impact on the molar ratio of H_2/H_2O (refer to Figure 3.12, 3.34 and 3.39).

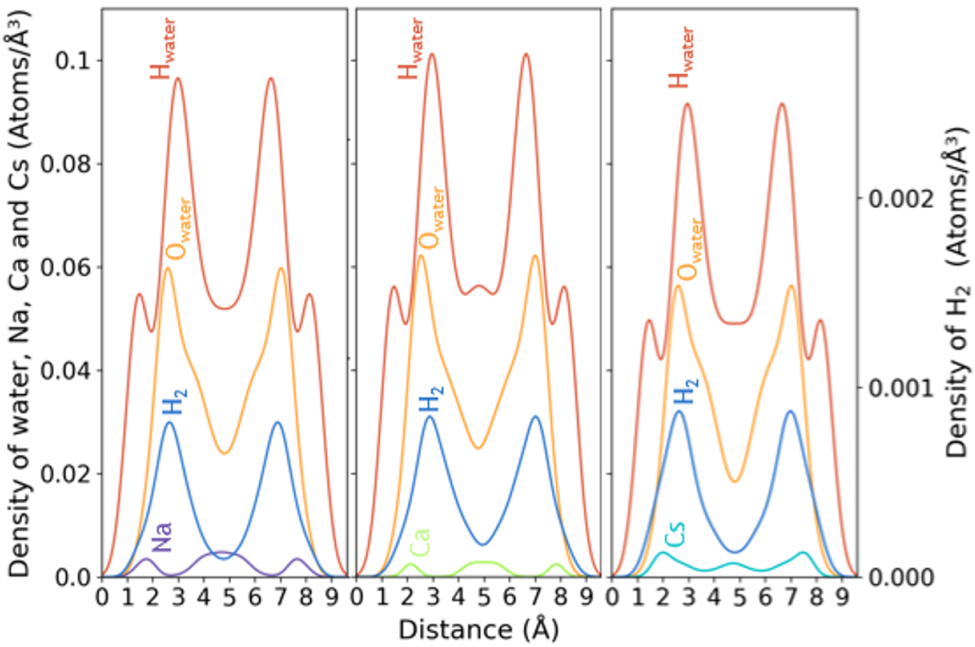

Figure 3.48 – Atomic density profiles of hydrogen molecules in the interlayers of 2W-Na-mmt, 2W-Ca-mmt and 2W-Cs-mmt

The atomic density profiles of hydrogen and oxygen of water, hydrogen molecules and, sodium, calcium and cesium ions in the bilayer hydrated Na-, Ca- and Cs-montmorillonite are given in Figure 3.48. The atomistic density profiles indicate that within the pores, Na and Ca ions are predominantly situated in the center of the pore, whereas Cs ions tend to be primarily located near the surface.

The surface atomic density maps are given in Figure 3.49. The color legend in the figure assigns black to H_2 molecules, orange to H_2O molecules, purple to Na ions, green to Ca ions, light blue to Cs ions, dark blue to Si atoms, and pink to Al atoms. Figures 3.49b, d, and f reveal that Na, Ca, and Cs ions are hydrated. Figure 3.49a indicates that Na ions are preferentially adsorbed near the tetrahedral substitutions (Si atoms replaced by Al atoms). Figure 3.49a indicates that Na ions tend to be preferentially adsorbed near tetrahedral substitutions (Si atoms replaced by Al atoms). Consequently, they inhibit hydrogen adsorption near Al substitutions. Figure 3.49c illustrates that some of the Ca

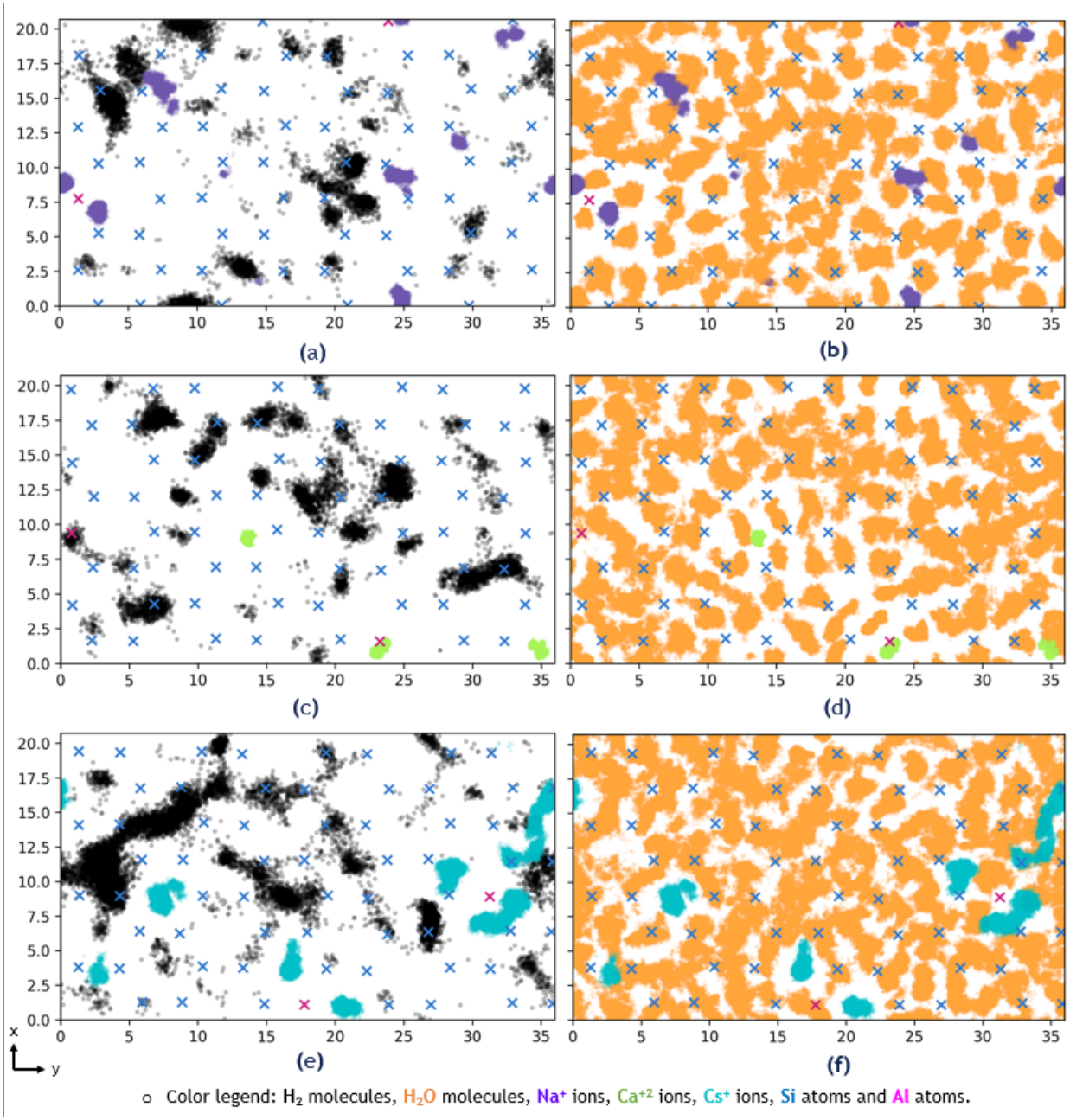

Figure 3.49 – Surface atomic distribution of hydrogen molecules a) 2W-Na-mmt, c) 2W-Ca-mmt, e) 2W-Cs-mmt and water oxygen atoms at b) 2W-Na-mmt, d) 2W-Ca-mmt, f) 2W-Cs-mmt at 298 K and 120 bar. Color legend: H_2 molecules (black), H_2O molecules (orange), Na ions (purple), Si atoms (blue) and Al atoms (pink)

ions are adsorbed near one of the Al substitutions, while the other one remains unoccupied. This indicates that there is no preferential location for Ca ions on the surface. Moreover,

some hydrogen molecules are observed close to the unoccupied Al substitution. Cs ions are mostly located within the hexagonal cavities of the clay surface (Figure 3.49) csimilarly observed by Ngouana W. and Kalinichev (2014). Interestingly, hydrogen molecules also preferentially adsorb on these hexagonal cavities. It is noteworthy that both Cs ions and hydrogen molecules are situated at the same distance from the surface (refer to Figure 3.48). Therefore, this implies that there is a competition for surface occupancy between Cs ions and H_2 molecules.

CONCLUSIONS

Previous atomistic simulations of gas adsorption and transport in clays were mostly focused on CO_2 and CH_4 adsorption and diffusion. The interest in CO_2 arises from its role in climate change and in developing carbon capture and storage technologies. CH_4, on the other hand, has been the subject of extensive research due to its significance in energy production, particularly in the context of shale gas extraction. Although there are few studies on CO_2-CH_4 and CO_2-CH_4-H_2O mixtures, gas adsorption processes are usually investigated for single components instead of gas mixtures. CH_4 and CO_2 adsorption are usually taken into account together since they illustrate comparative adsorption behavior in clay mineral pores. However, it is essential to note that the investigation of molecular hydrogen (H_2) adsorption in clay minerals has been relatively rare in comparison. This poor attention to H_2 is noteworthy, considering its prevalence as the most abundant gas in the context of deep geological radioactive waste disposal and storage. Understanding how H_2 interacts with clay materials is crucial for ensuring the safety and effectiveness of long-term storage solutions and strategies for radioactive waste.

Although there are a few experimental studies on hydrogen adsorption, simulations are usually focused on hydrogen diffusion in clay rather than its uptake. Therefore, there is a lack of literature on H_2 uptake in clays in temperature and pressure ranges that are typically expected to develop in repositories. To address these shortcomings, in this thesis, we presented a detailed quantitative investigation of the adsorption mechanisms of molecular hydrogen, H_2, in models of Callovo-Oxfordian clay rock by means of Monte Carlo and hybrid Monte Carlo/molecular dynamics computer simulations. This will help to develop reliable long-term strategies aimed at preventing chemical and mechanical destabilization of the radioactive waste repositories.

Within the scope of this thesis, findings can be summarized as follows:

— H_2 gas adsorption exhibits a proportional increase with increasing pressure, while a decrease is observed with increasing temperature in accordance with the solubility behavior of hydrogen gas in water.

— The amount of adsorbed hydrogen increases proportionally with the increase in pore size and hydration level.

— Hydrogen adsorption does not occur in the dry Na- and Ca- montmorillonite models due to their small pore size whereas it does occur in the dry Cs-montmorillonite.

— H_2 adsorption is not directly dependent on the presence of water; nevertheless, the amount of adsorbed hydrogen does increase with higher water content.

— In the monolayer hydrated Ca-montmorillonite model, a higher amount of H_2 is adsorbed compared to monolayer hydrated Na-montmorillonite and Cs-montmorillonite models due to difference in the void volume within the interlayer pores. However, there is no effect of interlayer cation type in bilayer hydrated models.

— The mole fraction of adsorbed hydrogen within the interlayers of hydrated clays exhibits over-solubility in comparison to its solubility in water due to the strong interaction of H_2 with clay surface. The magnitude of this difference becomes even more pronounced as the pressure increases. In the bilayer hydrated models at 298 K and 120 bar, the mole fraction of hydrogen is approximately 7 to 8 times greater than that of their respective solubility in bulk water. However, interlayer cation type has no significant impact on the ratio of H_2/H_2O.

— In the interlayers of monolayer hydrated montmorillonite, both hydrogen and water molecules tend to adsorb at the middle of the pore. Specifically, hydrogen molecules create a distinct peak at 3.3 Å distance relative to the surface, and the oxygen atoms of water molecules form a double peak, one being at 2.7 Å distance relative to the surface, all occurring at the same location due to the small pore size. Moreover, the hydrogen of the water forming a peak at 3.3 Å with a shoulder at 1.6 Å shows that one of the hydrogen atoms are positioned towards the surface.

— In the interlayers of bilayer hydrated montmorillonite, a different pattern emerges, where both hydrogen molecules and water molecules exhibit two peaks, the first ones being at approximately 2.7 Å distance relative to the surface (depending on the temperature, pressure and also interlayer cation type), and these peaks are positioned at the same relative location with respect to the surface.

— Within the interlayers of trilayer hydrated montmorillonite models, a similar distribution is observed as in bilayers, with hydrogen and water molecules primarily located near the surface. However, they also form weaker peaks at 6.8 Å in the center of the pore. This is attributed to the larger pore size.

— Atomic density profiles show that Na and Ca ions are mostly located in the center of the pores in bilayer hydrated montmorillonite. Moreover, Ca ions has the adsorption layers in the middle of the pore in monolayer montmorillonite while its adsorption layers are closer to the surface in trilayer hydrated montmorillonite. On the other hand, Cs ions are mostly located near to the surface at any hydration level and they are adsorbed in the middle of the pore in dry montmorillonite.

— Atomic surface density maps demonstrate Na ions tend to be preferentially adsorbed near tetrahedral substitutions, inhibiting hydrogen adsorption near the substitutions. Some Ca ions are adsorbed near one of the Al substitutions, while the other remains unoccupied, suggesting no preferential location for Ca ions on the surface. Both Cs ions and hydrogen molecules are predominantly located within the hexagonal cavities of the clay surface.

— Radial distribution functions show that there is no interlayer cation present in the first coordination sphere of H_2 molecule. The number of oxygens of water molecules and siloxane increases as hydration level rises.

— In any model with different cations, the hydrogen molecules have no specific orientation with respect to the surface regardless of temperature, pressure, hydration level and interlayer cation type. Considering that the tri-site H_2 model was used, this indicates that the atomic charge distribution in the model has no effect on the adsorption of hydrogen on the clay surface.

— In the deep geological radioactive waste repository, under the anticipated range of pressure and temperature conditions, the saturation of H_2 is not achievable. This indicates that H_2 does not pose a risk of pressure build-up within the expected and studied conditions.

— Furthermore, the results of H_2 adsorption at high pressure in both hydrated and dry montmorillonite contribute to improving strategies for hydrogen storage applications.

In the light of the findings of this thesis, future perspectives may enhance the understanding of H_2 adsorption in clay environments within the context of radioactive waste disposal and storage. Direct comparison with experimental results may enable one-to-one comparisons, which are not available at the moment. Moreover, conducting grand canonical Monte Carlo simulations of binary adsorption of H_2 and water on other clay types, such as illite, which has a higher charge than montmorillonite used in this work, would provide more insights into H_2 adsorption on other types of clays. Furthermore, GCMC simulations of H_2 adsorption within the interlayers of montmorillonite with pre-adsorbed water ensure distinct unsaturated conditions, which might provide better understanding as well as estimation for the adsorbed amount of H_2, more closely resembling real conditions. Additionally, performing GCMC simulations of binary and ternary gas mixtures of H_2 with other gases (such as CO_2 and/or CH_4) in both fully saturated and unsaturated conditions may provide valuable insights into the real environment of radioactive waste repositories. However, this may require additional Monte Carlo simulations using Gibbs ensemble to accurately determine reservoir composition. Lastly, performing molecular dynamics simulations using the data obtained using GCMC simulations in this thesis could prove invaluable in validating the results of GCMC simulations and analyzing H_2 adsorption and diffusion dynamics.

BIBLIOGRAPHY

Alavi, S., Ripmeester, J. A., & Klug, D. D., (2005), Molecular-dynamics study of structure II hydrogen clathrates, *Journal of Chemical Physics*, *123 2*, https://doi.org/10.1063/1.1953577

Alavi, S., Ripmeester, J. A., & Klug, D. D., (2006), Molecular-dynamics simulations of binary structure II hydrogen and tetrahydrofurane clathrates, *Journal of Chemical Physics*, *124 1*, 1–6, https://doi.org/10.1063/1.2141506

ANDRA, (2005a), *Dossier 2005 argile - phenomenological evolution of a geological repository.*

ANDRA, (2005b), *Dossier 2005 argile: architecture and management of a geological repository.*

ANDRA, (2021a), National inventory of radioactive materials and waste - essentials 2021, http://www.andra.fr/download/andra-international-en/document/editions/459.pdf

ANDRA, (2021b), Strategic vision of future scientific and technological rd at andra - major thematic orientations.

Article l542-1-1 - code de l'environnement - légifrance [Last accessed 19 April 2023], (2016), https://www.legifrance.gouv.fr/codes/article_lc/LEGIARTI000032043680

Bailey, S., (1988), *Hydrous phyllosilicates: (exclusive of micas)*, Mineralogical Society of America.

Bardelli, F., Mondelli, C., Didier, M., Vitillo, J. G., Cavicchia, D. R., Robinet, J.-C., Leone, L., & Charlet, L., (2014), Hydrogen uptake and diffusion in callovo-oxfordian clay rock for nuclear waste disposal technology [Geochemistry for Risk Assessment: Hazardous waste in the Geosphere], *Applied Geochemistry*, *49*, 168–177, https://doi.org/https://doi.org/10.1016/j.apgeochem.2014.06.019

Berendsen, H. J., Grigera, J. R., & Straatsma, T. P., (1987), The missing term in effective pair potentials, *Journal of Physical Chemistry*, *91 24*, 6269–6271, https://doi.org/10.1021/j100308a038

Berendsen, H., Postma, J., van Gunsteren, W., & Hermans, J., (1981), Interaction models for water in relation to protein hydration, https://doi.org/10.1007/978-94-015-7658-1_21

Bergaya, F., Theng, B., & Lagaly, G., (2006), *Handbook of clay science* (Vol. 1), Elsevier, https://books.google.fr/books?id=uVbam9Snw5sC

Berlepsch, T. V., & Haverkamp, B., (2016), Salt as a host rock for the geological repository for nuclear waste, *Elements*, *12*, 257–262, https://doi.org/10.2113/gselements.12.4.257

Boek, E. S., Coveney, P. V., & Skipper, N. T., (1995), Monte Carlo Molecular Modeling Studies of Hydrated Li-, Na-, and K-Smectites: Understanding the Role of Potassium as a Clay Swelling Inhibitor, *Journal of the American Chemical Society*, *11750*, 12608–12617, https://doi.org/10.1021/ja00155a025

Boinepalli, S., & Attard, P., (2003), Grand canonical molecular dynamics, *Journal of Chemical Physics*, *119 24*, 12769–12775, https://doi.org/10.1063/1.1629079

Botan, A., Rotenberg, B., Marry, V., Turq, P., & Noetinger, B., (2010), Carbon Dioxide in Montmorillonite Clay Hydrates: Thermodynamics, Structure, and Transport from Molecular Simulation, *J. Phys. Chem.*, *114*, 14962–14969.

Braun, E., Gilmer, J., Mayes, H. B., Mobley, D. L., Monroe, J. I., Prasad, S., & Zuckerman, D. M., (2019), Best practices for foundations in molecular simulations [article v1.0], *Living Journal of Computational Molecular Science*, *1*, 5957, https://doi.org/10.33011/livecoms.1.1.5957

Buch, V., (1994), Path integral simulations of mixed para-D2 and ortho-D2 clusters: The orientational effects, *6 May*, 7610–7629.

Charlet, L., Alt-Epping, P., Wersin, P., & Gilbert, B., (2017), Diffusive transport and reaction in clay rocks: a storage (nuclear waste, co2, h2), energy (shale gas) and water quality issue [Tribute to Professor Garrison Sposito: An Exceptional Hydrologist

and Geochemist], *Advances in Water Resources*, *106*, 39–59, https://doi.org/https://doi.org/10.1016/j.advwatres.2017.03.019

Cracknell, R. F., (2001), Molecular simulation of hydrogen adsorption in graphitic nanofibres, *Physical Chemistry Chemical Physics*, *311*, 2091–2097, https://doi.org/10.1039/b100144m

Creutz, M., (1983), Microcanonical monte carlo simulation, *Phys. Rev. Lett.*, *50*, 1411–1414, https://doi.org/10.1103/PhysRevLett.50.1411

Cygan, R. T., Greathouse, J. A., Heinz, H., & Kalinichev, A. G., (2009), Molecular models and simulations of layered materials, *Journal of Materials Chemistry*, *19*, 2470–2481, https://doi.org/10.1039/b819076c

Cygan, R. T., Liang, J. J., & Kalinichev, A. G., (2004), Molecular models of hydroxide, oxyhydroxide, and clay phases and the development of a general force field, *Journal of Physical Chemistry B*, *1084*, 1255–1266, https://doi.org/10.1021/jp0363287

Cygan, R. T., Romanov, V. N., & Myshakin, E. M., (2012), Molecular simulation of carbon dioxide capture by montmorillonite using an accurate and flexible force field, *The Journal of Physical Chemistry C*, *11624*, 13079–13091, https://doi.org/10.1021/jp3007574

Darkrim, F., & Levesque, D., (1998), Monte Carlo simulations of hydrogen adsorption in single-walled carbon nanotubes, *Journal of Chemical Physics*, *10912*, 4981–4984, https://doi.org/10.1063/1.477109

Didier, M., Leone, L., Greneche, J.-M., Giffaut, E., & Charlet, L., (2012), Adsorption of hydrogen gas and redox processes in clays, *Environmental science technology*, *46*, 3574–9, https://doi.org/10.1021/es204583h

Ding, L., & Yazaydin, A. O., (2013), Hydrogen and methane storage in ultrahigh surface area Metal-Organic Frameworks, *Microporous and Mesoporous Materials*, *182*, 185–190, https://doi.org/10.1016/j.micromeso.2013.08.048

Dubbeldam, D., Calero, S., Ellis, D. E., & Snurr, R. Q., (2016), Raspa: molecular simulation software for adsorption and diffusion in flexible nanoporous materials, *Molecular Simulation*, *422*, 81–101, https://doi.org/10.1080/08927022.2015.1010082

Dubbeldam, D., Torres-Knoop, A., & Walton, K. S., (2013), On the inner workings of monte carlo codes, *Molecular Simulation*, *39 14-15*, 1253–1292, https://doi.org/10.1080/08927022.2013.819102

Düren, T., Sarkisov, L., Yaghi, O. M., & Snurr, R. Q., (2004), Design of new materials for methane storage [PMID: 15835137], *Langmuir*, *20 7*, 2683–2689, https://doi.org/10.1021/la0355500

Eddaoudi, M., Li, H., & Yaghi, O. M., (2000), Highly porous and stable metalorganic frameworks: structure design and sorption properties, *Journal of the American Chemical Society*, *122 7*, 1391–1397, https://doi.org/10.1021/ja9933386

Edge, J., (2014), *Hydrogen adsorption and dynamics in clay minerals*, http://discovery.ucl.ac.uk/1462102/1/Jacqueline%20Edge%20Thesis%5C%5B1%5C%5D.pdf

Ewing, R. C., Whittleston, R. A., & Yardley, B. W., (2016), Geological disposal of nuclear waste: a primer, *Elements*, *12*, 233–237, https://doi.org/10.2113/gselements.12.4.233

Ford, D., Dubbeldam, D., Snurr, R., Künzel, V., Wehring, M., Stallmach, F., Kärger, J., & Müller, U., (2012), Self-diffusion of chain molecules in the metal–organic framework irmof-1: simulation and experiment, *The Journal of Physical Chemistry Letters*, *3*, 930–933, https://doi.org/10.1021/jz300141n

Frenkel, D., & Smit, B., (1996), *Understanding molecular simulation: from algorithms to applications*.

Gadikota, G., Dazas, B., Rother, G., Cheshire, M. C., & Bourg, I. C., (2017), Hydrophobic solvation of gases (co2, ch4, h2, noble gases) in clay interlayer nanopores, *Journal of Physical Chemistry C*, *121*, 26539–26550, https://doi.org/10.1021/acs.jpcc.7b09768

Garberoglio, G., Skoulidas, A. I., & Johnson, J. K., (2005), Adsorption of gases in metal organic materials: Comparison of simulations and experiments, *Journal of Physical Chemistry B*, *109 27*, 13094–13103, https://doi.org/10.1021/jp050948l

Ghasemi, M., Omrani, S., Mahmoodpour, S., & Zhou, T., (2022), Molecular dynamics simulation of hydrogen diffusion in water-saturated clay minerals; implications for

Underground Hydrogen Storage (UHS), *International Journal of Hydrogen Energy*, *47 59*, 24871–24885, https://doi.org/10.1016/j.ijhydene.2022.05.246

Gillespie, P. C., & Wilson, G. M., (1980), Vapor-liquid equilibrium data on water-substitute gas components: n/sub 2/-h/sub 2/o, h/sub 2/-h/sub 2/o, co-h/sub 2/o, h/sub 2/-co-h/sub 2/o, and h/sub 2/s-h/sub 2/o, https://doi.org/10.2172/6782591

Gotzias, A., Tylianakis, E., Froudakis, G., & Steriotis, T., (2012), Theoretical study of hydrogen adsorption in oxygen functionalized carbon slit pores, *Microporous and Mesoporous Materials*, *154*, 38–44, https://doi.org/10.1016/j.micromeso.2011.10.011

Grambow, B., (2016), Geological disposal of radioactive waste in clay, *Elements*, *12*, 239–245, https://doi.org/10.2113/gselements.12.4.239

Grekov, D. I., Suzuki-Muresan, T., Kalinichev, A. G., Pré, P., & Grambow, B., (2020), Thermodynamic data of adsorption reveal the entry of ch4 and co2 in a smectite clay interlayer, *Phys. Chem. Chem. Phys.*, *22*, 16727–16733, https://doi.org/10.1039/D0CP02135K

Grim, R., (1968), *Clay mineralogy* (Second), McGraw-Hill.

Hedin, A., & Olsson, O., (2016), Crystalline rock as a repository for swedish spent nuclear fuel, *Elements*, *12*, 247–252, https://doi.org/10.2113/gselements.12.4.247

Heinz, H., Lin, T.-J., Kishore Mishra, R., & Emami, F. S., (2013), Thermodynamically consistent force fields for the assembly of inorganic, organic, and biological nanostructures: the interface force field, *Langmuir*, *29 6*, 1754–1765, https://doi.org/10.1021/la3038846

Heinz, H., Vaia, R., & Farmer, B., (2006), Interaction energy and surface reconstruction between sheets of layered silicates, *Journal of Chemical Physics*, *124 22*, https://doi.org/10.1063/1.2202330

Hinchliffe, A., (2003), *Molecular modelling for beginners*, Chichester, West Sussex, England ; Hoboken, NJ : Wiley, c2003.

Hirschfelder, J. O., Curtiss, C. F. ., & Bird, R. B., (1954), Molecular theory of gases and liquids.

Hwang, J., Joss, L., & Pini, R., (2019), Measuring and modelling supercritical adsorption of co 2 and ch 4 on montmorillonite source clay, *Microporous and Mesoporous Materials*, *273*, 107–121, https://doi.org/10.1016/j.micromeso.2018.06.050

Hwang, J., & Pini, R., (2019), Supercritical co2 and ch4 uptake by illite-smectite clay minerals, *Environmental Science Technology*, *53*, 11588–11596, https://doi.org/10.1021/acs.est.9b03638

IAEA, (2020), *Design principles and approaches for radioactive waste repositories* (NW-T-1.27), INTERNATIONAL ATOMIC ENERGY AGENCY, https://www.iaea.org/publications/13510/design-principles-and-approaches-for-radioactive-waste-repositories

IAEA, (2022), *Iaea mission says finland committed to the safe regulation and management of radioactive waste*. https://www.iaea.org/newscenter/pressreleases/iaea-mission-says-finland-committed-to-the-safe-regulation-and-management-of-radioactive-waste

Ji, L., Zhang, T., Milliken, K. L., Qu, J., & Zhang, X., (2012), Experimental investigation of main controls to methane adsorption in clay-rich rocks, *Applied Geochemistry*, *2712*, 2533–2545, https://doi.org/10.1016/j.apgeochem.2012.08.027

Jin, Z., & Firoozabadi, A., (2013), Methane and carbon dioxide adsorption in clay-like slit pores by monte carlo simulations, *Fluid Phase Equilibria*, *360*, 456–465, https://doi.org/10.1016/j.fluid.2013.09.047

Jin, Z., & Firoozabadi, A., (2014), Effect of water on methane and carbon dioxide sorption in clay minerals by monte carlo simulations, *Fluid Phase Equilibria*, *382*, 10–20, https://doi.org/10.1016/j.fluid.2014.07.035

Jorgensen, W. L., Chandrasekhar, J., Madura, J. D., Impey, R. W., & Klein, M. L., (1983), Comparison of simple potential functions for simulating liquid water, *The Journal of Chemical Physics*, *792*, 926–935, https://doi.org/10.1063/1.445869

Kadoura, A., Nair, A., & Sun, S., (2016), Adsorption of carbon dioxide, methane, and their mixture by montmorillonite in the presence of water, *Microporous and Mesoporous Materials*, *225*, 331–341, https://doi.org/10.1016/j.micromeso.2016.01.010

Karki, S., & Chakraborty, S. N., (2021), A Monte Carlo simulation study of hydrogen adsorption in slit-shaped pores, *Microporous and Mesoporous Materials*, *317February*, 2–11, https://doi.org/10.1016/j.micromeso.2021.110970

Kaye, S. S., Dailly, A., Yaghi, O. M., & Long, J. R., (2007), Impact of preparation and handling on the hydrogen storage properties of zn4o(1,4-benzenedicarboxylate)3 (mof-5) [PMID: 17967030], *Journal of the American Chemical Society*, *12946*, 14176–14177, https://doi.org/10.1021/ja076877g

Laverov, N. P., Yudintsev, S. V., Kochkin, B. T., & Malkovsky, V. I., (2016), The russian strategy of using crystalline rock as a repository for nuclear waste, *Elements*, *12*, 253–256, https://doi.org/10.2113/gselements.12.4.253

Lee, J. H., & Guggenheim, S., (1981), Single-crystal x-ray refinement of pyrophyllite-1tc, *Am. Mineral*, *66*, 350–357.

Lee, M.-S., McGrail, B., Rousseau, R., & Glezakou, V.-A., (2018), A molecular level investigation of ch 4 and co 2 adsorption in hydrated ca-montmorillonite, *The Journal of Physical Chemistry C*, *122*, 1125–1134, https://doi.org/10.1021/acs.jpcc.7b05364

Li, H., Eddaoudi, M., Groy, T. L., & Yaghi, O. M., (1998), Establishing microporosity in open metalorganic frameworks: gas sorption isotherms for zn(bdc) (bdc = 1,4-benzenedicarboxylate), *Journal of the American Chemical Society*, *120*, 8571–8572.

Li, P., Roberts, B. P., Chakravorty, D. K., & Merz, K. M. J., (2013), Rational design of particle mesh ewald compatible lennard-jones parameters for +2 metal cations in explicit solvent [PMID: 23914143], *Journal of Chemical Theory and Computation*, *96*, 2733–2748, https://doi.org/10.1021/ct400146w

Li, P., Song, L. F., & Merz, K. M., (2015), Systematic parameterization of monovalent ions employing the nonbonded model, *Journal of Chemical Theory and Computation*, *114*, 1645–1657, https://doi.org/10.1021/ct500918t

Liu, J., Johnson, K., Culp, J., Natesakhawat, S., Bockrath, B., Sankar, S. G., Zande, B., & Garberoglio, G., (2007), Experimental and theoretical studies of gas adsorption in Cu3(Btc)2, *2007 AIChE Annual Meeting*, *3*, 9305–9313.

Liu, J., Wang, S., Javadpour, F., Feng, Q., & Cha, L., (2022), Hydrogen Diffusion in Clay Slit: Implications for the Geological Storage, *Energy and Fuels*, *36 14*, 7651–7660, https://doi.org/10.1021/acs.energyfuels.2c01189

Loganathan, N., Bowers, G. M., Yazaydin, A. O., Kalinichev, A. G., & Kirkpatrick, R. J., (2018), Competitive adsorption of h2o and co2 in 2-dimensional nanoconfinement: gcmd simulations of cs- and ca-hectorites, *Journal of Physical Chemistry C*, *122 41*, 23460–23469, https://doi.org/10.1021/acs.jpcc.8b06602

Loganathan, N., Bowers, G. M., Yazaydin, A. O., Schaef, H. T., Loring, J., Kalinichev, A. G., & Kirkpatrick, R. J., (2018), Clay swelling in dry supercritical carbon dioxide: effects of interlayer cations on the structure, dynamics, and energetics of co2 intercalation probed by xrd, nmr, and gcmd simulations, *Journal of Physical Chemistry C*, *122 8*, 4391–4402, https://doi.org/10.1021/acs.jpcc.7b12270

Loganathan, N., Yazaydin, A. O., Bowers, G. M., Kalinichev, A. G., & Kirkpatrick, R. J., (2017), Molecular dynamics study of co2 and h2o intercalation in smectite clays: effect of temperature and pressure on interlayer structure and dynamics in hectorite, *Journal of Physical Chemistry C*, *121 39*, https://doi.org/10.1021/acs.jpcc.7b06825

Loganathan, N., Yazaydin, A. O., Bowers, G. M., Ngouana-Wakou, B. F., Kalinichev, A. G., & Kirkpatrick, R. J., (2020), Role of cations in the methane/carbon dioxide partitioning in nano- and mesopores of illite using constant reservoir composition molecular dynamics simulation, *The Journal of Physical Chemistry C*, *124 4*, 2490–2500, https://doi.org/10.1021/acs.jpcc.9b10051

Ma, Z., Pathegama Gamage, R., Rathnaweera, T., & Kong, L., (2019), Review of application of molecular dynamic simulations in geological high-level radioactive waste disposal, *Applied Clay Science*, *168*, 436–449, https://doi.org/https://doi.org/10.1016/j.clay.2018.11.018

Martos-Villa, R., Mata, M. d. P., & Sainz-Díaz, C. I., (2014), Characterization of co2 and mixed methane/co2 hydrates intercalated in smectites by means of atomistic calculations, *Journal of molecular graphics modelling*, *49*, 80–90, https://doi.org/10.1016/j.jmgm.2014.01.008

Maruthi Sena, M., & Krishnan, M., (2019), Role of cations in adsorption of supercritical carbon dioxide at smectite mineral–water interfaces: molecular dynamics and adaptive biasing force simulation studies, *The Journal of Physical Chemistry C*, *123 2*, 1170–1184, https://doi.org/10.1021/acs.jpcc.8b08594

Marx, D., & Nielaba, P., (1992), Path-integral Monte Carlo techniques for rotational motion in two dimensions: Quenched, annealed, and no-spin quantum-statistical averages, *Physical Review A*, *45 12*, 8968–8971, https://doi.org/10.1103/PhysRevA.45.8968

Mayo, S. L., Olafson, B. D., & Goddard, W. A., (1990), DREIDING: A generic force field for molecular simulations, *Journal of Physical Chemistry*, *94 26*, 8897–8909, https://doi.org/10.1021/j100389a010

Metlay, D. S., (2016), Selecting a site for a radioactive waste respository: a historical analysis, *Elements*, *12*, 269–274, https://doi.org/10.2113/gselements.12.4.269

Metropolis, N., Rosenbluth, A. W., Rosenbluth, M. N., Teller, A. H., & Teller, E., (1953), Equation of State Calculations by Fast Computing Machines, *The Journal of Chemical Physics*, *6*, 1087–1092.

Misaelides, P., (2019), Clay minerals and zeolites for radioactive waste immobilization and containment: A concise overview. *In Modified clay and zeolite nanocomposite materials: environmental and pharmaceutical applications* (pp. 243–274), Elsevier, https://doi.org/10.1016/B978-0-12-814617-0.00004-9

Molpeceres, G., & Kästner, J., (2020), Adsorption of h2 on amorphous solid water studied with molecular dynamics simulations, *Phys. Chem. Chem. Phys.*, *22*, 7552–7563, https://doi.org/10.1039/D0CP00250J

Mondal, S., Ghosh, S., & Chattaraj, P. K., (2013), A molecular dynamics study on sI hydrogen hydrate, *Journal of Molecular Modeling*, *19 7*, 2785–2790, https://doi.org/10.1007/s00894-012-1625-7

Mondelli, C., Bardelli, F., Vitillo, J., Didier, M., Brendlé, J., Cavicchia, D., Robinet, J.-C., & Charlet, L., (2015), Hydrogen adsorption and diffusion in synthetic na-montmorillonites at high pressures and temperature, *International Journal of Hydrogen Energy*, *40*, https://doi.org/10.1016/j.ijhydene.2014.12.038

Murray, H. H., (2007), *Applied clay mineralogy: occurrences, processing and applications of kaolins, bentonites, palygorskite-sepiolite, and common clays.* (Vol. 2), Elsevier.

Nagra, (2002), *Project opalinus clay: safety report: demonstration of disposal feasibility for spent fuel, vitrified high-level waste and long-lived intermediate-level waste (entsorgungsnachweis).*

Najafabadi, R., & Yip, S., (1983), Observations of finite-temperature strain transformation (f.c.c.-b.c.c.) in monte carlo simulation of iron, *Scripta Metall.*, 1199–1204.

NEA, (2001), *Gas generation and migration in radioactive waste disposal safety-relevant issues*, OECD Publishing.

NEA, (2003), *Engineered barrier systems and the safety of deep geological repositories*, OECD Publishing, http://www.oecd-nea.org/rwm/reports/2003/nea3615-ebs.pdf

Ngouana W., B. F., & Kalinichev, A. G., (2014), Structural arrangements of isomorphic substitutions in smectites: molecular simulation of the swelling properties, interlayer structure, and dynamics of hydrated cs-montmorillonite revisited with new clay models, *Journal of Physical Chemistry C*, *118 24*, 12758–12773, https://doi.org/10.1021/jp500538z

Ngouana Wakou, B. F., (2014, April), *Modélisation moléculaire de l'hydratation, de la structure, et de la mobilité des ions et de l'eau dans l'espace interfoliaire et à la surface d'une argile smectitique* (Publication No. 2014EMNA0131) [Theses]. Ecole des Mines de Nantes, https://theses.hal.science/tel-01002256

Norman, G., & Filinov, V., (1969), Investigation of phase transitions by a monte-carlo method, *High Temp.(USSR)*, 216–222.

ONDRAF/NIRAS, (2011), *Waste plan for the long-term management of conditioned high-level and/or long-lived radioactive waste and overview of related issues* (NIROND 2011-02 E).

Owusu, J. P., Karalis, K., Prasianakis, N. I., & Churakov, S. V., (2022), Mobility of Dissolved Gases in Smectites under Saturated Conditions: Effects of Pore Size, Gas Types, Temperature, and Surface Interaction, *Journal of Physical Chemistry C*, *126 40*, 17441–17455, https://doi.org/10.1021/acs.jpcc.2c05678

Panagiotopoulos, A. Z., (1987), Direct determination of phase coexistence properties of fluids by monte carlo simulation in a new ensemble, *Molecular Physics*, *61 4*, 813–826, https://doi.org/10.1080/00268978700101491

Peng, D.-y., & Robinson, D. B., (1976), A New Two-Constant Equation of State, *15 1*, 59–64.

Pouvreau, M., Greathouse, J. A., Cygan, R. T., & Kalinichev, A. G., (2017), Structure of Hydrated Gibbsite and Brucite Edge Surfaces: DFT Results and Further Development of the ClayFF Classical Force Field with Metal-O-H Angle Bending Terms, *Journal of Physical Chemistry C*, *121 27*, 14757–14771, https://doi.org/10.1021/acs.jpcc.7b05362

Pouvreau, M., Greathouse, J. A., Cygan, R. T., & Kalinichev, A. G., (2019), Structure of Hydrated Kaolinite Edge Surfaces: DFT Results and Further Development of the ClayFF Classical Force Field with Metal-O-H Angle Bending Terms, *Journal of Physical Chemistry C*, *123 18*, 11628–11638, https://doi.org/10.1021/acs.jpcc.9b00514

Rahbari, A., Brenkman, J., Hens, R., Ramdin, M., van den Broeke, L. J. P., Schoon, R., Henkes, R., Moultos, O. A., & Vlugt, T. J. H., (2019), Solubility of water in hydrogen at high pressures: a molecular simulation study, *Journal of Chemical & Engineering Data*, *64 9*, 4103–4115, https://doi.org/10.1021/acs.jced.9b00513

Rappe, A. K., Casewit, C. J., Colwell, K. S., Goddard, W. A. I., & Skiff, W. M., (1992), Uff, a full periodic table force field for molecular mechanics and molecular dynamics simulations, *Journal of the American Chemical Society*, *114 25*, 10024–10035, https://doi.org/10.1021/ja00051a040

Ryan, P., Broadbelt, L. J., & Snurr, R. Q., (2008), Is catenation beneficial for hydrogen storage in metal–organic frameworks?, *Chem. Commun.*, 4132–4134, https://doi.org/10.1039/B804343D

Sabo, D., Rempe, S. B., Greathouse, J. A., & Martin, M. G., (2006), Molecular studies of the structural properties of hydrogen gas in bulk water, *Molecular Simulation*, *32 3-4*, 269–278, https://doi.org/10.1080/08927020600728621

Sadus, R. J., (2002), *Molecular simulations of fluids theory, algorithms and object-orientation.*

Sellin, P., & Leupin, O. X., (2014), The use of clay as an engineered barrier in radioactive-waste management - a review, *Clays and Clay Minerals*, *61*, 477–498, https://doi.org/10.1346/CCMN.2013.0610601

Sena, M. M., Morrow, C. P., Kirkpatrick, R. J., & Krishnan, M., (2015), Supercritical Carbon Dioxide at Smectite Mineral-Water Interfaces: Molecular Dynamics and Adaptive Biasing Force Investigation of CO2/H2O Mixtures Nanoconfined in Na-Montmorillonite, *Chemistry of Materials*, *2720*, 6946–6959, https://doi.org/10.1021/acs.chemmater.5b01855

Silvera, I. F., & Goldman, V. V., (1978), The isotropic intermolecular potential for H2 and D2 in the solid and gas phases, *The Journal of Chemical Physics*, *699*, 4209–4213, https://doi.org/10.1063/1.437103

Skoulidas, A. I., & Sholl, D. S., (2005), Self-diffusion and transport diffusion of light gases in metal-organic framework materials assessed using molecular dynamics simulations, *Journal of Physical Chemistry B*, *10933*, 15760–15768, https://doi.org/10.1021/jp051771y

Smirnov, G. S., & Stegailov, V. V., (2013), Toward determination of the new hydrogen hydrate clathrate structures, *Journal of Physical Chemistry Letters*, *421*, 3560–3564, https://doi.org/10.1021/jz401669d

Swift, P. N., & Bonano, E. J., (2016), Geological disposal of nuclear waste in tuff: yucca mountain (usa), *Elements*, *12*, 263–268, https://doi.org/10.2113/gselements.12.4.263

Teich-McGoldrick, S. L., Greathouse, J. A., Jové-Colón, C. F., & Cygan, R. T., (2015), Swelling Properties of Montmorillonite and Beidellite Clay Minerals from Molecular Simulation: Comparison of Temperature, Interlayer Cation, and Charge Location Effects, *Journal of Physical Chemistry C*, *11936*, 20880–20891, https://doi.org/10.1021/acs.jpcc.5b03253

Truche, L., Berger, G., Albrecht, A., & Domergue, L., (2013), Engineered materials as potential geocatalysts in deep geological nuclear waste repositories: a case study of the stainless steel catalytic effect on nitrate reduction by hydrogen, *Applied*

Geochemistry, *35*, 279–288, https://doi.org/https://doi.org/10.1016/j.apgeochem.2013.05.001

Truche, L., Joubert, G., Dargent, M., Martz, P., Cathelineau, M., Rigaudier, T., & Quirt, D., (2018), Clay minerals trap hydrogen in the earth's crust: evidence from the cigar lake uranium deposit, athabasca, *Earth and Planetary Science Letters*, *493*, 186–197, https://doi.org/https://doi.org/10.1016/j.epsl.2018.04.038

Tsimpanogiannis, I. N., Maity, S., Celebi, A. T., & Moultos, O. A., (2021), Engineering Model for Predicting the Intradiffusion Coefficients of Hydrogen and Oxygen in Vapor, Liquid, and Supercritical Water based on Molecular Dynamics Simulations, *Journal of Chemical and Engineering Data*, *66 8*, 3226–3244, https://doi.org/10.1021/acs.jced.1c00300

Walton, K. S., Millward, A. R., Dubbeldam, D., Frost, H., Low, J. J., Yaghi, O. M., & Snurr, R. Q., (2008), Understanding inflections and steps in carbon dioxide adsorption isotherms in metal-organic frameworks [PMID: 18154291], *Journal of the American Chemical Society*, *130 2*, 406–407, https://doi.org/10.1021/ja076595g

Wiebe, R., & Gaddy, V., (1934), The solubility of hydrogen in water at 0, 50, 75 and 100 from 25 to 1000 atmospheres, *J. Am. Chem. Soc.*, *56*, https://doi.org/10.1021/ja01316a022

Yang, N., Liu, S., & Yang, X., (2015), Molecular simulation of preferential adsorption of co2 over ch4 in na-montmorillonite clay material, *Applied Surface Science*, *356*, 1262–1271, https://doi.org/10.1016/j.apsusc.2015.08.101

Young, D. C., (2001), *A practical guide for applying techniques to real-world problems*.

Zhang, J., Clennell, M., Liu, K., Pervukhina, M., Chen, G., & Dewhurst, D., (2016), Methane and carbon dioxide adsorption on illite, *Energy Fuels*, *30*, https://doi.org/10.1021/acs.energyfuels.6b01776

Zhang, S., Liu, Q., Gao, F., Ma, R., Wu, Z., & Teppen, B. J., (2018), Interfacial Structure and Interaction of Kaolinite Intercalated with N-methylformamide Insight from Molecular Dynamics Modeling, *Applied Clay Science*, *158*, 204–210, https://doi.org/10.1016/j.clay.2018.03.032

Ziemiański, P. P., & Derkowski, A., (2022), Structural and textural control of high-pressure hydrogen adsorption on expandable and non-expandable clay minerals in geologic conditions, *International Journal of Hydrogen Energy*, *4767*, 28794–28805, https://doi.org/https://doi.org/10.1016/j.ijhydene.2022.06.204

Ziemiański, P. P., Derkowski, A., Szczurowski, J., & Kozieł, M., (2020), The structural versus textural control on the methane sorption capacity of clay minerals, *International Journal of Coal Geology*, *224 December 2019*, https://doi.org/10.1016/j.coal.2020.103483

Appendix A

Ca- and Cs-montmorillonite models

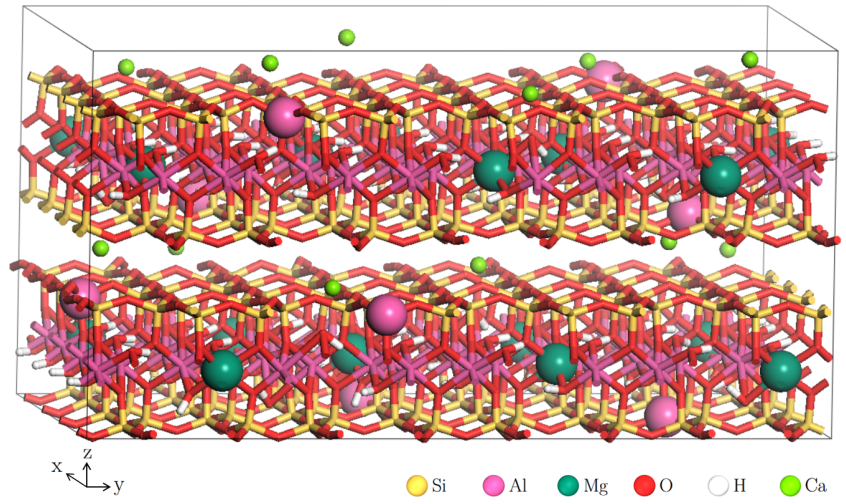

(a)

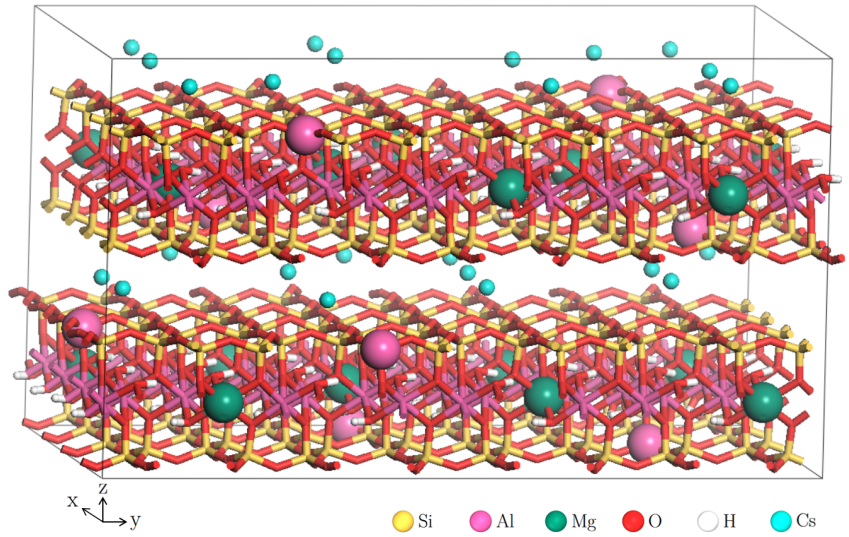

(b)

Figure A.1 – Snapshot of a) dry Ca-montmorillonite and b) dry Cs-montmorillonite model after energy minimization. Color legend: Si (yellow), Al (pink), Mg (dark green); O (red); H (white), Ca (light green), Cs (light blue).

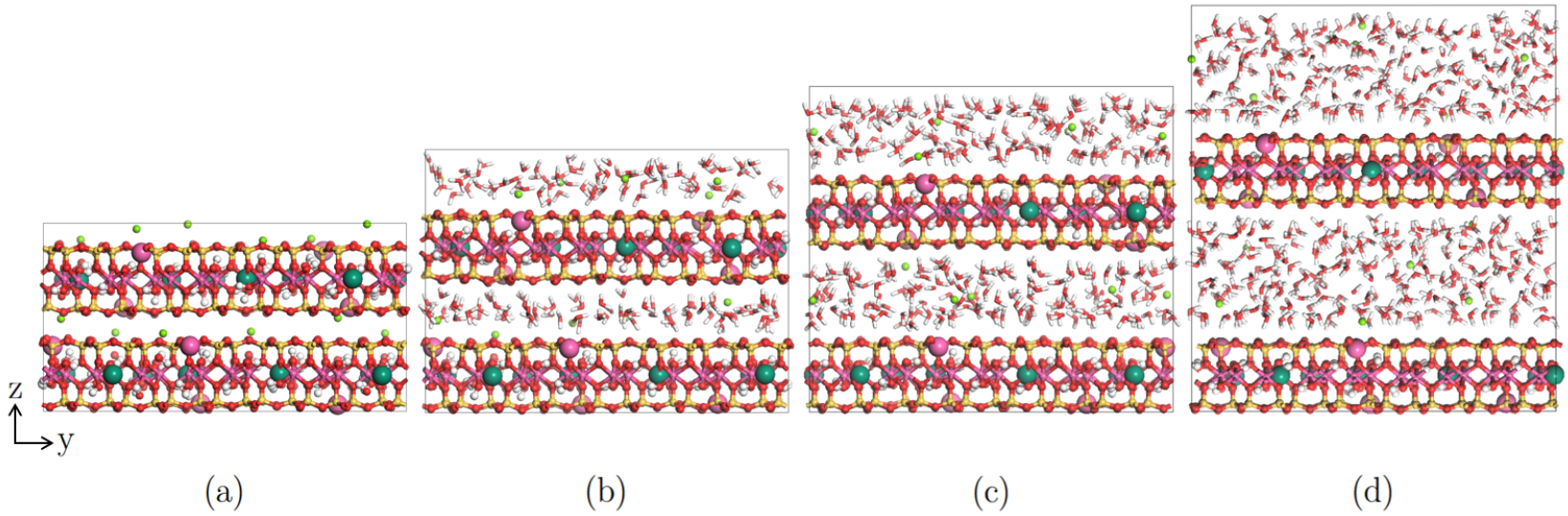

Figure A.2 – Snapshots of a) dry and b) mono-, c) bi- and d) tri-layer hydrated Ca-montmorillonite models. Color legend: Si (yellow), Al (pink), Mg (dark green); O (red); H (white), Ca (light green).

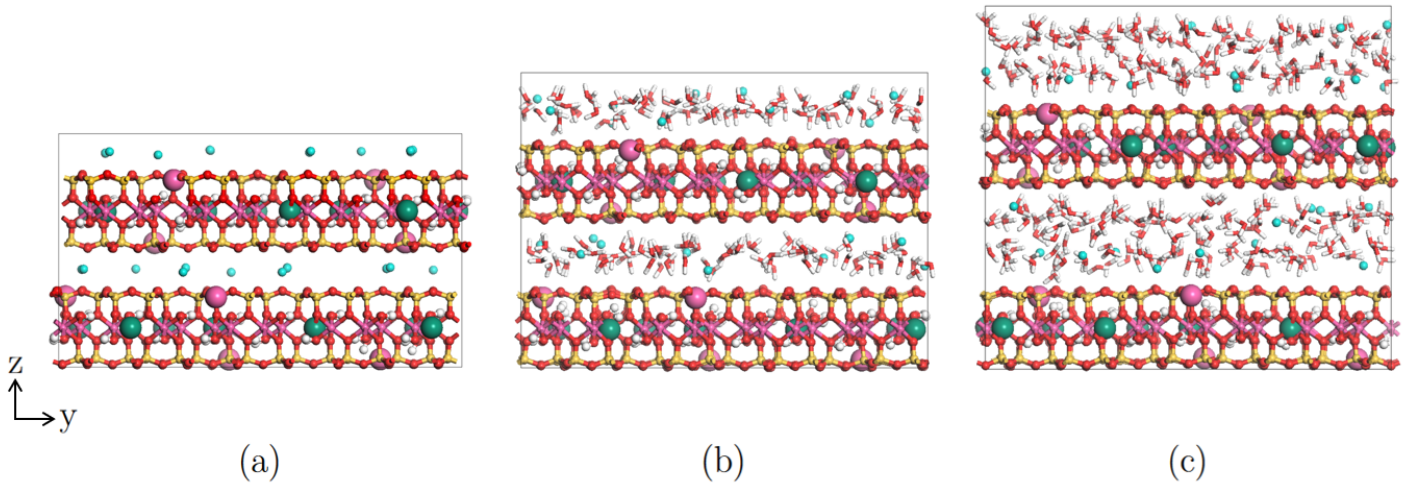

Figure A.3 – Snapshots of a) dry and b) mono-, c) bi- and d) tri-layer hydrated Cs-montmorillonite models. Color legend: Si (yellow), Al (pink), Mg (dark green); O (red); H (white), Cs (blue).

Appendix B

Mol fractions of H_2 and H_2O in H_2O-H_2 mixtures

Table B.1 – Mol fractions of H_2 and H_2O in H_2O-H_2 mixtures at 298 [1,2], 323 [1,2], and 363 [2,3] K up to 120 bar

Temperature (K)	Pressure (bar)	x_{H_2}	x_{water}
298 [1,2]	1	0.00005	0.99995
	20	0.00029	0.99971
	40	0.00055	0.99945
	60	0.00082	0.99918
	80	0.00110	0.99890
	100	0.00138	0.99862
	120	0.00166	0.99834
323 [1,2]	1	0.00004	0.99996
	20	0.00027	0.99973
	40	0.00051	0.99949
	60	0.00076	0.99924
	80	0.00102	0.99898
	100	0.00128	0.99872
	120	0.00153	0.99847
363 [2,3]	1	0.000001	0.999999
	20	0.00027	0.99973
	40	0.00055	0.99945
	60	0.00082	0.99918
	80	0.00109	0.99891
	100	0.00135	0.99865
	120	0.00161	0.99839

[1]Wiebe and Gaddy, 1934, [2]Rahbari et al., 2019, [3]Gillespie and Wilson, 1980

Table B.2 – Mol fractions of H_2 and H_2O in H_2O-H_2 mixtures at 298 K up to 1000 bar [1,2]

Pressure (bar)	x_{H_2}	x_{water}
200	0.00267	0.99733
300	0.00395	0.99605
400	0.00518	0.99482
500	0.00638	0.99362
600	0.00755	0.99245
700	0.00868	0.99132
800	0.00978	0.99022
900	0.01084	0.98916
1000	0.01187	0.98813

[1]Wiebe and Gaddy, 1934, [2]Rahbari et al., 2019

Appendix C

Tabulated data of H_2 adsorption and water content in Na-montmorillonite

Table C.1 – Adsorbed amount of H_2 and water content in 1W-Na-mmt at 298 K up to 120 bar in molecule per supercell

Pressure (bar)	Adsorbed H_2 (molecule/supercell)			Water content (molecule/supercell)		
	Absolute	Excess	Error	Absolute	Excess	Error
1	0.00	0.00	0.00	-	-	-
20	0.39	0.35	0.15	179.28	41.74	0.94
40	0.54	0.47	0.19	182.16	44.63	0.92
60	0.74	0.63	0.22	178.97	41.44	0.76
80	1.10	0.94	0.29	179.04	41.52	0.72
100	1.25	1.06	0.20	178.93	41.42	0.98
120	2.08	1.85	0.49	181.06	43.56	1.88

Table C.2 – Adsorbed amount of H_2 and water content in 1W-Na-mmt at 323 K up to 120 bar in molecule per supercell

Pressure (bar)	Adsorbed H_2 (molecule/supercell)			Water content (molecule/supercell)		
	Absolute	Excess	Error	Absolute	Excess	Error
1	0.00	0.00	0.00	-	-	-
20	0.00	0.00	0.00	-	-	-
40	0.27	0.20	0.06	178.17	42.97	0.80
60	0.40	0.30	0.06	178.51	43.31	1.17
80	0.58	0.44	0.14	176.84	41.64	1.03
100	0.63	0.45	0.14	177.60	42.39	0.71
120	0.77	0.57	0.19	177.07	41.86	1.03

Table C.3 – Adsorbed amount of H_2 and water content in 1W-Na-mmt at 363 K up to 120 bar in molecule per supercell

Pressure (bar)	Adsorbed H_2 (molecule/supercell)			Water content (molecule/supercell)		
	Absolute	Excess	Error	Absolute	Excess	Error
1	0.00	0.00	0.00	-	-	-
20	0.00	0.00	0.00	-	-	-
40	0.11	0.04	0.02	173.08	42.10	0.88
60	0.19	0.08	0.02	172.31	41.32	0.77
80	0.24	0.09	0.03	173.27	42.26	1.35
100	0.27	0.10	0.05	174.01	42.98	1.23
120	0.32	0.11	0.03	173.51	42.47	0.90

Table C.4 – Adsorbed amount of H_2 and water content in 2W-Na-mmt at 298 K up to 120 bar in molecule per supercell

Pressure (bar)	Adsorbed H_2 (molecule/supercell)			Water content (molecule/supercell)		
	Absolute	Excess	Error	Absolute	Excess	Error
1	0.00	0.00	0.00	-	-	-
20	0.67	0.59	0.08	346.75	82.77	1.13
40	1.21	1.06	0.20	347.45	83.47	2.11
60	1.83	1.62	0.21	347.27	83.30	1.24
80	2.49	2.20	0.30	345.90	81.95	0.99
100	3.46	3.10	0.40	343.08	79.15	1.46
120	4.13	3.69	0.50	342.48	78.56	2.28

Table C.5 – Adsorbed amount of H_2 and water content in 2W-Na-mmt at 323 K up to 120 bar in molecule per supercell

Pressure (bar)	Adsorbed H_2 (molecule/supercell)			Water content (molecule/supercell)		
	Absolute	Excess	Error	Absolute	Excess	Error
1	0.00	0.00	0.00	-	-	-
20	0.00	0.00	0.00	-	-	-
40	0.61	0.47	0.06	338.90	79.40	1.05
60	0.94	0.74	0.11	338.00	78.49	0.92
80	1.23	0.97	0.13	338.56	79.05	1.31
100	1.51	1.18	0.15	340.19	80.68	1.47
120	1.65	1.26	0.21	339.94	80.41	1.55

Table C.6 – Adsorbed amount of H_2 and water content in 2W-Na-mmt at 363 K up to 120 bar in molecule per supercell

Pressure (bar)	Adsorbed H_2 (molecule/supercell)			Water content (molecule/supercell)		
	Absolute	Excess	Error	Absolute	Excess	Error
1	0.00	0.00	0.00	-	-	-
20	0.00	0.00	0.00	-	-	-
40	0.26	0.12	0.02	330.05	78.66	1.23
60	0.36	0.15	0.03	330.14	78.71	1.50
80	0.48	0.21	0.04	330.68	79.23	1.61
100	0.61	0.27	0.05	329.54	78.06	1.43
120	0.75	0.35	0.09	328.93	77.41	1.55

Table C.7 – Adsorbed amount of H_2 and water content in 3W-Na-mmt at 298 K up to 120 bar in molecule per supercell

Pressure (bar)	Adsorbed H_2 (molecule/supercell)			Water content (molecule/supercell)		
	Absolute	Excess	Error	Absolute	Excess	Error
1	0.00	0.00	0.00	-	-	-
20	1.35	1.22	0.14	556.99	116.55	1.46
40	2.68	2.44	0.17	553.90	113.48	1.62
60	4.04	3.68	0.48	557.01	116.60	2.76
80	4.51	4.02	0.54	556.34	115.96	1.64
100	6.36	5.75	0.71	554.82	114.46	1.71
120	7.89	7.16	0.59	552.37	112.05	2.10

Table C.8 – Adsorbed amount of H_2 and water content in 3W-Na-mmt at 323 K up to 120 bar in molecule per supercell

Pressure (bar)	Adsorbed H_2 (molecule/supercell)			Water content (molecule/supercell)		
	Absolute	Excess	Error	Absolute	Excess	Error
1	0.00	0.00	0.00	-	-	-
20	0.00	0.00	0.00	-	-	-
40	1.15	0.93	0.08	547.74	114.79	2.52
60	1.88	1.55	0.15	546.37	113.40	1.92
80	2.25	1.81	0.21	546.16	113.19	2.14
100	2.91	2.36	0.23	547.72	114.74	1.98
120	3.25	2.59	0.32	547.17	114.18	2.38

Table C.9 – Adsorbed amount of H_2 and water content in 3W-Na-mmt at 363 K up to 120 bar in molecule per supercell

Pressure (bar)	Adsorbed H_2 (molecule/supercell)			Water content (molecule/supercell)		
	Absolute	Excess	Error	Absolute	Excess	Error
1	0.00	0.00	0.00	-	-	-
20	0.00	0.00	0.00	-	-	-
40	0.46	0.23	0.02	531.68	112.26	1.77
60	0.73	0.39	0.05	531.34	111.86	1.41
80	0.94	0.49	0.06	532.69	113.16	1.98
100	1.18	0.62	0.05	532.05	112.46	1.86
120	1.36	0.68	0.09	533.59	113.94	1.85

Table C.10 – Adsorbed amount of H_2 and water content in 2W-Na-mmt at 298K up to 1000 bar in molecule per supercell

Pressure (bar)	Adsorbed H_2 (molecule/supercell)			Water content (molecule/supercell)		
	Absolute	Excess	Error	Absolute	Excess	Error
1	0.00	0.00	0.00	-	-	-
20	0.67	0.59	0.08	346.75	82.77	1.13
40	1.21	1.06	0.20	347.45	83.47	2.11
60	1.83	1.62	0.21	347.27	83.30	1.24
80	2.49	2.20	0.30	345.90	81.95	0.99
100	3.46	3.10	0.40	343.08	79.15	1.46
120	4.13	3.69	0.50	342.48	78.56	2.28
200	6.74	6.03	0.67	341.76	77.88	1.73
300	9.84	8.79	1.10	338.85	75.02	2.15
400	11.86	10.49	1.42	338.19	74.41	2.61
500	13.85	12.16	1.20	339.03	75.30	2.53
600	16.62	14.61	1.63	336.73	73.03	2.04
700	19.85	17.55	1.81	333.42	69.75	2.99
800	20.45	17.84	1.02	336.17	72.54	1.80
900	22.27	19.38	1.45	334.49	70.88	2.15
1000	26.05	22.89	1.40	332.92	69.33	1.83

Table C.11 – Adsorbed amount of H_2 and water content in 2W-Na-mmt (mobile Na) at 298K up to 120 bar in molecule per supercell

Pressure (bar)	Adsorbed H_2 (molecule/supercell)			Water content (molecule/supercell)		
	Absolute	Excess	Error	Absolute	Excess	Error
1	0.00	0.00	0.00	-	-	-
20	0.77	0.68	0.11	347.80	63.50	1.60
40	1.01	0.85	0.13	352.72	68.44	1.21
60	2.05	1.82	0.21	348.14	63.87	1.63
80	2.75	2.44	0.39	346.49	62.23	1.31
100	3.76	3.36	0.60	343.37	59.13	2.19
120	4.13	3.66	0.57	346.09	61.87	1.77

Table C.12 – Adsorbed amount of H_2 and water content in 2W-Na-mmt (with flexible framework) at 298 K and, 20 and 40 bar in molecule per supercell

Pressure (bar)	Adsorbed H_2 (molecule/supercell)			Water content (molecule/supercell)		
	Absolute	Excess	Error	Absolute	Excess	Error
1	0.00	0.00	0.00	-	-	-
20	0.32	0.24	0.04	378.41	94.12	0.68
40	0.49	0.33	0.09	382.97	98.69	0.63

Appendix D

Tabulated data of H_2 adsorption and water content in Ca-montmorillonite

Table D.1 – Adsorbed amount of H_2 and water content in 2W-Ca-mmt at 298K up to 120 bar in molecule per supercell

Pressure (bar)	Adsorbed H_2 (molecule/supercell)			Water content (molecule/supercell)		
	Absolute	Excess	Error	Absolute	Excess	Error
1	0.00	0.00	0.00	-	-	-
20	1.13	1.04	0.14	353.54	61.81	1.63
40	1.92	1.76	0.22	350.45	58.73	1.26
60	2.50	2.26	0.40	356.14	64.44	1.50
80	3.05	2.73	0.49	354.38	62.69	1.93
100	4.09	3.69	0.38	356.90	65.23	1.44
120	5.36	4.88	0.74	354.34	62.69	2.47

Table D.2 – Adsorbed amount of H_2 and water content in 2W-Ca-mmt at 323 K up to 120 bar in molecule per supercell

Pressure (bar)	Adsorbed H_2 (molecule/supercell)			Water content (molecule/supercell)		
	Absolute	Excess	Error	Absolute	Excess	Error
1	0.00	0.00	0.00	-	-	-
20	0.00	0.00	0.00	-	-	-
40	0.73	0.59	0.08	354.02	73.92	1.21
60	1.05	0.84	0.16	348.50	68.39	2.39
80	1.67	1.39	0.19	348.30	68.19	1.73
100	1.87	1.51	0.29	349.19	69.07	1.65
120	2.11	1.68	0.34	351.00	70.88	1.91

Table D.3 – Adsorbed amount of H_2 and water content in 1W-Ca-mmt at 298K up to 120 bar in mmol/g

Pressure (bar)	Adsorbed H_2 (molecule/supercell)			Water content (molecule/supercell)		
	Absolute	Excess	Error	Absolute	Excess	Error
1	0.00	0.00	0.00	-	-	-
20	0.73	0.68	0.12	193.62	33.36	1.00
40	0.95	0.86	0.14	196.72	36.48	0.68
60	1.79	1.66	0.25	195.87	35.63	1.11
80	2.93	2.76	0.48	192.01	31.78	1.23
100	3.16	2.94	0.39	193.04	32.82	1.21
120	3.40	3.13	0.44	194.80	34.59	1.45

Table D.4 – Adsorbed amount of H_2 and water content in 3W-Ca-mmt at 298 K up to 120 bar in molecule per supercell

Pressure (bar)	Adsorbed H_2 (molecule/supercell)			Water content (molecule/supercell)		
	Absolute	Excess	Error	Absolute	Excess	Error
1	0.00	0.00	0.00	-	-	-
20	1.50	1.37	0.12	560.68	103.63	1.87
40	3.70	3.45	0.34	558.15	101.12	2.37
60	5.21	4.83	0.50	556.29	99.28	1.83
80	5.35	4.85	0.52	563.96	106.98	2.59
100	7.62	6.99	0.62	560.28	103.33	2.29
120	8.90	8.14	0.75	556.28	99.35	2.67

Appendix E

Tabulated data of H_2 adsorption and water content in Cs-montmorillonite

Table E.1 – Adsorbed amount of H_2 in dry-Cs-mmt at 298 K up to 120 bar

Pressure (bar)	Adsorbed H_2 (molecule/supercell)		Desorbed H_2 (molecule/supercell)	
	Absolute	Error	Absolute	Error
1	0.00	0.00	0.00	0.00
20	0.08	0.00	0.08	0.01
40	0.15	0.01	0.15	0.02
60	0.21	0.01	0.23	0.02
80	0.30	0.01	0.31	0.02
100	0.35	0.01	0.38	0.02
120	0.45	0.02	0.47	0.07

Table E.2 – Adsorbed amount of H_2 and water content in 1W-Cs-mmt at 298 K in molecule per supercell

Pressure (bar)	Adsorbed H_2 (molecule/supercell)			Water content (molecule/supercell)		
	Absolute	Excess	Error	Absolute	Excess	Error
1	0.00	0.00	0.00	-	-	-
20	0.52	0.48	0.08	159.29	32.30	1.12
40	0.67	0.60	0.17	159.79	32.81	0.78
60	1.32	1.22	0.21	157.77	30.79	0.74
80	1.71	1.57	0.25	157.82	30.86	1.39
100	2.04	1.86	0.41	156.87	29.92	1.48
120	2.19	1.98	0.52	158.68	31.73	1.22

Table E.3 – Adsorbed amount of H_2 and water content in 2W-Cs-mmt at 298 K up to 120 bar in molecule per supercell

Pressure (bar)	Adsorbed H_2 (molecule/supercell)			Water content (molecule/supercell)		
	Absolute	Excess	Error	Absolute	Excess	Error
1	0.00	0.00	0.00	-	-	-
20	0.80	0.71	0.13	323.73	45.29	1.66
40	1.52	1.37	0.23	324.55	46.12	0.94
60	2.14	1.91	0.37	325.82	47.39	1.85
80	2.86	2.55	0.52	324.78	46.38	2.05
100	4.08	3.69	0.55	322.60	44.21	2.48
120	4.49	4.02	0.56	325.34	46.97	2.02

Table E.4 – Adsorbed and desorbed amount of H_2 in dry-Cs-mmt at 298 K up to 10000 bar in molecule per supercell

Pressure (bar)	Adsorbed H_2 (molecule/supercell)		Desorbed H_2 (molecule/supercell)	
	Absolute	Error	Absolute	Error
1	0.00	0.00	0.00	0.00
20	0.08	0.00	0.08	0.01
40	0.15	0.01	0.15	0.02
60	0.21	0.01	0.23	0.02
80	0.30	0.01	0.31	0.02
100	0.35	0.01	0.38	0.02
120	0.45	0.02	0.47	0.07
200	0.81	0.03	0.81	0.06
300	1.23	0.05	1.21	0.07
400	1.67	0.05	1.59	0.08
500	2.09	0.07	2.18	0.10
600	2.55	0.08	2.73	0.04
700	3.27	0.11	3.28	0.24
800	3.79	0.14	3.87	0.32
900	4.29	0.11	4.54	0.22
1000	5.24	0.16	5.11	0.22
1200	6.94	0.15	-	-
1400	8.62	0.20	-	-
2000	13.57	0.31	14.24	1.03
3000	23.78	0.40	24.35	0.41
4000	31.72	0.25	31.99	0.59
5000	35.86	0.21	35.76	0.52
6000	38.09	0.15	38.18	0.23
7000	39.12	0.10	39.14	0.22
8000	39.61	0.06	39.60	0.16
9000	40.83	0.03	39.84	0.06
10000	39.94	0.03	39.91	0.05

COLLEGE DOCTORAL PAYS DE LA LOIRE
ED MATIERE, MOLECULES MATERIAUX ET GEOSCIENCES

IMT Atlantique
Bretagne-Pays de la Loire
École Mines-Télécom

Titre : Modélisation moléculaire de l'adsorption de l'hydrogène gazeux dans les environnements argileux hydratés dans le contexte de stockage géologique des déchets radioactifs

Mot clés : Simulations moléculaires, adsorption, argiles, montmorillonite, hydrogène

Résumé : Les formations riches en argile sont considérées comme des roches hôtes optimales pour les installations de stockage géologique en profondeur des déchets radioactifs de haute activité. Des gaz, notamment le H_2, peuvent se former au cours du stockage à long terme par des mécanismes tels que la corrosion anoxique et la radiolyse de l'eau, pouvant potentiellement entraîner une accumulation de pression de gaz et des fractures dans la roche hôte environnante. Une compréhension à l'échelle moléculaire du comportement du H_2 dans l'argile est essentielle pour un stockage géologique sûr et efficace, ainsi que pour le développement de stratégies efficaces. Dans cette thèse, la montmorillonite, largement présente dans les compositions de roches hôtes et utilisée comme barrière technique, est choisie comme modèle d'argile. Des simulations atomistiques de l'adsorption de H_2 dans les intercalaires des montmorillonites hydratées de Na, Ca et Cs sont réalisées à 25, 50 et 90°C, jusqu'à 120 bars, en utilisant des méthodes de Monte Carlo et hybrides. À cette fin, l'impact de plusieurs autres facteurs, y compris la présence d'eau et la taille des pores, est étudié, dans le but d'améliorer la compréhension fondamentale des processus physiques et chimiques régissant les interactions entre H_2, les solutions aqueuses et l'argile. De plus, l'adsorption d'hydrogène dans des conditions extrêmes est explorée pour déterminer le point de saturation dans les argiles.

Title: Molecular modeling of hydrogen gas adsorption in hydrated clay environments in the context of geological disposal of radioactive waste

Keywords: Molecular simulations, adsorption, clays, montmorillonite, hydrogen

Abstract: Clay-rich formations are considered as optimal host rock for deep geological repository facilities for high-level radioactive waste. Gas, particularly H_2, may form during long-term storage through mechanisms such as anoxic corrosion and water radiolysis, potentially leading to gas pressure build-up and fractures in the surrounding host rock. Molecular-scale understanding of H_2 behavior in clay is essential for safe geological disposal and storage, and for the developing effective strategies. In this thesis, montmorillonite, which is widely found in host rock compositions and used as an engineered barrier, is chosen as the clay model. Atomistic simulations of H_2 adsorption within the interlayers of hydrated Na-, Ca-, and Cs-montmorillonites are conducted at 25, 50, and 90°C, up to 120 bar using Monte Carlo and hybrid methods. To this end, the impact of several other factors factors, including the presence of water and pore size are investigated, aiming to improve the fundamental understanding of the physical and chemical processes governing interactions among H_2, aqueous solutions, and clay. Furthermore, hydrogen adsorption under extreme conditions is explored to determine the point of saturation in clays.